

Development of a Weakly-Coupled Hybrid Simulation Method for Seismic Assessment and its Application to Reinforced Concrete Building Structure

by

Georgios Giotis

A thesis submitted in conformity with the requirements
for the degree of Master of Applied Science

Department of Civil Engineering
University of Toronto

© Copyright by Georgios Giotis 2017

Development of a Weakly-Coupled Hybrid Simulation Method for Seismic Assessment and its Application to Reinforced Concrete Building Structure

Georgios Giotis

Master of Applied Science

Department of Civil Engineering
University of Toronto

2017

Abstract

Hybrid simulation methods have attracted significant interest from researchers in structural engineering to accurately assess the seismic performance of structures. To implement hybrid simulations in a testing facility, it is necessary to properly control the boundary conditions of physically tested specimens. The objective of this study is to propose and implement a methodology for performing hybrid simulations when a limited number of actuators are available and the full control of the boundary conditions is not possible. The developed methodology is employed to evaluate the seismic performance of a RC structure where one of the first storey columns is experimentally tested with testing equipment which can control only two DOF instead of the three required for columns subjected to planar motions. The seismic assessment is performed for the cases of an intact, repaired and retrofitted structure, where externally applied Carbon Fiber Reinforced Polymer (CFRP) fabric is used for repairing and retrofitting.

Acknowledgments

First and foremost, I would like to express special thanks to my supervisors, Dr. Oh-Sung Kwon and Dr. Shamim A. Sheikh for their continuous support during my graduate studies and my research project by providing me with their advice and expertise. During the course of my M.A.Sc, I was not only given the opportunity to work in a highly reputed university and to enhance my knowledge and technical skills, but my supervisors also instilled in me a general attitude toward studying and life that affected me as a person. I would like also to thank Dr. Anastasios Sextos, for his reference that resulted in my acceptance as a graduate student at the University of Toronto.

I would like to express my gratitude to the structural laboratory and machine shop technical staff of the University of Toronto, Renzo Basset, Giovanni Buzzeo, Michel Fiss, Xiaoming Sun, Bryant Cook and Alan McClenaghan. Without their support and technical advise this project wouldn't have been possible.

Additionally, I would like to thank the following individual fellow students, Zahra Kharal, Xu Huang, Mohamed Sayed, Xuguang Wang, Vahid Sadeghian, Pedram Mortazavi, Saeid Mojiri, Nikolaos Psyrras and Stamatina Chasioti for their advice and their encouragement during the course of my graduate studies and my research. Additionally, I would like to acknowledge the undergraduate student, Adam Parker, who did the editing and the proof reading for the current thesis, in addition to Hankun Ren and Jerry Zhai, without whom this project would have taken much longer.

Last but not least, I would like to express my deepest appreciation to my family for supporting me throughout my path in life, providing me with strong core values and helping me to become a successful member of the society.

This research is funded by the Ontario Early Researcher Award and grants from the Natural Sciences and Engineering Research Council of Canada. The experimental work was carried out in the Structures Laboratories of the University of Toronto.

Table of Contents

Acknowledgments.....	iii
Table of Contents.....	iv
List of Tables	x
List of Figures	xi
Chapter 1 Introduction	1
1 Introduction.....	1
1.1 General.....	1
1.2 Research Objectives.....	2
1.3 Thesis Organization	3
Chapter 2 Literature Review	5
2 Literature Review.....	5
2.1 Seismic Performance Assessment of Structural Systems	5
2.2 Critical Elements – Reinforced Concrete Columns	8
2.2.1 Reinforced Concrete Columns.....	8
2.2.2 FRP Confined Reinforced Concrete Columns.....	13
2.2.3 Conventional Column Testing Practices.....	15
2.3 Hybrid Simulation in Structural Testing.....	16
2.3.1 Background.....	16
2.3.2 Substructuring Techniques.....	18
2.3.3 Time Integration Techniques	19
2.3.4 Hybrid Simulation Frameworks.....	20
2.3.5 Experimental Challenges in Hybrid Simulation	22

Chapter 3 Reference Structure	24
3 Description of the Reference Structure Description and Input Ground Motion	24
3.1 Structure Overview	24
3.1.1 Reinforcement Layout	25
3.1.2 Gravity Load and Mass Distribution.....	27
3.2 Seismic Study Sequence	28
3.2.1 First Ground Motion	28
3.2.2 Second Ground Motion.....	28
3.3 Numerical Model	30
3.3.1 Numerical Model Overview	30
3.3.2 Material Level Modeling Technique	31
3.3.3 Element Level Modeling Technique.....	34
3.4 Preliminary Numerical Investigation.....	36
3.4.1 Eigenvalue Analysis.....	36
3.4.2 Nonlinear Static Pushover Analysis.....	37
3.4.3 Nonlinear Time History Analysis	38
3.5 Critical Element	41
3.5.1 Loading Characteristics	41
3.5.2 Critical Element Response Study.....	43
Chapter 4 Experimental Program.....	48
4 Construction of Column Specimens.....	48
4.1 Introduction.....	48
4.2 Material Properties.....	49
4.2.1 Steel Reinforcing Bars	49
4.2.2 Concrete	50
4.2.3 Carbon Fiber Reinforced Polymer Wrap	52

4.2.4	Repair Mortar	54
4.3	Construction Procedure	55
4.3.1	Reinforcement Cages	55
4.3.2	Formwork Assembly	57
4.3.3	Concrete Casting	59
4.3.4	Repairing and Retrofitting Procedure	59
4.4	Specimens' Instrumentation	64
4.4.1	Strain Gauges	64
4.4.2	Linear Variable Differential Transformers (LVDTs)	65
4.4.3	External Instrumentation used for the Deformation Measurement	66
4.5	Column Testing Frame Description	70
4.5.1	Testing Equipment Overview	70
4.5.2	Specimen Alignment	72
Chapter 5	Weakly-Coupled Hybrid Simulation	74
5	Weakly-Coupled Hybrid Simulation Method	74
5.1	Limitation of the Column Testing Frame	74
5.2	Weakly-Coupled Hybrid Simulation Method	75
5.3	Numerical Verification	77
5.3.1	Network Interface for Console Applications (NICA)	77
5.3.2	Weakly-Coupled Hybrid Simulation	78
5.3.3	Investigation under the Contraflexure Point Assumption	80
5.4	Generalized Weakly-Coupled Method	82
5.4.1	Analytical Study of Generalized Linear Element Cases	83
5.4.2	Parametric Study on the Applicability of WCHS using Nonlinear Frame Element	87
5.4.3	Study Structure and Critical Element Case Applicability	94

Chapter 6 Application of the Weakly-Coupled Method to the Reference Structure	101
6 Application of the Experimental Weakly-Coupled Method to the Reference Structure	101
6.1 Hybrid Simulation Implementation	101
6.1.1 Hybrid Simulation Framework	101
6.1.2 Dedicated Network Interface for Controllers (NICON) for Column Tester Frame	103
6.1.3 Experimental Setup Control System	106
6.2 Coordinate Transformation	108
6.2.1 Displacement Command Transformation	109
6.2.2 Transformation of Measured Force	110
6.2.3 Verification of Coordinate Transformation	111
6.3 Error Compensation Architecture	113
6.3.1 Error Sources	113
6.3.2 Error Compensation Scheme	115
6.3.3 I-modification	116
6.4 Investigation on Axial Response	117
6.4.1 Axial Force and Deformation Fluctuation	117
6.4.2 Axial Response Investigation	119
Chapter 7 Seismic Performance of Intact, Repaired and Retrofitted Reinforced Concrete Structure	122
7 Seismic Performance Assessment of the Structure	122
7.1 Experimental Study Overview	122
7.2 Multiplatform Simulation	125
7.2.1 Multiplatform Simulation Framework	125
7.2.2 Performance Assessment	126
7.3 Intact Structure	130
7.3.1 Hybrid Simulation using the First Specimen	130

7.3.2 Hybrid Simulation using the Second Specimen.....	138
7.4 Repaired Structure	145
7.4.1 Numerical Model Calibration	146
7.4.2 Hybrid Simulation Performance	147
7.4.3 Global Response of the Structure	147
7.4.4 Local Response of the Critical Element.....	149
7.4.5 Numerical Study of the Response of a Non-repaired Damaged Structure	153
7.5 Retrofitted Structure.....	154
7.5.1 Numerical Model Calibration	154
7.5.2 Hybrid Simulation Performance	155
7.5.3 Global Response of the Structure	155
7.5.4 Local Response of the Critical Element.....	157
7.6 Retrofitted Structure under Increased Gravity Loads	161
7.6.1 Numerical Model Modification	161
7.6.2 Hybrid Simulation Performance	164
7.6.3 Global Response of the Structure	164
7.6.4 Local Response of the Critical Element.....	166
7.7 Performance Comparison.....	169
7.8 Repaired Specimens' Constitutive Response.....	171
7.8.1 Quasi-Static Test under Low Constant Axial Load	172
7.8.2 Quasi-static Test under Moderate Constant Axial Load.....	174
7.8.3 Quasi-static Test under High Constant Axial Load	176
Chapter 8 Conclusions	179
8 Conclusions	179
8.1 Summary	179
8.2 Conclusions.....	180

8.3 Recommendations	182
References	184
Appendix A	192
Appendix B	212

List of Tables

Table 2-1: Steel-reinforced column database (Tavassoli 2013).	10
Table 2-2: CFRP-retrofitted columns' database.	14
Table 4-1: Mechanical properties of reinforcing steel.....	50
Table 4-2: Mechanical properties of concrete materials.....	51
Table 4-3: Mechanical properties of CFRP	53
Table 4-4: Mechanical properties of EMACO ® S88 CI Repair Mortar	54
Table 4-5: External Instrument 12 calibration results and reputability errors	69
Table 4-6: Calibration factors for string potentiometers.....	70
Table 5-1: Moment ratio and location of actual contraflexure point (h_2) as a function of stiffness ratio (f)	89
Table 5-2: Stiffness ratio for the internal and external first storey joints.	95
Table 7-1: Test sequence overview.....	123
Table 7-2: Various tests notation as presented in Chapter 7.....	124
Table 7-3: Mechanical properties of concrete materials used for the hybrid simulations with Specimen #1.....	131
Table 7-4: Hybrid simulation performance for the intact structure case using the Specimen #1 (Tests 1.2 & 1.4).	131
Table 7-5: Hybrid simulation performance for the intact structure case using the Specimen #2 (Test 2.1).	138
Table 7-6: Hybrid simulation performance for the repaired structure case using the repaired Specimen #2 (Test 2.2).	147
Table 7-7: Hybrid simulation performance for the retrofitted structure case using the Specimen #3.....	155
Table 7-8: Hybrid simulation performance for the increased weight retrofitted structure (Test 3.2).	164
Table 7-9: Hybrid simulation performance assessment for the various structure cases.	169

List of Figures

Figure 2-1: SEAOC Vision 2000 performance matrix (SEAOC Vision2000 1995).....	6
Figure 2-2: Performance levels according to FEMA-356 (Heintz et al. 2014).	8
Figure 2-3: Calculation of member and section ductility parameters (Sheikh & Khoury 1993)....	9
Figure 2-4: Quasi-static lateral displacement protocol (Ghosh & Sheikh 2008).....	15
Figure 2-5: Schematic diagram of hybrid simulation method (Carrion & Spencer 2007).	18
Figure 3-1 Reference structure's (a) plan and (b) elevation view.	25
Figure 3-2 Beam reinforcement profile (symmetric) (Bracci et al. 1992).....	25
Figure 3-3 Beam typical sections (Bracci et al. 1992).....	26
Figure 3-4 Column reinforcing details: (a) Interior and exterior columns, and (b) middle (Section M) and end (Section 3) column sections.....	26
Figure 3-5 Gravity load and mass distribution.	27
Figure 3-6 First seismic event acceleration time history.	29
Figure 3-7 Second seismic event acceleration time history.....	29
Figure 3-8: Numerical model discretization.	31
Figure 3-9: (a) Concrete cyclic tension-compression response envelope of “Concrete04 Material”, and (b) Steel backbone curve of “Reinforcing Steel Material” as presented in OpenSees manual (Mazzoni et al. 2007).	34
Figure 3-10: Fiber section modeling technique for (a) the columns and (b) the beams of the reference structure.....	35
Figure 3-11: Curvature distribution in displacement beam-column elements (Mazzoni et al. 2007).	35
Figure 3-12: Elastic acceleration response spectra for the study seismic events (Left: Bucharest, Romania 1977& Right: Imperial Valley, USA 1979).	36
Figure 3-13: Normalized response modes.	37
Figure 3-14: Pushover curve (left) and qualitative representation of the failure mechanism (right).	37

Figure 3-15: Storeys' displacement response history.	40
Figure 3-16: Interstorey drifts' response history.	40
Figure 3-17: Moment-curvature response at the lowest integration points of the first storey columns (Left to right as illustrated in Figure 3-1). Initiation of the nonlinear response at $t=1.61s$	40
Figure 3-18: Deformation response history of the critical element during the initial numerical investigation.	42
Figure 3-19: Developed forces history in the critical element during the initial numerical investigation.	42
Figure 3-20: Hysteretic response of the critical element during the initial numerical investigation.	43
Figure 3-21: Sectional response study using Response-2000. (a) Left: monotonic axial loading, and (b) Right: axial load – developed moment relationship curve	44
Figure 3-22: Section discretization into an equivalent orthogonal-composed section	45
Figure 3-23: (a) Left: Membrane discretization in VecTor2, and (b) Right: three-dimensional representation of the specimen in Augustus.	46
Figure 3-24: Cantilever column study. (a) Left: monotonic and quasi-static loading using VecTor2, and (b) Right: monotonic loading in VecTor2 and hysteretic response from preliminary investigation (OS)	47
Figure 4-1: Reinforced concrete specimen: (a) constructed specimen and (b) isometric view.	48
Figure 4-2: Steel coupon testing: (a) necking development in 10M rebar and (b) ruptured 20M rebar coupons.	49
Figure 4-3: Steel coupon testing: (a) necking development in 10M rebar and (b) ruptured 20M rebar coupons.	50
Figure 4-4: Concrete stress-strain curves at 28 days and at the testing time (~180 days).	51
Figure 4-5: Cylinders Testing. (a) Left: Testing Setup (b). Right: Crushed cylinders set.	51
Figure 4-6: Stress-strain curves of confined concrete. Left: columns' confinement. Right: beams' confinement.	52
Figure 4-7: (a) Left: CFRP coupons notated with failure modes (ASTM D3039/3039M 2006), and (b) Right: porcupine roller.	53

Figure 4-8: CFRP stress strain curves.....	53
Figure 4-9: EMACO ® S88CI repair mortar stress strain curves.....	54
Figure 4-10: Construction of the stub reinforcing cages.	55
Figure 4-11: Column reinforcing cages' construction.	56
Figure 4-12: Steel formwork designed by Tavassoli (Tavassoli 2015).	57
Figure 4-13: Formwork assembly stages.	58
Figure 4-14: Concrete casting stages.	60
Figure 4-15: Crushed concrete repair stages.....	61
Figure 4-16: Crack treatment stages.	62
Figure 4-17: Left: Second specimen before (upper figure) and after (lower figure) the repair. Right: Retrofitted third specimen.....	63
Figure 4-18: Strain gauges locations.....	64
Figure 4-19: Strain gauges' installation stages.	65
Figure 4-20: LVDTs' configuration. The red instruments are used for capturing the longitudinal strains and the curvature response, while the blue instruments are used for capturing the shear response.....	66
Figure 4-21: String potentiometers external instrumentation (EI) configuration.	66
Figure 4-22: Geometry, instruments and reference points' notation.	68
Figure 4-23: Left: Calibration equipment. Right: junction box and connection to DAQ.....	69
Figure 4-24: Column Testing Frame (CTF).....	71
Figure 4-25: Idealized cases studied to eliminate the effect of gravity.	73
Figure 5-1: Weakly-coupled hybrid simulation architecture.	76
Figure 5-2: Storeys' displacement comparison between the preliminary investigation (Reference) and the weakly-coupled numerical hybrid simulation (WCHS).....	79
Figure 5-3: Hysteretic response comparison between the preliminary investigation (Reference) and the weakly-coupled numerical hybrid simulation (WCHS).....	79

Figure 5-4: Modified numerical model for the pinned connection case investigation.	81
Figure 5-5: Storeys' displacement comparison between the preliminary investigation and the pinned connection case.....	81
Figure 5-6: Hysteretic response comparison between the preliminary investigation and the pinned connection case.....	82
Figure 5-7: (0) Idealization of linear element and discretization of the (e) experimental and (s) surrogate module.....	83
Figure 5-8: Study element (left) and column's rotational stiffness at the top (right).	88
Figure 5-9: Lateral loading protocol at the top of the column.	89
Figure 5-10: Parametric analysis study cases.	89
Figure 5-11: Local hysteretic response and energy dissipation when $f=1$ and the interface point is considered at the column's mid-height.	91
Figure 5-12: Global hysteretic response and energy dissipation when $f=1$ and the interface point is considered at the column's mid-height.	91
Figure 5-13: Local hysteretic response and energy dissipation when $f=1$ and the interface point is considered at the actual contraflexure location.....	92
Figure 5-14: Global hysteretic response and energy dissipation when $f=1$ and the interface point is considered at the actual contraflexure location.	92
Figure 5-15: Applicability figures of the WCHS for frame elements ranging from wall to column equivalent response.	94
Figure 5-16: Modified numerical model for the rotational stiffness ratio evaluation. Left: joint's rotational stiffness, right: column's rotational stiffness.....	95
Figure 5-17: Fully and weakly-coupled cantilever element.	96
Figure 5-18: Fixed beam deformed shape.	98
Figure 5-19: Coupling variation during the dynamic time history analysis.	100
Figure 6-1: University of Toronto Simulation Framework (UT-SIM) architecture and employed components for the current study.....	102
Figure 6-2: Weakly-coupled hybrid simulation architecture dedicated for the column testing.	103

Figure 6-3: Right: NI USB-6218 BNC data acquisition system. Left: Cabling configuration of the DAQ and connection with the junction box.	106
Figure 6-4: Proportional-integral-derivative (PID) control loop feedback mechanism.....	107
Figure 6-5: Experimental setup and hybrid simulation hardware architecture.....	107
Figure 6-6: Thermal model representation of the coordinate transformation validation.....	112
Figure 6-7: Coordinate transformation validation using the thermal element study.	113
Figure 6-8: Loading frame reaction for positive (left) and negative (right) applied lateral deformation.	114
Figure 6-9: Western pins slackness representation for various loading cases.	115
Figure 6-10: Axial force and deformation response during the first hybrid simulation.	117
Figure 6-11: Axial force difference histogram (Difference: Preliminary Study - Experiment).	118
Figure 6-12: Axial response investigation. Left: Loading protocol. Right: Measured deformation.	119
Figure 6-13: Instrumentation employed for the axial response investigation.....	120
Figure 7-1: Interface node configuration for the frame to membrane elements transition.	125
Figure 7-2: Storeys' displacement response history. Multiplatform simulation for intact structure case.....	127
Figure 7-3: Interstorey drifts' response history. Multiplatform simulation for intact structure case.....	127
Figure 7-4: Critical element's lateral response. Multiplatform simulation for intact structure case.	129
Figure 7-5: Damage developed in the critical column. Multiplatform simulation for intact structure case.....	129
Figure 7-6: Storeys' displacement response history. Hybrid simulation for the intact structure case using the first specimen (Tests 1.2 & 1.4).	133
Figure 7-7: Interstorey drifts' response history. Hybrid simulation for the intact structure case using the first specimen (Tests 1.2 & 1.4).	133

Figure 7-8: Critical element's deformation response history. Hybrid simulation for the intact structure case using the Specimen #1 (Tests 1.2 & 1.4).	134
Figure 7-9: Critical element's developed forces response history. Hybrid simulation for the intact structure case using the Specimen #1 (Tests 1.2 & 1.4).	135
Figure 7-10: Critical element's hysteretic response presented for the full test (upper figure) and separated to four equal time intervals for clarity (lower figures). Hybrid simulation for the intact structure case using the Specimen #1 (Tests 1.2 & 1.4).	136
Figure 7-11: Dissipated energy in the critical element using the shear force – lateral deformation hysteretic response. Hybrid simulation for the intact structure case using the Specimen #1 (Tests 1.2&1.4).	136
Figure 7-12: Moment-curvature relationship at the critical region. Hybrid simulation for the intact structure case using the Specimen #1 (Tests 1.2 & 1.4).	137
Figure 7-13: Damage developed on the specimen after the second earthquake event (cracks' widths in mm). Hybrid simulation for the intact structure case using the Specimen #1 (Tests 1.2 & 1.4).	137
Figure 7-14: Storeys' displacement response history. Hybrid simulation for the intact structure case using the Specimen #2 (Test 2.1).	139
Figure 7-15: Interstorey drifts' response history. Hybrid simulation for the intact structure case using the Specimen #2 (Test 2.1).	139
Figure 7-16: Critical element's deformation response history. Hybrid simulation for the intact structure case using the Specimen #2 (Test 2.1).	140
Figure 7-17: Critical element's developed forces response history. Hybrid simulation for the intact structure case using the Specimen #2 (Test 2.1).	141
Figure 7-18: Critical element's hysteretic response presented for the full test (upper figure) and separated to four equal time intervals for clarity (lower figures). Hybrid simulation for the intact structure case using the Specimen #2 (Test 2.1).	142
Figure 7-19: Dissipated energy in the critical element using the shear force – lateral deformation hysteretic response. Hybrid simulation for the intact structure case using the Specimen #2 (Test 2.1).	142
Figure 7-20: Moment-curvature relationship at the critical region. Hybrid simulation for the intact structure case using the Specimen #2 (Test 2.1).	143

Figure 7-21: Shear force – shear strain relationship at the critical region. Hybrid simulation for the intact structure case using the Specimen #2 (Test 2.1).	143
Figure 7-22: Damage developed on the specimen after the second earthquake event (cracks' widths in mm). Hybrid simulation for the intact structure case using the Specimen #2 (Test 2.1).	144
Figure 7-23: Calibrated numerical model for the columns of the repaired case structure.....	146
Figure 7-24: Storeys' displacement response history. Hybrid simulation for the repaired structure case using the repaired Specimen #2 (Test 2.2).....	148
Figure 7-25: Interstorey drifts' response history. Hybrid simulation for the repaired structure case using the repaired Specimen #2 (Test 2.2).....	148
Figure 7-26: Critical element's deformation response history. Hybrid simulation for the repaired structure case using the repaired Specimen #2 (Test 2.2).....	149
Figure 7-27: Critical element's developed forces response history. Hybrid simulation for the repaired structure case using the repaired Specimen #2 (Test 2.2).....	150
Figure 7-28: Critical element's hysteretic response presented for the full test (upper figure) and separated in four equal time intervals for clarity (lower figures). Hybrid simulation for the repaired structure case using the repaired Specimen #2 (Test 2.2)...	151
Figure 7-29: Dissipated energy in the critical element using the shear force – lateral deformation hysteretic response. Hybrid simulation for the repaired structure case using the repaired Specimen #2 (Test 2.2).	151
Figure 7-30: Moment-curvature relationship at the critical region. Hybrid simulation for the repaired structure case using the repaired Specimen #2 (Test 2.2).....	152
Figure 7-31: Shear force – shear strain relationship at the critical region. Hybrid simulation for the repaired structure case using the repaired Specimen #2 (Test 2.2).....	152
Figure 7-32: Repaired Specimen #2 (Test 2.2) condition after the repaired case structure hybrid simulation.....	152
Figure 7-33: Interstorey drifts for the numerical study an intact structure excited twice by the study seismic sequence.	153
Figure 7-34: Calibrated response for the numerical model development of the retrofitted case structure.....	154

Figure 7-35: Storeys' displacement response history. Hybrid simulation for the retrofitted structure case using the retrofitted Specimen #3.	156
Figure 7-36: Interstorey drifts' response history. Hybrid simulation for the retrofitted structure case using the retrofitted Specimen #3.	156
Figure 7-37: Critical element's deformation response history. Hybrid simulation for the retrofitted structure case using the retrofitted Specimen #3.	157
Figure 7-38: Critical element's developed forces response history. Hybrid simulation for the retrofitted structure case using the retrofitted Specimen #3.	158
Figure 7-39: Critical element's hysteretic response presented for the full test (upper figure) and separated to four equal time intervals for clarity (lower figures). Hybrid simulation for the retrofitted structure case using the retrofitted Specimen #3.....	159
Figure 7-40: Dissipated energy in the critical element using the shear force – lateral deformation hysteretic response. Hybrid simulation for the retrofitted structure case using the retrofitted Specimen #3.....	159
Figure 7-41: Moment-curvature relationship at the critical region. Hybrid simulation for the retrofitted structure case using the retrofitted Specimen #3.	160
Figure 7-42: Shear force – shear strain relationship at the critical region. Hybrid simulation for the retrofitted structure case using the retrofitted Specimen #3.	160
Figure 7-43: Modified load and mass distribution for the increased gravity load case retrofitted structure.....	162
Figure 7-44: Constitutive models' notation used for the increased gravity load structure.	162
Figure 7-45: Constitutive models' notation used for the increased gravity load structure.	163
Figure 7-46: Storeys' displacement response history. Hybrid simulation for the increased weight retrofitted structure case performed with Specimen #3 (Test 3.2).....	165
Figure 7-47: Interstorey drifts' response history. Hybrid simulation for the increased weight retrofitted structure case performed with Specimen #3 (Test 3.2).....	165
Figure 7-48: Critical element's deformation response history. Hybrid simulation for the increased weight retrofitted structure case performed with Specimen #3 (Test 3.2).....	166
Figure 7-49: Critical element's developed forces response history. Hybrid simulation for the increased weight retrofitted structure case performed with Specimen #3 (Test 3.2).....	167

Figure 7-50: Critical element's hysteretic response presented for the full test (upper figure) and separated in four equal time intervals for clarity (lower figures). Hybrid simulation for the increased weight retrofitted structure case performed with Specimen #3 (Test 3.2).....	168
Figure 7-51: Dissipated energy in the critical element using the shear force – lateral deformation hysteretic response. Hybrid simulation for the increased weight retrofitted structure case performed with Specimen #3 (Test 3.2).	168
Figure 7-52: Moment-curvature relationship at the critical region. Hybrid simulation for the increased weight retrofitted structure case performed with Specimen #3 (Test 3.2).....	169
Figure 7-53: Axial force fluctuation histograms for the various hybrid simulations performed.	171
Figure 7-54: Repaired Specimen's #1 response under quasi-static cyclic lateral loading and low constant axial load.....	172
Figure 7-55: Moment-curvature relationship of the repaired Specimen #1 tested under quasi-static cyclic lateral loading and low constant axial load.....	173
Figure 7-56: Damage developed in the repaired Specimen #1 after the quasi-static testing under low constant axial load (Test 1.5).	173
Figure 7-57: Retrofitted Specimen's #3 response under quasi-static cyclic lateral loading and moderate constant axial load.....	174
Figure 7-58: Moment-curvature relationship of the retrofitted Specimen #3 tested under quasi-static lateral loading and moderate constant axial load.	175
Figure 7-59: Shear strain response of the retrofitted Specimen #3 tested under quasi-static lateral loading and moderate constant axial load.....	175
Figure 7-60: Damage developed on the retrofitted Specimen #3 after the quasi-static lateral testing under moderate constant axial load (Test 3.3).	176
Figure 7-61: Repaired Specimen's #2 response under quasi-static lateral loading and high constant axial load.....	177
Figure 7-62: Moment-curvature relationship of the repaired Specimen #2 tested under quasi-static lateral loading and high constant axial load.	177
Figure 7-63: Shear strain response of the repaired Specimen #2 tested under quasi-static lateral loading and high constant axial load.....	178
Figure 7-64: Damage developed on the repaired Specimen #2 after the quasi-static testing under high constant axial load (Test 2.3).....	178

Chapter 1

Introduction

1 Introduction

1.1 General

The accurate performance assessment of a structure's response under extreme excitation scenarios is becoming increasingly important, given the greater interest in performance-based design, whose overall objective is to achieve the most efficient structural design to meet certain performance requirements (Priestley 2000). For most conventional structures, the main design load except for the gravity is the earthquake excitation which has been proven considerably to be destructive when the structures do not meet the proper design standards. For such cases, appropriate tools for the seismic performance assessment should be developed to capture the realistic response of the structure, which can be used for potential retrofitting or for cases of new structures where these tools can be employed for improving the design techniques and efficiency.

The two most popular tools for the performance assessment are numerical studies and experimental testing of the structure's response. The numerical studies can be described as time and cost efficient and are suitable for parametric studies, but their accuracy is dependent on the constitutive models that are employed for the element's materials in addition to the models employed for the interaction mechanisms. For example, two of the most common assumptions in numerical studies of reinforced concrete structures is that the reinforcement's response may be considered as bilinear and that the reinforcement and the concrete are perfectly bonded. It becomes apparent that the accuracy of a numerically conducted performance assessment is related to the assumptions made during the development of the model, and in some cases they induce bias into the structure's response, resulting in an unrealistic assessment.

On the other hand, the experimental testing, which has been proven to be the most realistic evaluation methodology, can be described as resource prohibitive due to its requirements for extensive experimental facilities. Additionally, the testing of a whole structure is usually restricted to reduced scale models, which may call into question the accuracy of the observed structure's response (Nakashima 2008). Yet, the experimental testing has been efficiently employed for single elements' testing under predefined loading protocols for understanding their response. This

methodology is widely employed for testing new materials or for new reinforcing and retrofitting techniques such as column upgrades using externally applied Fiber Reinforced Polymer (FRP) fabrics, which are utilized in this study. These retrofitting techniques aim to improve the response of existing structures designed with insufficient seismic provisions or to improve the response of damaged structures and restore their seismic performance. While the single element tests can capture the elements' responses, this testing method does not account for the potential interaction of the tested specimen with the structure, such as the force redistributions during the nonlinear response of the structure.

An additional well established and more efficient tool for the seismic performance assessment of structures is the hybrid simulation in structural testing, which integrates the benefits from the two assessment techniques mentioned above. In the conventional hybrid simulation, a structure is divided into two or more substructures (Dermitzakis and Mahin 1985), each of which is represented by either a numerical model or a physically tested component. The substructures that are critical for the structure's response or their response cannot be fully characterized with numerical models are typically experimentally tested, while the rest of the structure is numerically represented. In this way, the critical elements' response, which is experimentally tested, can be accurately captured. As a result, the seismic performance assessment of the structure can be realistically accomplished since the critical elements' response is free from the numerical modeling assumptions.

1.2 Research Objectives

In this study, the seismic performance of a three-storey, three-bay, moment-resisting reinforced concrete structure designed without seismic provisions is evaluated by employing a hybrid simulation method. One of the first floor columns, which is most critical to the structural performance, is experimentally tested in the Structural Laboratories at the University of Toronto. Because the available column testing frame cannot impose moment at the top of a specimen, the proper boundary conditions cannot be applied during the hybrid simulation. The first objective of this study is to develop a weakly-coupled hybrid simulation methodology (WCHS) which allows overcoming the limitation of the column testing frame for running a hybrid simulation.

The second objective is the application of the proposed WCHS methodology for experimentally conducting the seismic performance assessment of a three storey moment-resisting reinforced

concrete structure. By running hybrid simulations, the inaccuracies induced by the numerical modeling assumptions are identified, while the performance of the structure excited by the study earthquake sequence can be more accurately evaluated in comparison with purely numerical models.

Finally, after validating the applicability of the methodology and identifying the performance level of the reference structure, the seismic performance assessment using the developed hybrid simulation framework is performed for the case of a repaired and a retrofitted structure. Through the hybrid simulations, not only the critical element's response but also the interaction of the critical element with the global structural response can be adequately measured, resulting in a realistic assessment of the influence that the repairing or retrofitting techniques may have on the response of an existing or damaged structure.

1.3 Thesis Organization

This thesis consists of eight main chapters and two appendices. The overview of the thesis is outlined as follows.

Chapter 1 includes the introduction of the research project in addition to the background information and the objectives of the current study.

Chapter 2 discusses the recent literature related to the seismic performance assessment of RC structures in addition to the common techniques for experimental testing in structural engineering. Additionally, some relevant literature on hybrid simulation techniques is reviewed and summarized.

Chapter 3 focuses on the design of the reference structure, the applied ground motions and the numerical modeling methods of the structure. Also, a preliminary numerical investigation is performed for the structural response, the critical elements, and structural failure mechanisms.

Chapter 4 discusses the experimental program undertaken for the construction of four specimens as part of this study. Initially, the descriptions of the materials that were used for this study are described in addition to their experimentally measured properties. Subsequently, the construction stages are briefly presented as well as the repairing and retrofitting techniques are described. Finally, the employed instrumentation and the column testing frame are introduced.

Chapter 5 includes the detailed discussion of the proposed weakly-coupled methodology. The limitation of the experimental facility is first introduced which is followed by the proposed weakly coupled hybrid simulation method. The WCHS method is numerically verified using the reference structure. Finally, the proposed method is generalized. The applicability of the WCHS method to the reference structure of this study is examined within the context of the generalized weakly coupled hybrid simulation method.

Chapter 6 discusses the technical details of the hybrid simulation method as implemented in this study. More specifically, the hybrid simulation architecture in addition to the software and hardware employed are described, and the developed algorithms for the coordinate transformation and error compensation scheme are presented. Finally, the error sources are investigated, and an additional experimental investigation is performed for understanding the observed inconsistencies in the axial response.

Chapter 7 is devoted to the experimental results. Initially, a multiplatform simulation is performed in order to predict the potential damage in the tested specimen and subsequently the seismic performance assessment is experimentally evaluated for the intact, the repaired and the strengthened structures. This chapter ends with a description of the response of the retrofitted and repaired specimens as measured during quasi-statics tests after their use as part of the reference structure during the hybrid simulation.

Chapter 8 presents the summary, the conclusions of this research, and recommendations for further work.

Chapter 2 Literature Review

2 Literature Review

2.1 Seismic Performance Assessment of Structural Systems

The seismic performance assessment of structures has been a major thrust area in the earthquake and structural engineering community for the past 10 to 20 years. Significant efforts have been made for developing quantitative tools for characterizing the seismic hazard, the nonlinear response of the structure and the potential damages and losses (Kam and Jury 2015). Traditionally the performance of new conventional buildings is not usually assessed because the modern seismic design standards ensure that the structure's response is within a safe level of performance. Seismic design codes provide prescriptive criteria that specify the minimum level of strength, stiffness, and ductility of the structure, while detailed outlines are established regarding the acceptable materials in addition to their detailing and configuration. However, there is a significant number of existing structures which were designed prior to the introduction and the implementation of the modern design codes and did not comply with the modern design standards. For such cases, in-depth understanding of the seismic performance of the structures is required to adequately retrofit the structure such that the seismic performance of the structure is within the acceptable level defined in the new standards.

A catalyst for the performance-based seismic assessment was the SEAOC Vision 2000 report (1995), in which seismic performance was explicitly described as a selection of seismic performance objectives, which are defined by the coupling between the expected performance level and the seismic ground motion intensity. The performance matrix as established in Vision 2000, including the relationship between earthquake design level and performance level, is presented in Figure 2-1. Based on the nature of the facility and the earthquake design level, the structure's performance can be characterized by the four following performance levels as: Fully Operational, when the facility continues its operation with negligible damage; Operational, where minor damage and minor disruption in nonessential services is observed; Life Safe, when the life safety is protected but moderate to extensive damages are observed; and Near Collapse, when life safety is at risk, the damage is severe, but a structural collapse is prevented.

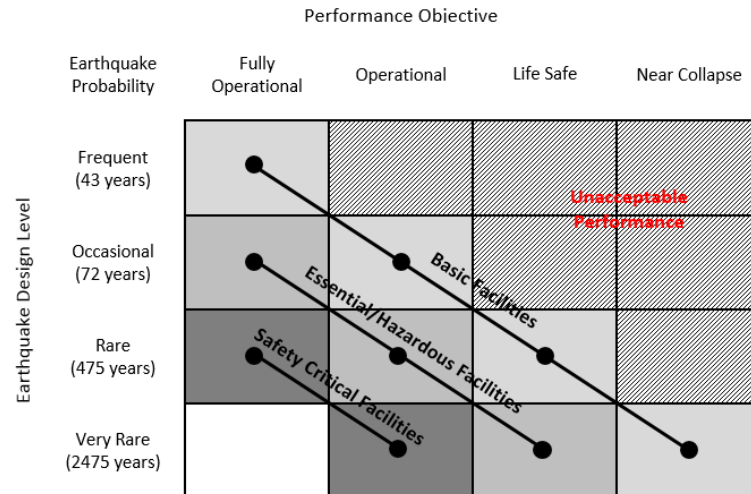


Figure 2-1: SEAOC Vision 2000 performance matrix (SEAOC Vision2000 1995).

However, using such a “pass or fail” criterion may not be practical since it requires the assessment of the building’s behavior under multiple earthquakes with various intensities. Furthermore, once the building response is within the nonlinear range, determining the interaction between the structure’s performance as a whole and the behavior of the individual structural components that may compromise the integrity of the structure and its assessment is a significant challenge.

To address the difficulties mentioned above, a new set of rules and procedures have been proposed for the seismic assessment of existing buildings in the first-generation FEMA-356 report (FEMA 356 2000). Within this report, the definitions of various performance levels and the performance of structural and non-structural elements are included, while techniques for the nonlinear analysis of the structure and the definition of the acceptance criteria are presented. According to FEMA-356 the structural performance level for the vertical elements of the concrete frames can be classified into three discrete performance levels. The first is the Immediate Occupancy level, where minor hairline cracks are developed, limited yielding is possible at few locations, and no concrete crushing occurs in the primary elements of the structure, while the transient drift is below 1% and there is negligible residual drift. The second is the Life Safety level, where extensive damage occurs to the beams, spalling of the cover and shear cracking develop in the ductile columns, and minor spalling occurs in the non-ductile columns, while the transient drift is below 2% and there is residual drift below 1%. The last performance level is the Collapse Prevention level, where extensive cracking and hinge formation occurs in the ductile elements, limited cracking and/or splice failure takes place in some non-ductile elements, and significant damages happen in the

short columns, while the transient or residual drift is below 4%. These discrete performance levels are illustrated in Figure 2-2 in addition to the case that the response is below the Immediate Occupancy Level, namely the Operational State. These performance assessment criteria have been employed for the present study.

The modern, second-generation performance-based seismic assessment guidelines published by FEMA (FEMA 445 2006) suggest that the proper understanding of the building's response to a seismic excitation would allow for the qualitative or quantitative assessment of its seismic performance. More specifically, a probabilistic procedure (FEMA P-58-1 2012) is proposed where the uncertainties are explicitly considered since it is widely accepted that an accurate performance prediction is not possible given the inherent uncertainties of the performance assessment study. Within these guidelines, the seismic performance is expressed in terms of probable consequences such as human losses, and direct and indirect economic losses.

In the present study, the hybrid simulation is used as a tool for reducing the uncertainties related to the modeling technique and the response of the structure's elements. In this way, the response of the critical element is captured experimentally, which results in a more realistic evaluation of the seismic performance of the structure in comparison with purely numerical studies. However, this study includes uncertainties such as the ground motion selection or the mass and weight distribution. A combination of probabilistic analysis with hybrid simulation may result in a more realistic and meaningful assessment of the structure's response, with respect to its seismic hazard and mitigation in terms of risk, damage, reparability and human and economic cost.

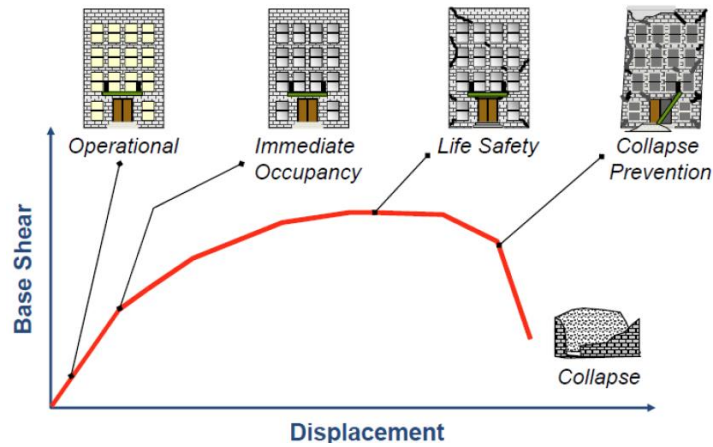


Figure 2-2: Performance levels according to FEMA-356 (Heintz et al. 2014).

2.2 Critical Elements – Reinforced Concrete Columns

Taking into account the uncertainties described in the previous chapter, it can be understood that the response of the critical elements is of significant importance for the realistic assessment of a building during seismic excitation. In this study, the critical element has been proven to be an internal column on a ground floor. Its response is experimentally evaluated using a hybrid simulation. For that purpose, a brief discussion related to the reinforced concrete column's response and capacity is presented based on the relevant literature.

2.2.1 Reinforced Concrete Columns

A considerable amount of research has been dedicated to the study of reinforced concrete columns. Recently, more research is in progress related to their seismic performance, and the employment of new materials to improve the seismic performance or to move towards more resilient systems than the conventional reinforced concrete column. In this section, various mechanisms related to the conventional reinforced concrete column's capacity are presented, while the experimental responses from different investigations are compared.

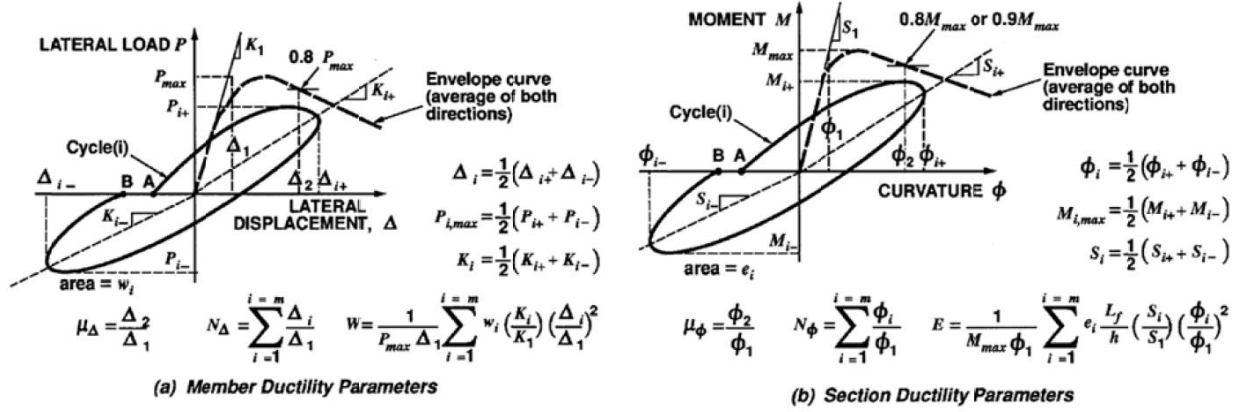


Figure 2-3: Calculation of member and section ductility parameters (Sheikh and Houry 1993).

2.2.1.1 Ductility Parameters

For quantifying the seismic performance of columns, various ductility indices have been introduced in the literature. The displacement and curvature ductility factors, μ_{Δ} and μ_{ϕ} , the cumulative ductility ratios, N_{Δ} and N_{ϕ} , and the energy and work damage indicators, E and W , are some of the most widely employed parameters for evaluating a column's response, as proposed by Sheikh and Houry (1993). The equations for calculating these indices are presented in Figure 2-3. By using consistent indices, the performance between the various experimental program cases can be compared with the same performance parameters, and the influence of the reinforcing techniques or loading conditions can be consistently identified.

2.2.1.2 Reinforced Concrete Column Database

As has already been introduced, an extensive column testing program has been performed at the University of Toronto in the past 20 years. The response of these experimentally tested columns using the same testing protocol was presented by Tavassoli (2013) as shown in Table 2-1. The strength and ductility development mechanisms in reinforced concrete columns are discussed in the following sections with respect to the column database presented in Table 2-1

Table 2-1: Steel-reinforced column database (Tavassoli 2013).

Specimen	Column		Compressive Strength f'_c (MPa)	Lateral Steel		Longitudinal Steel		Axial Load Level P_o/P	Max, Moment (kNm)	Ductility Factors		Energy Damage Indicator E_{80}
	Size B or D (mm)	Length (mm)		Size @ spacing (mm)	Ratio (%)	Yielding Strength f'_y (MPa)	Ratio (%)			Yielding Strength f'_y (MPa)	μ_Δ	
“Confinement of high-strength concrete columns” (Sheikh et al. 1994).												
AS-3H	305	1,473	54.1	9.5@108	1.68	507	2.44	0.59	237	3.2	10.5	178
AS-18H			54.7	12.7@108	3.06	464		0.61	253	3.9	14.0	384
AS-20H			53.6	12.7@76.2	4.30	464		0.61	283	5.4	16.5	935
A-17H			59.1	9.5@108	1.68	507		0.62	261	2.0	5.0	36
“Confined Concrete Columns with Stubs” (Sheikh and Khoury 1993).												
AS-3	305	1,473	33.2	9.5@108	1.68	507	2.44	0.50	193	4.7	>19	610
AS-17		2,438	31.3	9.5@108	1.68	507		0.63	180	3.8	10.5	402
AS-18		1,473	32.8	12.7@76.2	3.06	464		0.63	204	6.7	14.5	897
AS-19		1,473	32.3	9.5/6@108	1.3	457		0.36	202	4.0	19	631
“High-strength concrete columns under simulated earthquake loading” (Bayrak and Sheikh 1997).												
ES-IHT	305	1,473	72.1	15M@95	3.15	463	2.58	0.50	-	4.6	6.6	80
AS-2HT			71.7	10M@90	2.84	542		0.36		6.2	15.8	631
AS-3HT			71.8	10M@90	2.84	542		0.50		5.0	10.1	161
AS-4HT			71.9	15M@100	5.12	463		0.50		7.0	21.2	997
“Seismic behavior of concrete columns confined with steel and fiber-reinforced polymers” (Sheikh and Yau 2002).												
S-1NT	356	1,473	40.1	US#3@80	1.12	507	3.00	0.54	192	2.0	8.8	69
S-2NT			40.1	US#3@80	1.12			0.27	212	2.7	12.6	778
S-3NT			39.2	US#3@300	0.30			0.54	212	2.4	2.1	5
S-4NT			39.2	US#3@300	0.30			0.27	215	2.1	3.4	9
“Seismic Performance of Circular High-Strength Concrete Columns” (Paultre et al. 2009)												
C100S100N15	300	2,150	109	10M@100	1.43	440	2.55	0.16	168	5.3	14	129
C100SH100N15			101	US#3@100	1.00	425		0.16	172	5.0	12	100
C100S70N25			103	10M@70	2.04	440		0.27	203	4.8	11.4	114
C100SH70N25			97	US#3@70	1.43	425		0.26	191	5.8	15.4	155
C100S37N40			100	10M@37	3.85	440		0.43	228	7.4	26	209
C100SH37N40			103	US#3@37	2.71	425		0.43	235	6.7	21.3	148

Specimen	Column		Compressive Strength f'_c (MPa)	Lateral Steel		Longitudinal Steel		Axial Load Level P_o/P	Max, Moment (kNm)	Ductility Factors		Energy Damage Indicator	
	Size B or D (mm)	Length (mm)		Size @ spacing (mm)	Ratio (%)	Yielding Strength f'_y (MPa)	Ratio (%)			Yielding Strength f'_y (MPa)	μ_A		μ_ϕ
"Seismic Behaviour of Reinforced Concrete Columns" (Liu 2013).													
P27-NF-1	356	1,473	40	US#3@150	0.60	496	3.01	490	0.27	204	4.3	11.3	
P27-NF-2				US#3@100	0.90	496			0.27	220	4.6	15.6	
P40-NF-5				US#3@300	0.30	496			0.40	180	3.0	3.6	
P40-NF-6				US#3@100	0.90	496			0.40	205	3.5	11.9	
P40-NF-7				US#3@70	1.20	496			0.40	230	4.5	11.1	
P56-NF-10				US#3@300	0.30	496			0.56	188	2.3	1.9	
P56-NF-11				10M@100	1.22	450			0.56	203	3.4	10.7	
P56-NF-12				10M@75	1.63	450			0.56	197	3.2	13.2	
"Retrofit of Square Concrete Columns with Carbon Fiber-Reinforced Polymer for Seismic Resistance" (Iacobucci et al. 2003).													
AS-1NS	305	1,473	31.4	US#3@300	0.61	457	2.58	465	0.33	180	3.7	5.3	10.8
AS-7NS			37.0						0.33	208	-	-	-
AS-8NS			42.3						0.56	168	-	-	-
"Seismic performance of high-strength concrete square columns confined with carbon fiber reinforced polymers (CFRPs)" (Hosseini et al. 2005).													
CI4	260	1,650	56	10@120	1.24	400	400	0.15	98	5.1	9.4	231	
CI8			54	10@120	1.80				3.0	141	5.2	10.3	350
CS4			54	12@70	3.10				1.5	105	6.5	12.2	385
CS8			53	10@70	3.20				3.0	145	6.5	10.4	919
"Seismic behavior of square high-strength concrete columns" (Memon and Sheikh 2005).													
AS-1NSS	305	1,473	42.4	9.5@300	0.61	457	2.58	465	0.56	168	2.9	2.6	-
"Seismic behavior of square high-strength concrete columns" (Azizinamini et al. 1994).													
D60-7-3C-1 5/8-0.2P	305	1,070	53.7	12.7@67	2.73	414	2.44	414	0.2	248	7	-	-
D60-15-4-2 5/8-0.2P			50.8	9.5@41.3	3.82	414			0.2	238	8		
D60-15-3C-1 5/8-0.2P			100.8	12.7@67	2.73	414			0.2	271	4		
D120-15-3C-2 5/8-0.2P			100.2	9.5@41.3	3.82	414			0.2	295	6		
D120-15-3C-1 5/8-0.2P			101.6	9.5@67	2.36	828			0.2	380	4		
D60-4-3C-2 5/8-0.2P			101.7	9.5@41.3	3.82	828			0.2	288	5		
D60-4-3C-2 5/8-0.4P			26.2	9.5@67	2.36	414			0.2	173	5		
			27.0	9.5@67	2.36	414			0.4	168	4		
"Behavior of high-strength concrete columns under cyclic flexure and constant axial load" (Légeron and Paultre 2000)													
CB100B60N15	305	2150	92.4	10M@60	4.26	391	2.15	470	0.15	246	8.8	-	567
CB100B60N25			93.3	10M@60	4.26	404			0.30	326	8.2	26.9	380
CB100B60N40			98.2	10M@60	4.26	418			0.42	377	5.2	7.6	114
CB100B130N15			94.8	10M@130	1.96	391			0.15	225	4.4	-	39.7
CB100B130N25			97.7	10M@130	1.96	404			0.28	335	2.3	3.3	4.2
CB100B130N40			104.3	10M@130	1.96	418			0.40	373	1.6	2.9	5.6

2.2.1.3 Effect of Axial Load

The level of the axial load applied at the column influences both the column's strength and ductility. Characteristically, an initial increase in the axial load level results in an enhancement of the moment capacity, but any further increase beyond 30% of the column's capacity results in a drop in the column's moment capacity. This response can be observed by comparing the specimens CB100B60N15 to CB100B60N25 and S-1NT to S-2NT in Table 2-1, which have identical properties and reinforcement layouts, but different axial loads are being applied to each case. The increase of the axial load level from $0.15P_o$ to $0.3P_o$ for the CB-series specimens results in a moment capacity increase of 32%, while the increase of the axial load from $0.27P_o$ to $0.54P_o$ for the S-series specimens results in a moment capacity decrease equal to 9.4%. This mechanism is investigated numerically for the critical specimen for this study and is presented in Figure 3-21 in Chapter 3 as the axial load-moment capacity curve. On the other hand, any increase in the axial load negatively influences the column's ductility and, as a result, its energy dissipation mechanism. This response can be identified by comparing the specimens AS-2HT and AS-3HT in Table 2-1, where the axial load is increased from $0.36P_o$ to $0.50P_o$ and results in a displacement ductility reduction from 6.2 to 5.0 and a curvature ductility reduction from 15.8 to 10.1, while the energy dissipation was reduced by 75%.

2.2.1.4 Effect of Confining Reinforcement

By evaluating the response of the columns in the available database (Tavassoli 2013), it can be observed that the lateral confining reinforcement significantly enhances the ductility of the specimen. Higher confining reinforcement ratios result in a greater ductile response and greater energy dissipation. This response can be identified both in rectangular and circular columns, by comparing the specimens AS-18H to AS-20H and S-2NT to S-4NT in Table 2-1. From these specimen series, it can be observed that the closely-spaced ties or spirals increase both the ductility factors and the energy dissipation indicators, when the rest of the variables, such as the axial load and the concrete strength, remain constant. This enhancement occurs due to the fact that a denser lateral reinforcement configuration not only increases the shear capacity of the specimen but also delays the longitudinal reinforcement buckling and provides lateral confinement, which develops a triaxial compression state in the concrete's core that increases the compressive strength of the concrete and delays its crushing.

2.2.1.5 Effect of Concrete Strength

Finally, the last mechanism that can be identified to influence the column's response is the concrete strength. A higher strength concrete results in an increase in the column's capacity, but the column's ductility is deteriorated as a consequence of the brittle post-peak response of high strength concretes. This response can be verified by comparing the specimens D60-7-4-2 5/8-0.2P to D60-15-4-2 5/8-0.2P in Table 2-1, where the concrete strength is 53.7 and 100.8 MPa, respectively, while the rest of the properties are identical. The moment capacity increases from 248 kN·m to 271 kN·m with the concrete's strength increase, but the displacement ductility decreases from 7 to 4. As a result, it can be understood that the unconditional increase of the concrete's strength is not always beneficial when increased ductility is required, and for such cases, the lateral reinforcement configuration is of significant importance for achieving a ductile response.

2.2.2 FRP Confined Reinforced Concrete Columns

As part of this study, the influence of the columns' retrofitting in the reference structure's performance is experimentally evaluated using hybrid simulation. The retrofitting technique that is employed is the external application of fiber reinforced polymer (FRP) unidirectional wraps in the circumferential direction. In this section, the confinement mechanism and the experimental response of FRP confined columns available in the literature is presented.

Contrary to steel reinforcement, where the confining pressure does not increase further after the steel yielding, the FRP behavior remains linear up to significantly high strains and the applied pressure increases with an increasing axial load. This response results in an improvement in confinement efficiency, which is uniformly applied in a circular cross section without the existence of non-confined area as developed when conventional steel lateral reinforcement is employed. Various analytical models have been developed for capturing the FRP confined column's response and are extensively discussed by Liu (2013), but not presented in this thesis as they are considered out of the scope of this study. Instead, the experimental results of the Carbon FRP (CFRP) retrofitted specimens from the studies performed by Liu (2013), and Sheikh and Yau (2002) are presented in Table 2-2. Additionally, the control non-retrofitted specimens, with equivalent reinforcing properties and loading conditions, are presented for comparison purposes.

Table 2-2: CFRP-retrofitted columns' database.

Specimen	Column (mm)		Compressive Strength f'_c (MPa)	Lateral Steel		CFRP Layers Number	Longitudinal Steel		Axial Load Level P_o/P	Max, Moment (kNm)	Ductility Factors		Energy Damage Indicator	
	Size	Length		Size @ spacing (mm)	Ratio (%)		Yielding Strength f'_y (MPa)	Ratio (%)			Yielding Strength f'_y (MPa)	μ_Δ		μ_ϕ
“Seismic Behavior of Reinforced Concrete Columns” (Liu 2013).														
P27-NF-2	Diam.:356	1,473	40	US#3@100	0.9	-	3.00	490	0.27	220	4.6	11.3	-	
P27-1CF-3				US#3@300	0.3	1			0.27	264	5.2	18.9		
P40-NF-5				US#3@300	0.3	-			0.4	180	3.0	3.6		
P40-1CF-8				US#3@300	0.3	1			0.4	262	6.9	17.2		
P56-NF-10				US#3@300	0.3	-			0.56	188	2.3	1.9		
P56-2CF-13				US#3@300	0.3	2			0.56	331	7.5	21.0		
“Seismic behavior of concrete columns confined with steel and fiber-reinforced polymers” (Sheikh and Yau 2002).														
S-3NT	Diam.:356	1,473	39.2	US#3@300	0.3	507	-	3.00	507	0.54	212	2.4	2.1	5
ST-3NT			40.4				1 (1mm)			0.54	279	3.9	8.9	202
S-4NT			39.2				-			0.27	215	2.1	3.4	9
ST-4NT			44.8				1 (0.5mm)			0.27	259	4.3	15.0	1028

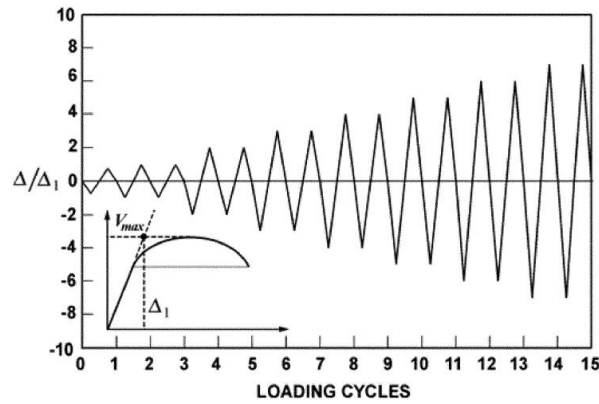


Figure 2-4: Quasi-static lateral displacement protocol (Ghosh and Sheikh 2008).

Overall, it can be observed that the responses of the retrofitted specimens are significantly enhanced. Initially, for an axial load of $0.27P_o$ on specimens S-4NT and ST-4NT in Table 2-2, it can be observed that there is a significant increase both in the curvature ductility factor and in the energy damage indicator, which is accompanied by a less significant increase at the moment capacity and the displacement ductility. Similar is the response of the S-3NT and ST-3NT specimens in Table 2-2, in which a higher axial load is applied ($0.54P_o$). For these specimens, the curvature ductility and the energy damage indicator are increased at a lower rate compared to the S-series specimens, but there is a significant improvement in the moment capacity of the specimen. These enhanced responses demonstrate the efficiency achieved when externally applied FRP is used for retrofit. As a result, this retrofitting technique is employed in the current study for the upgrade of the reference structure.

2.2.3 Conventional Column Testing Practices

The previously described experimental studies have been conducted with the conventional quasi-static testing method, where a constant or pre-defined variable axial load is applied at the top of the column in addition to a quasi-static lateral displacement history until the specimen develops failure. During the quasi-static test, the loads and/or the displacements are applied at a slow rate, allowing for identifying the damage (crack development/propagation, concrete spalling, etc.) on the specimen between the various load stages. A typical lateral displacement history as used during most of the aforementioned studies is presented in Figure 2-4. This loading profile, while having been proven to be beneficial for understanding the column's behavior (Kharal and Sheikh 2014, Tavassoli and Sheikh 2017), is not a realistic representation of the loading history of a column

when the structure is subjected to seismic excitation. During an earthquake event, the axial loads of the vertical elements continuously change due to the overturning moment and vertical ground motion. Additionally, in the quasi-static testing, the inertial, and damping forces developed in the structure's elements are not captured.

To address the limitations resulting from the quasi-static testing, in the current study, a hybrid simulation technique is adopted where a critical column is tested in the lab while the rest of the structural system is numerically represented. The two components (i.e. the physical column and the numerical model) fully interact throughout the simulation. In this way, the axial force fluctuation during the seismic excitation can be captured, while the inertia and damping properties of the structure are numerically evaluated. It has been demonstrated that by employing hybrid simulations for structures where the columns are the critical elements, their responses can be efficiently assessed, even for cases of close to near-collapse responses (Murray et al. 2015, Murray and Sasani 2016).

2.3 Hybrid Simulation in Structural Testing

The term hybrid simulation in structural testing is used to describe the experimental and numerical coupled simulations for the seismic response of a structure, in which a part of the structure that is critical for its response or is a significant challenge to numerically model is physically tested, while the rest of the structure is numerically assessed (McCrum and Williams 2016). This testing methodology was developed to address the requirement for the realistic testing of engineering structures without the difficulties and the costs associated with full-scale structural testing using shaking tables. In the sections below, the background and the developments related to hybrid simulation are briefly introduced in addition to state of the art applications and the challenges that are still at the forefront of experimental hybrid simulation.

2.3.1 Background

As has already been introduced, hybrid simulation has been developed to overcome the disadvantages and difficulties related to quasi-static testing and full-scale testing using shaking tables. The first hybrid simulations (Hakuno et al. 1969) date back to the late 1960's, when pseudo-dynamic (PsD) hybrid simulation was proposed. During the PsD hybrid simulation, the restoring forces are experimentally evaluated and fed back into the numerical model for predicting the

deformations for the next time step. This procedure is repeated up to the end of the test. The other terms in the equation of motion, such as inertial force, damping force, and applied excitation, are numerically evaluated. During the PsD test, the structure is represented by lumped masses in which locations the dynamic loading is applied by the actuators in the form of target displacements, while the inertia and damping are numerically modeled. For such cases, an actuator is required for each controlled degree of freedom (DOF) as it is illustrated in Figure 2-5 for a two DOF system.

Within the PsD hybrid simulation framework, the equation of motion is solved over a series of time steps Δt . Equation 2-1 shows a discrete equation of motion at the $(i+1)$ time step.

$$\mathbf{M}\ddot{\mathbf{x}}_{i+1} + \mathbf{C}\dot{\mathbf{x}}_{i+1} + \mathbf{R}_{i+1} = \mathbf{F}_{i+1} \quad \text{Equation 2-1}$$

where \mathbf{M} is the mass matrix, $\ddot{\mathbf{x}}_{i+1}$ is the nodal acceleration vector, \mathbf{C} is the damping matrix, $\dot{\mathbf{x}}_{i+1}$ is the nodal velocity vector, \mathbf{R}_{i+1} is the restoring force vector and \mathbf{F}_{i+1} is the external excitation force vector applied to the system. For a linear system, $\mathbf{R}_{i+1} = \mathbf{K}\mathbf{x}_{i+1}$ where \mathbf{K} is the stiffness matrix and \mathbf{x}_{i+1} is the nodal displacement vector. However, for non-linear systems, the relationship between the stiffness matrix and the restoring forces becomes more complex due to the stiffness degradation that takes place within the element for deformations beyond the elastic range. When a hybrid simulation is performed, the restoring force vector \mathbf{R}_{i+1} is experimentally measured and fed back to the numerical integration scheme, and the target displacement vector for the next step is calculated.

Because in PsD hybrid simulation, the inertial force and damping force are numerically modeled, this testing methodology is not suitable for cases of structures in which rate dependent elements, such as dampers, exist. The need for rate dependent elements testing using hybrid simulation resulted in the development of a purely dynamic testing method, namely the Real Time Hybrid Simulation (RTHS) (Nakashima et al. 1992), which was initially employed for relatively small and simple problems, and was later expanded to more complicated MDOF systems (Nakashima and Masaoka 1999). Because rate dependent element does not exist in this study, the well-established PsD hybrid simulation is used as described in the next section.

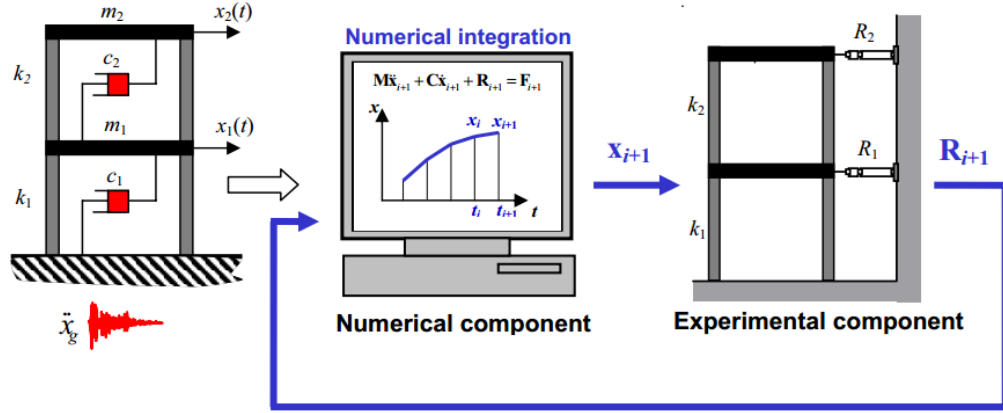


Figure 2-5: Schematic diagram of hybrid simulation method (Carrion and Spencer 2007).

2.3.2 Substructuring Techniques

The concept of substructuring in PsD hybrid simulations was first introduced by Dermitzakis and Mahin (1985) and was widely employed within the research community (Pegon and Pinto 2000, Hashemi and Mosqueda 2014). When substructuring is employed, only the most critical components (substructures) of the structure response or the components that are of greater uncertainty when numerically modeled are experimentally tested, while the rest of the structure is numerically evaluated. In this way, the testing of large, heavy structures, which could be costly and inefficient, can be replaced with the testing of single components or subassemblies of the structure because the majority of the structural system is numerically modeled.

During the substructured PsD hybrid simulation, the experimentally and numerically tested substructures are evaluated simultaneously, and their restoring forces are fed back into the integration scheme for predicting the displacements of the next time step. The substructuring architecture can be expressed with the following modification to the equation of motion.

$$\mathbf{M}\ddot{\mathbf{x}}_{i+1} + \mathbf{C}\dot{\mathbf{x}}_{i+1} + \mathbf{R}_{N,i+1} + \mathbf{R}_{E,i+1} = \mathbf{F}_{i+1} \quad \text{Equation 2-2}$$

where $\mathbf{R}_{N,i+1}$ is the restoring force vector from the substructures that are numerically modeled, while $\mathbf{R}_{E,i+1}$ is the restoring force vector measured from the substructures that are experimentally modeled. For the correct implementation of the substructured hybrid simulation, the proper control of the boundary conditions at the interface points should be performed. The interface points are nodes where one substructure is connected with the rest. The specimen's deformation needs to be

controlled at the interface point. To impose proper boundary condition, the number of actuators need to equal to or greater than the number of the DOF at the interface point. For example, when a three-dimensional structure with frame elements is evaluated, six or more actuators are required to impose boundary conditions.

In this research, substructured PsD hybrid simulation is used for the seismic performance assessment of an RC frame structure. A first storey column is experimentally tested. Because the boundary conditions cannot be fully controlled due to the limitation of the available experimental setup, a Weakly Coupled Hybrid Simulation (WCHS) approach is proposed and employed for the experimental hybrid simulation, which is discussed in Chapter 5.

2.3.3 Time Integration Techniques

Various time integration techniques have been proposed and used to run hybrid simulations, and can be discretized in three different categories: the explicit, the implicit, and the operator-splitting numerical integration schemes. The explicit methods were mainly used in the early hybrid simulation applications since the equation of motion for a new step is solved based on the previous steps' states only. This characteristic renders the explicit integration techniques easy to implement and computationally efficient. Due to conditionally stable characteristics, the explicit schemes limit the maximum time step that can be used. On the other hand, the implicit numerical schemes are based both on the current step's and previous step's responses. The implicit schemes were avoided during the early research because they require iterations in order to satisfy the equilibrium. These iterations may result in the undesirable loading and unloading of the specimen, which can be difficultly predicted before the test or taken into account during the test. However, the implicit algorithms are unconditionally stable, and there are no limitations regarding the employed time step. Currently, significant progress has been made regarding proposed time integration schemes, and there are both explicit and implicit integration algorithms which can be efficiently employed in hybrid simulation as summarized in McCrum and Williams (2016).

In the current study, an operator-splitting scheme (OSM) is employed for the time integration algorithm. The OSM is an improved non-iterative implicit-explicit scheme, which was initially proposed by Hunkles et al. (1979) and was first implemented in PsD testing by Nakashima et al. (1990). The OSM uses an implicit approach for linear response and explicit approach for nonlinear response through the utilization of the tangent stiffness of the tested structure in order to eliminate

the iteration requirements. In this study, the α -OSM developed by Combescure and Pegon (1997) is adopted, which is based on the use of α -damping. The α -OSM combines the speed of computation of the explicit method with the numerical dissipation of spurious oscillation. Additionally, within the α -OS methodology, and for the error compensation related to the experimental control, a technique called I-Modification is employed (Nakashima and Kato 1987), which has been proven beneficial for mitigating the effect of the difference between the measured and command displacement and the related experimental energy dissipation errors.

The α -OS method is based on a predictor step for estimating the displacement and velocity vectors based on the previous steps' displacement, velocity and acceleration vectors. The predicted displacement or velocity vectors are subsequently imposed on the structure. Next, the developed displacement and restoring force vectors are measured and are appropriately modified by the I-Modification algorithm. Then, pseudo-excitation force is computed and employed for the acceleration calculation of the current step. Finally, the predicted displacement vector is corrected, and the α -OS algorithm proceeds to the next time step. This algorithm is extensively discussed in Combescure and Pegon (1997) and is not explained further in the current study. Overall, the α -OS integration scheme has been efficiently employed for a broad range of hybrid simulation cases (Pegon and Pinto 2000, Kwon et al. 2008, Murray et al. 2015, Murray and Sasani 2016) and is considered the most efficient scheme for the current study.

2.3.4 Hybrid Simulation Frameworks

Various hybrid simulation frameworks have been developed since the conception of hybrid simulation, which nowadays allows for geographically distributed hybrid simulation combining more than one experimental site for the testing of physical substructures (Mosqueda and Stojadinović 2008, Sextos et al. 2014). In this section, the most important hybrid simulation frameworks are briefly introduced, while the one employed for this study is highlighted.

The first implementation consists of a client/server framework that has been proposed and used by Watanabe et al. (2001) for testing a steel and concrete viaduct between Kyoto University (KU) and Osaka City University (OCU). This framework consists of the main computer (server) which is responsible for the dynamic analysis and the client system which is in charge of controlling the local servers at the experimental sites. The target displacements are transmitted through the internet and are controlled by each local server, while the restoring forces and the measured displacements

are fed back to the client through the web. The communication is performed with the well-known transmission control protocol/internet protocol (TCP/IP), and the framework was proven most efficient when Windows-based computers were used, reaching an average elapsed time equal to 22 sec per analysis step. A similar client-server based framework called ISEE was developed by Wang et al. (2007), which relies on a database and application protocol approach and employs a structured query language (SQL) for the communication between the analysis engine, the facility controller and the data center. This framework demonstrates improved capabilities for solving complex data communication issues compared to the one proposed by Watanabe et al. (2001) and was successfully employed for the distributed testing between the Taiwan University (TU) and the National Center for Research on Earthquake Engineering (NCREE) for the test of a double skinned, concrete filled, steel tube, hollow column from a single-storey, three-bay pinned structure.

An important improvement in the hybrid simulation frameworks was achieved by Pan et al. (2005), who included the use of FEM software in the distributed testing by employing a tangent stiffness approach based on previous steps for avoiding the undesirable iterations in the FEM components. In this method the client/server scheme is referred to as Host/Station, the communication between the various components is established with an HTTP protocol, and the data exchange was implemented using a dynamic link library (.dll). This method was further improved by the introduction of a socket mechanism (Wang et al. 2008) instead of the online protocols, while enhanced stability and accuracy integration schemes have been implemented (Pan et al. 2006). However, the performance was slow because the method had to deal with the nonlinearities of the FEM programs.

The enhanced implementation of FEM packages within hybrid simulation frameworks has been developed by Kwon et al. (2005) with the developed UI-SimCor framework for distributed hybrid simulation tests, which is based on a separation of the simulated model and the integration scheme. The simulation coordinator, which is responsible for the integration scheme, communicates with the clients with a set of requested actions (proposals), which are either accepted and executed by the client or are rejected and the entire test can be canceled by the client. This framework was employed in its early stages in the MOST experiment (Spencer et al. 2004), which combined both numerical and experimental components and demonstrated a significantly improved efficiency with an average required time of 12 sec per analysis step. This framework was further developed to host the application of advanced FEM software packages (Kwon et al. 2008) and consists of the

predecessor of the recently developed UT-SIM hybrid simulation framework that was developed at the University of Toronto, which is employed for this study (Huang and Kwon 2017, Mortazavi et al. 2017). The UT-SIM framework has been successfully employed for the performance assessment of a high-rise building (Huang et al. 2017), the multi-axial hybrid simulation of shear-critical RC elements (Sadeghian et al. n.d.) and for the fragility assessment of telescoping self-centering energy dissipative bracing systems by Kammula et al. (2014).

Finally, a hybrid simulation framework well-worth mentioning is the OpenFresco framework (Schellenberg et al. 2007) developed in a similar server/client approach within the Pacific Earthquake Engineering Research (PEER) Center, which allows for testing to be undertaken at different laboratories, with different test equipment and without specific knowledge related to the underlying software required by the user. The main advantages of OpenFresco are the predefined classes library for various experimental setups (OneActuator, TwoActuators, etc.), experimental elements (e.g., beamColumn, two-NodeLine, truss, etc.) and experimental control hardware (e.g. LabVIEW, SCRAMNet, etc.), which have been employed by various researchers (Schellenberg et al. 2009, McCrum and Broderick 2013).

2.3.5 Experimental Challenges in Hybrid Simulation

Despite of the fact that extensive research has been performed in the hybrid simulation field, there are still challenges that are common or are only partly addressed for case-specific problems. During conventional hybrid simulation, a displacement-controlled technique is employed in the experimental substructure. However, as Bousias highlights (Bousias 2014), the control of the deformation of stiff specimens is a source of difficulty. In a stiff specimen, minor displacement control error may develop significant force fluctuations, induce additional damping or overestimate the stiffness during the dynamic response (Chang et al. 2015). This response deteriorates when the stiffness of the specimen is similar or greater than the loading frame's stiffness, resulting in elastic deformation development on the loading frame, which is conventionally considered as rigid. For addressing the difficulties in deformation control, various error compensation schemes have been developed which are based on deformation measurement by external high accuracy instrumentation (Chang et al. 2015, Whyte and Stojadinovic 2016). Additionally, some mixed-control frameworks have been developed, in which the actuators are controlled through mixed a force and displacement architecture (Bousias 2014, Molina Ruiz et al.

2016, Yang et al. 2017). However, this approach is not well-established yet, and further research is required for its implementation in hybrid simulation applications.

Another challenge of similar importance to the previously described one is the hybrid simulation of multi-DOF structures, where more than one actuator is attached to a substructure, and their strokes are coupled. For the MDOF cases, a coordinate transformation scheme is required, which is responsible for the displacement deformation from the integration module coordinate system to the local actuator's strokes and vice versa, in addition to the equivalent force transformation. For this purpose, various generic hybrid simulation application platforms have been proposed and implemented (Chang et al. 2015, Zhan and Kwon 2015), which, however, are not able to facilitate any potential experimental facility architecture. For such cases, the development of case-specific control platforms may be required as was the case with the present study.

Last but not least, an additional reported challenge within the hybrid simulation literature is the potential friction development in the actuators' swivels in addition to potential force relaxation issues observed during the hybrid simulation. These challenges have been successfully addressed using the continuous movement of the actuators and performing the so-called continuous PsD testing method, in which the architecture is based on non-discrete control of the deformation using small time steps and eliminating the hold periods between the various load stages (Magonette 2001).

In the current study, an RC column which consists of a significantly stiff specimen in terms of axial deformation is experimentally tested, and the specimen's response is controlled by a jack in the axial direction and an actuator in the lateral direction. As a result, the strokes corresponding to the two controlled DOF are coupled, and additionally, the hydraulics are installed at the same loading frame. These circumstances render the use of external instrumentation necessary for the deformation control error compensations, while a case-specific coordinate transformation has been developed. The architecture of the solutions employed for addressing the aforementioned challenges is discussed in the following chapters. Finally, a continuous PsD hybrid simulation was not employed because it was not considered as necessary and would induce additional complexity in the hybrid simulation architecture developed for the current study.

Chapter 3 Reference Structure

3 Description of the Reference Structure Description and Input Ground Motion

In this chapter, the reference structure is presented in addition to the input ground motion. The developed numerical models are discussed, and the results from the preliminary numerical study are presented. The numerical study for the critical element's response is performed. The chapter concludes with the identification of the critical element for the structure's response.

3.1 Structure Overview

The reference structure is a three storey moment resisting reinforced concrete building, with three bays in the E-W direction and four bays in the N-S direction designed and tested in reduced scale by Bracci et al. (1992). The structure is representative of low-rise structures of the mid-1970s, designed primarily to carry gravity loads without any seismic provisions. For this study, a typical frame of the structure along the E-W direction is investigated and is subjected to planar motion. The storey height is 3.66 m (12 f), and the length of each span is 5.49 m (18 f). The study frame in addition to the structure's plan and elevation view is presented in Figure 3-1. For this study, the column sections were modified from square to circular to facilitate the construction of specimens. The circular columns were designed in a way that their contribution to the structure's lateral load resisting capacity is analogous with the original square columns used by Bracci et al. (1992). The updated column detailing is discussed in the next section. The reinforcement overlapping that exists in the experimental investigation conducted by Bracci et al. is not considered in this study for the purpose of simplification due to the uncertainty surrounding the rebar slipping mechanism when it is numerically modeled, and the requirement for experimentally calibrated models to be realistically assessed. As a result, the modified structure employed can be considered as a case study structure for the current work.

In the next sections, the reinforcement layout of the structure is presented in addition to the distribution of mass and gravity load. The material properties of the structure are discussed in Chapter 4.

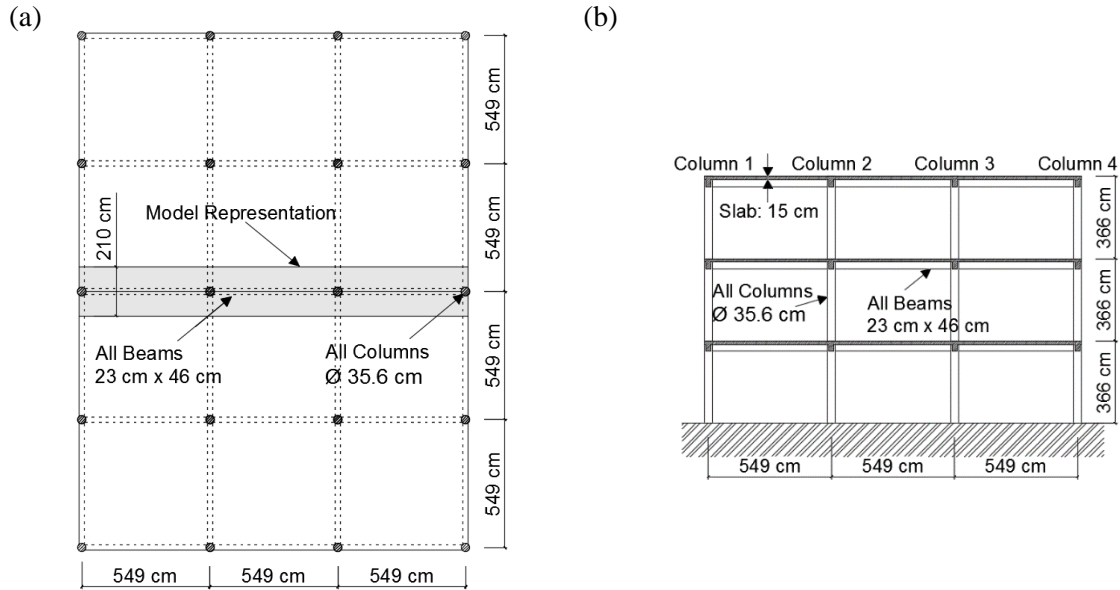


Figure 3-1 Reference structure's (a) plan and (b) elevation view.

3.1.1 Reinforcement Layout

The beam's reinforcing details are the ones designed by Bracci et al. (1992) and is presented in Figure 3-2, while the beam's cross sections along its length are presented in Figure 3-3. The modified column sections and their reinforcing details are presented in Figure 3-4. It should be mentioned that for the reinforcement, deformed bars are assumed which are perfectly bonded with the concrete.

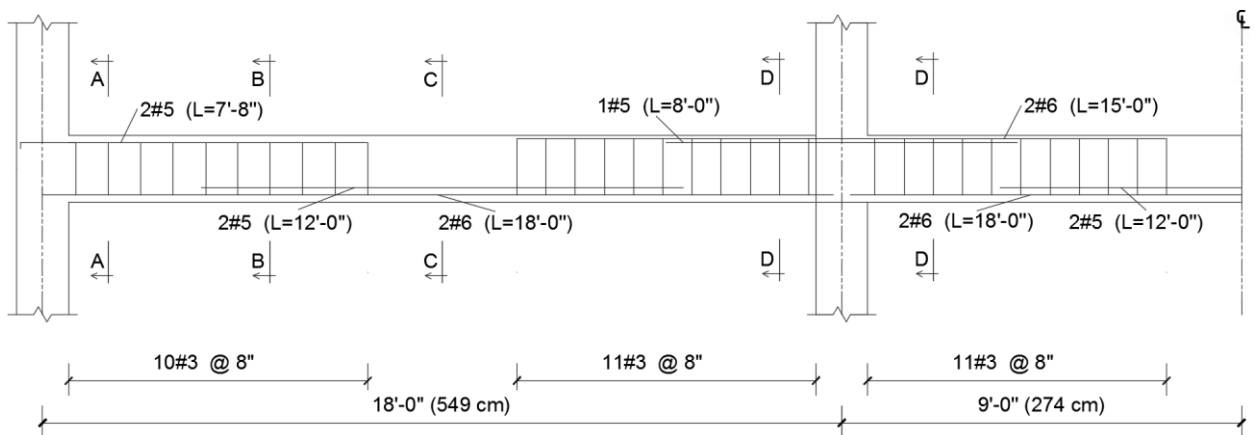


Figure 3-2 Beam reinforcement profile (symmetric) (Bracci et al. 1992).

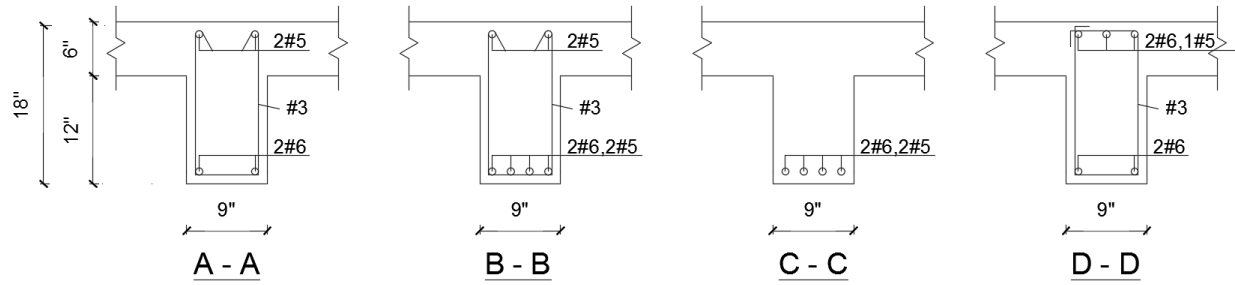


Figure 3-3 Beam typical sections (Bracci et al. 1992).

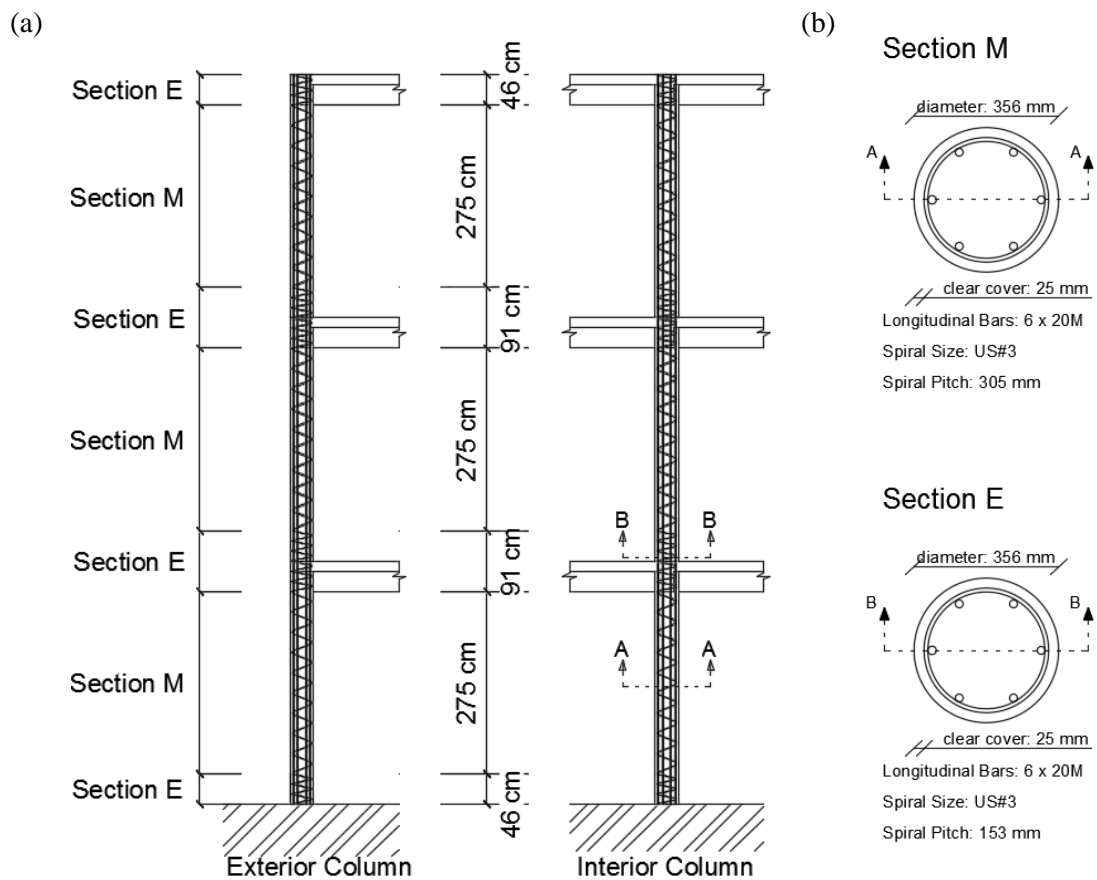


Figure 3-4 Column reinforcing details: (a) Interior and exterior columns, and (b) middle (Section M) and end (Section 3) column sections.

3.1.2 Gravity Load and Mass Distribution

The gravity loads and mass distributions described in Kwon & Elnashai (2006) were to develop a study case equivalent to previous studies available in the literature. In this way, the dynamic response of the structure can be verified against the numerical and experimental studies conducted by different researchers (Bracci et al. 1992, Kwon and Elnashai 2006). The gravity load and the mass distributions in the structure are presented in Figure 3-5. The gravity loads are applied uniformly to the beams using equal point loads, while the masses are assigned to the structure's joints in order to avoid local response modes along the beams. The described gravity load and mass distribution constitute the reference case distribution, which is the one used for most of the experimental program. For the cases where a modified gravity load and mass distribution were used, an additional discussion is included for the related experimental results in Chapter 7.

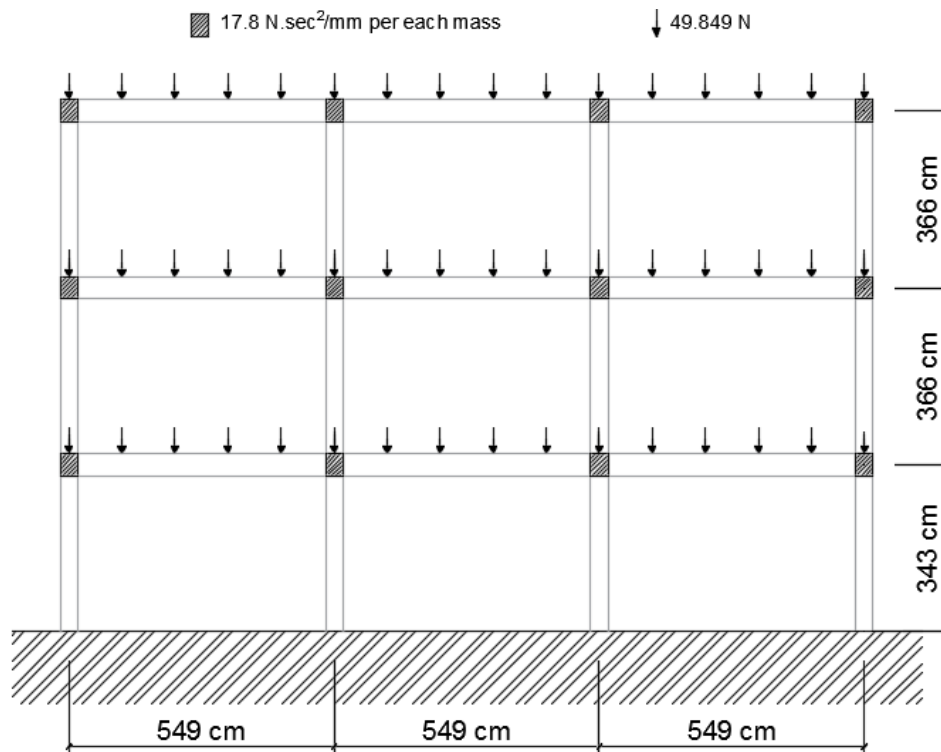


Figure 3-5 Gravity load and mass distribution.

3.2 Seismic Study Sequence

For this study, a sequence of two ground motions was selected. The definition of two ground motions as a seismic sequence and not as two separate excitation cases is a result of the damage developed in the structure and the physical specimen after the first ground motion, and they should be considered as such. Additionally, the ground motions were selected such that the predominant excitation frequency is low, by using the PGA to PGV ratio (α/v). According to Sawada et al. (Sawada et al. 1992) low α/v ratios ($< 0.8 \text{ g/ms}^{-1}$) represent seismic events with low predominant frequencies, broader response spectra, longer durations, medium-to-high magnitudes, and long epicentral distances and site periods. On the other hand, high α/v ratios ($> 1.2 \text{ g/ms}^{-1}$) signify high predominant frequencies, narrow response spectra, short durations, small-to-moderate magnitudes and short epicentral distances and site periods. A final ground motion selection criterion was the development of the damage into the first storey with a soft-storey mechanism, which is a common failure mechanism for structures similar to the case study structure. The selected ground motions are presented in the next two sections.

3.2.1 First Ground Motion

The first earthquake of the study seismic scenario is the excitation recorded in Bucharest, Romania (March 4, 1977) with PGA equal to $0.17g$ and α/v ratio equal to 0.55 g/ms^{-1} . The ground motion duration was defined using the significant duration approach, and the 99% of the arias intensity was captured. The acceleration time history is presented in Figure 3-6. It should be noted that after the first seismic event, 10 sec of free vibration analysis is performed to allow for the structure to return to its equilibrium position before the second seismic event.

3.2.2 Second Ground Motion

The second earthquake of the seismic study scenario is the excitation recorded in Imperial Valley, USA (October 15, 1979), scaled by 1.45. The scaled ground motion PGA is equal to $0.46g$, and the α/v ratio is equal to 1.00 g/ms^{-1} . The ground motion duration was defined using the significant duration and capturing 99% of the Arias Intensity. The acceleration time history is presented in Figure 3-7. Similar to the first seismic event, 3 sec of free vibration analysis was performed after the ground motion record. The integration time step was 0.01 sec for both the ground motions.

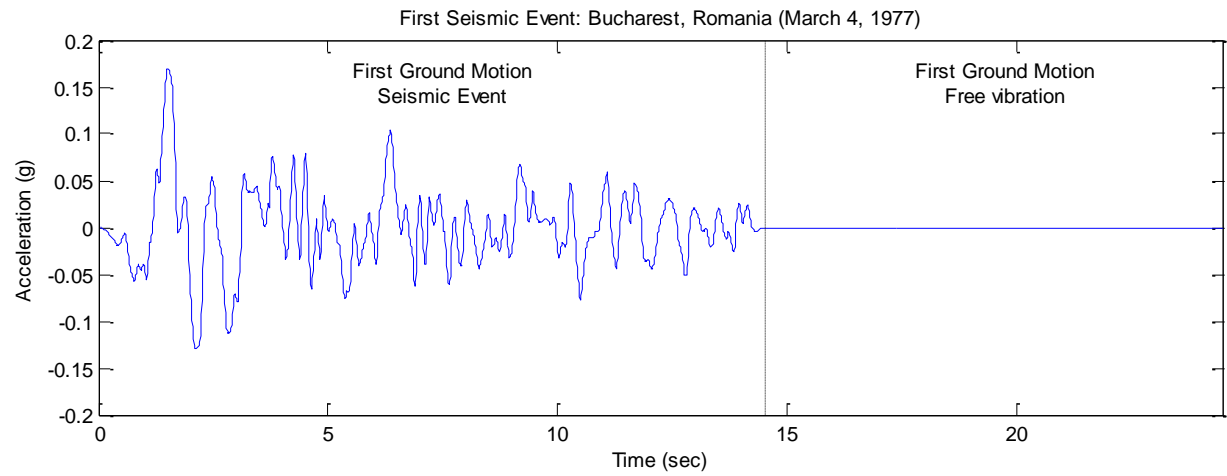


Figure 3-6 First seismic event acceleration time history.

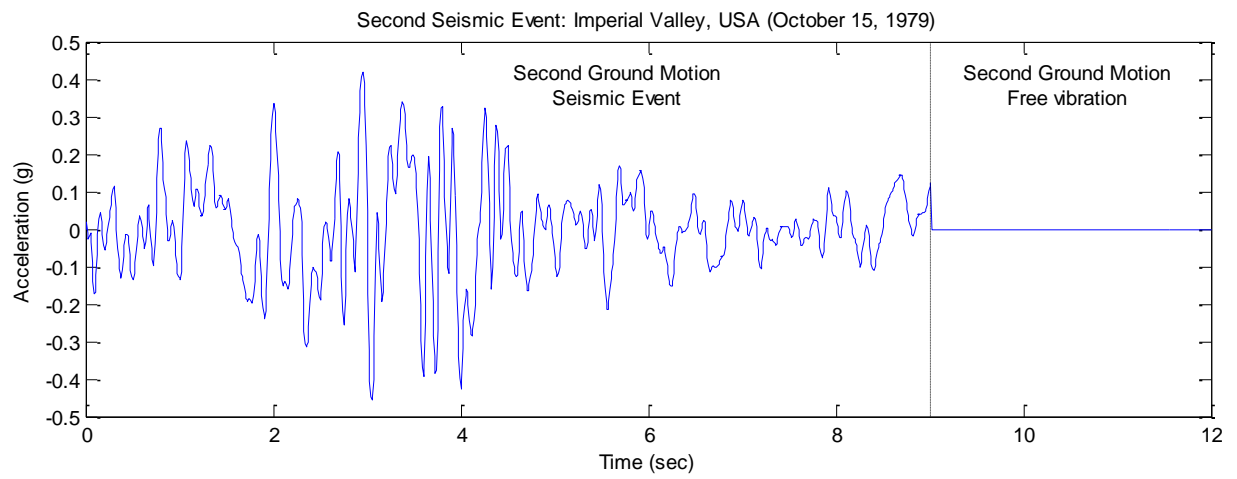


Figure 3-7 Second seismic event acceleration time history.

3.3 Numerical Model

The software framework Open System for Earthquake Engineering Simulation (OpenSees) was employed for developing the numerical model of the structure. OpenSees is an open source software, which allows for the simulation of the structural and geotechnical systems subjected to earthquakes and other hazards, and was developed at the University of California, Berkeley (Mazzoni et al. 2007).

The numerical model discussed in this chapter is the representative numerical model for the reference case, the intact structure. Additional information about the modeling techniques will be given when required for the modified numerical models of the repaired and retrofitted structure. In this section, the employed modeling techniques will be presented in addition to the necessary assumptions and approximations used for the development of the model. Special care will be given on the modeling assumptions.

3.3.1 Numerical Model Overview

For the development of the numerical element, the structure's frame is discretized as shown in Figure 3-8. A mesh sensitivity analysis was performed for a single column response to develop the structure's discretization. It can be observed that the discretization becomes denser at the elements' ends, where the development of nonlinearities is expected. The script developed for the reference structure's numerical model is attached in Appendix B.

The first most significant assumption is that in the developed numerical model no specific care was given to the beam-column joints' connections, which are considered as rigid connections. This modeling assumption consists one of the most significant sources of error for the structure's response since it has been proven that a common failure mechanism of equivalent frequency to the column's failure is the failure in the beam-column joints (Moehle et al. 2006). Furthermore, the action of the diaphragm on each storey was taken into account by defining equal horizontal degrees of freedom at each storey level. The diaphragm assumption of each storey can be considered a realistic means of accounting for the slab participation in the frame's deformation. Finally, the ground floor columns are considered perfectly fixed to the foundation, which may not be a realistic assumption given the structure-to-soil stiffness ratio (NEHRP Consultants Joint Venture 2012).

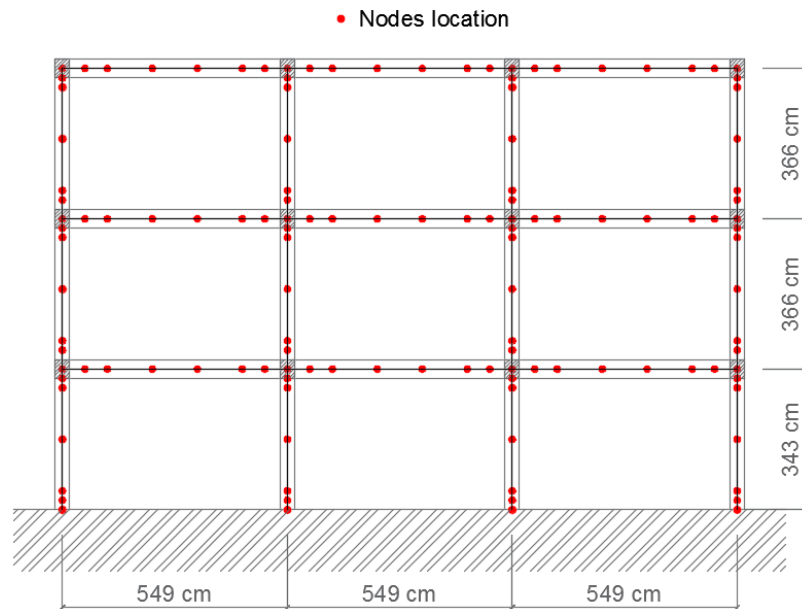


Figure 3-8: Numerical model discretization.

3.3.2 Material Level Modeling Technique

In this section, the constitutive models used for the numerical model are discussed. The employed fiber-section modeling technique (see Section 3.3.3) requires the use of uniaxial materials for defining the material properties of the element. Two different constitutive models were utilized for the concrete and the steel materials which are presented as follows.

Concrete Constitutive Model

The constitutive model used for the concrete material is the Concrete04 Material – Popovics Concrete Material (Mazzoni et al. 2007). The initial stiffness, K_{in} , of the concrete is defined as equal to $57000\sqrt{f'_c}$, where K_{in} and f'_c in psi, and the envelope curve of the constitutive model is identical to the one proposed by Mander et al. (Mander et al. 1988). The cyclic tension compression response envelope is presented in Figure 3-9 (a). Under compression, the curve not only follows the concrete compression model proposed by Popovics (1973) up to the point of concrete crushing but is also able to capture the post-peak concrete response. For unloading and reloading in compression, the model proposed by Karsan and Jirsa (1969) is built-in to the constitutive model Concrete04. In the current study, the tensile strength of concrete is neglected, which is a common assumption for concrete structures, and the rest of the input material properties are presented in the concrete properties chapter (Section 4.2.2).

The effect of the confinement on the columns' and beams' cores was taken into account for calculating the confined concrete compressive strength by using the theoretical stress-strain model for confined concrete proposed by Mander et al. (1988). The enhanced confined concrete strength and stain are presented later in Section 4.2.2. Finally, the ultimate concrete strain was set equal to 0.02 to avoid convergence issues in the numerical model that may occur from the sudden stress drop illustrated in Figure 3-9 (a).

The aforementioned Mander's theoretical stress-strain model for confined concrete can be summarized in the following equations for circular sections confined with spirals:

$$k_e = \frac{1}{1 - \rho_{cc}} \left(1 - \frac{s'}{2d_s} \right)^2 \quad \text{Equation 3-1}$$

$$\rho_s = \frac{4A_{sp}}{d_s s} \quad \text{Equation 3-2}$$

$$f_l' = \frac{1}{2} k_e \rho_s f_{yh} \quad \text{Equation 3-3}$$

$$f_{cc}' = f_{co}' \left(-1.254 + 2.254 \sqrt{1 + \frac{7.94 f_l'}{f_{co}'}} - 2 \frac{f_l'}{f_{co}'} \right) \quad \text{Equation 3-4}$$

where, k_e is the confinement effectiveness, ρ_{cc} is the ratio of the longitudinal reinforcement area to the core section area, s' is the clear vertical spacing of the spiral, d_s is the diameter of the spiral between the spiral bar centers, ρ_s is the ratio of the column's transverse confining steel to the volume of confined concrete core, A_{sp} is the area of transverse reinforcement bar, s is the center to center pitch of the spiral, f_l' is the effective lateral confining stress, f_{yh} is the yield strength of the transverse reinforcement, f_{cc}' is the confined concrete core compressive strength and f_{co}' is the unconfined concrete compressive strength. The confined concrete peak strain ϵ_{cc} is calculated as proposed by Priestley et al. (Priestley et al. 1996) using the following equation.

$$\epsilon_{cc} = 0.002 \left[1 + 5 \left(\frac{f_{cc}'}{f_{co}'} - 1 \right) \right] \quad \text{Equation 3-5}$$

Similarly, Mander's theoretical stress-strain model for confined concrete for rectangular beam sections can be summarized as follows:

$$A_i = \sum_{i=1}^n \frac{(w_i')^2}{6} \quad \text{Equation 3-6}$$

$$k_e = \frac{1}{1 - \rho_{cc}} \left(1 - \sum_{i=1}^n \frac{(w_i')^2}{6b_c d_c} \right) \left(1 - \frac{s'}{2b_c} \right) \left(1 - \frac{s'}{2d_c} \right) \quad \text{Equation 3-7}$$

$$\rho_x = \frac{A_{sx}}{d_c s}, \rho_y = \frac{A_{sy}}{b_c s} \quad \text{Equation 3-8}$$

$$f'_{1x} = k_e \rho_x f_{yh}, f'_{1y} = k_e \rho_y f_{yh} \quad \text{Equation 3-9}$$

where, A_i is the total plan area of the ineffectually confined core concrete at the level of the hoops when there are n number of bars, w_i' is the i -th clear distance between adjacent longitudinal bars, k_e is the confinement effectiveness, ρ_{cc} is the ratio of longitudinal reinforcement area to the core section area, s' is the clear vertical spacing of the hoops, b_c and d_c are the core dimensions to centerlines of the perimeter hoops, ρ_x and ρ_y are the transverse reinforcement ratios, A_{sx} and A_{sy} are the total transverse reinforcement areas, and f'_{1x} and f'_{1y} are the effective lateral confining stresses in the x and y direction respectively. The confined core compressive strength f'_{cc} and the confined concrete peak strain ϵ_{cc} are calculated as in the circular sections using the equations Equation 3-4 and Equation 3-5.

Steel Constitutive Model

The constitutive model used for the steel material is Reinforcing Steel Material (Mazzoni et al. 2007). The required input parameters can be obtained from simple steel rebar tensile coupon tests and are presented in Section 4.2.1. The employed constructive model accounts for the change in the area when the rebar is stressed allowing for a single backbone to represent both the tensile and the compressive stress-strain relationship (Figure 3-9 (b)). Finally, this constitutive model can capture the buckling and the fatigue that occurs in the reinforcement, a feature that was not employed in the current study because of the extensive number of required input parameters which may induce bias in the developed numerical model.

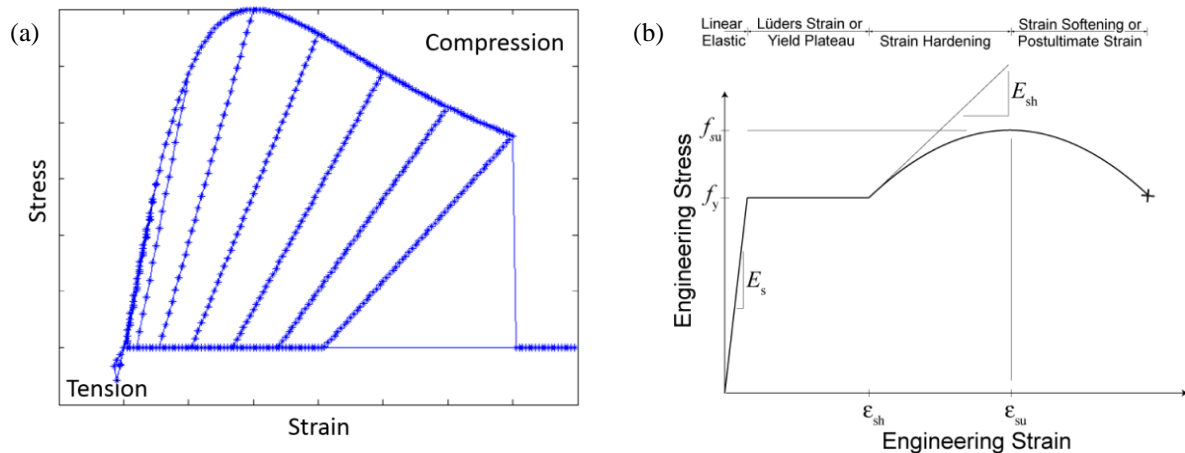


Figure 3-9: (a) Concrete cyclic tension-compression response envelope of “Concrete04 Material”, and (b) Steel backbone curve of “Reinforcing Steel Material” as presented in OpenSees manual (Mazzoni et al. 2007).

3.3.3 Element Level Modeling Technique

A distributed plasticity modeling technique was selected, which is implemented with the use of fiber sections (Huang and Kwon 2015) and displacement beam column elements (Mazzoni et al. 2007). In the fiber element modeling technique, the sections are discretized into fibers as shown in Figure 3-10 and each fiber spans along the element length. For the beams, an effective length equal to 2.1 m is used to account for the slab effect into the beam’s bending. Each fiber’s response is defined by using a uniaxial material constitutive model as described in the previous section and the elements’ response is calculated using the plain sections remain plain assumption at each integration point. For this study, nine integration points are used for each element, and a denser element discretization is performed in the critical regions (Figure 3-8). This technique is required because for the displacement beam-column elements the distributed plasticity is employed with a linear curvature distribution between the integration points (Figure 3-11). As a result, by considering reasonable enough elements and integration points in the critical regions, the nonlinear response can be adequately captured. A mesh sensitivity analysis was performed and is highly recommended for defining the most efficient number of elements and integration points.

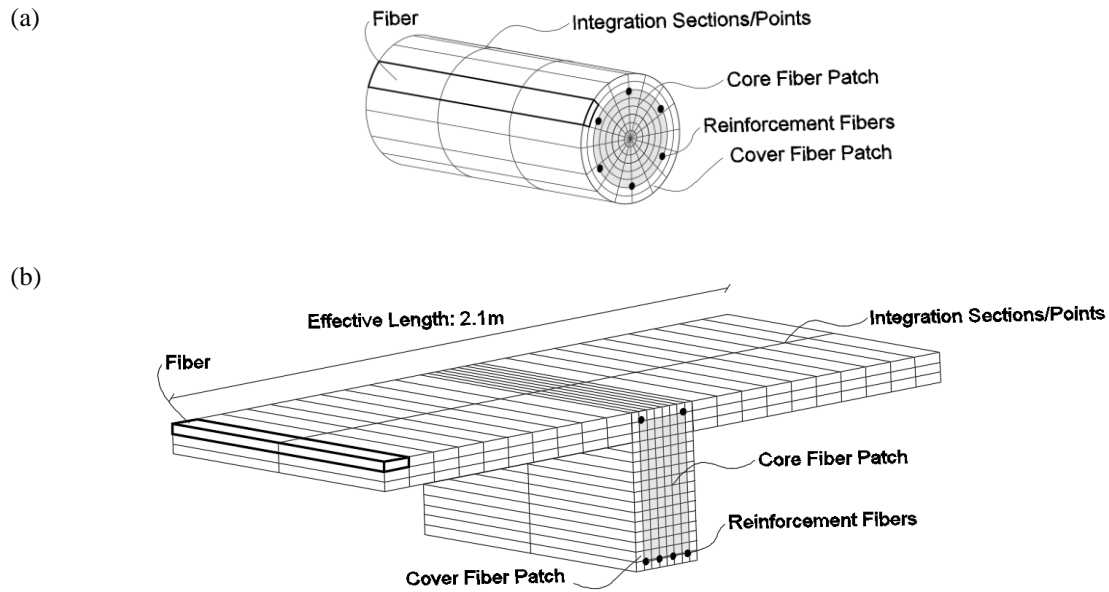


Figure 3-10: Fiber section modeling technique for (a) the columns and (b) the beams of the reference structure.

The most important deficiency of the fiber element section modeling technique is that it is not able to capture the shear response and degradation that occurs in the element. There are available modeling techniques to reduce the effect of that deficiency, like the section aggregator method (Mazzoni et al. 2007) or the use of shear springs (Moehle et al. 2006, Huang and Kwon 2015); however, the development of a complicated numerical model was not within the scope of this study because the critical element of the structure that is experimentally assessed is primarily flexure controlled.

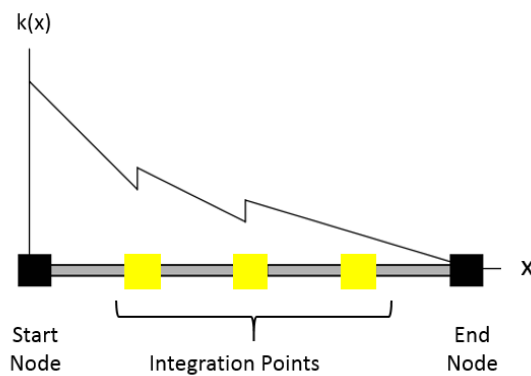


Figure 3-11: Curvature distribution in displacement beam-column elements (Mazzoni et al. 2007).

3.4 Preliminary Numerical Investigation

Before conducting the hybrid simulation, a purely numerical study is required for the verification of the developed numerical model, the preliminary performance assessment of the structure and the identification of the critical element. The preliminary numerical study includes the eigenvalue, the static pushover, and the nonlinear time history analysis using the sequence of ground motions introduced in Section 3.2.

3.4.1 Eigenvalue Analysis

For the verification of the initial elastic dynamic properties of the model, an eigenvalue analysis was conducted. The first, second and third periods of the structure are 0.859, 0.295 and 0.200 sec while the effective modal mass for each mode is 87.4%, 10.1% and 2.4 % respectively, accounting for 99.9% of the total mass of the structure. The time periods reported by Bracci et al. (1992) and Kwon and Elnashai (2006) are 0.932, 0.307, 0.206 sec and 0.898, 0.305 and 0.200 sec, respectively, which give credence to the elastic properties of the numerical model. Given the first natural period of 0.86 sec and the elastic acceleration response spectra of the ground motions (Figure 3-12), the estimated spectral acceleration for the first mode is 0.43g and 0.41g for the first and the second event, respectively. Finally, the three modes resulting from the eigenvalue analysis are presented in Figure 3-13.

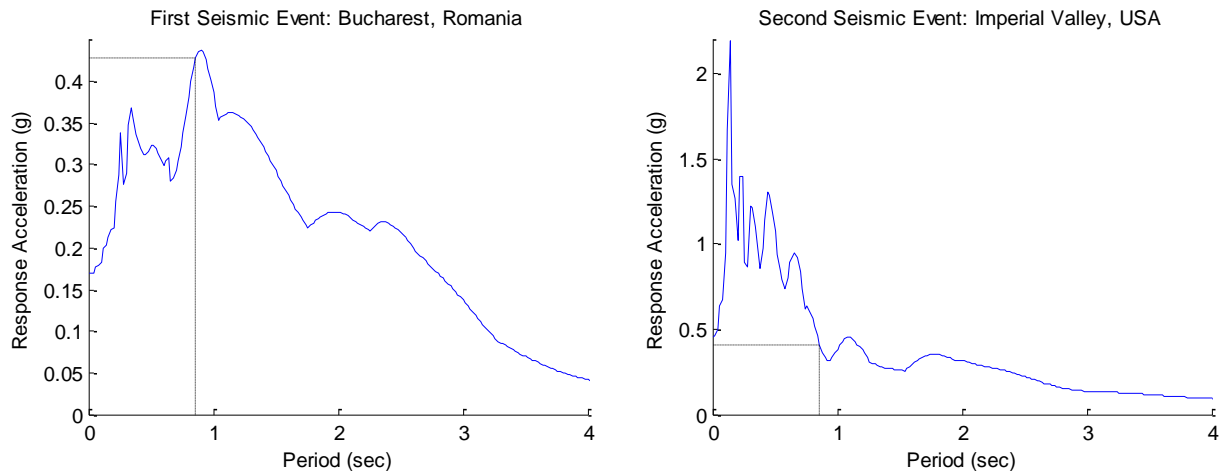


Figure 3-12: Elastic acceleration response spectra for the study seismic events
(Left: Bucharest, Romania 1977& Right: Imperial Valley, USA 1979).

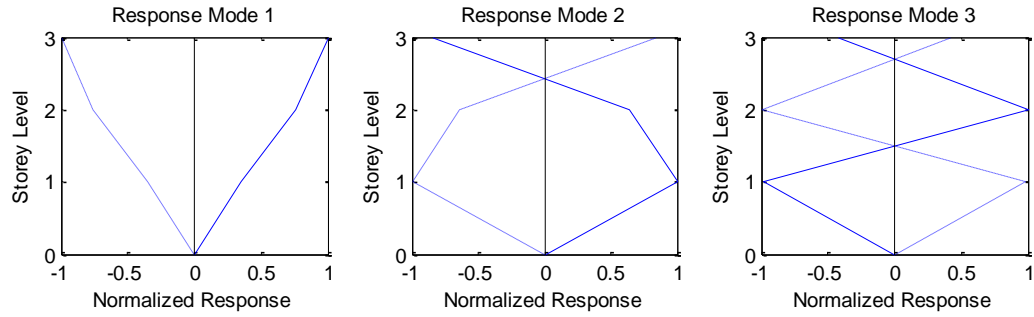


Figure 3-13: Normalized response modes.

3.4.2 Nonlinear Static Pushover Analysis

Before running the nonlinear time history analysis, the nonlinear static pushover analysis was performed to understand the response of the structure under monotonically increasing lateral deformation. The pushover analysis does not replicate the actual dynamic response of the structure but is a handy tool for a quick evaluation the strength, ductility, and failure mechanism of the lateral load resisting system. For the pushover analysis, the control displacement was the top storey displacement while the lateral force distribution along the height was in accordance with the first mode force distribution. The pushover curve in addition to the qualitative representation of the failure mechanism is presented in Figure 3-14.

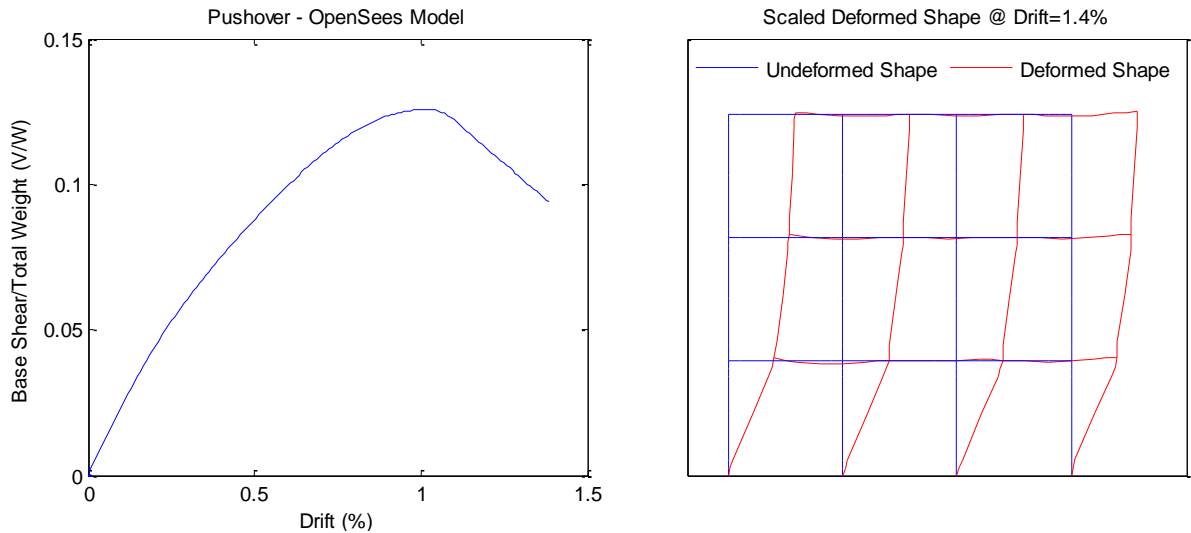


Figure 3-14: Pushover curve (left) and qualitative representation of the failure mechanism (right).

From the pushover curve, it can be observed that the structure presents a flexible and low in strength lateral response, which is reasonable given the absence of a significantly stiff lateral load resisting system, such as shear walls. Additionally, the failure mechanism of the developed model is a soft storey mechanism developed in the first storey. This failure mechanism is common for gravity load designed moment resisting frames (Sadjadi et al. 2007).

3.4.3 Nonlinear Time History Analysis

For the nonlinear time history analysis, the inherent damping is modeled using Rayleigh damping with a damping ratio equal to 0.05 for the first and third mode. Rayleigh damping is a viscous damping that is proportional to a linear combination of mass and stiffness (Chopra 2007). For this study, the initial stiffness of the structure is used for developing the damping matrix. In OpenSees the user can define Rayleigh damping as the linear combination of the current, the last committed, and the initial stiffness, in addition to the mass-proportional damping for defining the damping matrix (Mazzoni et al. 2007). Finally, the α -OS (Combescure and Pegon 1997) integration scheme is used for the pseudo-dynamic analysis, which is an implicit method and has already been discussed in the literature review (Chapter 2).

The response of the structure from the time history analysis is presented in Figure 3-15 in terms of storeys' displacement and in Figure 3-16 in terms of interstorey drifts. Given the performance levels described in FEMA-356 and the interstorey drift's response history, the structure exceeds the Life Safety level but satisfies the Collapse Prevention level with a maximum transient interstorey drift equal to 3.4% and maximum residual drift equal to 0.5% at the first storey. The largest interstorey drift occurs in the first storey during the second ground motion of the seismic sequence and is accompanied with reduced drift demand for the second and the third storeys, indicating the development of soft storey mechanism in the first storey.

Because of the experimental facility, where only one specimen can be tested at time, the first storey column that develops the most significant damage should be identified. For that purpose, the moment-curvature response at the lower integration point for all the four first storey columns is presented in Figure 3-17. From this figure, the initiation of the nonlinear response at t equal to 1.61 sec can be identified in addition to the most critical column (the third column from the left), where both the curvature and the developed moment are greater compared to the other three first storey columns. As a result, the third column of the first floor is the one that will be physically tested during the hybrid simulation.

Finally, for understanding the stiffness deterioration that occurs in the structure during the seismic sequence, two additional eigenvalue analyses were performed after each seismic event. The structure's first, second and third period were modified to 1.406, 0.448 and 0.312 sec after the first ground motion, and to 1.473, 0.468 and 0.316 after the second ground motion. Contrary to the most important displacement demand which occurs during the second ground motion, the most significant period elongation occurs during the first ground motion, which is in agreement with the stiffness degradation demonstrated in Figure 3-17.

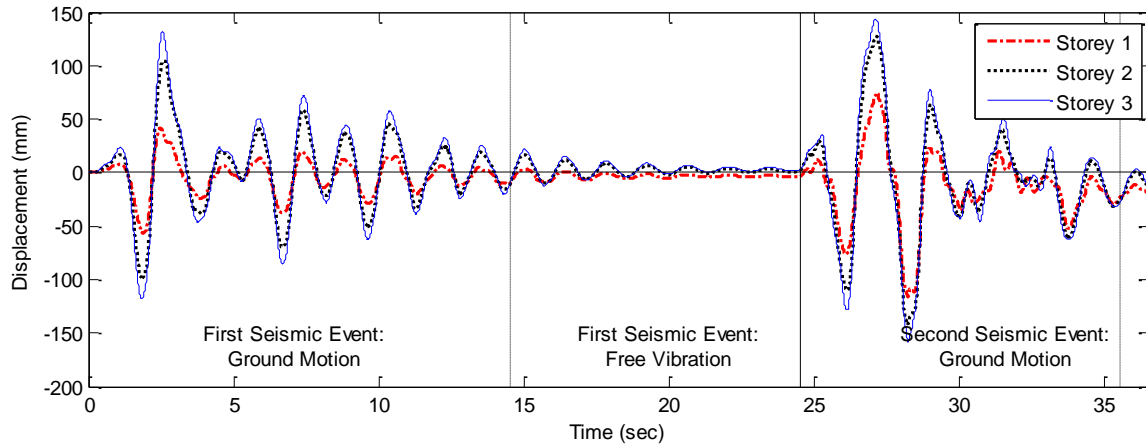


Figure 3-15: Storeys' displacement response history.

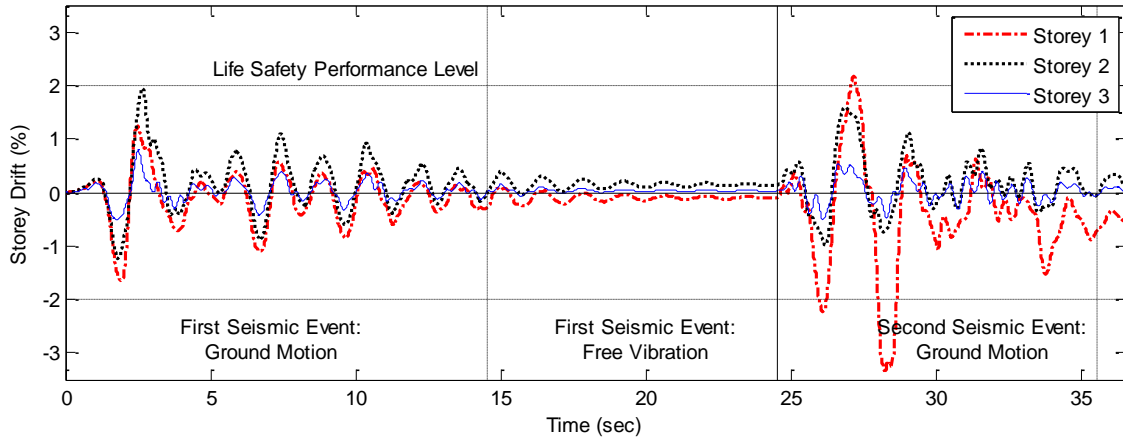


Figure 3-16: Interstorey drifts' response history.

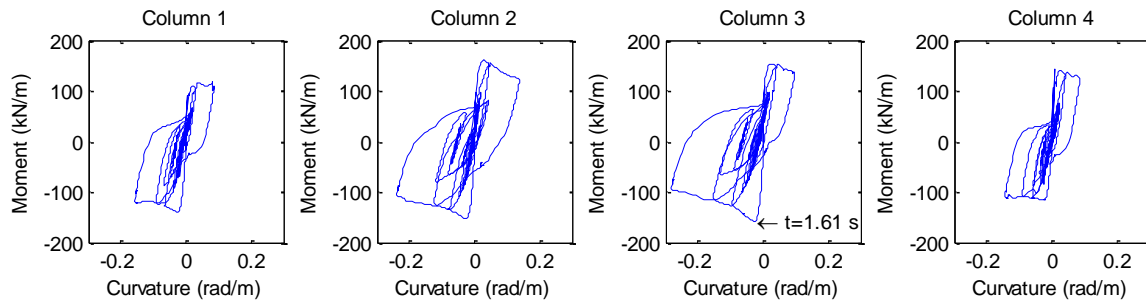


Figure 3-17: Moment-curvature response at the lowest integration points of the first storey columns (Left to right as illustrated in Figure 3-1). Initiation of the nonlinear response at $t=1.61$ s.

3.5 Critical Element

From the preliminary investigation in the previous chapter, the third column (from the left in Figure 3-17) of the first storey was identified as the most critical element for the structure's response. In this chapter, the response of the critical element is numerically studied. Initially, the loading characteristics of the critical element during the seismic sequence are presented, and subsequently, the response of a single cantilever column equivalent to the critical element is numerically investigated.

3.5.1 Loading Characteristics

Before developing a detailed numerical model for understanding the behavior of the element that will be physically tested, the force and deformation response history during the previous numerical investigation of the same element is presented. It should be noted that only the lower half of the column is considered because of the experimental facility setup which accounts for the contraflexure point at the column's mid-height. In Figure 3-18 the axial and lateral deformation response history of the first storey's third column is presented. In the axial deformation response history, the deformation imposed by the gravity loads is -0.43mm. During the seismic sequence, unrealistic positive deformation is developed even though the axial force is always in compression (Figure 3-19). This response is due to the assumption that the plane sections remain plain. The lateral deformation results in a reduction of the compression area in the column section and a sectional rotation occurs around the offset neutral axis. This rotation, in addition to the reference point of the section that is located at the geometric center, results in the positive deformation recorded in the axial direction. As for the lateral response, the critical element's deformation response history is consistent with the storey's displacement response history (Figure 3-15) and a residual deformation of -8 mm is observed.

In Figure 3-19 the axial and lateral force histories of the critical element are presented. The axial force developed by the gravity loads is 740 kN, while during the seismic sequence the axial load varies between 668 and 813 kN as a result of the overturning moment developed in the structure. As for the lateral response, the developed shear force varies between -100 and 100 kN regardless of the fact that the negative lateral deformation is 50% more than the positive, indicating that the element reached its maximum capacity in both directions and significant stiffness degradation may occur.

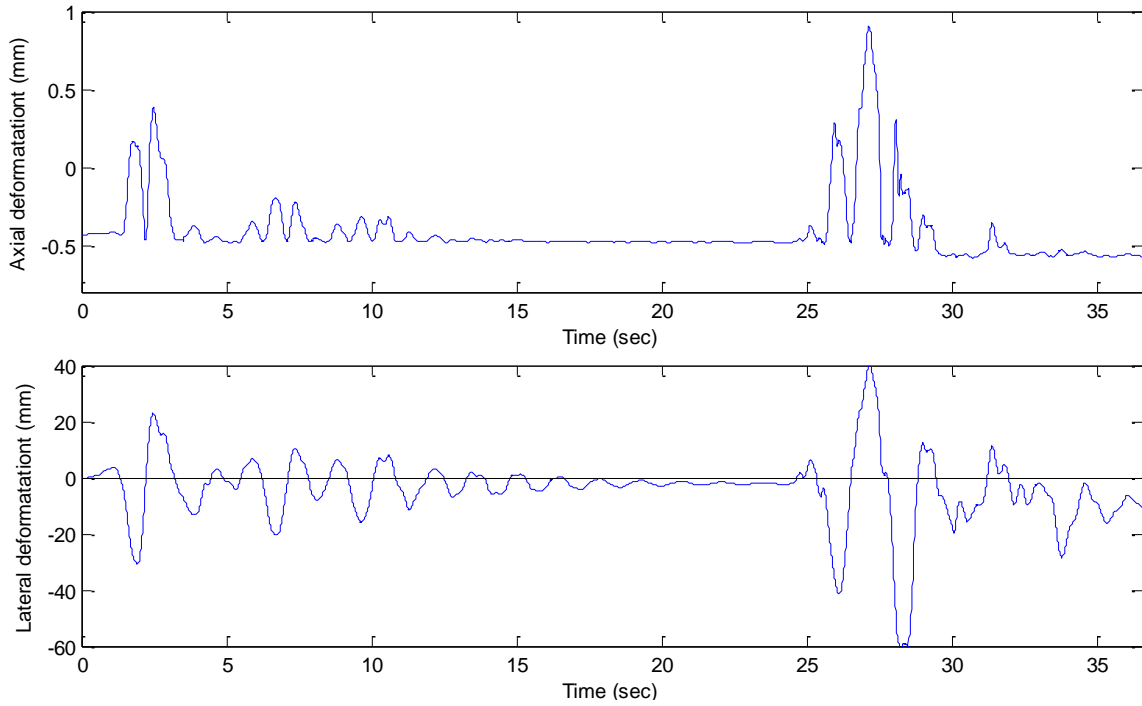


Figure 3-18: Deformation response history of the critical element during the initial numerical investigation.

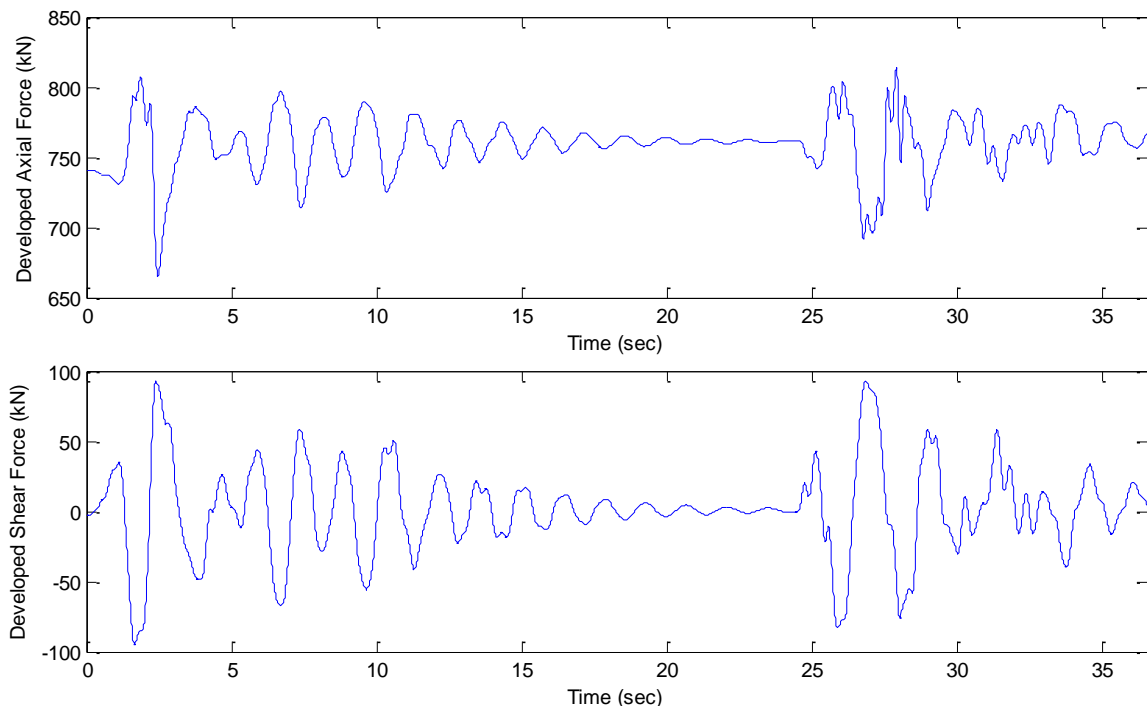


Figure 3-19: Developed forces history in the critical element during the initial numerical investigation.

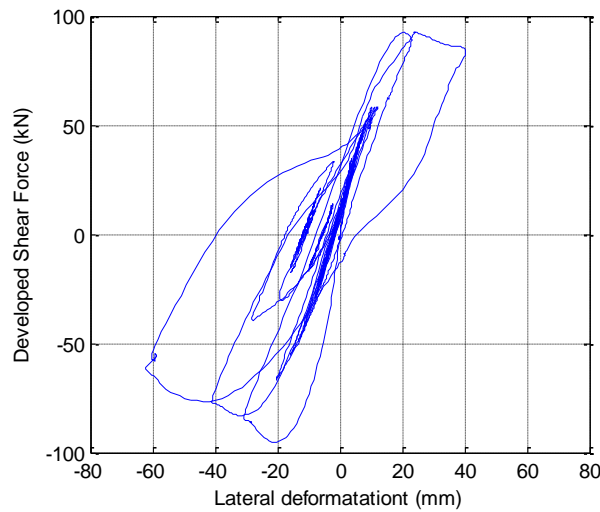


Figure 3-20: Hysteretic response of the critical element during the initial numerical investigation.

To understand the lateral response of the critical element, the hysteretic response is presented in Figure 3-20. Although the hysteretic response using the force-deformation loops was proven not to be an adequate measure for assessing seismic performance (Kazantzi and Vamvatsikos 2012), it serves well as a general indicator of the element's performance, which becomes more important as the system approaches the global collapse state (Ibarra et al. 2005). In the study element, a strength degradation equal to 30% is observed for the negative deformation side, while a few thick hysteretic loops are formed. Finally, a significant pinching effect can be observed in the two major hysteretic loops, which is an indication of significant damage development in the study element.

3.5.2 Critical Element Response Study

In order to understand the element's response, a numerical investigation of a single cantilever column with material and section properties same as the study specimen was performed. Initially, a sectional analysis was conducted, and subsequently, the response of the cantilever was investigated both using a monotonic and a quasi-static analysis.

3.5.2.1 Section Level Study

For the sectional study, the software developed in University of Toronto Response-2000 was used (Bentz 2000). Response-2000 is an extension of the well-known fiber section model (Taucer and Spacone 1991), which is equivalent to the previously discussed fiber model in OpenSees, but

includes the shear effects (Collins 1978, Vecchio and Collins 1986, 1988). The material properties of the numerical model for the sectional analysis are the ones that are discussed in Chapter 4.

Initially, the axial response of the section was investigated under monotonically increasing axial deformation to evaluate the specimen's axial load capacity (Figure 3-21a). The peak compressive load P_o is equal to -4,415 kN with a corresponding compressive peak strain equal to 2 mm/m. Because of the gravity loads, the critical element is always under compression with a ratio P/P_o equal to 16.7%, while during the seismic sequence the axial load is changing and the ratio P/P_o varies between 15.1 and 18.4% (Figure 3-19). Additionally, an axial load – moment capacity investigation was performed, and the results are presented in Figure 3-21b. The balanced axial load and moment combination is for an axial load equal of 1,260 kN ($0.26P_o$) when the moment capacity is equal to 168 kN·m. For the study structure case, the axial load is 740 kN ($0.167P_o$) and the moment capacity is 152 kN·m, which results in the conclusion that the design is efficient, because, at the applied axial gravity load level, the moment capacity is only 10% less than the maximum moment capacity.

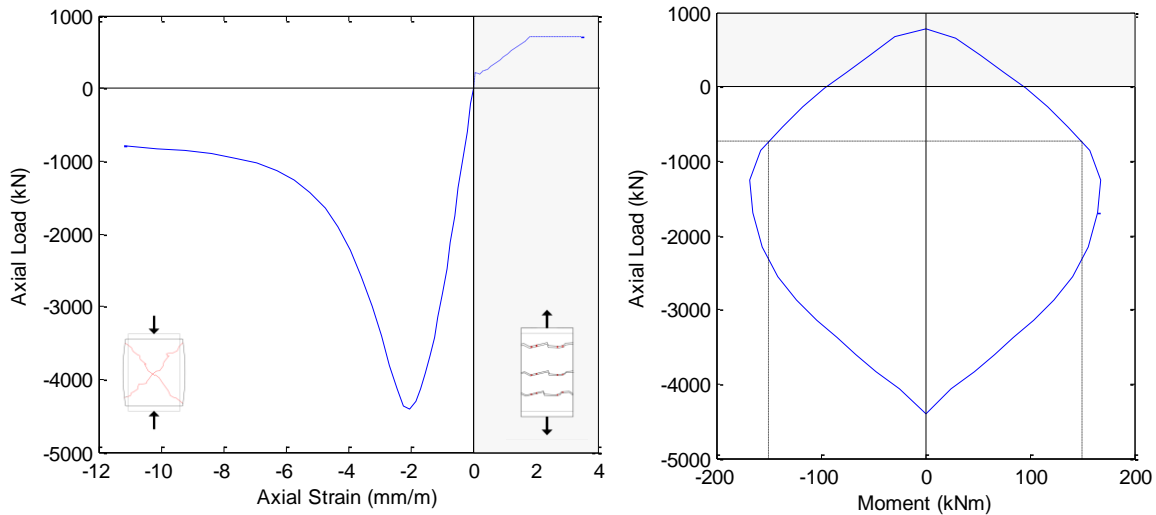


Figure 3-21: Sectional response study using Response-2000. (a) Left: monotonic axial loading, and (b) Right: axial load – developed moment relationship curve

3.5.2.2 Element Level Study

For understanding the critical element's response, the software developed in the University of Toronto VecTor2 is used (Vecchio and Collins 1986, Vecchio 2000). VecTor2 is a nonlinear finite element analysis software for the analysis of two-dimensional reinforced concrete membrane structures subjected to quasi-static and dynamic conditions. For this study, a numerical model of the critical element was developed, where it is considered as a cantilever with a height equal to the height of specimen that the experimental setup is able to test (1.84m). The development of the numerical model is briefly discussed, and subsequently, the two study loading cases are presented in addition to their results.

3.5.2.2.1 Numerical Model

For developing the numerical model, a pre-processor named "Formworks" is employed. A detailed discussion regarding the development of the numerical model is considered as out of the scope of this study and can be found in the Formworks manual (Wong et al. 2012) and in the related literature (Sadeghian and Vecchio 2015) where the latest advancement in Formworks are discussed. However, some of the most important modeling techniques are presented as follows. The developed numerical model in VecTor2 that is discussed in this section is used later for the multiplatform simulation in Chapter 7.

Since VecTor2 is a program working with two-dimensional membrane elements, and the critical element's section is circular, an extensive surface discretization is required for developing an equivalent orthogonal-composed section as illustrated in Figure 3-22. Additionally, the discretization of the membrane (Figure 3-23a) was performed using quadrilaterals elements, which allow for the development of P- Δ effects. The fixation of the cantilever and the uniform application of the loads at the top are performed using two rigid zones as shown in Figure 3-23a (upper and lower block).

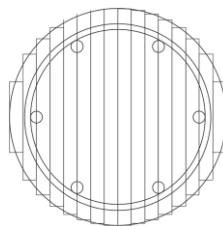


Figure 3-22: Section discretization into an equivalent orthogonal-composed section

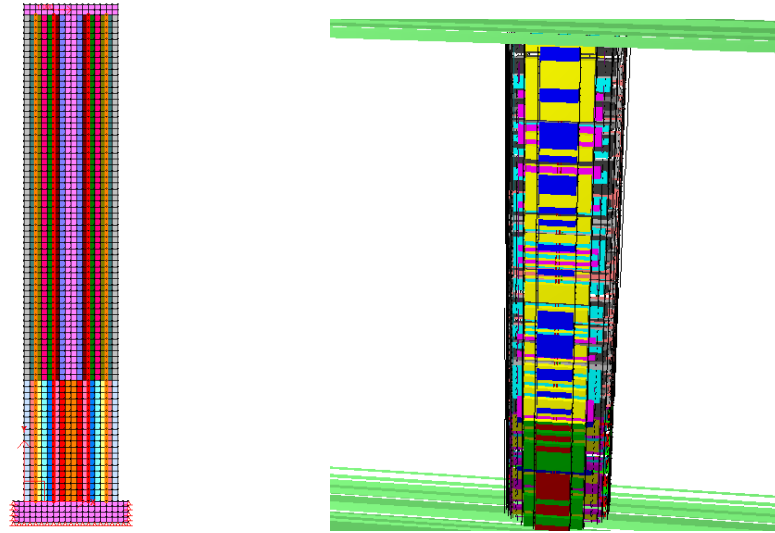


Figure 3-23: (a) Left: Membrane discretization in VecTor2, and (b) Right: three-dimensional representation of the specimen in Augustus.

The concrete and reinforcement material properties that were used are consistent with the ones given in Chapter 4, while the constitutive models used are the ones defined in the “Advanced” option available in Formworks. For the rigid zones, a significantly stiff steel material was used for replicating a rigid block response. The longitudinal bars are defined as discrete bars, which allows for considering of the potential buckling by defining the unsupported length ratio b/t as the ratio of the spiral pitch over the diameter of the longitudinal bars. The longitudinal bars are considered to develop perfect bond with the concrete. The transverse reinforcement is modeled as smeared for both the in-plane and out-of-plane direction and is defined as a reinforcement percentage ratio in each direction.

Finally, the post-process of the results was performed using the software Augustus, which was also developed at the University of Toronto. Augustus is a post-analysis visualization software for the global and local load-deformation response, element stress and strain conditions, deflection and cracks pattern, damage indicators, and other pertinent data. It is also able to produce a three-dimensional representation of the developed numerical model which can be used for the verification of the column’s geometry (Figure 3-23b).

3.5.2.2.2 Monotonic and Quasi-static Analysis

The developed numerical model of the critical element was employed for performing a monotonic and quasi-static analysis. Both these analyses were conducted under a constant axial load equal to 740 kN, which is the load imposed on the specimen during the gravity state.

In Figure 3-24 the results of the monotonic and quasi-static analysis using VecTor2 are presented. It can be observed that the monotonic loading is almost identical to the envelope of the quasi-static response. Both for the monotonic loading and the envelope of the quasi-static response, there is a gradual strength degradation, and the element's failure can be described as brittle. The specimen fails due to the combination of the concrete crushing in the compressive zone and the rebar buckling. The maximum base shear is 84 kN, and when the 1.84 m height of the cantilever is considered, the developed moment at the base is 155 kN·m, consistent with Figure 3-21. Finally, in Figure 3-24b the response from the initial investigation (OS) is compared with the response from VecTor2. It can be observed that the initial stiffness is equal for both cases, but the numerical model developed in OpenSees displays a higher capacity because it cannot capture the failure mechanisms of the critical element as accurately as VecTor2 does.

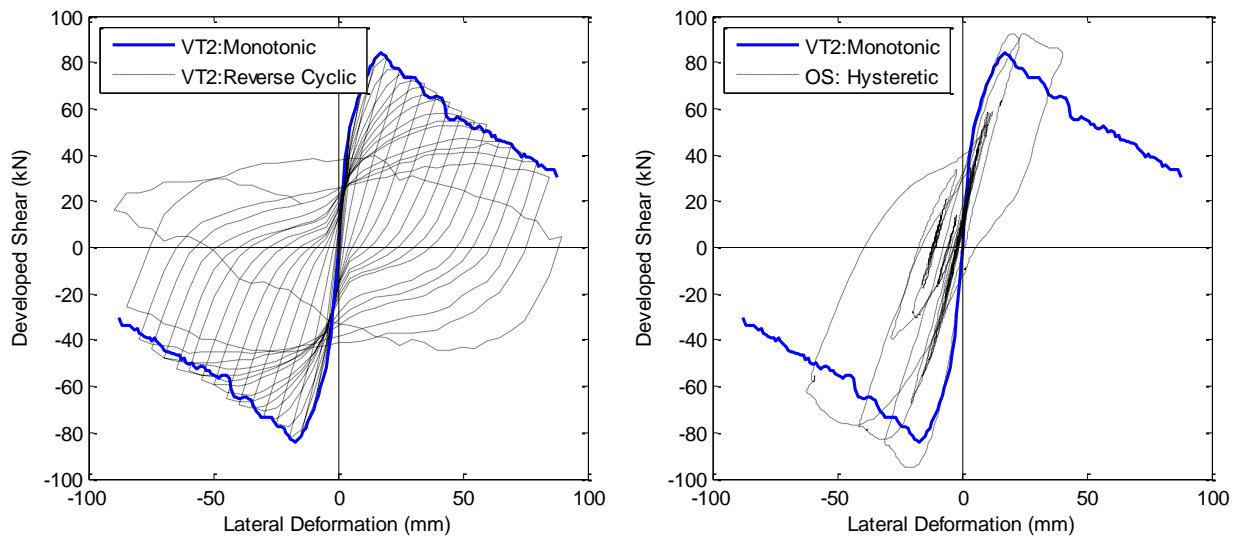


Figure 3-24: Cantilever column study. (a) Left: monotonic and quasi-static loading using VecTor2, and (b) Right: monotonic loading in VecTor2 and hysteretic response from preliminary investigation (OS)

Chapter 4 Experimental Program

4 Construction of Column Specimens

In this chapter, the construction of the physical specimens is discussed, including their material properties and repairing and upgrading techniques. Also, the employed instrumentation on the specimen is discussed in detail, and the chapter ends with a description of the test setup.

4.1 Introduction

As part of this study, four circular reinforced concrete columns were constructed in the Structural Testing Laboratories at the Department of Civil Engineering at the University of Toronto. The columns' heights are 1,470 mm, and the cross section diameters are 356 mm. The columns were cast integrally with 484 x 700 x 500 mm stubs, which is used to impose lateral deformation. The four specimens were identically cast. The specimen is presented in addition to its isometric view with the reinforcement details.

(a)



(b)

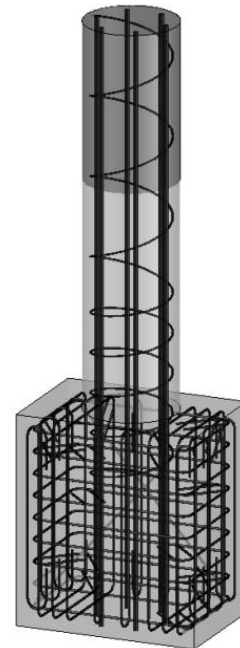


Figure 4-1: Reinforced concrete specimen: (a) constructed specimen and (b) isometric view.

4.2 Material Properties

4.2.1 Steel Reinforcing Bars

Grade 400W deformed reinforcement bars were used for the construction of the specimens. For the longitudinal reinforcement, six 20M bars were used for each specimen, whose length was 2,240 mm. For the transverse reinforcement, US#3 bars were formed into spirals with a pitch equal to 152 mm and 305 mm for the critical and the noncritical area as shown in Figure 3-4. The 10M bars were used to make stirrups for the stubs of the specimens.

The mechanical properties of the reinforcing bars were measured from tensile coupon tests using the MTS 1,000 kN testing setup. Three coupons of each bar size were tested in accordance with ASTM A370 – 15 (ASTM 2014). In Figure 4-2, the development of necking is depicted for a 10M rebar in addition to the three ruptured 20M rebar coupons. The stress-strain curves as averaged from the three coupon tests of each rebar size are presented in Figure 4-3. It can be observed that the tensile response is not only affected from the grade of the steel but also it is related to the rebar size. Finally, the reinforcement properties are summarized in Table 4-1 which are used to develop numerical models.

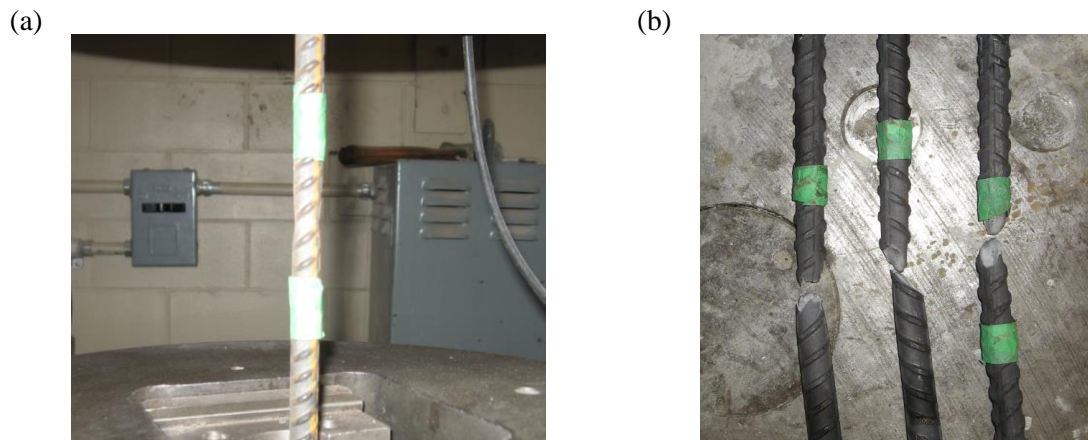


Figure 4-2: Steel coupon testing: (a) necking development in 10M rebar and (b) ruptured 20M rebar coupons.

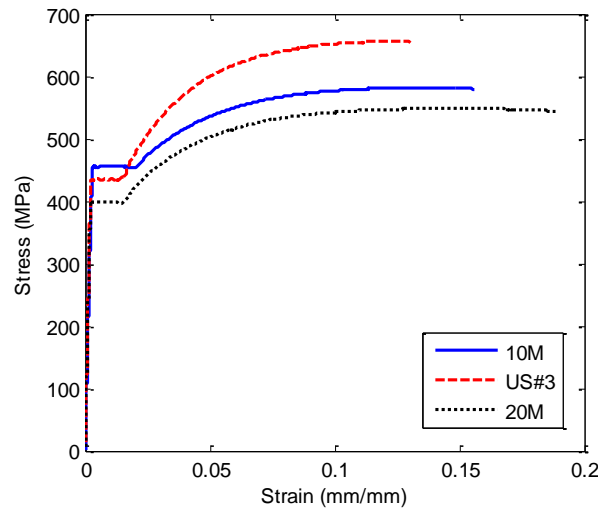


Figure 4-3: Steel coupon testing: (a) necking development in 10M rebar and (b) ruptured 20M rebar coupons.

Table 4-1: Mechanical properties of reinforcing steel

Size	Reinforcement Type	Grade	Yield Stress f_y (MPa)	Ultimate Stress f_{ult} (MPa)	Elasticity Modulus E (MPa)	Tangent Elasticity of Modulus at Strain Hardening E_{sh} (MPa)	Strain Corresponding to Initial Strain Hardening ϵ_{sh} (MPa)	Ultimate Strain ϵ_{ult}
20M	Longitudinal Bars		400	550	191,555	5,000	0.0150	0.164
US#3	Spiral and Stirrups	400W	435	656	196,500	7,200	0.0145	0.130
10M	Stub Reinforcement		455	585	170,000	5,500	0.0200	0.155

4.2.2 Concrete

Three cubic meters of concrete were ordered for casting the four specimens, in addition to the cylinders used for measuring the concrete properties. The target compressive strength was 25 MPa with a slump equal to 100 mm and maximum aggregate size equal to 14 mm. The concrete strength was measured 3 days after the cast and up to the day before each test using 100 x 200 mm (4 inch) cylinders tested according to ASTM C39 (ASTM-C39 2012) in the 4,500-kN MTS Stiff Frame. The concrete stress-strain curve for the 28th day and for the testing time range (almost identical for all the tests) are presented in Figure 4-4. The peak compressive strength f_{co}' of the unconfined concrete at the time that the specimens were tested was 39 MPa with a corresponding strain equal to 0.0024 mm/mm. The testing setup in addition to a tested cylinder set (three cylinders were tested at a time) is presented in Figure 4-5.

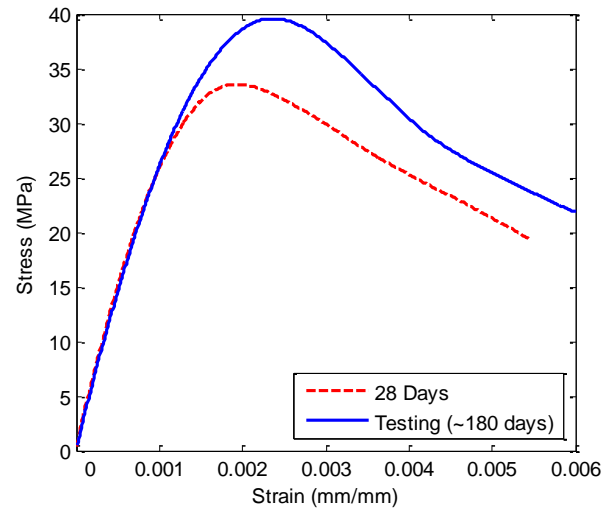


Figure 4-4: Concrete stress-strain curves at 28 days and at the testing time (~180 days).

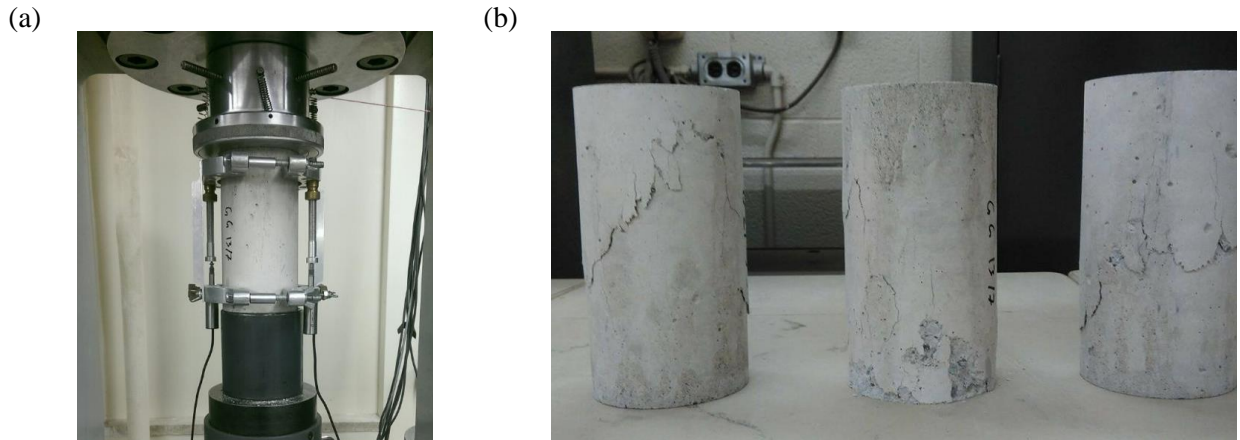


Figure 4-5: Cylinders Testing. (a) Left: Testing Setup (b). Right: Crushed cylinders set.

Table 4-2: Mechanical properties of concrete materials.

Material	Material Type	Compressive Strength f'_c (MPa)	Concrete Peak Strain ϵ_{co} (mm/mm)	Elasticity Modulus E (MPa)	Concrete Ultimate Strain ϵ_{cu} (mm/mm)
1	Unconfined Concrete	39.0	0.0024		
2	Columns Confined @ 6''	45.7	0.0037	29,557	0.02 [†]
3	Columns Confined @ 12''	41.1	0.0026		
4	Beams Confined	40.0	0.0024		

[†] The concrete ultimate strain was set equal to 0.02 in OpenSees to avoid numerical instabilities

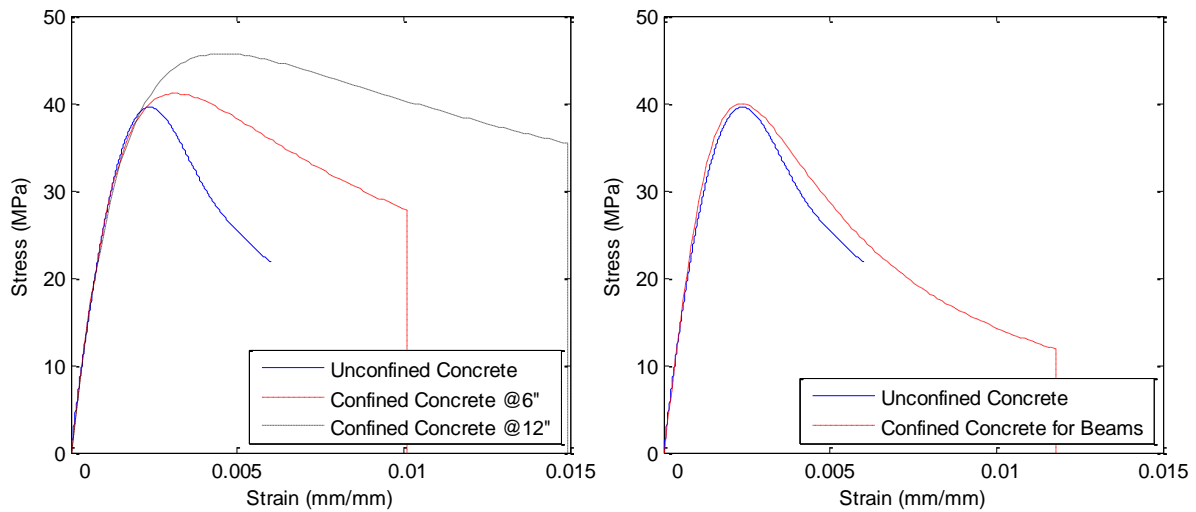


Figure 4-6: Stress-strain curves of confined concrete. Left: columns' confinement. Right: beams' confinement.

Finally, the confined concrete stress-strain curves for the columns' and beams' confined sections as calculated using Equation 3-1 to Equation 3-9 are presented in Figure 4-6. The concrete material properties that were defined in the numerical models are summarized in Table 4-2.

4.2.3 Carbon Fiber Reinforced Polymer Wrap

Unidirectional carbon fiber reinforced polymer (CFRP) sheets were used to wrap the upper parts of the specimens to avoid any premature failure in the non-critical areas. The same CFRP sheets were also used to repair or retrofit the specimens. The CFRP properties were identified by performing tensile coupon tests using the Instron 45 kN setup according to ASTM-D3039 (ASTM D3039/3039M 2006). One layer of CFRP supplied from NIPPOL OIL CORP with the specification ST200-25 & 50 was used. The CFRP was applied to the specimens using Tyfo S saturant epoxy supplied from FYFE. Additionally, a heat-shrink tape was used externally to impose temporary pressure on the CFRP surface during the curing in to improve the bonding between the concrete surface and CFRP sheet. The use of heat-shrink tape requires the penetration with a porcupine roller and a heat treatment to activate its shrinkage mechanism. In order to evaluate any potential damage to the fibers developed during its penetration, two sets of CFRP coupons were tested. The reference coupon set is notated as R_i , and the penetrated coupon set is notated as P_i , where i is the individual coupon number. The tested coupons, in addition to the porcupine roller, are presented in Figure 4-7.

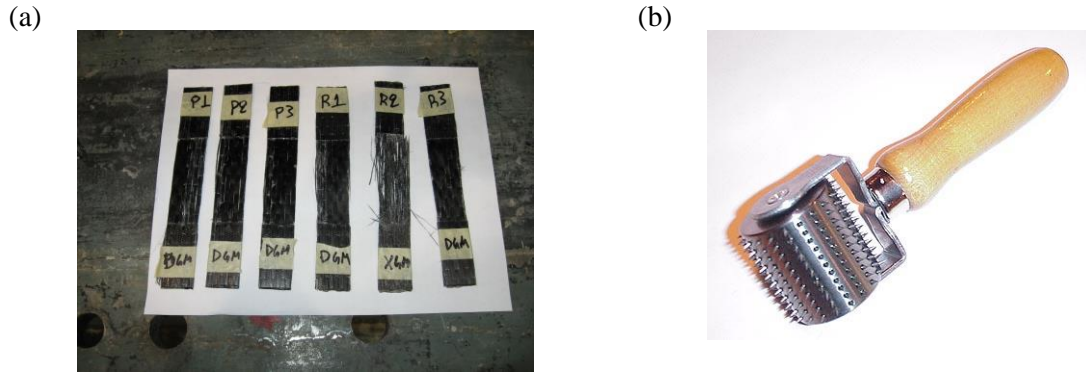


Figure 4-7: (a) Left: CFRP coupons notated with failure modes (ASTM D3039/3039M 2006), and (b) Right: porcupine roller.

The measured and the averaged stress-strain curves are presented in Figure 4-8 and the CFRP properties are summarized in Table 4-3. The reference coupon R2 was not properly measured during testing and the stiffness differences for P1 and R3 in Figure 4-8 are a result of developed out-of-plane bending in the coupon sample due to eccentric axial loading.

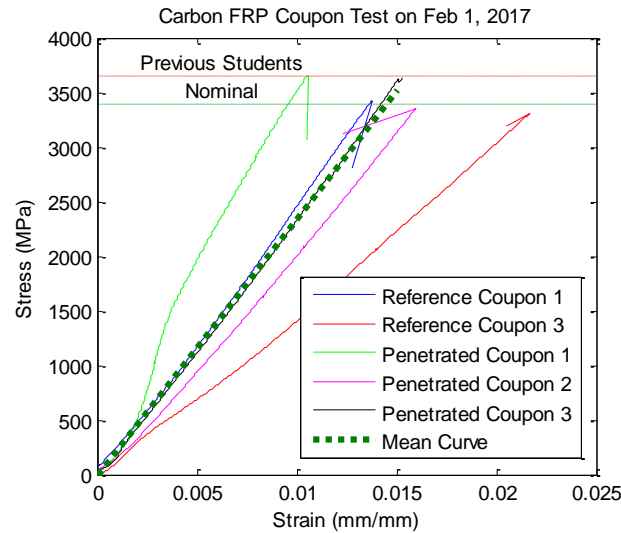


Figure 4-8: CFRP stress strain curves.

Table 4-3: Mechanical properties of CFRP

Type	Supplier	Roll width (mm)	Thickness (mm)	Area weight (g/m ²)	Fiber Density (g/m ³)	Tensile Strength (MPa)	Elasticity Modulus E (MPa)	Ultimate Strain ϵ_u
ST200-50	NIPPOL	50						
	OIL		0.111	200	1.80	3,396 [3,518] †	[234,524] †	[0.015] †
ST200-25	CORP	25						

† The values into brackets are the ones measured from coupon tests. The rest are nominal values.

4.2.4 Repair Mortar

For the repair of the crushed concrete on the damaged specimens, the repair mortar Emaco ® S88 CI produced by the BASF chemical company was used. Emaco ® S88 CI is a one-component rheoplastic, shrinkage-compensated, fiber-reinforced product that contains silica fume to offer high strength and superior performance for structural concrete repairs (BASF: The Chemical Company 2007). Two different mortar batches were made for repairing the first and second specimens, respectively. The water to cement ratio was set initially equal to 0.14, but it was empirically modified during the mixing of the repair mortar to achieve the desired workability for the repair. The repair mortar properties were measured one day before each test and are summarized in Table 4-4. The resultant stress-strain curves from the mortar cylinder tests are presented in Figure 4-9. The potential sources for the different post-peak responses between the two batches are the premature aging of the repair mortar (14 instead of 21 days), and the smaller water to cement ratio of the second batch compared to the first, which was necessary to improve workability.

Table 4-4: Mechanical properties of EMACO ® S88 CI Repair Mortar

Repair Mortar EMACO ® S88 CI	Test day	Modulus of elasticity (MPa)	Direct tensile bond strength (MPa)	Direct shear bond strength (MPa)	Flexural strength (MPa)	Compressive strength (MPa)
Nominal	-	34500	2.1	4.8	9	62.1
First batch	21	27500	-	-	-	57.3
Second batch	14	27000	-	-	-	60.2

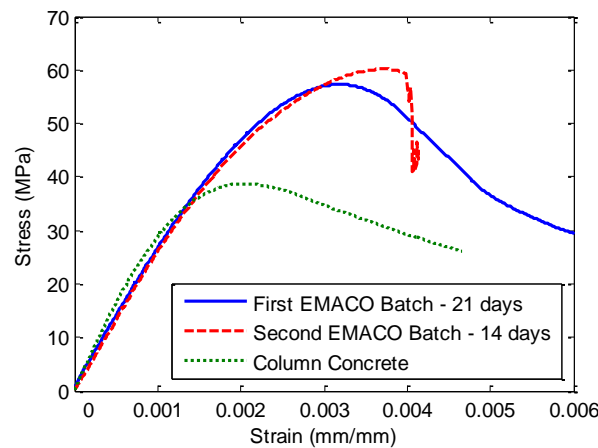


Figure 4-9: EMACO ® S88CI repair mortar stress strain curves.

4.3 Construction Procedure

In this section, the construction stages of the specimens are described. Four 356 mm diameter circular columns, each 1,470 mm long, were cast integrally with a concrete stub of 484×500×800 mm at one end, representative of a fixed joint or foundation. The construction stages are presented in the same sequence as they took place.

4.3.1 Reinforcement Cages

The first part of the construction procedure was the preparation of the reinforcement cages. The reinforcement cages are composed of two pieces, the stub, and the column reinforcement cage. Straight 10M rebars were cut and bent to formulate the five different pieces of hooks and stirrups used for the heavily reinforced stubs. The pieces used for the formulation of the stub cages, in addition to the cage's assembly, are presented in Figure 4-10. The stub reinforcement was designed in that way in order to avoid any damage in the stub region and to ensure its response as a rigid body.

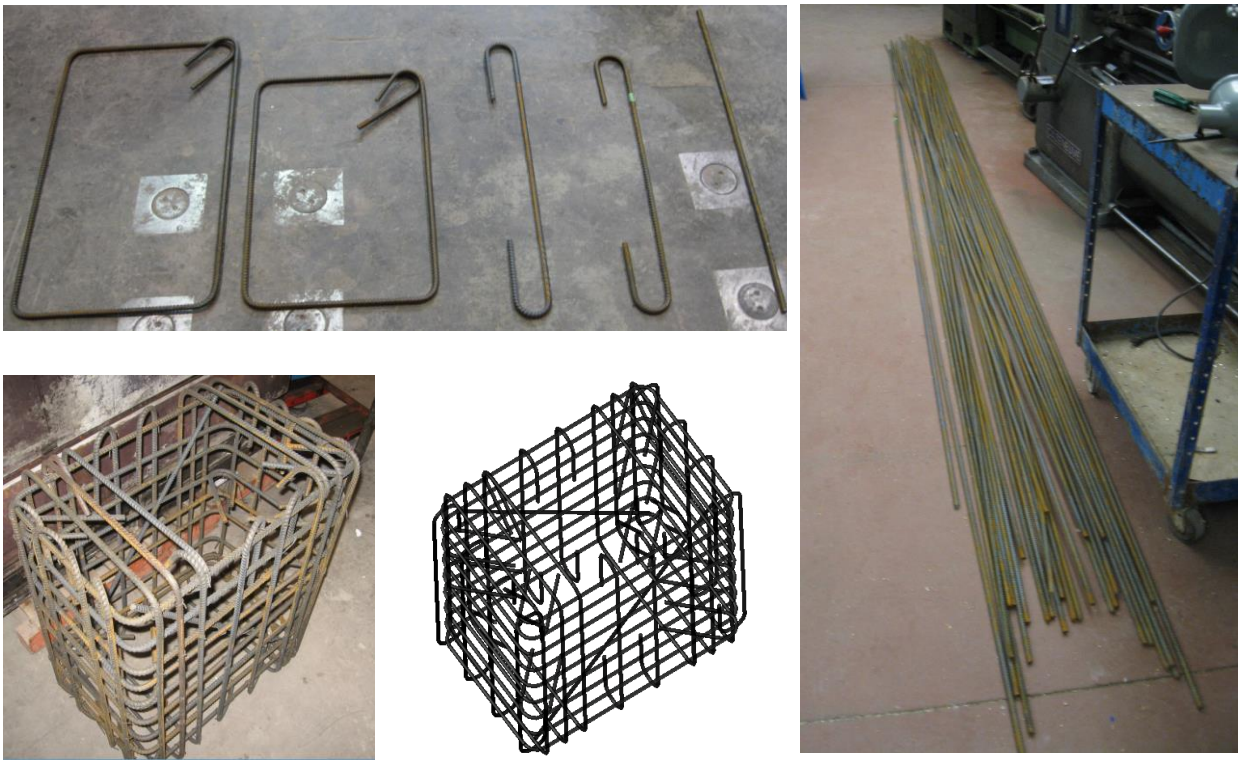


Figure 4-10: Construction of the stub reinforcing cages.

Next, the column cages were constructed. Each column's reinforcement is composed of six straight 20M, 2,240 mm long bars and two #3 spirals with spacing equal to 152 mm and 305 mm for the critical and non-critical regions, respectively. The spirals were formed in-house by bending straight #3 rebars and adjusting them to the desired hoop diameter and spacing requirements. For the columns' cage assembly, the 20M straight rebars were placed in properly designed wooden holders to secure them in the correct position, and auxiliary steel pieces were welded between them at the end sections. The adjusted spirals were placed in the correct position and fixed on the longitudinal bars using wire ties. For each cage, a 152 mm and a 305 mm spacing spiral was used, and their splicing (150 mm) was enhanced by welding the overlapping spiral lengths. After assembling the column cages, the reinforcement strain gauges were installed with the procedure discussed in Section 4.4.1. The four column cages were identical, and their construction stages are presented in Figure 4-11.

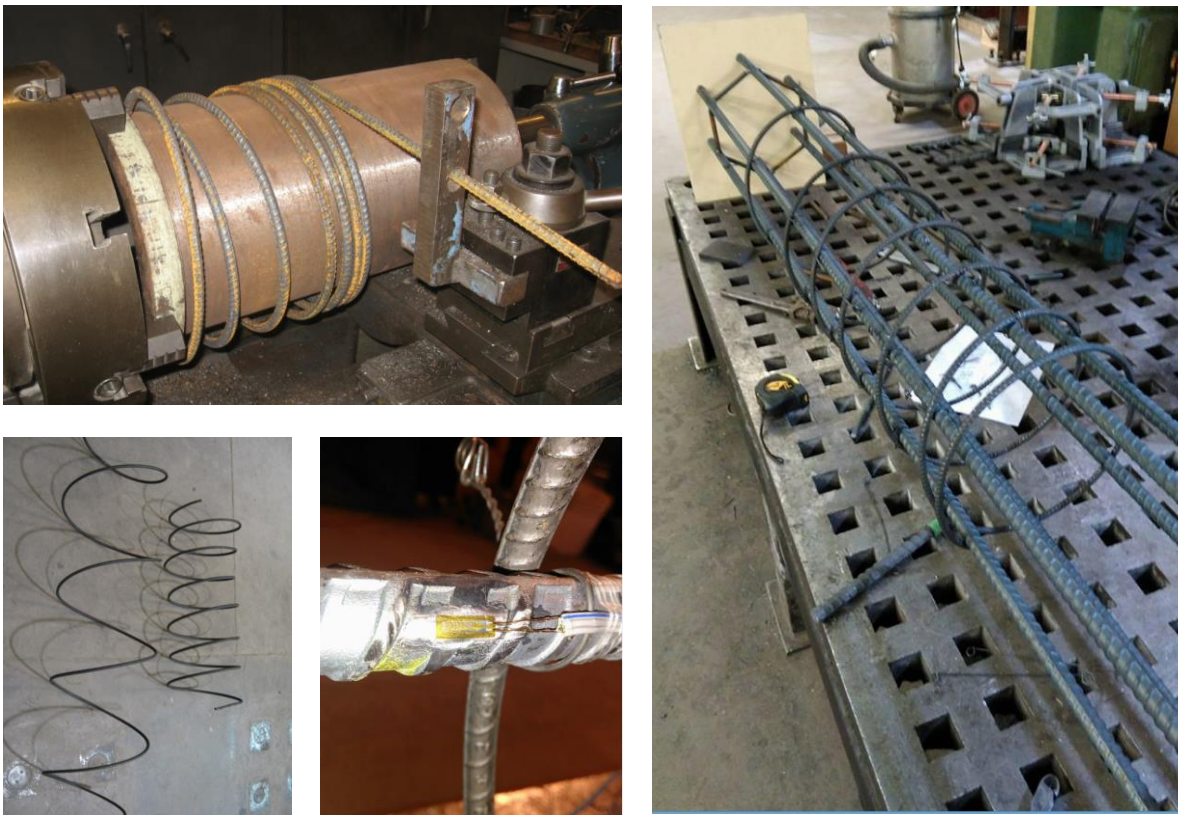


Figure 4-11: Column reinforcing cages' construction.

4.3.2 Formwork Assembly

After preparing the reinforcement cages for the stubs and the columns, the formwork and the cages were assembled for the concrete casting. The steel formwork designed and first used by Tavassoli (Tavassoli 2015) was used and is presented as designed in Figure 4-12. Initially, the lower part of the formwork was assembled, and one steel plate designed for facilitating four steel anchors at each column was placed and fixed at the bottom of each cage's formwork. Consequently, four anchors were placed at each steel plate and two wooden partitions were placed for each column to reduce the stub volume to the desired dimensions. Next, the stub and column cages were placed in the steel formwork, and the upper cardboard formwork in addition to the treaded rods used for the instrumentation was installed. Finally, the top aluminum truss was assembled which is required to align and restrain the columns' upper formwork in the correct position. Steel plates equivalent to ones used at the bottom of the column were used at the upper end for installing the same set of steel anchors, which is required for installing the specimen into the testing frame. The formwork assembly stages are presented in Figure 4-13.

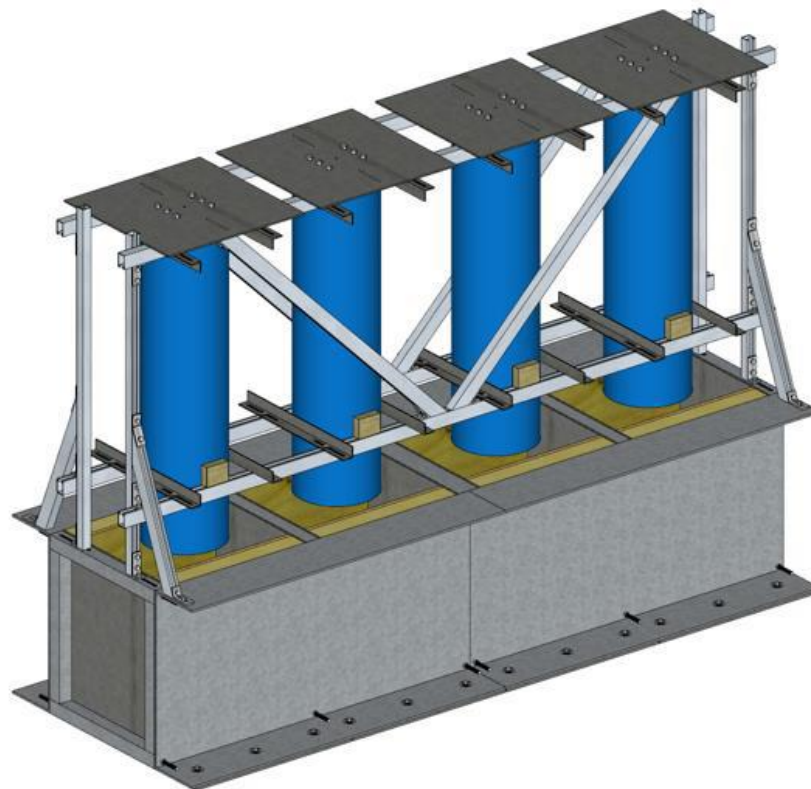


Figure 4-12: Steel formwork designed by Tavassoli (Tavassoli 2015).



Figure 4-13: Formwork assembly stages.

4.3.3 Concrete Casting

Three cubic meters of concrete were ordered. The slump of the delivered concrete was 90 mm which was not considered adequate. Thus, superplasticizer was added to the mix, and the cast of the specimen was started and completed without any issue with the workability. Initially, the concrete was poured into the stub formwork of each column by the sides of the stub, and subsequently, it was poured in multiple layers in each column. During the whole process, internal vibrators were used to consolidate the concrete. At the end of the casting, the upper plates with the steel anchors were placed, and the upper surface of the stubs was leveled. In addition to the four specimens, multiple concrete cylinders were cast in order to measure the concrete strength with time. The concrete curing during the first days included covering of the exposed surfaces with damp hessian fabric protected with plastic membranes to reduce the moisture evaporation. After four days the formworks were removed, and the specimens remained exposed to the lab environment up to the test day. Various concrete casting stages are shown in Figure 4-14.

4.3.4 Repairing and Retrofitting Procedure

For the hybrid simulation with a repaired structure, the specimen needs to be damaged first due to possible seismic excitation, and be repaired. The damaged specimen was repaired according to S448.1-10 “Repair of reinforced concrete in buildings and parking structures” (CSA-S448.1-10 2015). The specimen was repaired in three steps; the crushed concrete repair, the crack treatment and the CFRP application. Each of these steps is described in the next sections. It should be noted that the reinforcement bars did not buckle during the first tests at the region where the damage occurred. The same repair procedure was followed both for the first and second specimens. The retrofitting procedure includes only the application of the CFRP which is performed in the same manner as for the repairing case.



Figure 4-14: Concrete casting stages.

4.3.4.1 Crushed Concrete Repair

For the concrete repair in the crushed surface, the identification of the damaged concrete is required. For that purpose the hammer tap survey was employed, where non-destructive impacts are imposed on the specimen's surface. By using the hammer tap survey, the spalled, debonded and delaminated concrete can be identified by the change of the produced sound during the survey. A delaminated surface emits a hollow or drum sound, while a healthy, not delaminated surface emits a ringing noise. After detecting the damaged concrete, the loose concrete parts were removed up to the depth of the healthy concrete. When it was possible, vertical faces to the concrete surface were formed in order to enhance the concrete bond with the repair mortar. The healthy concrete surface was air blasted in order to remove any debris and a formwork made of properly cut Sonotube was used to facilitate the repair mortar patching. In this way, a surface similar to the rest of the specimen was developed, which is essential for the uniform CFRP application. After preparing the repair mortar, the clean surface was soaked, and a thin layer of the repair mortar was meticulously applied on the entire repairing surface in order to enhance the bond between the two surfaces. Subsequently, the repaired mortar was poured and consolidated into the formwork, which was sealed after the end of the procedure in order to reduce the moisture evaporation. Finally, the mortar was allowed to cure for 7 days before applying the CFRP wraps. Various stages of the concrete repair are presented in Figure 4-15.



Figure 4-15: Crushed concrete repair stages.

4.3.4.2 Crack Treatment

On the opposite faces of the crushed concrete, significant cracks were developed, and the ones greater than 0.2 mm were repaired. The repair starts with the drilling of holes across the crack that will be repaired at a distance of less than 10 cm. The positions of these holes are the locations where injection T-ports will be installed. Next, the cracks were cleaned using air blasting and the ports were installed using fast epoxy glue. The same epoxy glue was used for sealing the cracks. The repair epoxy was injected from the lower port. When the epoxy started flowing out from an adjacent injection point, the overflowing point was sealed. When the first point reaches the point of refusal, it was sealed, and the procedure continued to the next lower open injection point. After the curing of the epoxy, the injection points were removed, and the surface was smoothed in order to facilitate the application of the CFRP. The epoxy that was used is Crack Fix, produced by Sika, which is a low-viscosity and high-strength epoxy resin for crack injection and repair. Various stages of the crack treatment are shown in Figure 4-16.



Figure 4-16: Crack treatment stages.

4.3.4.3 Fiber Reinforced Polymer Wrap Application

Both the repaired (Specimen #1 and #2) and the intact (Specimen #3) specimens were wrapped with one unidirectional CFRP layer in their transverse directions. The third specimen was retrofitted with CFRP for upgrade. Initially, the concrete surface was cleaned of dust, and a coat of Tyfo ® epoxy was applied to the dry concrete surface. The CFRP sheets were cut to the desired lengths, saturated with Tyfo ® epoxy using roller brushing and wrapped around the column with an overlapping of 15 cm to ensure that no slip will occur at the fabric ends. During the FRP application, care was taken to make sure that each layer was tightly wrapped and no entrapped air bubbles or distortion of the fabric existed. The application of the layer was enhanced by wrapping the specimen with shrink tape. The shrink tape was penetrated using a porcupine roller and was heated using a heat gun. This process resulted in the shrinkage of the tape and the surplus epoxy flowing out through the penetrated tape surface. The second specimen before and after the repair and the third retrofitted specimen are shown in Figure 4-17.

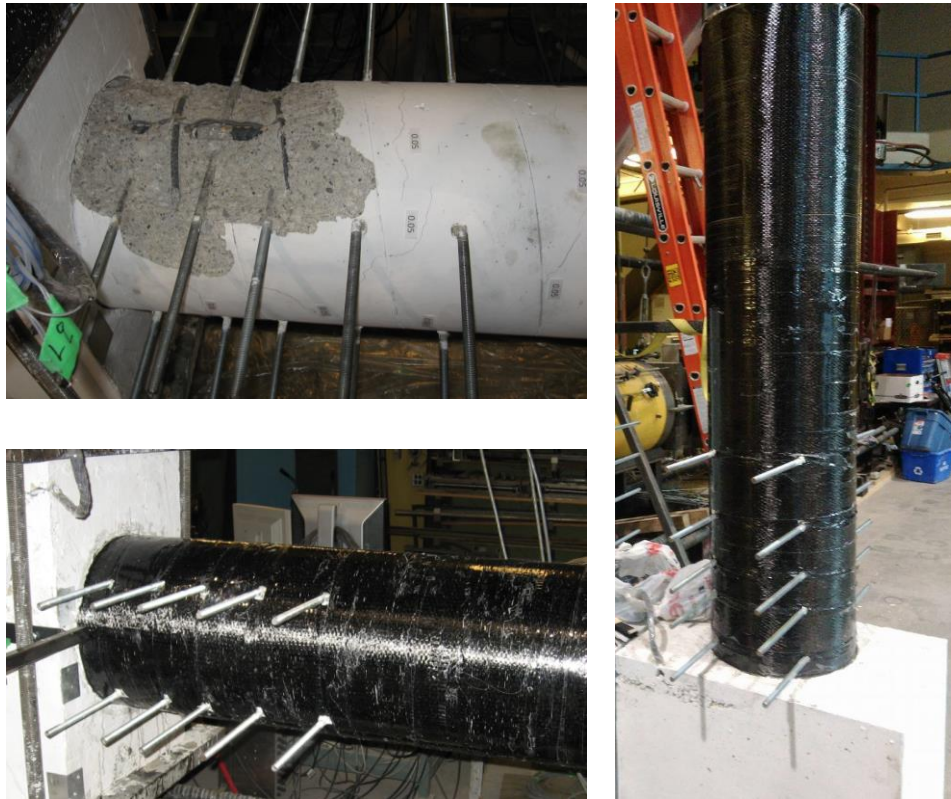


Figure 4-17: Left: Second specimen before (upper figure) and after (lower figure) the repair.
Right: Retrofitted third specimen.

4.4 Specimens' Instrumentation

Extensive instrumentation including strain gauges, linear variable differential transformers (LVDTs) and string potentiometers were used to capture the columns' behavior during the test and to measure deformation as required for the hybrid simulation. Additionally, the test was recorded from a video camera throughout the entire process.

4.4.1 Strain Gauges

Nineteen electric resistance type YEFLA-5-5LT strain gauges were installed on each specimen. Fourteen and five strain gauges were installed in the longitudinal and the transverse reinforcement, respectively. The positions of the strain gauges on each specimen are presented in Figure 4-18. More specifically, four strain gauges each were placed on L1 and L4 bars, two strain gauges each were placed on L3 and L6 bars, and one strain gauge each was placed on L2 and L5 bars. The positions of the strain gauges on the spiral are notated with the letters A, B, C, D, and E along the specimen length, while their positions on the spiral are next to the bars L2, L4 and L6 successively as illustrated in the cross section in Figure 4-18.

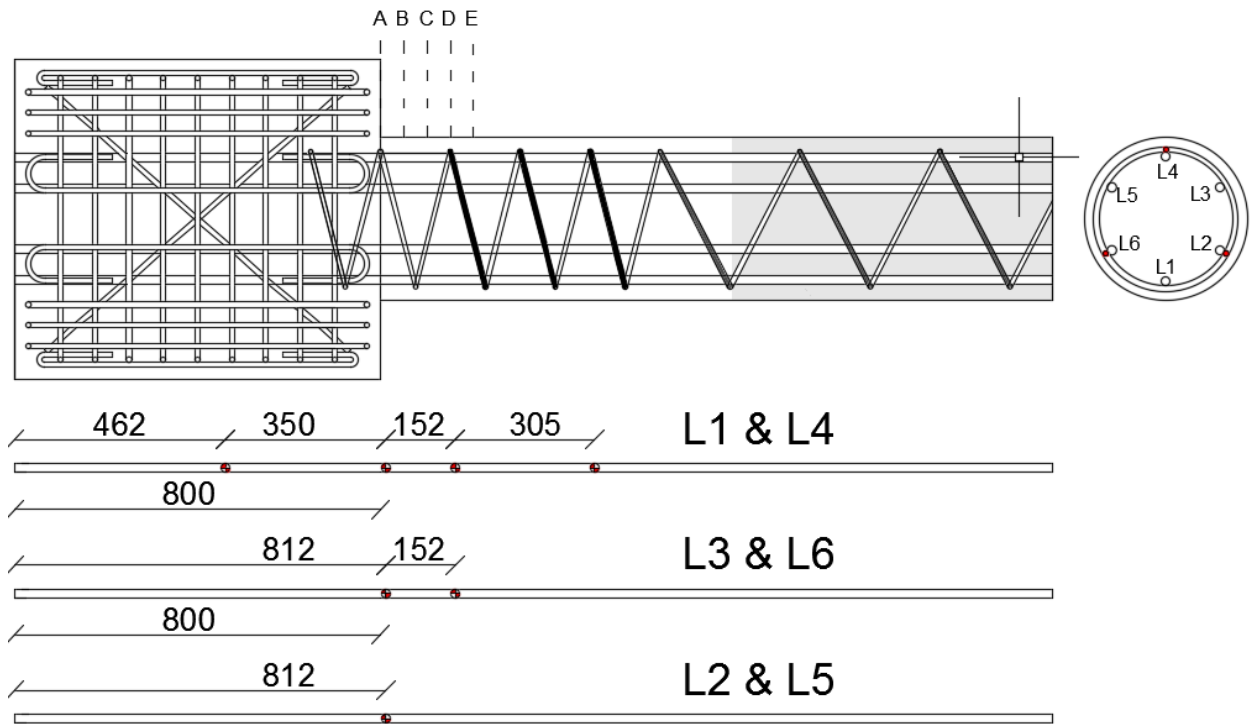


Figure 4-18: Strain gauges locations. All the dimensions are in mm.



Figure 4-19: Strain gauges' installation stages.

The strain gauges' installation stages are presented in Figure 4-19. Initially, the steel rebar was grinded to form a smooth surface, which was cleaned by a wet cloth water-based acidic surface cleanser and neutralized using an alkaline neutralizer (M-Prep). Subsequently, the strain gauge was installed using CN-Y strain gauge adhesive, and two layers of air-drying polyurethane coating material (M-Coat) were painted on the strain gauges for waterproofing. Finally, the strain gauges were covered with a thick layer of wax, and the bar was wrapped with self-adhesive aluminum foil at the gauge location.

4.4.2 Linear Variable Differential Transformers (LVDTs)

Nineteen linear variable differential transformers (LVDTs) were used to determine the curvature and the shear deformation of the specimen. Ten and six LVDTs were mounted horizontally on the north and south face, respectively, for measuring the longitudinal strains close to the top and the bottom of the specimen, which are used for capturing the curvature response. The other three LVDTs were installed properly on the south face to measure the shear strain developed in the critical area. All the LVDTs used for the longitudinal strains and the ones used for capturing the shear strains are shown in Figure 4-20 colored red and blue, respectively. The LVDTs were mounted with machined aluminum pieces on half inch threaded rods, which were installed in the specimens before the casting. Finally, the readings from the LVDTs are more reliable before the spalling of the concrete, which results in their dislocation.

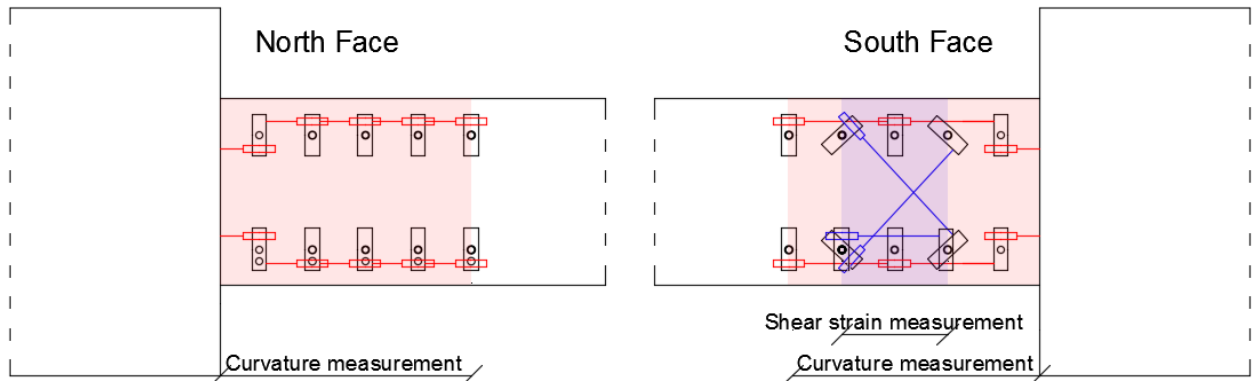


Figure 4-20: LVDTs' configuration. The red instruments are used for capturing the longitudinal strains and the curvature response, while the blue instruments are used for capturing the shear response.

4.4.3 External Instrumentation used for the Deformation Measurement

As it will be discussed further in Chapter 6, the measurement of the specimen's deformation is required for the error compensation scheme in the hybrid simulation framework. For that purpose, an external instrumentation that consists of twelve string potentiometers was employed. The configuration of the string potentiometer external instrumentation (EI) is presented in Figure 4-21.

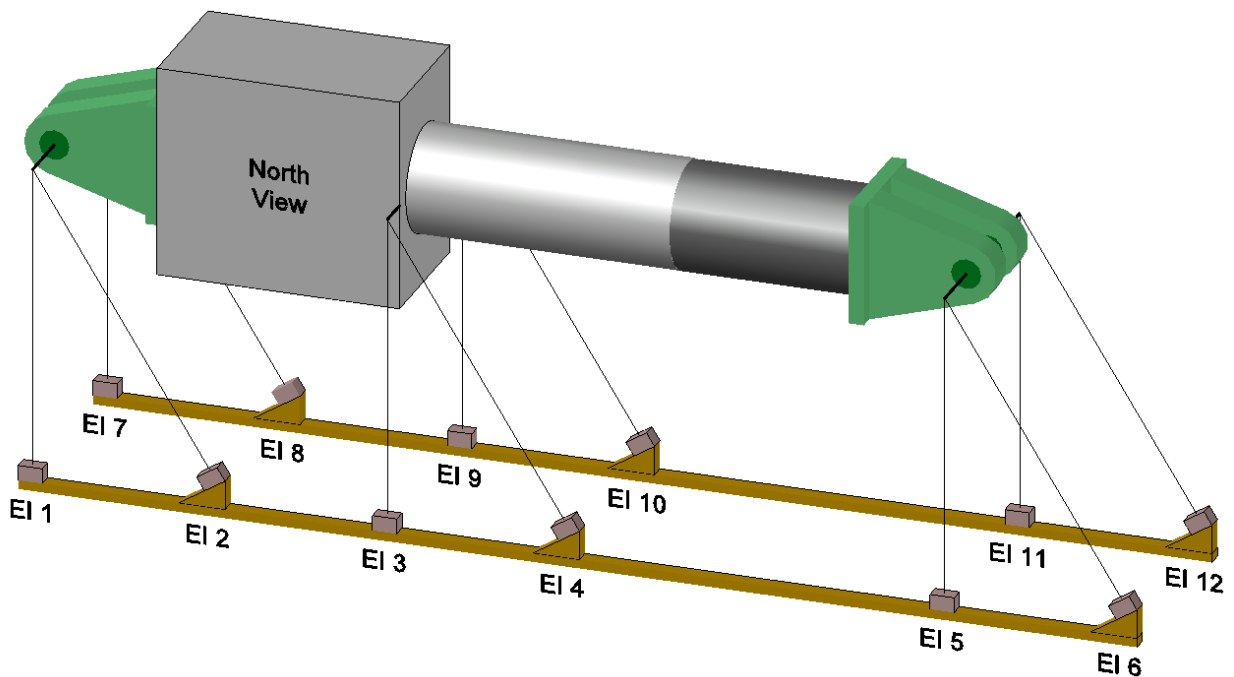


Figure 4-21: String potentiometers external instrumentation (EI) configuration.

Ten 2-inch and two 5-inch AMETEK Rayelco™ position transducers (string potentiometers) were mounted on the pins and the column/stub interface point using properly designed holders. The 5-inch potentiometers were placed in the EI 3 and EI 9 positions to facilitate the increased measurement range requirement. The functionality of the external instrumentation configuration is based on the cosine law, and the developed deformation can be calculated by using the coordinates of the reference points P1 to P3 as shown in Figure 4-22. The instrumentation was installed on both sides of the specimen to compensate for the effect of any potential out of plane deformation or torsional response of the specimen, which can be initiated due to minor accidental eccentricities on the experimental setup or because of construction deficiencies on the specimens.

Initially, the coordinates of the instruments EI 1 to EI 12 were measured using a three-dimensional scanner, and a relative two-dimensional coordinate system was defined. During the hybrid simulation, and by employing a real time feedback of the string potentiometers readings through the data acquisition system the reference points' coordinates can be calculated as follows.

$$x_1^{\text{north}} = x_{EI1} + l_1 \cos \left[\cos^{-1} \left(\frac{l_1^2 + l_{b1}^2 - l_2^2}{2 \cdot l_1 \cdot l_2} \right) + \tan^{-1} \left(\frac{y_{EI2} - y_{EI1}}{x_{EI2} - x_{EI1}} \right) \right] \quad \text{Equation 4-1}$$

$$y_1^{\text{north}} = y_{EI1} + l_1 \sin \left[\cos^{-1} \left(\frac{l_1^2 + l_{b1}^2 - l_2^2}{2 \cdot l_1 \cdot l_2} \right) + \tan^{-1} \left(\frac{y_{EI2} - y_{EI1}}{x_{EI2} - x_{EI1}} \right) \right] \quad \text{Equation 4-2}$$

$$x_1 = \frac{x_1^{\text{north}} + x_1^{\text{south}}}{2}, y_1 = \frac{y_1^{\text{north}} + y_1^{\text{south}}}{2} \quad \text{Equation 4-3}$$

where x_{EIi} and y_{EIi} are the coordinates of the string potentiometer i , l_i is the variable length of the string in the instrument i which is calculated from the instrument's reading, l_{bi} is the distance between the instruments EI 1 and EI 2 as shown in Figure 4-22, x_1^{north} and y_1^{north} are the coordinates of the east pin (P1) on the north side, x_1^{south} and y_1^{south} are the coordinates of the east pin (P1) on the south side, and, x_1 and y_1 are the averaged coordinates of the north and south face for the east pin (P1). The same equations can be derived for all the coordinates of the reference points P1 to P3 for both the south and the north face. These calculations take place in accordance with the analog input rate which is a predefined time interval for which all the measurements are performed. For the tests of this study, the analog input rate was equal to 10 ms which signifies that 100 measurements took place each second.

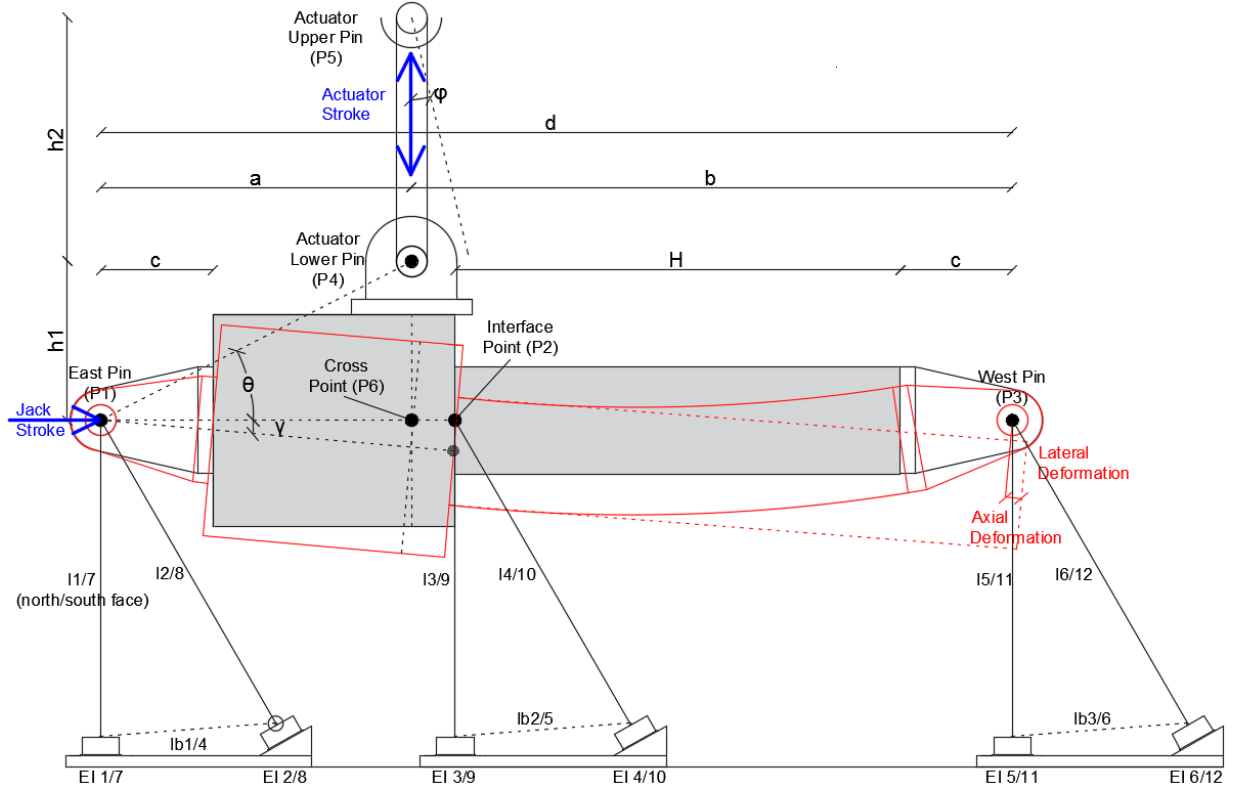


Figure 4-22: Geometry, instruments and reference points' notation.

Subsequently, the actual deformation of the specimen is calculated by employing the cosine law as well, and the formulated equations are summarized as follows.

$$\text{ang}_i = \cos^{-1} \left(\frac{l_{ij}^2 + l_{ki}^2 - l_{jk}^2}{2 \cdot l_{ij} \cdot l_{ki}} \right), \text{ for } i, j, k = 1, 2, 3 \text{ but } i \neq j \neq k \quad \text{Equation 4-4}$$

$$u_x^{\text{msd}} = f \cdot l_{23} \cdot \sin(\text{ang}_1 + \text{ang}_3), \text{ where } f = -1 \text{ if } \left(\frac{y_2 - y_1}{x_2 - x_1} > \frac{y_3 - y_1}{x_3 - x_1} \right), \text{ else, } f = 1 \quad \text{Equation 4-5}$$

$$u_y^{\text{msd}} = l_{23} \cdot \cos(\text{ang}_1 + \text{ang}_3) - H - c \quad \text{Equation 4-6}$$

where l_{ij} is the distance between the points P_i and P_j calculated from their coordinates, ang_i is the angle formed between the $P_i P_j$ and $P_i P_k$ vectors, f is a modification factor which is either a negative or positive unit as described in Equation 4-5, x_i and y_i are the coordinates of the reference point i , H is the column's height, C is the steel pins' length, and, u_x^{msd} and u_y^{msd} are the measured lateral and axial deformation of the tested specimen as drawn in Figure 4-22. The modification factor f is employed for measuring the deformation consistent with the global coordinate system of the numerical model.

All the instruments were re-calibrated using the developed platform and the hardware that is to be employed in the hybrid simulation. The hardware used for the external instrumentation consists of a junction box responsible for providing a constant power supply of 5V to the string potentiometers and feeding back their readings to the data acquisition (DAQ) system. The junction box and the calibration equipment used for the re-calibration of the string potentiometers are presented in Figure 4-23. In this way, the influence of the hardware error sources can be eliminated. However, the error induced by the instrumentation used is equal to 0.25% of the full stroke for each instrument. This error along with the mechanical nature of the instruments (friction, resistance properties) results in repeatability errors, which are of significant importance when the stroke changes direction. The results during the calibration of the 2-inch instrument placed in position EI 12 are presented in Table 4-5. The imposed stroke was applied as shown in Table 4-5 from left to right. It can be observed that when the zero tared stroke (“Tared”) is approached from lower actual stroke (“Actual”) the value of the measurement (“Msd”) is below the target stroke, whereas when it is approached from greater values, the measurement is greater than the target stroke. The maximum observed error is equal to 0.14 mm which is almost same as the 0.25% of the full stroke error reported by the manufacturer (0.25% of 2 inch=0.127 mm). The measured stroke (“Msd”) occurs by employing the calibration factors through a linear equation.

Table 4-5: External Instrument 12 calibration results and reputability errors

Actual (mm)	0	25.3	27.8	30.3	32.8	35.3	32.8	30.3	27.8	25.3	22.8	20.3	17.8	15.3	17.8	20.3	22.8	25.3
Tared (mm)	-25.3	0	2.5	5	7.5	10	7.5	5	2.5	0	-2.5	-5	-7.5	-10	-7.5	-5	-2.5	0
Input (V)	-0.004	-2.409	-2.648	-2.896	-3.136	-3.379	-3.155	-2.907	-2.67	-2.428	-2.185	-1.944	-1.701	-1.463	-1.687	-1.925	-2.163	-2.404
Msd (mm)	0.23	25.21	27.69	30.27	32.76	35.29	32.96	30.38	27.92	25.41	22.88	20.38	17.85	15.39	17.71	20.19	22.66	25.16

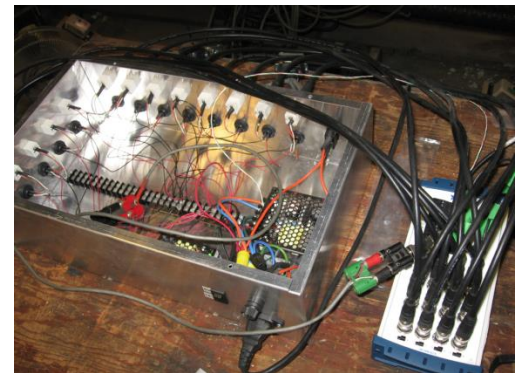
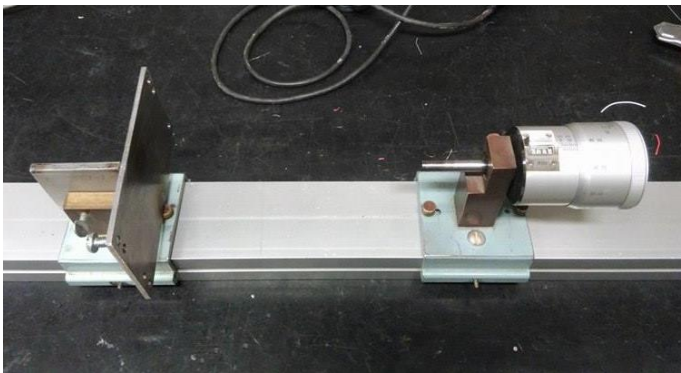


Figure 4-23: Left: Calibration equipment. Right: junction box and connection to DAQ.

Table 4-6: Calibration factors for string potentiometers

North Side				South Side			
Type	Serial Number	g	h	Serial Number	Serial Number	g	h
P-2A	1104-22490	0.4658	-10.3475	P-2A	1104-22490	0.4008	-10.3484
P-2A	1104-22485	0.4363	-10.3878	P-2A	1104-22485	0.1435	-10.4341
P-5A	1104-22495	-0.0803	-25.6219	P-5A	1104-22495	-0.3851	-26.1678
P-2A	1104-22477	0.1282	-10.3182	P-2A	1104-22477	-0.1237	-10.3430
P-2A	1104-22486	-0.6928	-10.3303	P-2A	1104-22486	0.8885	-10.3772
P-2A	1104-22484	-0.0250	-10.3466	P-2A	1104-22484	0.1875	-10.3873

Finally, the calibration factors and the serial numbers of the instruments used for this study are presented in Table 4-6 for future reference. The equation that described the relationship between the voltage and displacement measurement is below.

$$D = g + h \cdot V \quad \text{Equation 4-7}$$

where D is displacement measurement with unit of mm, V is the voltage input when the excitation voltage is 5V, and g and h are the calibration factors, which are presented in Table 4-6.

4.5 Column Testing Frame Description

The Column Testing Frame (CTF) facility at the Structural Testing Facility at the University of Toronto is used for the experimental hybrid simulation of the reinforced concrete column specimens. In this section, the testing equipment and the column testing frame properties are discussed in addition to the proposed method to eliminate undesirable loading conditions that may occur from the improper alignment of the specimen and to reduce the gravity effect on the column's testing configuration.

4.5.1 Testing Equipment Overview

The schematic of the Column Testing Frame (Tavassoli 2015) and the testing frame with an intact specimen installed are presented in Figure 4-24. The CTF is equipped with an MTS1000 actuator, with a force capacity equal to 1,000 kN, which is installed vertically to apply lateral deformation at the stub, and a horizontally installed jack to apply a compression force up to 9,000 kN. Recently, the jack was equipped with an independent pump, servo-valve, and a controller to facilitate the control requirements of the hybrid simulation, while the actuator is connected to the central

hydraulic line in the structural laboratory. Both the actuator and the pump work under a pressure of 3,000 psi (20.7 MPa).

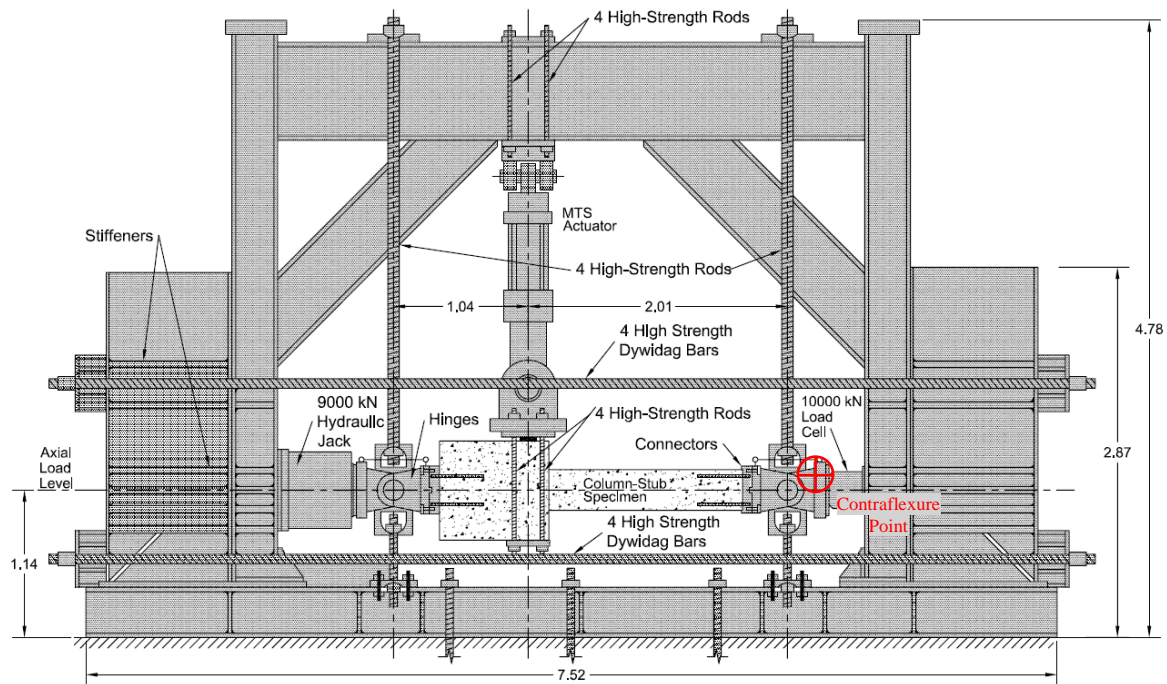


Figure 4-24: Column Testing Frame (CTF)

The simultaneous control of the actuator and the jack is performed through an MTS Flextest 40, which is connected to a terminal and is responsible for transforming the manual input from the user, or the external input voltage command from the hybrid simulation platform, to actuator and jack strokes through a PID algorithm. The main drawback of the current setup is that due to the number of available actuators/jacks installed, only the lateral and the axial deformation can be controlled. As a result, the assumption of the contraflexure point is a prerequisite for testing reinforced concrete columns subjected to planar motions given the available testing setup. This fact was one of the most significant challenges, and an extensive discussion about said limitation is performed in Chapter 5.

4.5.2 Specimen Alignment

In the current testing configuration, the column is tested horizontally, rotated by 90 degrees compared to its position in the structure. This rotation results in the unwilling effect of gravity on the lateral response of the column. In other words, the force required to deform the column by the same magnitude towards the positive or towards the negative direction is different because of its self-weight. In order to eliminate this effect, the reactions at the supports for the two idealized cases were calculated under the self-weight of the specimen. Both the cases are presented in Figure 4-25.

The first, intact specimen case, represents the conditions where an intact specimen is installed in the testing setup. For this case, the reaction at the actuator support when the specimen is undeformed was estimated equal to 7.44 kN. The second case, the perfect hinge case, represents the idealization of a perfect hinge developed in the column/stub interface. For the second case, the reaction at the actuator support when the specimen is undeformed is equal to 6.11 kN. After the initiation and during the test, the condition of the stub/column interface is modified from an intact connection to a plastic hinge, and the reaction of the actuator at the zero deformation position varies between 7.44 and 6.11 kN. In order to eliminate the effect of the specimen's self-weight, the zero state (start of the test) was set as the location where 7 kN of force is developed in the actuator. The stub and the steel pins were considered as rigid elements for this study because of their significantly higher stiffness compared to the column's axial and lateral stiffness.

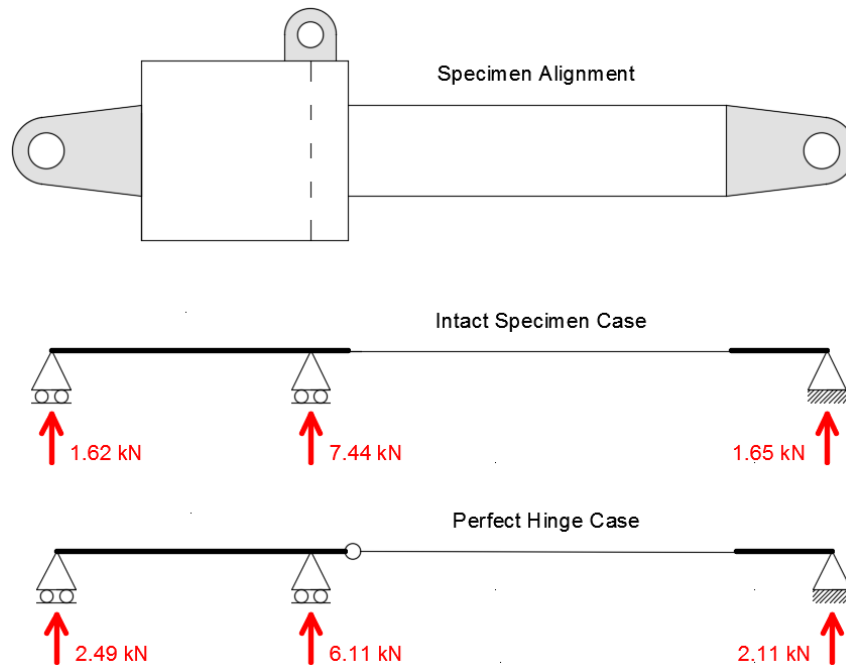


Figure 4-25: Idealized cases studied to eliminate the effect of gravity.

Finally, in order to reduce the potential out of plane deformation and the development of eccentric axial load, the specimen was aligned after its installation. The alignment procedure includes the axial loading of the specimen up to 1,000 kN in four 250 kN intervals. By monitoring the strain gauges and the LVDTs' measurements, the out of plane deformation and the unwanted eccentric loading were identified and reduced to the extent that was considered adequate. The remaining inconsistencies may be a result of construction related errors or are embedded into the CTF setup.

Chapter 5 Weakly-Coupled Hybrid Simulation

5 Weakly-Coupled Hybrid Simulation Method

In this chapter, the limitation of the column testing frame related to the control of boundary conditions is presented methodology is developed for overcoming that limitation. The proposed weakly-coupled hybrid simulation methodology is generalized, and the applicability of the methodology for the study structure case is investigated.

5.1 Limitation of the Column Testing Frame

As discussed in Chapter 2, when a substructured hybrid simulation is performed, it is necessary to control the boundary conditions of the physically tested specimens accurately. More specifically, actuators equal to or greater than the number of the degrees of freedom (DOF) at the interface between a numerical model and a physical specimen are required. Therefore, for a frame subjected to planar motion, the simultaneous control of all three DOF is necessary, requiring at least three hydraulic actuators at each interface point, all synchronized through a control scheme. However, as discussed in Section 4.5, the column testing frame is equipped with a servo-controlled jack for the application of the axial force or deformation, and an actuator for the application of the lateral deformation. Thus, it is only able to control the translational DOF at the contraflexure point at the column's upper end (Figure 4-24). In the available experimental setup, the physical specimen represents only the lower half of the structure's column accounting for the length below the contraflexure point. The contraflexure point assumption close to the mid-height of the column may be a realistic assumption for experimental investigations using quasi-static loading protocols, but during nonlinear dynamic analysis the position of the contraflexure point varies, and the column can even be in single curvature at times (Park and Paulay 1975). As a result, the assumption of a fixed contraflexure point is not realistic, and the hybrid simulation cannot be performed based on the conventional approach, where all the DOF between the experimental and the numerical model are coupled. The proposed solution relies on a weakly-coupled architecture where some of the DOF are coupled between the experimental and the numerical models, while the rest are coupled with a surrogate numerical model as explained in the following sections.

5.2 Weakly-Coupled Hybrid Simulation Method

In order to overcome the limitation described in the previous section, a weakly-coupled hybrid simulation (WCHS) approach is proposed and implemented. The overall method is illustrated in the flowchart of Figure 5-1. In contrast to the conventional substructured hybrid simulation discussed in Section 2.3, in this weakly-coupled method only the force components of the degrees of freedom that are able to be experimentally controlled, namely the axial deformation u_y and the lateral deformation u_x , are reported to the integration module (structure) from the physically represented column (Substructure 1). Because the testing equipment is unable to control rotation and obtain a corresponding moment, the restoring force vector is incomplete and composed of only two restoring forces instead of the three that are required for the full coupling; namely, two translational restoring forces and one moment restoring force.

For restoring this inconsistency, it is proposed to employ a surrogate numerical column model (Substructure 2) which overlaps the physical specimen. The surrogate numerical model is developed in OpenSees, and the properties are identical with the structure's model properties discussed in Section 3.3. This surrogate numerical model is subjected to the full displacement boundary conditions as obtained from the integration module; however, only the moment from the surrogate numerical model is returned to the integration module. The restoring force vector of the tested column is assembled using the measured forces (F_{x1} , F_{y1}) from the experimentally tested substructure and the restoring moment (M_2) of the surrogate numerical model (Substructure 2). Subsequently, the restoring force vector is fed into the integration module, and the hybrid simulation using substructuring techniques can be conducted.

It should be noted that the WCHS remains an approximation because 1) the physically tested specimen is not subjected to a proper displacement boundary condition at the interface (i.e. the moment at the interface node is always zero) and 2) the response from the surrogate numerical model depends on the modeling assumptions. By selecting the interface node at the contraflexure point, the error resulting from the first approximation can be minimized because minor moment is developed in that location, which is not expected to have a significant influence on the element's response. Before the experimental application of the proposed methodology, a numerical application is performed to identify the weaknesses resulting from the weakly-coupled approach, which is discussed in the following chapter.

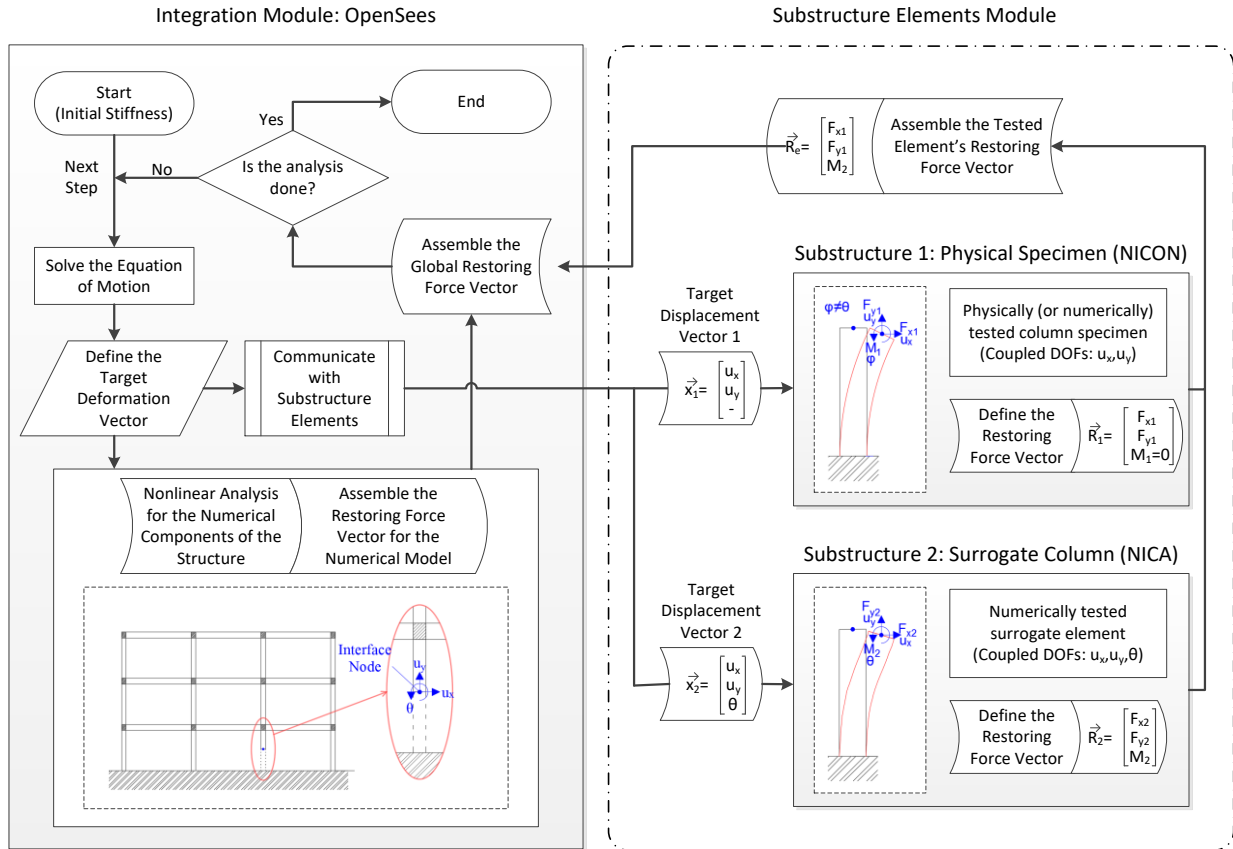


Figure 5-1: Weakly-coupled hybrid simulation architecture.

5.3 Numerical Verification

In this section, the numerical investigation of the WCHS is performed to validate its applicability before conducting experimental testing. For this purpose, the experimental substructure (Figure 5-1, Substructure 1) is replaced with a numerical model of a column. Both the Substructures 1 and 2 numerical models are identical to the one discussed in Section 3.3. Subsequently, a nonlinear time history analysis is conducted, and the results are compared with those from the initial investigation performed in Section 3.4. Because the same modeling technique is used for all analysis cases, the differences stemming from the approximation of the proposed methodology can be isolated and identified. The script developed for the numerical WCHS is presented in Appendix B. Finally, the case where a pin connection is located at the contraflexure point is examined in order to prove the necessity of the weakly-coupled methodology for performing hybrid simulation when control limitations exist, and to prove the unrealistic assumption of the contraflexure point during dynamic loading. An extensive discussion regarding the employed simulation framework is conducted in Chapter 6.

5.3.1 Network Interface for Console Applications (NICA)

For performing numerical hybrid simulation (multi-platform hybrid simulation), an interface program called Network Interface for Console Applications (NICA) is used (Huang and Kwon 2017). NICA has been developed as part of the University of Toronto Simulation Framework (UT-SIM, Mortazavi et al. 2017) to facilitate the communication between an integration module and one or more numerical substructures. NICA is responsible for sending the target deformation vector produced by an integration module to substructure modules and report back the calculated restoring forces from the substructure modules to the integration module. In this way, the coupling between the integration and the substructure modules' DOF is restored, and the numerical hybrid simulation can be performed.

For the numerical investigation of this section, the experimental substructure (Figure 5-1, Substructure 1) was replaced with a numerical model using NICA. However, for replicating the control conditions of the experimental setup, only the translational DOF, u_x and u_y were coupled. This modification consists of a weak coupling between the integration module and the substructure module 1 and is equivalent to the one of the experimental facility. For the experimental testing, a different interface platform called NICON is used, which is discussed in Chapter 6.

For the integration with the surrogate module (Figure 5-1, Substructure 2), a modified version of NICA has been employed both for the experimental and the numerical hybrid simulations performed in this section. This modification was required for the WCHS because, for the surrogate module, all the DOF were coupled between the integration module and the substructure module, but not all the restoring forces were fed back to the integration scheme. Without this modification, the restoring forces that correspond to the translational DOF would be accounted twice, owing to the overlapping substructures developing significant inconsistencies. The restoring force modification was accomplished by defining the first two components of the restoring force vector in the Substructure 2 as explicitly equal to zero in the NICA source code. In this way, it was possible to couple all the DOFs between the integration module and the Substructure 2 for consistently applying the target deformation in the surrogate module, but only the restoring moment was returned to the integration module. This development allows for the numerical application of the WCHS in order to evaluate its applicability and identify the differences emerging from the approximate nature of the proposed methodology.

5.3.2 Weakly-Coupled Hybrid Simulation

The modified model for numerically replicating the weak coupling of the experimental setup was subjected to the study earthquake sequence (Figure 3-6 & Figure 3-7). The results of this numerical investigation are compared with the reference OpenSees standalone case both for the storey displacements and for the hysteretic response of the critical element in Figure 5-2 and Figure 5-3. Overall in Figure 5-2, it can be noted that fair matching is achieved between the storeys' displacement responses. Some differences are developed during the second seismic event in the first storey displacement which can also be identified from the hysteretic response of the critical element presented in Figure 5-3.

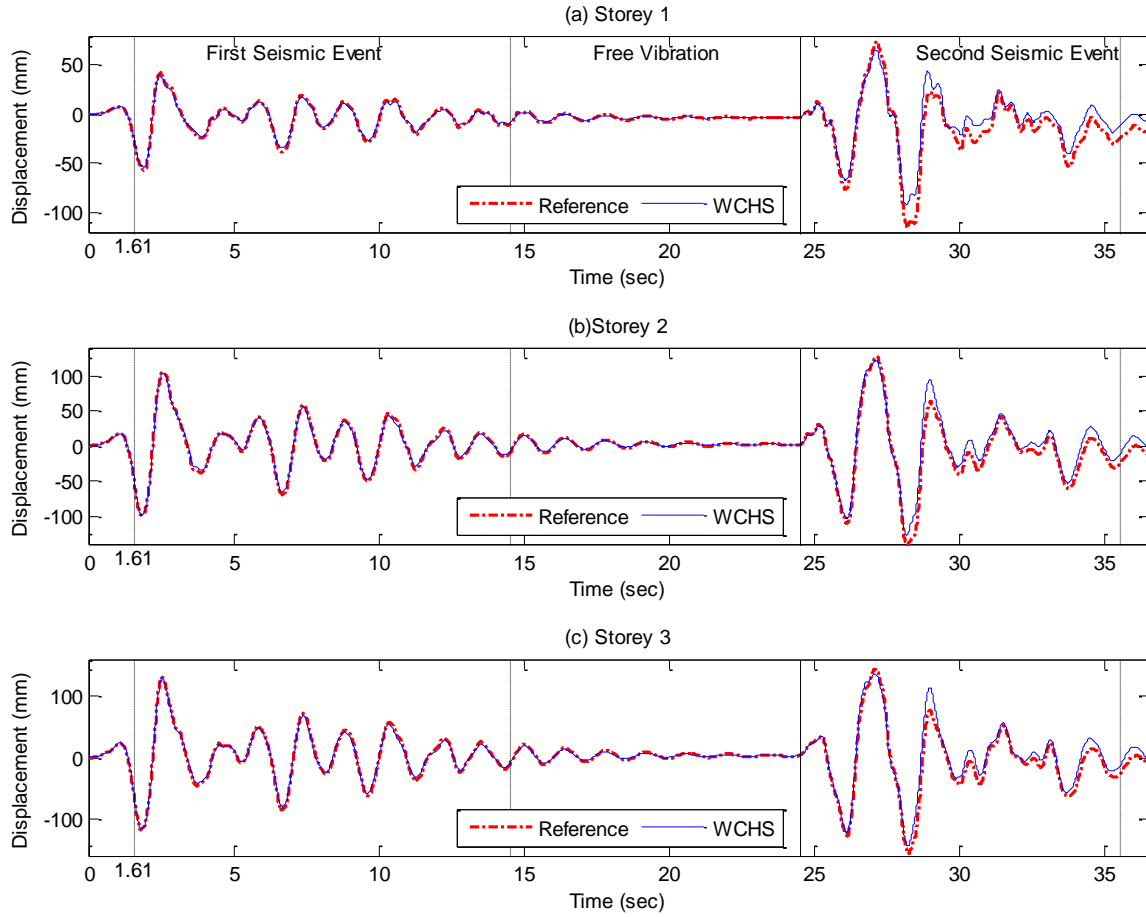


Figure 5-2: Storeys' displacement comparison between the preliminary investigation (Reference) and the weakly-coupled numerical hybrid simulation (WCHS).

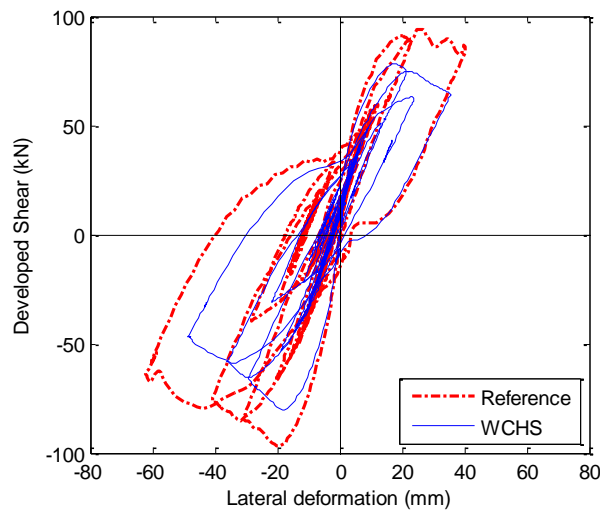


Figure 5-3: Hysteretic response comparison between the preliminary investigation (Reference) and the weakly-coupled numerical hybrid simulation (WCHS).

By comparing the hysteretic response of the critical element between the reference and the WCHS case it can be stated that overall the deformation history from WCHS matches well with the deformation history from the reference analysis case. However, as it can be noticed from Figure 5-3, the response for the WCHS case at the maximum deformation demand is less accurate compared to the reference response history. Additionally, the developed shear in the critical element for the WCHS case is approximately 20% less than the reference case. When the element's deformation is significantly nonlinear, the position of the contraflexure point is considerably offset and the differences mentioned above become more dominant. This inconsistency is embedded into the approximate nature of the proposed weakly-coupled methodology. As will be proven in Section 5.3.3, this method is an important improvement compared to the case where the contraflexure point assumed at the column mid-height and is considered applicable to the experimental investigation.

5.3.3 Investigation under the Contraflexure Point Assumption

For identifying the necessity of the weakly-coupled hybrid simulation, the case where a pin is explicitly defined in the mid-height of the third, ground floor column is studied for replicating the contraflexure point assumption (Figure 5-4). Ideally, if the position of the contraflexure point is constant during the dynamic analysis, the developed moment in the pin's position would be equal to zero, and the pinned case would be equivalent to the reference case. However, as it can be observed from Figure 5-5, if it is assumed that there is a pin located at the contraflexure point, the analysis results significantly differ from the reference case and the numerical model does not converge during the seismic performance assessment. A first storey failure mechanism is developed during the second seismic event. This failure mechanism can be identified from the hysteretic response of the critical element (Figure 5-6) where the lateral deformation before the convergence failure becomes 200% more than the reference case, indicating a significant drift development. The comparison between the Figure 5-2 and Figure 5-5 demonstrates the improvement in the accuracy of the structure's performance assessment when the WCHS approach is used. The effectiveness of this methodology, especially when the experimental limitation is taken into account, allows for the experimental investigation of the structure's and critical specimen's response under seismic excitation.

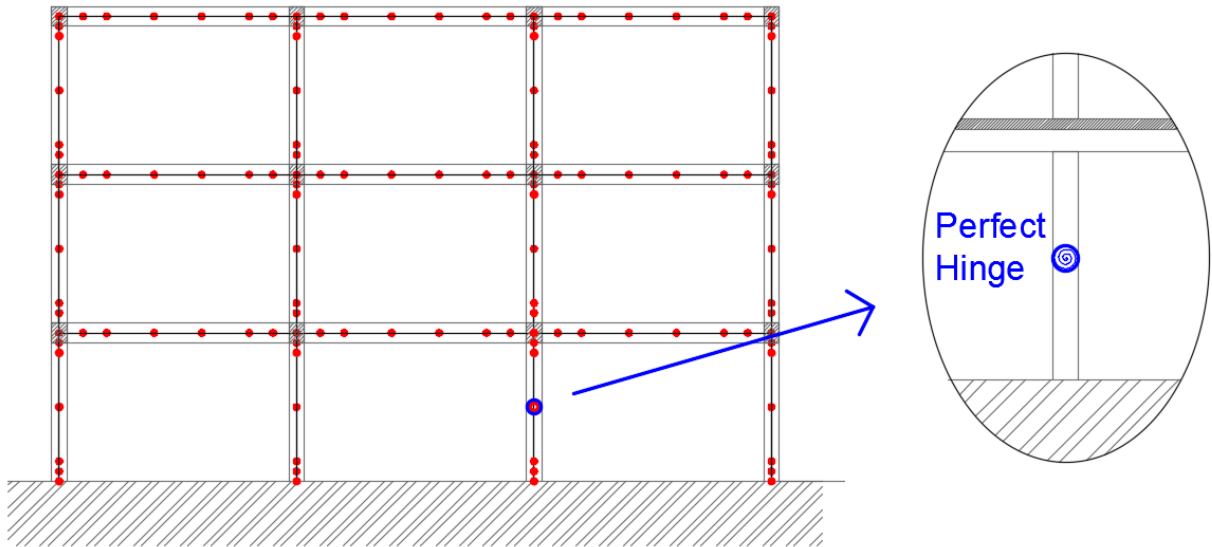


Figure 5-4: Modified numerical model for the pinned connection case investigation.

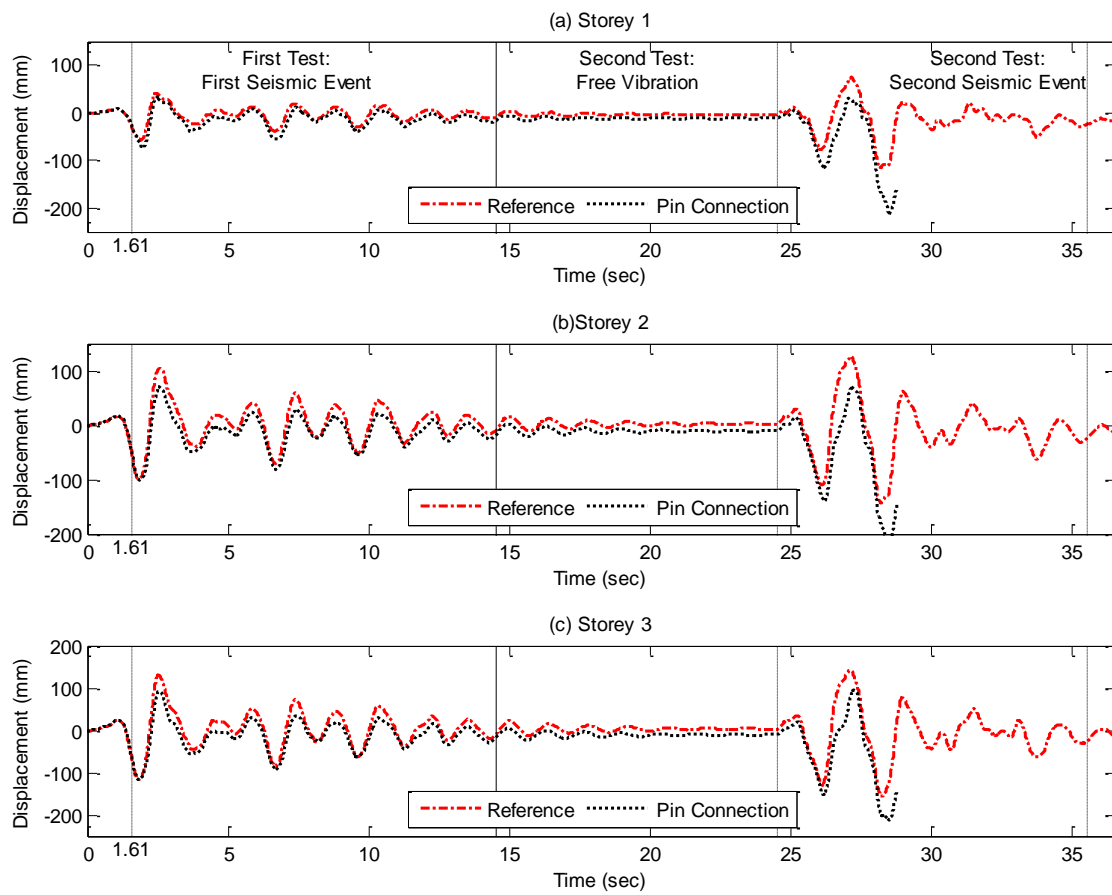


Figure 5-5: Storeys' displacement comparison between the preliminary investigation and the pinned connection case.

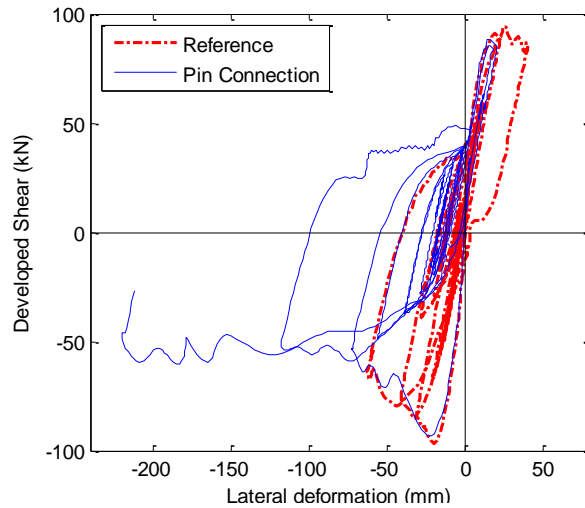


Figure 5-6: Hysteretic response comparison between the preliminary investigation and the pinned connection case.

5.4 Generalized Weakly-Coupled Method

Before the experimental implementation of the proposed methodology, an analytical investigation has been performed to generalize the weakly-coupled hybrid simulation method and to quantify its applicability. Initially, an analytical study of a generalized linear element was conducted to identify the parameters that influence the applicability of the WCHS, and subsequently, a single frame element study case was defined in order to evaluate the nonlinear characteristics of the proposed methodology. During that study, a parametric analysis of the frame element response, which ranges from a fixed column to a shear wall equivalent response, was performed and an applicability figures was developed. Finally, the applicability of the study structure is investigated using the developed generalized methodology and the characteristics of the reference structure related to the WCHS applicability are discussed.

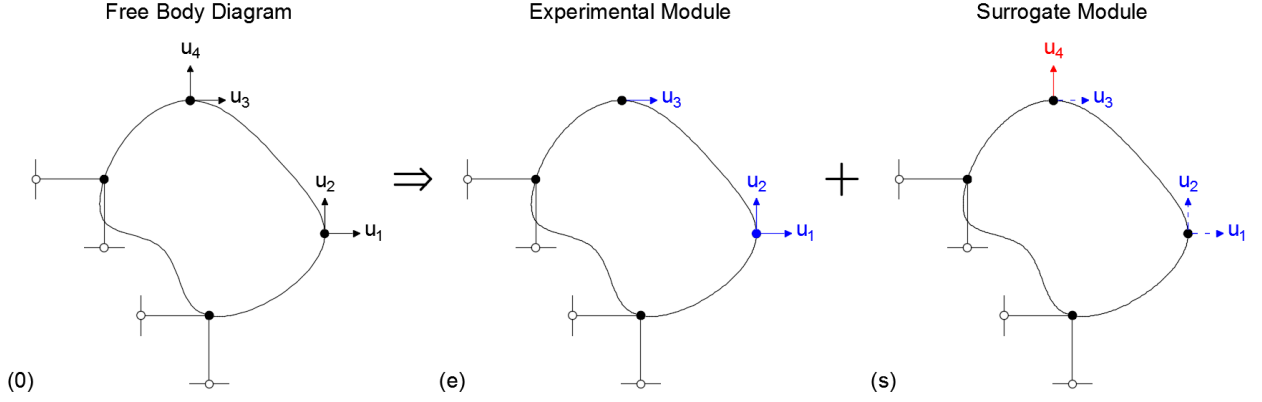


Figure 5-7: (0) Idealization of linear element and discretization of the (e) experimental and (s) surrogate module.

5.4.1 Analytical Study of Generalized Linear Element Cases

For the generalization of the proposed methodology, the idealized two-dimensional linear element consists of four nodes with two DOF at each node and is presented in Figure 5-7. This element can be idealized as a part of a superstructure and is going to be experimentally tested using hybrid simulation under limited control over the boundary conditions. In this investigation, the part of the substructure that is going to be experimentally tested is denoted as experimental module for clarity even if, for this section, it is numerically assessed. More specifically, assuming that the DOF u_1 , u_2 , and u_3 can be experimentally controlled for obtaining their restoring forces (Figure 5-7(e)), a surrogate numerical model is employed for the last DOF, u_4 , restoring force measurement. This implementation consists in a sense a generalization of the case described in Section 5.1.

The equation of motion for the above linear element (Figure 5-7(0)) after the static condensation can be written as follows.

$$\begin{bmatrix} \mathbf{F}_{1,e} \\ \mathbf{F}_{2,e} \\ \mathbf{F}_{3,e} \\ \mathbf{F}_{4,s} \end{bmatrix} = \begin{bmatrix} \mathbf{K}_{11} & \mathbf{K}_{12} & \mathbf{K}_{13} & \mathbf{K}_{14} \\ \mathbf{K}_{21} & \mathbf{K}_{22} & \mathbf{K}_{23} & \mathbf{K}_{24} \\ \mathbf{K}_{31} & \mathbf{K}_{32} & \mathbf{K}_{33} & \mathbf{K}_{34} \\ \mathbf{K}_{41} & \mathbf{K}_{42} & \mathbf{K}_{43} & \mathbf{K}_{44} \end{bmatrix} \begin{bmatrix} \mathbf{u}_1 \\ \mathbf{u}_2 \\ \mathbf{u}_3 \\ \mathbf{u}_4 \end{bmatrix} \quad \text{Equation 5-1}$$

where $\mathbf{F}_{1,e}$, $\mathbf{F}_{2,e}$ and $\mathbf{F}_{3,e}$ are the restoring forces that are going to be experimentally measured, $\mathbf{F}_{4,s}$ is the restoring force that is going to be evaluated using the surrogate module, \mathbf{K}_{ij} is the stiffness term and \mathbf{u}_i is the displacement for the i -th DOF.

After separating the equation of motion into the DOF that can be experimentally controlled and the ones that cannot, the Equation 5-1 can be condensed into the following matrix form.

$$\begin{bmatrix} \mathbf{F}_{i,e} \\ \mathbf{F}_{j,s} \end{bmatrix} = \begin{bmatrix} \mathbf{K}_{ii} & \mathbf{K}_{ij} \\ \mathbf{K}_{ji} & \mathbf{K}_{jj} \end{bmatrix} \cdot \begin{bmatrix} \mathbf{u}_i \\ \mathbf{u}_j \end{bmatrix} \quad \text{Equation 5-2}$$

where $\mathbf{F}_{i,e}$ is the force vector that contains the restoring forces as measured in the experimental (analytical equivalent) module at the DOF that are experimentally controlled, $\mathbf{F}_{j,s}$ is the force vector that contains the restoring forces as measured in the surrogate module at the DOF that are not experimentally controlled, \mathbf{K}_{ii} is a matrix term that includes all the stiffness matrix terms between the DOF that are experimentally controlled, \mathbf{K}_{jj} is a matrix term that includes all the stiffness matrix terms between the DOF that are not experimentally controlled, \mathbf{K}_{ij} and \mathbf{K}_{ji} are matrix terms which include the non-diagonal stiffness matrix terms between the experimentally controlled and non-controlled DOF, \mathbf{u}_i is a vector that includes the experimentally controlled DOF and \mathbf{u}_j is a vector that includes the DOFs that are not experimentally controlled.

Let's now examine the restoring forces measured at the experimental and the surrogate module separately, which can be described by the following equations.

$$\begin{bmatrix} \mathbf{F}_i \\ 0 \end{bmatrix}_e = \begin{bmatrix} \mathbf{K}_{ii} & \mathbf{K}_{ij} \\ \mathbf{K}_{ji} & \mathbf{K}_{jj} \end{bmatrix} \cdot \begin{bmatrix} \mathbf{u}_i \\ \mathbf{u}'_j \end{bmatrix} \quad \text{Equation 5-3}$$

$$\begin{bmatrix} \mathbf{F}_i \\ \mathbf{F}_j \end{bmatrix}_s = \begin{bmatrix} \mathbf{K}_{ii} & \mathbf{K}_{ij} \\ \mathbf{K}_{ji} & \mathbf{K}_{jj} \end{bmatrix} \cdot \begin{bmatrix} \mathbf{u}_i \\ \mathbf{u}_j \end{bmatrix} \quad \text{Equation 5-4}$$

where Equation 5-3 contains the restoring forces measured from the experimental module, and Equation 5-4 contains the restoring forces measured at the surrogate module.

In Equation 5-3, the force vector that corresponds to the DOF that are not experimentally controlled is equal to zero, since these DOF are free to deform without the development of resisting forces. Additionally, the developed deformation \mathbf{u}'_j for the DOF that are not experimentally controlled in Equation 5-3 is different from \mathbf{u}_j Equation 5-4.

Next, by rearranging Equation 5-3, the relationship between the controlled and the free DOF's deformations can be obtained, and the restoring force vector measured in the experimental module can be expressed as follows.

$$\mathbf{K}_{ji} \cdot \mathbf{u}_i + \mathbf{K}_{jj} \cdot \mathbf{u}_j' = 0 \quad \text{Equation 5-5}$$

$$\mathbf{F}_{i,e} = \left(\mathbf{K}_{ii} - \mathbf{K}_{ij} \cdot \mathbf{K}_{jj}^{-1} \cdot \mathbf{K}_{ji} \right) \cdot \mathbf{u}_i \quad \text{Equation 5-6}$$

During the weakly-coupled hybrid simulation, the restoring force vector that is fed back into the integration module is assembled from the restoring forces measured in the experimental module, $\mathbf{F}_{i,e}$, and the surrogate module, $\mathbf{F}_{j,s}$, without accounting twice the restoring forces measured both in the two modules. This property can be expressed in a matrix formulation by taking the summation of the restoring forces at each module multiplied by a selection matrix as follows.

$$\begin{bmatrix} \mathbf{F}_{i,e} \\ \mathbf{F}_{j,s} \end{bmatrix}_w = \begin{bmatrix} 1 & 0 \\ 0 & 0 \end{bmatrix} \begin{bmatrix} \mathbf{F} \\ 0 \end{bmatrix}_e + \begin{bmatrix} 0 & 0 \\ 0 & 1 \end{bmatrix} \begin{bmatrix} \mathbf{F} \\ \mathbf{F} \end{bmatrix}_s \quad \text{Equation 5-7}$$

where $[\mathbf{F}_{i,e}]_w$ is the restoring force vector as used in the weakly-coupled approach. Now, by employing Equation 5-4 and Equation 5-6, Equation 5-7 can be rewritten as follows.

$$\begin{bmatrix} \mathbf{F}_{i,e} \\ \mathbf{F}_{j,s} \end{bmatrix}_w = \begin{bmatrix} \left(\mathbf{K}_{ii} - \mathbf{K}_{ij} \cdot \mathbf{K}_{jj}^{-1} \cdot \mathbf{K}_{ji} \right) \cdot \mathbf{u}_i \\ 0 \end{bmatrix} + \begin{bmatrix} 0 \\ \mathbf{K}_{ji} \cdot \mathbf{u}_i + \mathbf{K}_{jj} \cdot \mathbf{u}_j \end{bmatrix} \quad \text{Equation 5-8}$$

By rearranging the terms, Equation 5-8 reduces to the following equation, which described the restoring forces used in the weakly-coupled hybrid simulation as a function of the stiffness matrix terms and the deformation at each DOF.

$$\begin{bmatrix} \mathbf{F} \\ \mathbf{F} \end{bmatrix}_w = \begin{bmatrix} \mathbf{F}_{i,e} \\ \mathbf{F}_{j,s} \end{bmatrix}_w = \begin{bmatrix} \left(\mathbf{K}_{ii} - \mathbf{K}_{ij} \cdot \mathbf{K}_{jj}^{-1} \cdot \mathbf{K}_{ji} \right) & 0 \\ \mathbf{K}_{ji} & \mathbf{K}_{jj} \end{bmatrix} \cdot \begin{bmatrix} \mathbf{u}_i \\ \mathbf{u}_j \end{bmatrix} \quad \text{Equation 5-9}$$

By considering the system presented in Figure 5-7(0) which is a standalone, not weakly-coupled system, the following equation constitutes its theoretical solution.

$$\begin{bmatrix} \mathbf{F} \\ \mathbf{F} \end{bmatrix}_t = \begin{bmatrix} \mathbf{K}_{ii} & \mathbf{K}_{ij} \\ \mathbf{K}_{ji} & \mathbf{K}_{jj} \end{bmatrix} \cdot \begin{bmatrix} \mathbf{u}_i \\ \mathbf{u}_j \end{bmatrix} \quad \text{Equation 5-10}$$

By comparing Equation 5-9 and Equation 5-10, it can be observed that the second component of the restoring force vector is the same for both the weakly-coupled and the theoretical case, while the first component is different. By performing the stiffness multiplication and isolating the first component in the restoring force vector, the Equation 5-9 and Equation 5-10 can be written as follows.

$$\mathbf{F}_{1,w} = \mathbf{K}_{ii} \cdot \mathbf{u}_i - \mathbf{K}_{ij} \cdot \mathbf{K}_{jj}^{-1} \cdot \mathbf{K}_{ji} \cdot \mathbf{u}_i \quad \text{Equation 5-11}$$

$$\mathbf{F}_{1,t} = \mathbf{K}_{ii} \cdot \mathbf{u}_i + \mathbf{K}_{ij} \cdot \mathbf{u}_i \quad \text{Equation 5-12}$$

$$\text{or} \quad \mathbf{F}_{1,w} = \mathbf{P}_{1,w} + \mathbf{P}_{2,w} \quad \text{Equation 5-13}$$

$$\mathbf{F}_{1,t} = \mathbf{P}_{1,t} + \mathbf{P}_{2,t} \quad \text{Equation 5-14}$$

where $\mathbf{P}_{1,w} = \mathbf{K}_{ii} \cdot \mathbf{u}_i$, $\mathbf{P}_{2,w} = -\mathbf{K}_{ij} \cdot \mathbf{K}_{jj}^{-1} \cdot \mathbf{K}_{ji} \cdot \mathbf{u}_i$, $\mathbf{P}_{1,t} = \mathbf{K}_{ii} \cdot \mathbf{u}_i$ and $\mathbf{P}_{2,t} = \mathbf{K}_{ij} \cdot \mathbf{u}_i$. It can be observed that the first terms ($\mathbf{P}_{1,w}$ and $\mathbf{P}_{1,t}$) in Equation 5-13 and Equation 5-14 are identical while the second terms ($\mathbf{P}_{2,w}$ and $\mathbf{P}_{2,t}$) are different. That difference is the most important parameter for defining the applicability of the weakly-coupled approach.

Ideally, if the experimentally controlled DOF are fully uncoupled with the ones that are not experimentally controlled (i.e. $\mathbf{K}_{ij} = 0$), the second terms in Equation 5-13 and Equation 5-14 become equal to zero. In such a case, no difference is expected between the reference and the numerical WCHS. If the off-diagonal matrix is not zero (i.e. there is coupling, $\mathbf{K}_{ij} \neq 0$), the accuracy and the applicability of the WCHS becomes a function of the relative relationship between the terms $\mathbf{P}_{2,w}$ and $\mathbf{P}_{2,t}$. In general, the second terms ($\mathbf{P}_{2,w}$, $\mathbf{P}_{2,t}$) are expected to be of similar magnitude or their values should be significantly lower in comparison with the first terms ($\mathbf{P}_{1,w}$, $\mathbf{P}_{1,t}$). For these cases, the restoring forces of Equation 5-13 and Equation 5-14 are close enough in order to designate the WCHS as applicable.

Finally, it should be stated that the relationship between $\mathbf{P}_{2,w}$ and $\mathbf{P}_{2,t}$ should remain similar during the nonlinear response of the specimen for retaining the WCHS accuracy. Two of the most important cases that may influence the aforementioned condition are a change in the stiffness matrix values due to the development of damage in the specimen and a change in the loading and boundary conditions of the specimen. However, the *a priori* assessment of a change in the loading and the boundary conditions cannot be analytically expressed for a generalized element, is case

sensitive and the relationship between $P_{2,w}$ and $P_{2,t}$ terms becomes more complex during the nonlinear response of the element. To that end, an initial investigation is proposed to be performed for each study case as described in Section 0.

5.4.2 Parametric Study on the Applicability of WCHS using Nonlinear Frame Element

In this chapter, a parametric analysis for developing a preliminary assessment tool for the applicability of the WCHS to common civil engineering elements is performed. A single element's response is studied for structural systems ranging from a fixed column response to a cantilever equivalent to a shear wall response. This parametric analysis results are used for the development of an applicability figure which relates the structural system that is going to be experimentally studied to the range of accuracy that can be achieved by using the weakly-coupled methodology.

5.4.2.1 Parametric Analysis Overview

For the parametric study, a nonlinear frame element was performed with varying boundary conditions. For simplicity, the cross section, the material properties of the study element and the modeling technique are same as the first storey columns of the study structure as discussed in Chapter 3 and Chapter 4. The height of the study element is 3,680 mm. The study element is fixed at the bottom while there is a rotational spring at the top, whose stiffness varies in order to cover the range from a fixed ended column to a cantilever column case. Additionally, a constant axial load equal to 21% of the column's axial load capacity is applied at the top of the study element, while a lateral deformation protocol is imposed as shown in Figure 5-8. The lateral load protocol consists of seven loading cycles with different magnitudes, as presented in Figure 5-9. Before performing the parametric analysis with respect to the rotational stiffness of the spring, the rotational stiffness at the top of the specimen was estimated, as presented in Figure 5-8. The two translational DOF at the top of the column were supported, and a unit rotation was applied at the top resulting in a rotational stiffness equal to 28,713 kN·m.

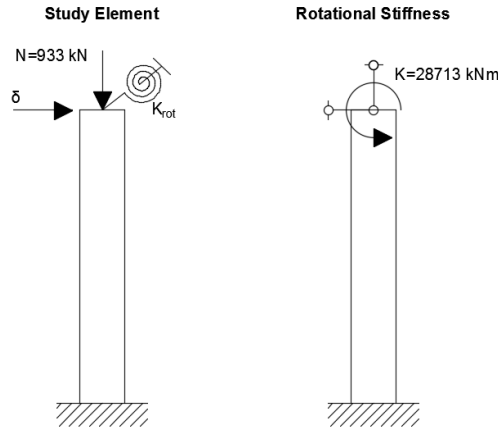


Figure 5-8: Study element (left) and column's rotational stiffness at the top (right).

For the parametric analysis, a stiffness factor, f , is used which is equal to the rotational stiffness of the spring, K_{rot} , divided by the rotational stiffness at the top of the column element, K (Figure 5-8). The analysis is performed for values of the factor, f , ranging from zero, which represents the cantilever case, to ten, which is equivalent to fixed-fixed column conditions. This parametric analysis was performed for three different cases that are illustrated in Figure 5-10.

The three study cases presented in Figure 5-10 are 1) the OS standalone case which is used as the reference case for comparison with the next two cases, 2) the pinned connection case, where a pin is explicitly defined at the position of the interface point similar to the case outlined in Section 5.3.3 and 3) the weakly-coupled case as proposed in the current methodology. This study is equivalent to the study case for the reference structure, and the experimentally investigated substructure is the part of the column below the contraflexure/pin location.

Additionally, for each of the pinned connections and WCHS simulation cases, two series of case studies were performed. The first case is when the pin/interface point is located at the mid-height of the column and the second case is when the pin/interface point is located at the actual contraflexure point of the linear column system. For the second case, the actual contraflexure point is a function of the stiffness ratio, f , between the lumped spring (K_{rot}) and the rotational stiffness at the top of the column. The ratio of moments developed at the bottom and at the top, in addition to the actual position of the contraflexure point for the second case, is presented in Table 5-1.

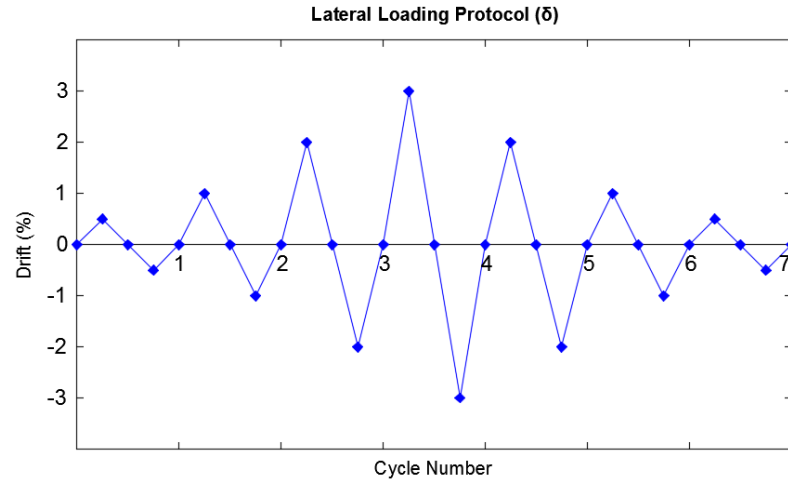


Figure 5-9: Lateral loading protocol at the top of the column.

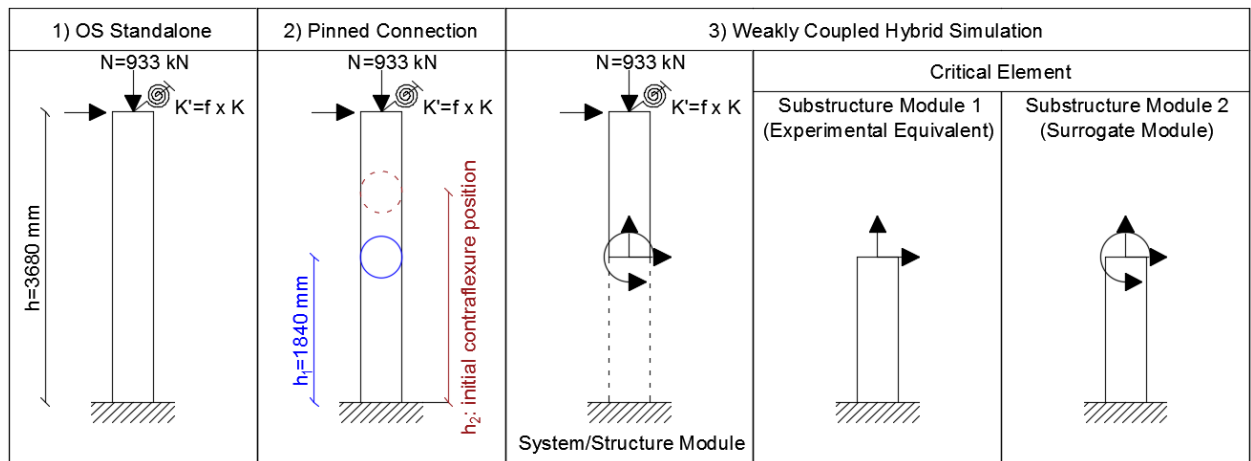


Figure 5-10: Parametric analysis study cases.

Table 5-1: Moment ratio and location of actual contraflexure point (h_2) as a function of stiffness ratio (f)

f	0	0.1	0.2	0.3	0.4	0.5	0.6	0.7	0.8	0.9	1	1.5	2	3	4	5	10
M_b/M_t	-	0.688	0.611	0.579	0.562	0.551	0.544	0.538	0.534	0.530	0.527	0.519	0.514	0.509	0.507	0.506	0.503
h_2 (mm)	3680	2531	2247	2132	2070	2029	2000	1979	1964	1951	1940	1908	1892	1875	1866	1861	1851

5.4.2.2 Applicability Measurement Tool

For comparing the previously described cases, an error evaluation tool is required. For that purpose, the developed shear force and lateral deformation hysteresis response are used for evaluating the local and the global response error. As local response, the lateral deformation of the lower part of the column is considered (below to contraflexure/interface point), while as global response the lateral deformation of the whole column is used (displacement at the column's top). By plotting the hysteretic response, the accumulated dissipated energy during the nonlinear response is calculated and is compared with the energy dissipation of the reference case as an error measurement tool. A relative error is employed as described in the following equation.

$$\text{error} = 100 \cdot \frac{E_i - E_r}{E_r} (\%) \quad \text{Equation 5-15}$$

where the error is expressed as a percentage, E_i is the total dissipated energy for either the pin connection or the weakly-coupled case and E_r is the total dissipated energy for the reference OpenSees standalone case.

For demonstration purposes, the hysteretic response figures for the case of the stiffness ratio, f , equal to 1 are presented in Figure 5-11 to Figure 5-14. The hysteretic response and the dissipated energy for the case where the interface point is at the mid-height of the column is presented for the local response in Figure 5-11 and for the global response in Figure 5-12. The case when the stiffness ratio was 1 but the interface point is located at the actual contraflexure point of the linear system is also studied to demonstrate the significant of the proper interface point location selection. For that case the hysteretic response and the energy dissipation are presented in Figure 5-13 and Figure 5-14 for the local and global response of the column, respectively.

In these figures, the global response can be described as less sensitive to the approximate nature of the WCHS and cannot work as a standalone measure to assess the applicability of the proposed WCHS. Instead, both the local and global response should be used to evaluate the applicability of the WCHS. Additionally, the proposed WCHS is able to alleviate the inconsistency that is developed due to experimental limitation when a pin connection is considered, and the case when the interface point is located at the initial contraflexure point shows better performance compared to the case when the pin is considered at the mid-height of the column. The initial stiffness and structural system properties should be considered when the applicability of the methodology

related to the experimental limitations and the physical specimen's geometry is investigated and can work as a preliminary indication for the DOF that can be exempted from the experimental control. In other words, when WCHS is used the interface point should be located at the position where decoupling of the experimentally controlled and the free DOF is of less influence for the modified system's consistency, like the initial contraflexure point of the linear system.

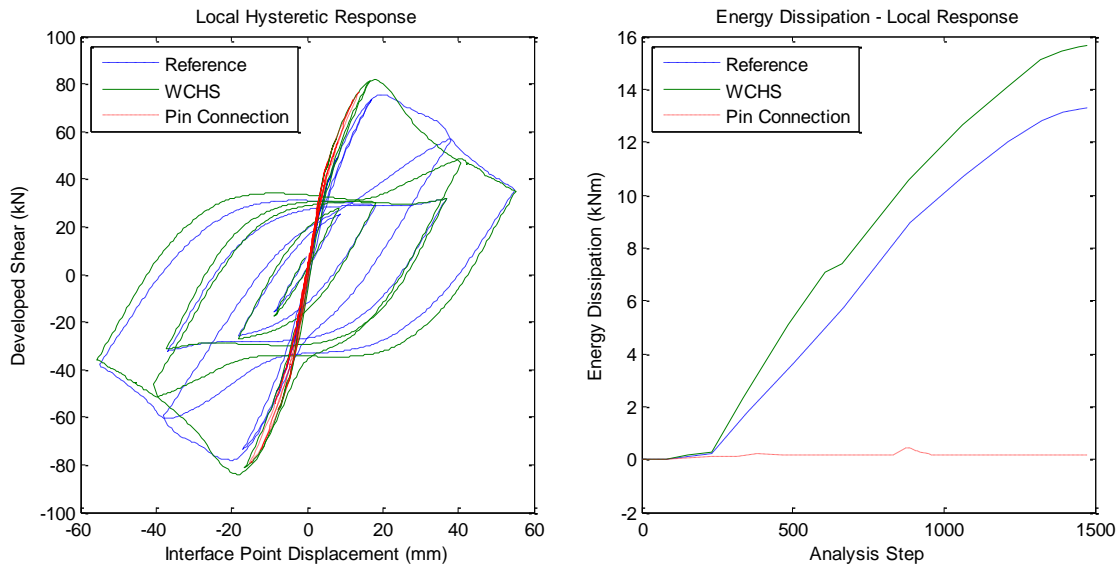


Figure 5-11: Local hysteretic response and energy dissipation when $f=1$ and the interface point is considered at the column's mid-height.

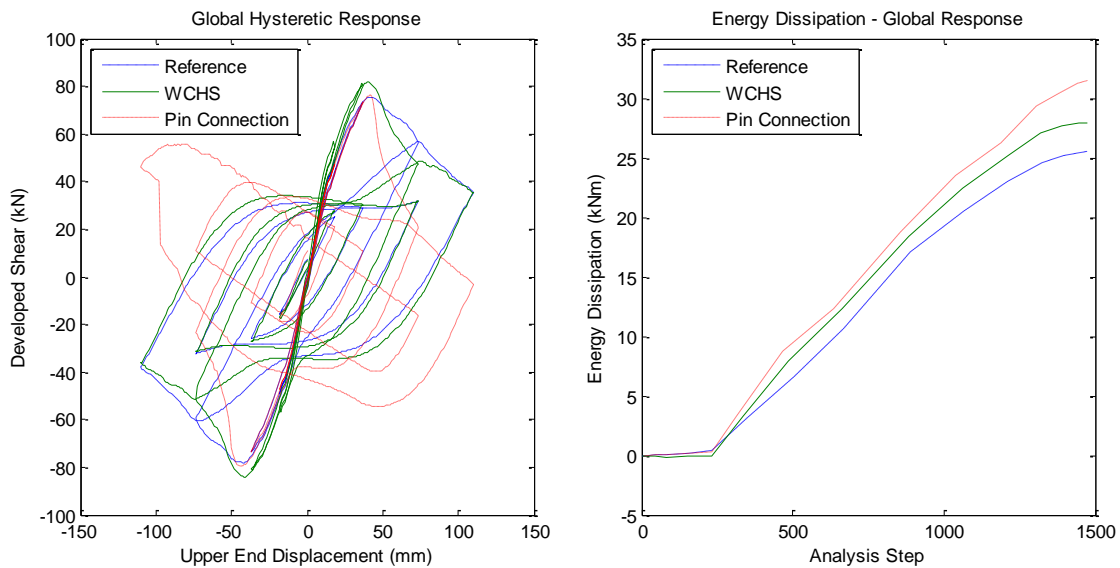


Figure 5-12: Global hysteretic response and energy dissipation when $f=1$ and the interface point is considered at the column's mid-height.

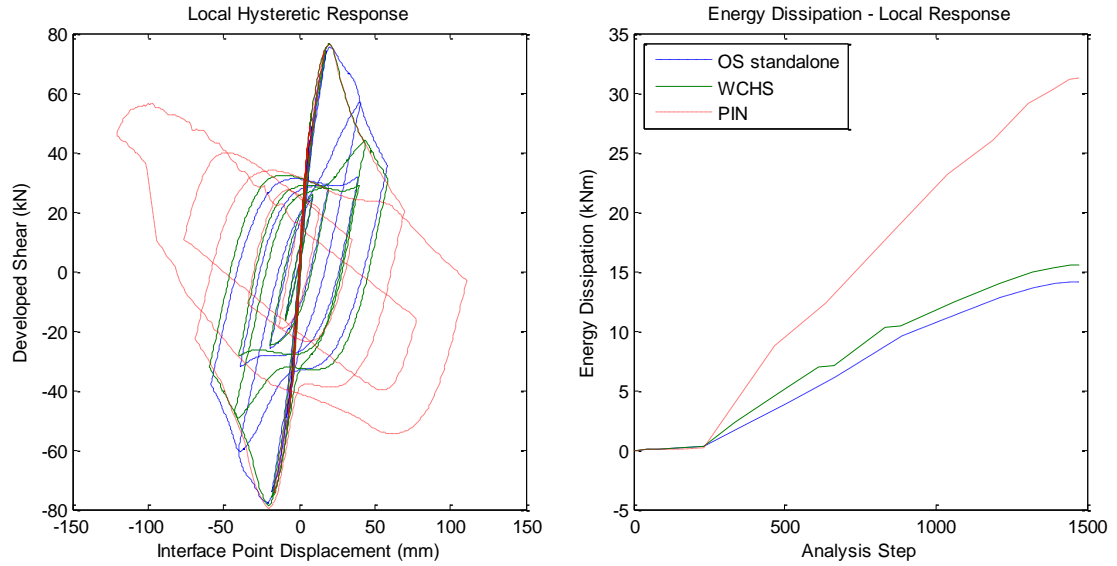


Figure 5-13: Local hysteretic response and energy dissipation when $f=1$ and the interface point is considered at the actual contraflexure location.

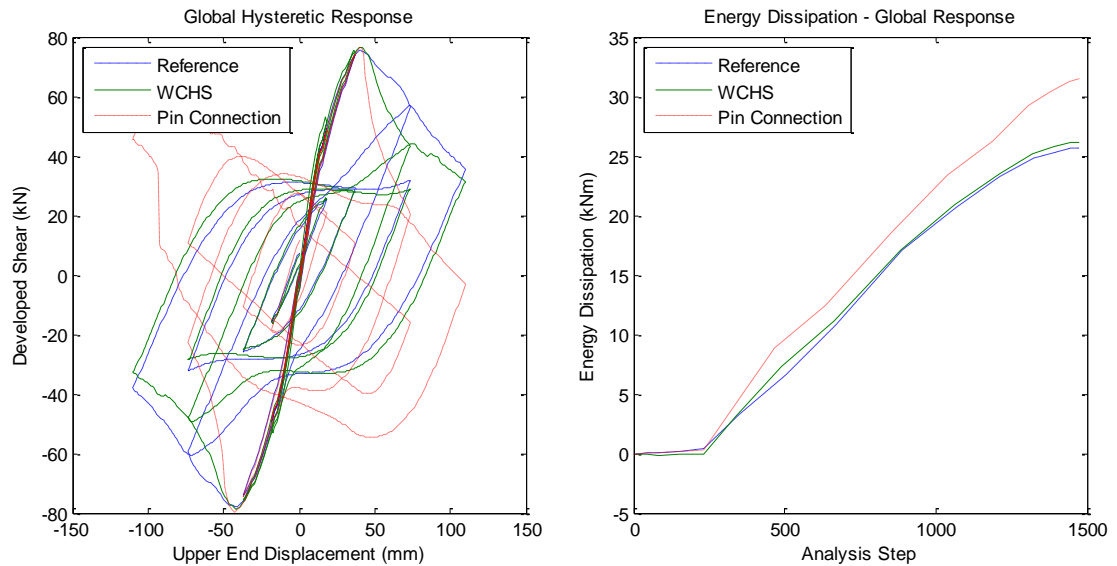


Figure 5-14: Global hysteretic response and energy dissipation when $f=1$ and the interface point is considered at the actual contraflexure location.

5.4.2.3 Weakly-Coupled Method Applicability

For developing the applicability figures of the WCHS with respect to various structural system cases, the previously described analyses were replicated for a range of values of the stiffness factor, f , from zero to ten and the error in the dissipated energy was calculated using Equation 5-15 for each case. The value of f equal to zero is representative of a cantilever, shear wall equivalent system, while the value of f equal to ten is representative of a fixed element, equivalent to a fixed column response. The applicability figures for the local, tested element's response and the global, system level response are presented in Figure 5-15. The horizontal axis represents the value of the stiffness factor f expressed in logarithmic scale, while the vertical axis represents the error in the dissipated energy for the four different studied cases. The proposed methodology is notated as WCHS- and the pin connected case is notated as Pin-, while the cases where the interface point is located in the middle of the specimen are notated as –Mid., and the ones where the interface point is located at the initial contraflexure point are notated as –Init.

Overall it can be observed that the WCHS shows significant improvements in the local and global response compared to the pinned connection case. Both the WCHS and the pinned connection cases demonstrate adequate matching in the area of the 'equivalent to column' response. However, for the WCHS case, the response both at the global and local level is improved in the transition area from wall to column equivalent response. None of the cases show adequate response for the case of the wall equivalent response. Additionally, the WCHS case, when the interface point is located at the initial contraflexure point, shows improved response compared to the WCHS case where the mid-height is used as the interface point. The case of the pinned connection at the column mid-height demonstrates good response when the stiffness factor f is close to 10. Interestingly, as it can be observed for the case of the pinned connection when the interface point is located at the initial contraflexure position, the matching deteriorates for f greater than 4 and a sudden increase in the dissipated energy is observed. This response is a result of the existence of the pin and the difference in the upper and lower element lengths. More specifically, due to the employed numerical modeling technique, the initialization of the damage occurs in the lower, longer element and the free rotation of the pin allows for the concentration of the damage at the same element.

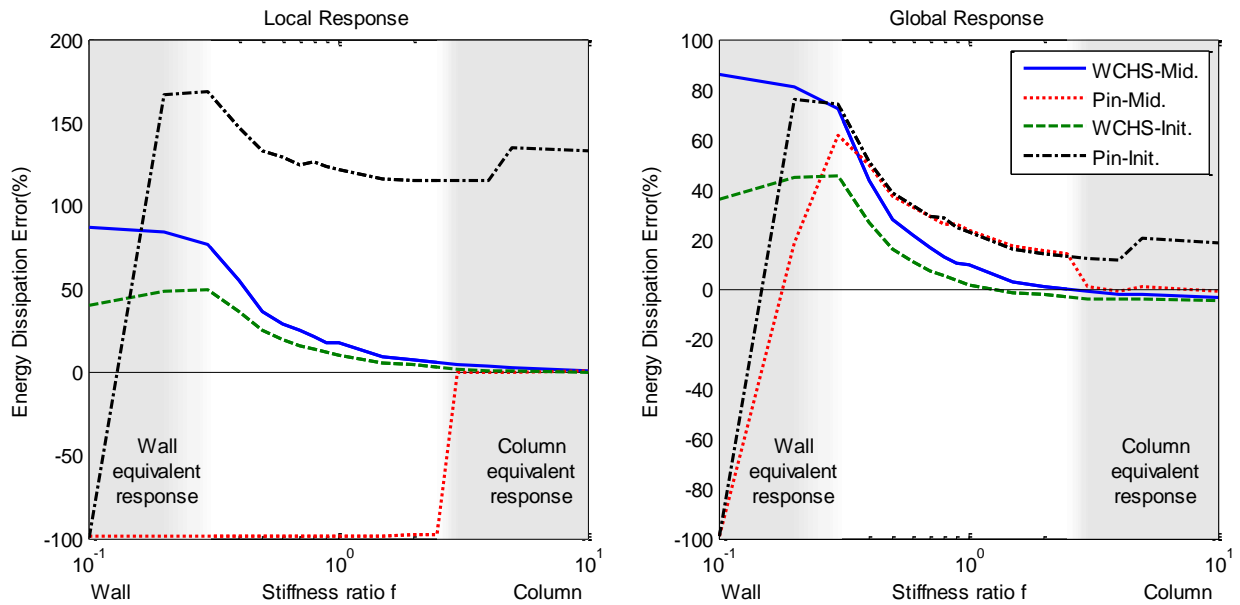


Figure 5-15: Applicability figures of the WCHS for frame elements ranging from wall to column equivalent response.

To conclude, the WCHS improves the response significantly compared to the pin connection case, and for the case that the element's response is equivalent or close to the column's response (stiffness factor great that 2), the methodology can be considered as applicable. However, it should be noted that these figures serve only as an initial assessment tool of the methodology's applicability, and for any case, a numerical investigation, such as the one discussed in Section 5.3.2, should be performed in order to accurately assess the applicability of the methodology.

5.4.3 Study Structure and Critical Element Case Applicability

From the numerical study of the reference structure of this study, the critical element seems to be suitable for employing the weakly-coupled hybrid simulation. However, it is of great interest to evaluate the applicability for the study structure by employing the generalized context developed in Sections 5.4.1 and 5.4.2.

First of all, the rotational stiffness ratio of the inner joint over the column rotational stiffness at its upper end should be calculated. For that purpose, the structure's numerical model was modified as shown in Figure 5-16 and the stiffness ratio f for the third column of the first storey was calculated by applying a unit rotation at the inner joint. The same investigation was performed for all the first storey columns, and the results are summarized in Table 5-2. Two values of stiffness ratio were calculated for each joint as a result of the difference in the system response when either a positive or negative unit rotation is applied. Also, it can be observed that the stiffness ratio is greater for the inner joints than the external joints because of the beams' participation. Taking into consideration the Table 5-2 and the Figure 5-15 the WCHS is considered more applicable for the interior columns, which is the case in this study.

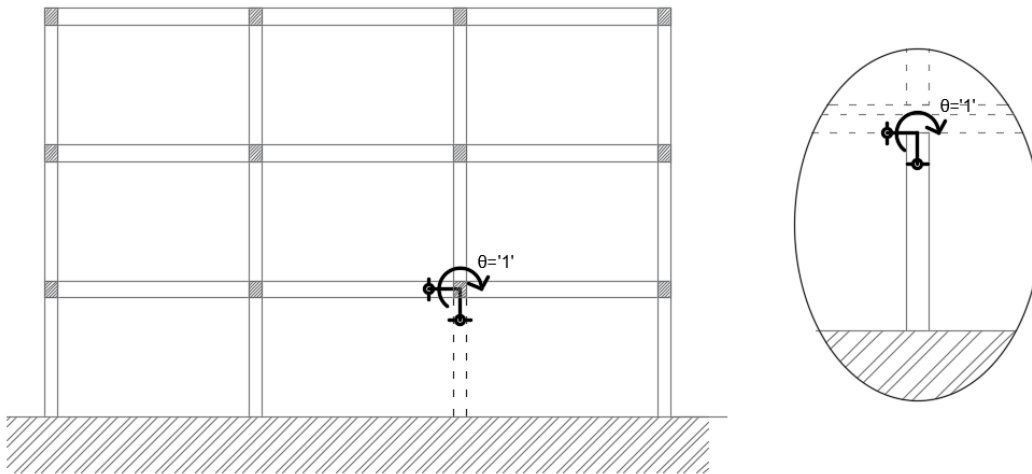


Figure 5-16: Modified numerical model for the rotational stiffness ratio evaluation.

Left: joint's rotational stiffness, right: column's rotational stiffness.

Table 5-2: Stiffness ratio for the internal and external first storey joints.

Joint	f	min	max
Internal	K_{int}/K_{col}	5.21	5.51
External	K_{ext}/K_{col}	2.19	4.50

Next, the investigation of the applicability for the study case using an analytical investigation equivalent to the one described in Section 5.4.1 is performed. The column that is going to be experimentally tested is presented in Figure 5-17 for the ideal fully-coupled case and for the proposed weakly-coupled case. First, for the fully coupled case, the stiffness matrix after the static condensation for the linear elastic properties reduces as follows.

$$[K]_f = \begin{bmatrix} \frac{12EI}{L^3} & 0 & -\frac{6EI}{L^2} \\ 0 & \frac{EA}{L} & 0 \\ -\frac{6EI}{L^2} & 0 & \frac{4EI}{L} \end{bmatrix} \quad \text{Equation 5-16}$$

where E is the initial modulus of elasticity, I is the moment of inertia, A is the cross section area of the composite section and L is the length of the study element as illustrated in Figure 5-17. The restoring force vector for the fully coupled case, which is the theoretical restoring force vector, is the one described in Equation 5-17.

$$\begin{bmatrix} F_x \\ F_y \\ M \end{bmatrix}_f = \begin{bmatrix} \frac{12EI}{L^3}u_1 - \frac{6EI}{L^2}u_3 \\ \frac{EA}{L}u_2 \\ -\frac{6EI}{L^2}u_1 + \frac{4EI}{L}u_3 \end{bmatrix} \quad \text{Equation 5-17}$$

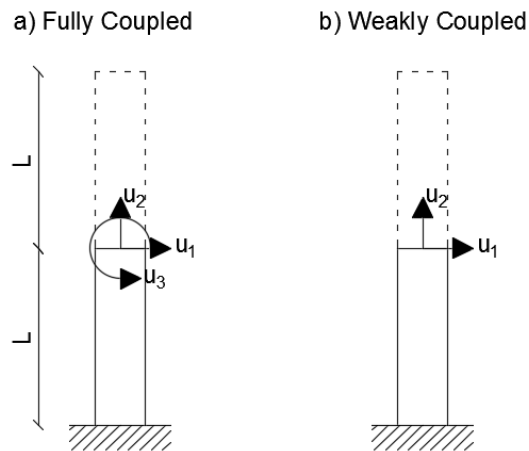


Figure 5-17: Fully and weakly-coupled cantilever element.

On the other hand, the experimental component's stiffness matrix of the weakly-coupled case when only the two translational DOF are experimentally controlled after static condensation reduces as follows.

$$[K]_w = \begin{bmatrix} \frac{3EI}{L^3} & 0 \\ 0 & \frac{EA}{L} \end{bmatrix} \quad \text{Equation 5-18}$$

By implementing the weakly-coupled approach that is described in Section 5.2, the restoring forces for the weakly-coupled simulation are presented in Equation 5-19.

$$\begin{bmatrix} F_x \\ F_y \\ M \end{bmatrix}_w = \begin{bmatrix} F_{x,w} \\ F_{y,w} \\ M_f \end{bmatrix} = \begin{bmatrix} \frac{3EI}{L^3} u_1 \\ \frac{EA}{L} u_2 \\ -\frac{6EI}{L^2} u_1 + \frac{4EI}{L} u_3 \end{bmatrix} \quad \text{Equation 5-19}$$

By comparing the restoring forces in Equation 5-17 and in Equation 5-19, it can be noted that only the restoring force at the horizontal axis $F_{x,w}$ is different, while the rest are identical between the fully coupled and the weakly-coupled simulation. For investigating the relationship between the first restoring force for the fully-coupled and the weakly-coupled cases, let us consider the deformed case of a fixed column illustrated in Figure 5-18. Accounting for the initial conditions illustrated in Figure 5-18 on the linear system the equation that described the deformed shape of the column is the following.

$$u_1(x) = \left(-\frac{u}{2L^3} \right) \cdot x^3 + \left(\frac{3u}{2L^2} \right) \cdot x^2 \quad \text{Equation 5-20}$$

By differentiating the deformed shape Equation 5-20 with respect to x , the equation that described the rotation at each position can be derived as follows.

$$u_3(x) = \varphi = \left(-\frac{3u}{2L^3} \right) \cdot x^2 + \left(\frac{6u}{2L^2} \right) \cdot x \quad \text{Equation 5-21}$$

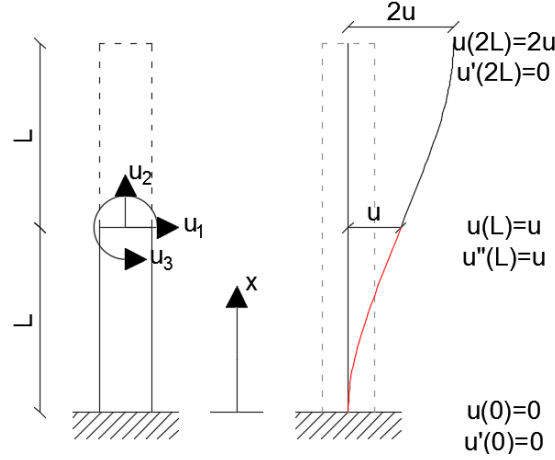


Figure 5-18: Fixed beam deformed shape.

In the current study, the interface point is located close to the column mid-height. Let's assume that the location of the interface point is exactly at the mid-height where $x = L$. By simplifying Equations 5-20 and Equation 5-21 the relationship between the u_1 and u_3 can be derived at that specific location as follows.

$$u_3 = \frac{3u_1}{2L}, \text{ when } x = L \quad \text{Equation 5-22}$$

Subsequently, by substituting Equation 5-22 into the first restoring force of equation Equation 5-17, it is proved that the first terms of equation Equation 5-17 and Equation 5-19 are identical (Equation 5-23), rendering the weakly-coupling applicable as observed in Equation 5-23.

$$F_{x,f} = \frac{12EI}{L^3}u_1 - \frac{6EI}{L^2}u_3 = \frac{6EI}{L^3}u_1 = F_{x,w} \quad \text{Equation 5-23}$$

However, this derivation applies to a linear elastic system and when the interface point is exactly at the mid-height of the column. In Figure 5-15, it is shown that the minor offset of the interface point from the mid-height (1.84 m instead of 1.83 m) does not greatly influence the response, but the response during the nonlinear range can be deteriorated significantly.

For the evaluation of the contraflexure point offset influence, the coupling between the non-diagonal terms is investigated during the nonlinear dynamic response. The relationship between the terms, $\underline{P}_{2,w} = -\underline{K}_{ij} \cdot \underline{K}_{jj}^{-1} \cdot \underline{K}_{ji} \cdot \underline{u}_i$ and $\underline{P}_{2,t} = \underline{K}_{ij} \cdot \underline{u}_i$ (Equation Equation 5-11 to Equation Equation 5-14) during the dynamic time history analysis should be studied in order to obtain an insight regarding the applicability of the WCHS. By substituting the stiffness terms as discussed

previously for the fixed column case, the second terms of the aforementioned equations can be rewritten as follows.

$$P_{2,e} = \begin{bmatrix} -\frac{6EI}{L^2} \\ 0 \end{bmatrix} \cdot \begin{bmatrix} L \\ 4EI \end{bmatrix} \cdot \begin{bmatrix} -\frac{6EI}{L^2} & 0 \end{bmatrix} \cdot \begin{bmatrix} u_1 \\ u_2 \end{bmatrix} = \begin{bmatrix} \frac{9EI}{L^3} & 0 \\ 0 & 0 \end{bmatrix} \cdot \begin{bmatrix} u_1 \\ u_2 \end{bmatrix} \quad \text{Equation 5-24}$$

$$P_{2,t} = \begin{bmatrix} -\frac{6EI}{L^2} \\ 0 \end{bmatrix} \cdot [u_3] \quad \text{Equation 5-25}$$

Ideally, the previous terms are equal and remain as such during the nonlinear response. For the current study case, where the interface point is located at L equal to 1,840 mm and given the fact that Equation 5-24 is equal to Equation 5-25, the relationship between the coupled DOF during the dynamic analysis should be constant and can be described by the Equation 5-26.

$$P_{2,w} = P_{2,t} \Rightarrow \begin{bmatrix} \frac{9EI}{L^3} u_1 \\ 0 \end{bmatrix} = \begin{bmatrix} -\frac{6EI}{L^2} u_3 \\ 0 \end{bmatrix} \Rightarrow \frac{u_1}{u_3} = \frac{6L}{9} = \frac{6 \cdot 1840}{9} = 1227 \quad \text{Equation 5-26}$$

However, the relationship between the coupled DOF may vary during the nonlinear response, but this potential variation can be easily identified by examining the response time history of the coupled DOF during the dynamic time history analysis. Evaluating the u_1 to u_3 ratio as defined in Equation 5-26 is not convenient, because the rotational DOF value, u_3 , is close to zero when the lateral deformation is minor resulting to a non properly defined ratio (division by zero). Because of that difficulty, the relationship between the measured value of the horizontal DOF u_1 and the ideal value of the same DOF $u_{1,i} = 1227 u_3$, as can be derived from Equation 5-26, is presented in Figure 5-19.

In Figure 5-19 the level of fluctuation in the coupling between the critical DOF can be identified. When the ideal value, $u_{1,i}$, is close to the measured value, u_1 , the Equation 5-26 is true, the contraflexure point remains close to the assumed position, and the WCHS is perfectly applicable. On the other hand, when these two values are different at the peak deformations, the contraflexure point position is offset, and the WCHS becomes an approximation. The time intervals where the measured and the ideal value of u_1 are different, are the ones where the response during the experimental application of the WCHS is expected to be deficient.

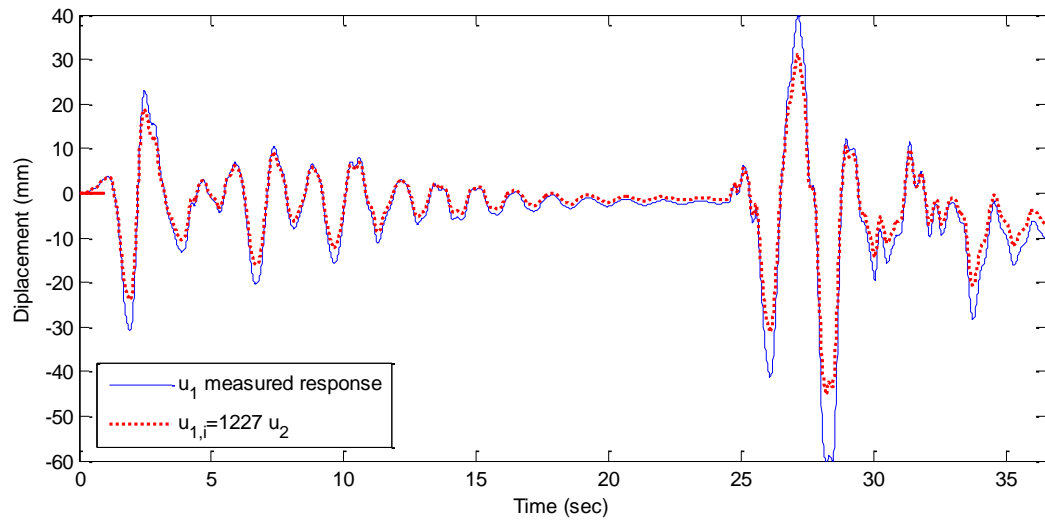


Figure 5-19: Coupling variation during the dynamic time history analysis.

To conclude, it is clear that initially and before the damage development in the critical specimen, the error related to the testing limitation is minor, but during the damage development, the contraflexure point position varies and the error is increased. However, by employing the WCHS the error is limited to the peak deformation time intervals only, where the actual deformation conditions of the critical specimen cannot be replicated with the current setup.

Chapter 6

Application of the Weakly-Coupled Method to the Reference Structure

6 Application of the Experimental Weakly-Coupled Method to the Reference Structure

In this chapter, the experimental application of the proposed weakly-coupled hybrid simulation method is discussed. Initially, the hybrid simulation architecture is presented, and the developed control platform for the experimental module is introduced. Subsequently, the challenges related to the experimental aspects of hybrid simulation are introduced and their solutions presented. Finally, some additional investigations that were performed for the in-depth understanding of the developed methodology and the potential error sources identification are presented.

6.1 Hybrid Simulation Implementation

For the implementation of the hybrid simulation, the weakly-coupled approach discussed in Chapter 5 and shown in Figure 5-1 is experimentally applied. In this section, the requirements in terms of equipment and application platforms are presented, and special attention is given to the architecture of the hybrid simulation.

6.1.1 Hybrid Simulation Framework

The hybrid simulation architecture employed in this study is the University of Toronto Simulation Framework (UT-SIM) (Huang and Kwon 2017, Mortazavi et al. 2017). The current simulation framework can be characterized with three main components. The first is the standardized communication protocol and data exchange format which is responsible for the data communication between the various modules (integration, experimental and surrogate module). The second component is the integration module, which is a software tool responsible for running a time integration scheme and in some cases is used to model the majority of the structural system. The last component is the substructure modules component, where one or more small regions in the structural system that are either critical for the response or required for complex numerical modeling techniques are physically tested or are modeled in advanced modeling software. The first component is responsible for the communication between the last two and in this way the structure is studied as a whole. More information about the aforementioned components can be found in the

study published by Huang and Kwon and in the UT-SIM manual (Huang and Kwon 2017, Mortazavi et al. 2017).

In the current study, the integration module is the OpenSees software, where the structure except for the critical column component is modeled and is responsible for solving the numerical time integration scheme for a pseudo-dynamic problem. For employing the OpenSees as substructure module, a specially developed substructure element is used, which is responsible for developing the communication with the substructure modules (Huang and Kwon 2017). The substructure modules for the experimental application of the methodology are the experimental substructure (NICON) and the numerical surrogate model substructure (NICA) as presented in Figure 5-1. The surrogate model has already been discussed in Section 5.3.1, while the experimental substructure is discussed extensively in the following section. The overall architecture of UT-SIM is presented in Figure 6-1, where the components used for the current study are highlighted.

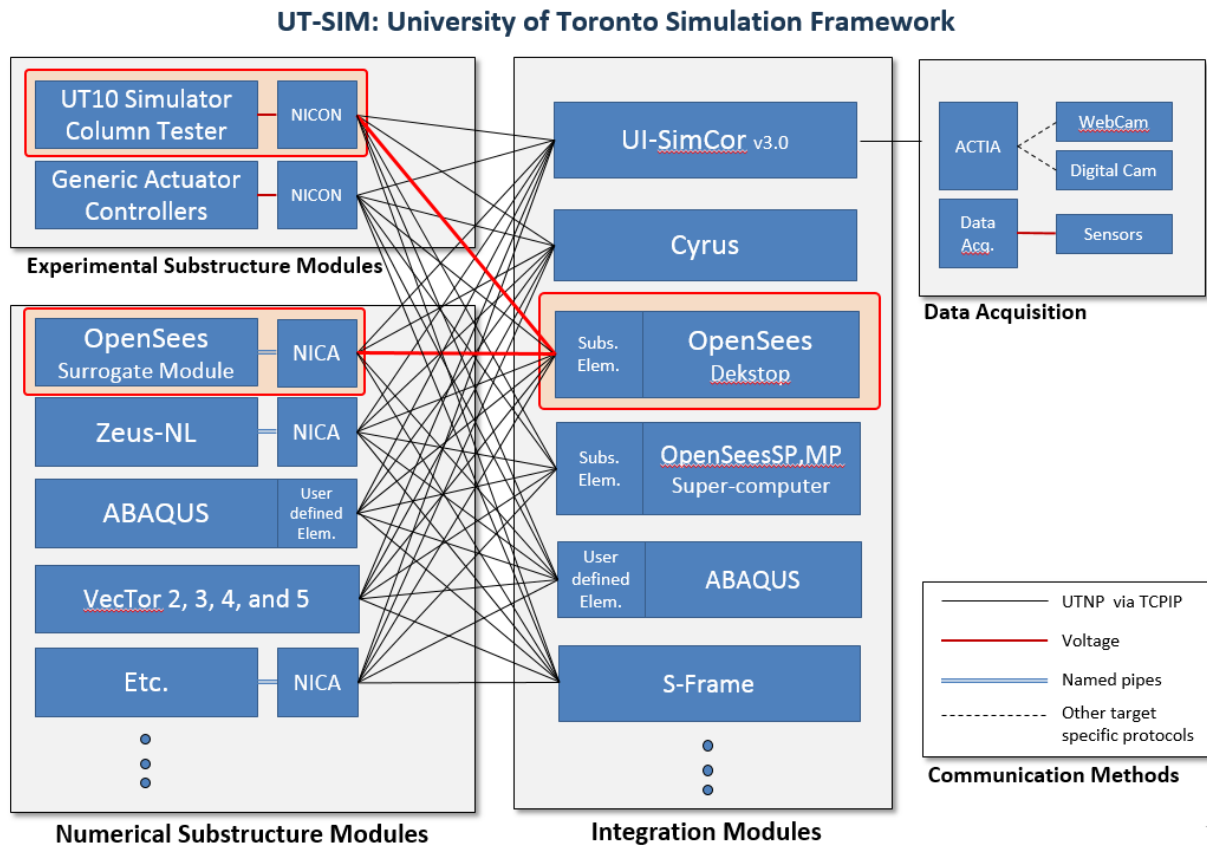


Figure 6-1: University of Toronto Simulation Framework (UT-SIM) architecture and employed components for the current study.

6.1.2 Dedicated Network Interface for Controllers (NICON) for Column Tester Frame

For performing the experimental hybrid simulation, the communication between the integration module and the experimental component, in addition to the controlling of the actuators' strokes in the experimental setup, is required to be performed through an automated procedure. These tasks are accomplished through the Network Interface for Controllers (NICON), which is an application developed for experimental hybrid simulation (Figure 6-2). The NICON version developed in this study is a modification of the generic version developed by Zhan (Zhan 2014, Zhan and Kwon 2015) and is dedicated to the column testing frame. NICON is composed of two components, the software written in LabVIEW and the hardware for the data communication between the software and the experimental setup. Both the software and the hardware are supplied by National Instruments (National Instruments 2016). The overall objective of NICON is the transformation of the target deformation as received from the integration module to actuator strokes and the transformation of the load cell readings into restoring forces feedback to the integration module. This procedure occurs at each time step of the integration scheme, and all the data are exchanged in the predefined protocol (Huang and Kwon 2017). In the next two sections, the software and hardware components of NICON are described, and a guideline regarding how to use the developed version of NICON is attached in Appendix A.

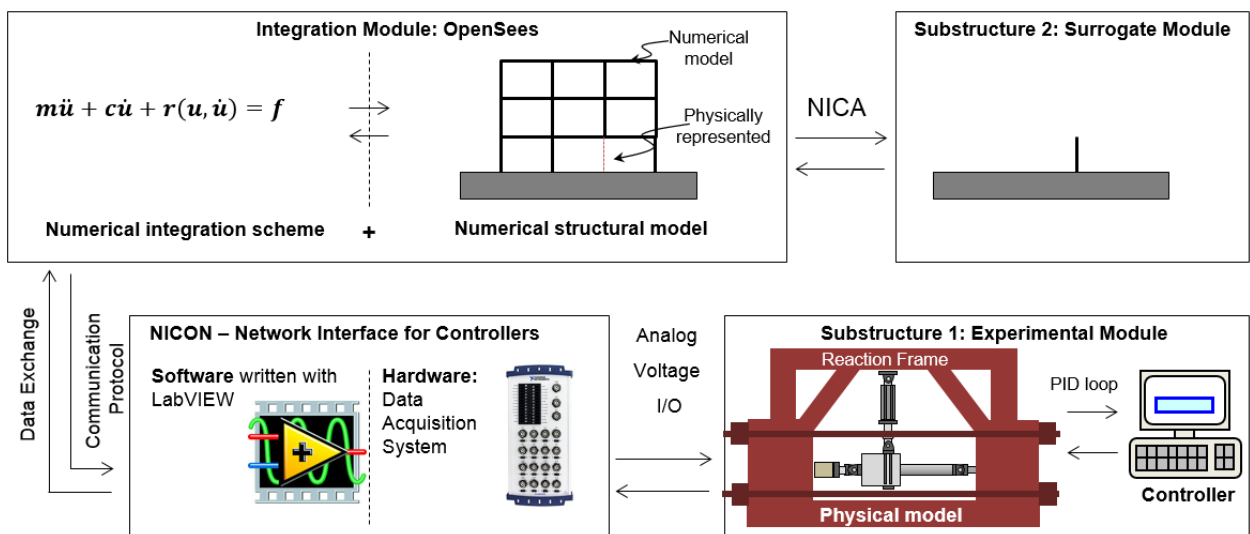


Figure 6-2: Weakly-coupled hybrid simulation architecture dedicated for the column testing.

6.1.2.1 Network Interface for Controllers (NICON)

All the required force and deformation transformations, as well as the synchronization and the data communication, occurs in the NICON. The NICON is developed in LabVIEW which is a system design software developed by National Instruments. One of the main advantages of LabVIEW is that it provides a user-friendly customizable interface which allows for the modification of the developed platform easily according to the experimental needs. Additionally, it is based on a graphical programming syntax, which visually replicates the data and the processes' sequence, making it a straightforward task to understand the architecture and identify potential error sources. The NICON written in LabVIEW communicate with general input/output hardware manufactured by National Instruments. An extensive library is implemented in the software for the data acquisition and the signal processing required for the hybrid simulation. In this study and within the UT-SIM framework, the hybrid simulation is performed with the analog voltage input and output technique, since most controller systems support such functionalities and because this architecture is reliable and cost-efficient for structural testing.

In the analog I/O method all the communications between the software and the experimental facility are performed as voltage signals generated and read by the hardware. More specifically, the software component is responsible for receiving the target deformation from the integration module through the Internet, transform it into actuator strokes through a coordinate transformation scheme and generate the voltage commands to the hardware for controlling the testing setup. After applying the target deformation, the load cells' measurements are returned as voltage inputs through the hardware, and the software is responsible for their transformation into force measurements. These measured forces are finally transformed into restoring forces compatible with the coordinate system of the integration module and are fed back to the integration scheme. These tasks, described as coordinate transformations, took place at each analysis step and their developed algorithms are presented in Section 6.2.

In addition to the load cell and actuator commands and measurements, the external instrumentation discussed in Section 4.4.3 is connected through hardware to the controller platform. The readings of this instrumentation set are transformed from voltage readings to deformation measurements, as discussed in Section 4.4.3, and are used during the hybrid simulation for the deformation control of the specimen through a developed error compensation scheme. This error compensation scheme is required for applying the correct deformation on the specimen and is discussed in detail in Section 6.3.2. Except for the hybrid control of the specimen's deformation, the developed NICON version allows for the manual control of the specimen deformation performed by the user which is an important feature for the alignment of the specimen or the manual testing using a quasi-static testing protocol. The detailed discussion regarding the development procedure of NICON and the techniques employed in LabVIEW is beyond the scope of the current study and is not presented. Further details on the generic version of NICON can be found in Zhan (2014). Some features required for performing hybrid simulation with the version of NICON developed for this research are presented in Appendix A in addition to the user guidelines.

6.1.2.2 Network Interface for Controllers (NICON) Hardware

The general purpose data acquisition system adopted in this study is the NI USB-6218 BNC system from National Instruments (National Instruments 2009) and is presented in Figure 6-3 in addition to the junction box used for the string potentiometer instrumentation connection and the cabling configuration. The employed DAQ provides two channels for voltage output, which were used to control the jack and the actuator strokes, and 16 differential voltage input channels, four of which were used for the two channels of displacements and two channels of forces measured from the jack and the actuator. The remaining 12 channels were utilized for the external instrumentation. The NI USB-6218 BNC system is a portable device which is connected to a personal computer that runs NICON and communicates with the device through a USB port. The connections of the analog channels are established using BNC cables as can be observed from the cabling configuration in Figure 6-3.



Figure 6-3: Right: NI USB-6218 BNC data acquisition system. Left: Cabling configuration of the DAQ and connection with the junction box.

6.1.3 Experimental Setup Control System

The control system consists of the high bandwidth memory (HBM) hardware and FlexTest 40 controller from MTS Systems Corporation. The FlexTest 40 is controlled by a terminal computer which runs the control station software. All the signal processing tasks take place in the FlexTest 40 hardware. The output from the DAQ is used as an external signal command in the FlexTest 40, and the stroke control of the jack and the actuator is performed through NICON. The proper control of the actuators' strokes is performed through a proportional-integral-derivative (PID) control loop feedback mechanism which takes place in the FlexTest 40 controller. A PID loop is used for the control of the hydraulics through the jack and the actuator's servo-valves such as the applied stroke to matches the target one in an optimum and consistent way. This control optimization scheme is based on 1) the proportional term (P) which accounts for the current control error value, 2) the integral term (I), which is the sum of the instantaneous error over time and gives the accumulated offset that should have been corrected previously, and 3) the derivative term (D) which is calculated by determining the slope of the error over time and is responsible for predicting the system behaviour over time, thus improving the time and the stability characteristics of the system. The PID loop architecture is presented in Figure 6-4.

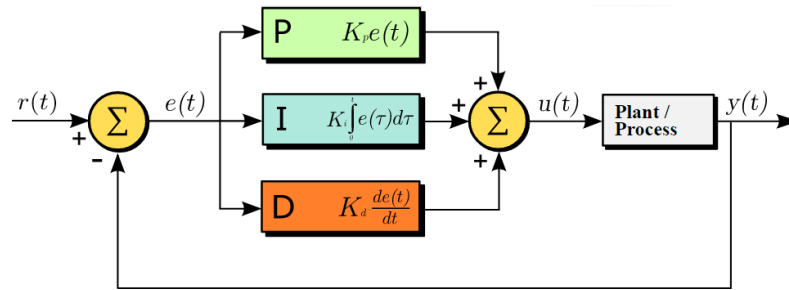


Figure 6-4: Proportional-integral-derivative (PID) control loop feedback mechanism.

The experimental setup with all the required hardware for hybrid simulation is presented in Figure 6-5. The named features are sorted according to the data flow during testing. First is the personal computer, where both the integration module and NICON run, which is connected to the data acquisition system (DAQ). The DAQ is connected both to the junction box used for the external instrumentation and to the FlexTest 40 controller which is controlled by the terminal. The last component of the hybrid simulation setup is the physical model, where the specimen of the retrofitted case structure is depicted. Finally, in Figure 6-5 the additional instrumentation setup (HBM) is presented which is used for the LVDTs and the strain gauge measurement recordings. The HBM setup is not connected with the DAQ, and the measurements are not used for the hybrid simulation.

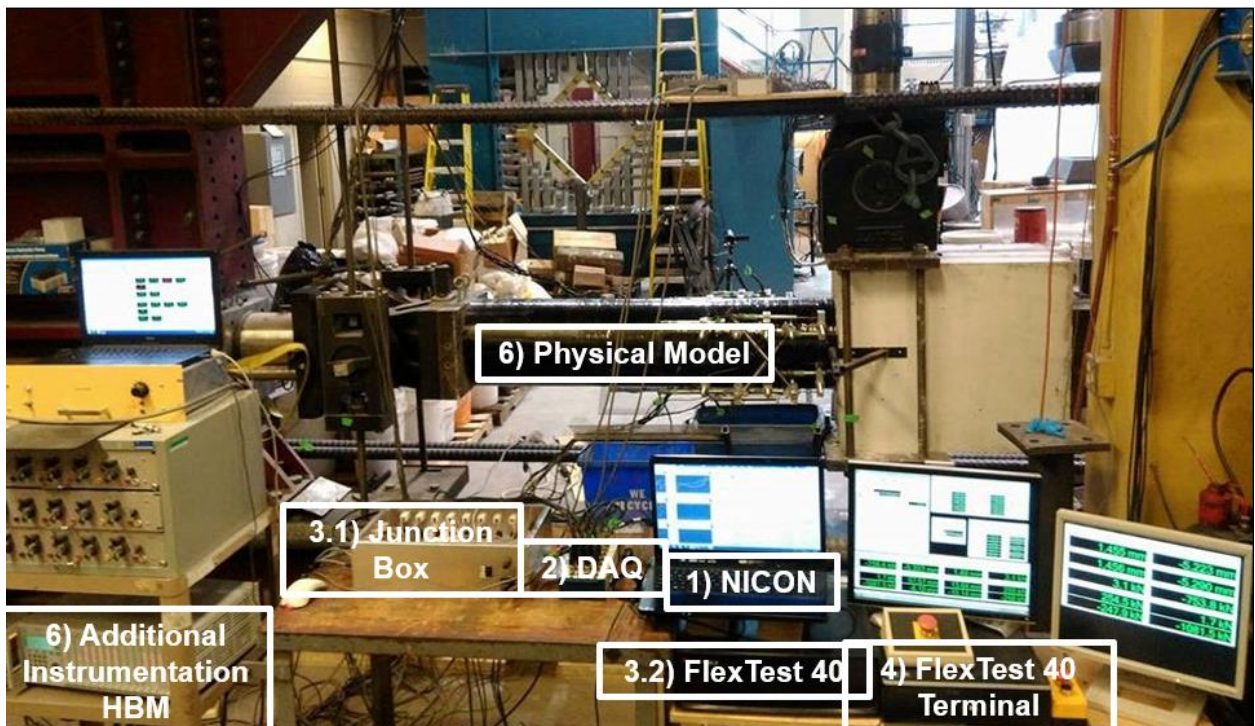


Figure 6-5: Experimental setup and hybrid simulation hardware architecture.

6.2 Coordinate Transformation

In this section, the coordinate transformation required for the experimental testing is discussed. The term coordinate transformation refers to all the deformation and force conversions that are covered in this section. The developed transformation scheme is required because of the different coordinate system between the integration module and the experimental setup, as well as because of the coupling between the hydraulics' strokes. In order to understand the necessity for the developed scheme and elaborate more on the coordinate transformation architecture, Figure 4-22 is repeated below. From the geometry representation in the figure, it can be noted that a change in the jack stroke requires for a modification of the actuator stroke in order to retain the same lateral deformation level and vice versa for the axial deformation. Additionally, this transformation scheme is required due to the load cells' alignment with the jack and actuator axis, as long as the force measurements should be transformed back to the integration module coordinate system before being fed back to the integration module. These tasks are of significant geometric nonlinearity, and the algorithms developed to address these challenges are presented in the following sections. Finally, a numerical model where the actuators' response is replicated using thermal elements is used for the verification of the developed coordinate transformation scheme.

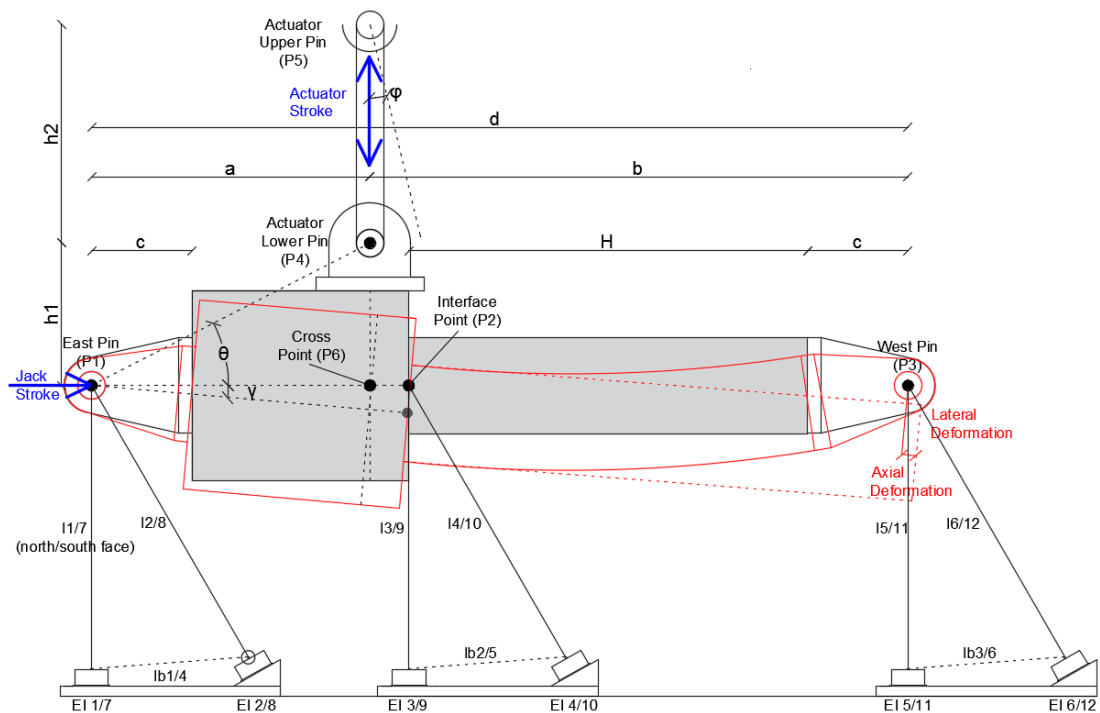


Figure 4-22: Geometry, instruments and reference point notation.

6.2.1 Displacement Command Transformation

The first algorithm that is used for the deformation control is the displacement command transformation. The displacement transformation is composed of two discrete procedures. The first procedure is the forward transformation algorithm, which is responsible for converting the target deformation as received from the integration module to target strokes of the jack and the actuator. For this task the geometric quantities illustrated in Figure 4-22 are used in addition to the measured coordinates of the reference points as described in Equation 4-1 to Equation 4-3. The equations derived for the transformation of the target deformation to jack and actuator strokes are summarized as follows.

$$u'_y = \frac{H}{H+c} u_y \quad \text{Equation 6-1}$$

$$-u'_y = (a+b) - (a+b-\delta_{\text{jack}}) \cdot \cos \left[\sin^{-1} \left(\frac{-u_x}{a+b-\delta_{\text{jack}}} \right) \right] \quad \text{Equation 6-2}$$

$$x'_2 = \delta_{\text{jack}} + \sqrt{a^2 + h_1^2} \cdot \cos \left[\sin^{-1} \left(\frac{-u_x}{a+b-\delta_{\text{jack}}} \right) \right] \quad \text{Equation 6-3}$$

$$y'_2 = h_1 - \sqrt{a^2 + h_1^2} \cdot \left\{ \sin \left[\tan^{-1} \left(\frac{h_1}{a} \right) \right] - \sin \left[\tan^{-1} \left(\frac{h_1}{a} \right) - \sin^{-1} \left(\frac{-u_x}{a+b-\delta_{\text{jack}}} \right) \right] \right\} \quad \text{Equation 6-4}$$

$$\delta_{\text{act}} = \sqrt{(x'_2 - a)^2 + (h_1 + h_2 - y'_2)^2} - h_2 \quad \text{Equation 6-5}$$

where u_x and u_y are the lateral and the axial command deformation respectively as sent from the integration module, u'_y is the modified axial deformation for the elimination of the steel pin effect, a , b , h_1 and h_2 are the geometric quantities as illustrated in Figure 4-22, x'_2 and y'_2 are the predicted coordinates of the interface point after the stroke's application, and δ_{jack} and δ_{act} are the jack and actuator strokes respectively. The steel pin effect is related to the influence of the pin at the top of the column in the axial deformation of the specimen and is discussed in detail in Section 6.2.3. The coordinates x'_2 and y'_2 represent the predicted position of the interface point which is used for defining the command strokes, and are different from the measured coordinates used for the force transformation and the backward deformation measurement. In the previously developed algorithm, the jack and actuator strokes are defined as positive when the jack and the actuator are extended, while the axial and lateral deformation is consistent with the global coordinate system of the numerical model.

The deformed state of the specimen illustrated in Figure 4-22 is when both the axial and lateral deformation commands from the integration module are negative.

The second procedure is the backward deformation measurement, which is responsible for measuring the deformed state of the specimen at a given time. This task is required for the error compensation scheme and it was presented in Section 4.4.3 in Equation 4-4 to Equation 4-6. Finally, all the derivations conducted for the coordinate transformation are based on the assumption that no deformation occurs in the stub or the steel pins.

6.2.2 Transformation of Measured Force

The forces measured with load cells are converted to restoring forces in the numerical model's global coordinate system. This task is performed using the measured coordinates of the reference points and the geometric characteristics illustrated in Figure 4-22. The force transformation is performed every time that the slackness tolerance is satisfied and before the communication between the physical substructure (NICON) and the integration module. The equations derived for the force transformation are described as follows.

$$F_{\text{pin},v} = \frac{F_{\text{act}} \cdot l_{14} \cdot \sin \varphi \cdot \sin \theta + F_{\text{act}} \cdot l_{14} \cdot \cos \varphi \cdot \cos \theta + F_{\text{jack}} \cdot d \cdot \sin(-\text{ang}_1)}{d \cdot \cos(\text{ang}_1)} \quad \text{Equation 6-6}$$

$$F_x = -F_{\text{jack}} \cdot \sin \gamma - F_{\text{pin},v} \cdot \cos \gamma \quad \text{Equation 6-7}$$

$$F_y = -F_{\text{jack}} \cdot \cos \gamma + F_{\text{pin},v} \cdot \sin \gamma \quad \text{Equation 6-8}$$

Where φ , θ , and d are the geometric properties as illustrated in Figure 4-22, F_{act} and F_{jack} are the readings from the actuator's load cell and the load cell installed in the direction of the yellow jack, l_{14} and ang_1 are the length and the angle as defined in Equation 4-4, $F_{\text{pin},v}$ is the vertical reaction at the western pin and F_x and F_y are the lateral and axial restoring forces as fed back into the integration module. In the equations for the force transformation, the load cell readings are positive when the jack and the actuator are extended.

6.2.3 Verification of Coordinate Transformation

For the verification of the displacement and force transformation scheme, a numerical model was developed in OpenSees to replicate the testing frame response. In this numerical model, the jack and the actuator were represented by elastic thermal elements with stiffness significantly higher than the tested specimen's (Jiang and Usmani 2013), and are able to replicate the extension and the contraction of the equipment by defining the corresponding thermal loading time history. The developed numerical model is presented in Figure 6-6. The dark red and the dark gray elements represent the thermal and the rigid elements, respectively, while the tested specimen is illustrated in light gray and is modeled using the modeling method discussed in Chapter 3.

For the transformation of the stroke commands to the thermal loads, the following relationship is used for both the jack and the actuator thermal elements.

$$\Delta T_{i,t} = \frac{\delta_{i,t}}{L_i \cdot a_i} \quad \text{Equation 6-9}$$

where $\Delta T_{i,t}$ is the thermal load command, $\delta_{i,t}$ is the stroke command as occurring from the coordinate transformation at a given time step t , and L_i and a_i are the element length and the material thermal coefficient used for the jack ($i=1$) and the actuator ($i=2$) thermal elements. The thermal time histories were developed by transforming the stroke commands to thermal load commands at every analysis time step.

For this numerical study, the first 10 sec of the input ground motion were used. The target axial and lateral deformations that were fed into the coordinate transformation scheme were the ones recorded at the interface point of the specimen during the preliminary investigation (Section 3.4.3) and are presented in Figure 3-18. These deformation response histories were transformed into thermal load histories and imposed on the developed numerical thermal model. For the replication of the load cell's response, axial force recorders were used for the thermal elements in OpenSees. These force measurements were transformed into restoring forces using the force transformation discussed earlier in this chapter and were compared with the developed axial and shear force in the critical element during the preliminary investigation.

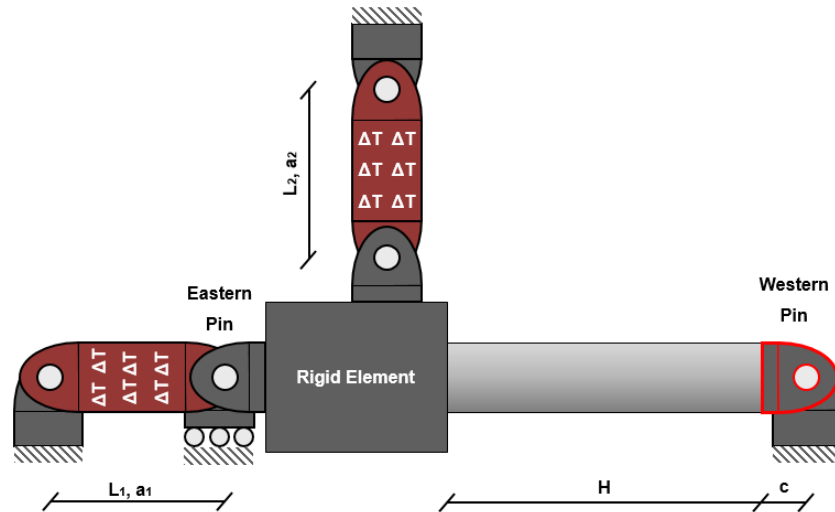


Figure 6-6: Thermal model representation of the coordinate transformation validation.

After performing the previously described thermal study, the axial restoring forces occurring from the force transformation were proven inconsistent with the developed forces during the preliminary investigation. The “Reference” forces from the preliminary study in addition to the forces of this “Initial” thermal study are presented in Figure 6-7.

The source of this inconsistency is the axial response of the western pin, first introduced in Equation 6-1. Because of the fact that the interface point for the hybrid simulation is the western pin, the steel pin length with notation “c” in Figure 6-6 is part of the structure. However, the stiffness of the steel pin is significantly higher compared to the concrete stiffness, and by imposing the unfactored target deformation from the integration module, higher axial strains are developed in the concrete part, which results in the development of a higher axial load. It can be observed that the pin’s effect exists only in the axial restoring force because in the lateral direction the softer response of the concrete column and the minor curvature developed in the pin area do not change the developed shear force. This inconsistency was addressed by imposing a reduction factor in the axial target deformation as shown in Equation 6-1. In this way, the imposed axial deformation is reduced with respect to column and steel pin lengths and the strain developed in the column is consistent with the one of the preliminary case. Consequently, the coordinate transformation and the thermal study were repeated, and the developed forces are notated as “Factored” and are presented in Figure 6-7, in addition to the reference and the initial thermal study. These results give credence to the developed coordinate transformation scheme and allow for its implementation into NICON.

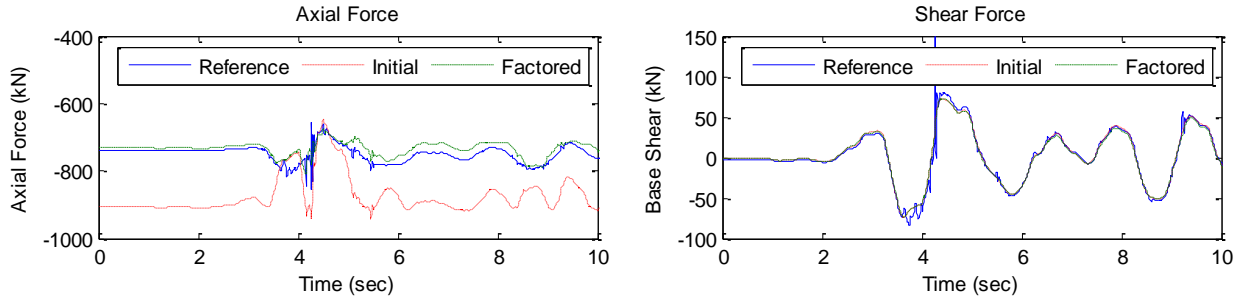


Figure 6-7: Coordinate transformation validation using the thermal element study.

6.3 Error Compensation Architecture

To perform hybrid simulation, the proper control of the specimen's deformation is of significant importance. This task becomes more challenging when a multi-DOF simulation is performed, where coupling between the controlled DOF exists, and the efficiency of the deformation control is highly affected by the loading frame to specimen stiffness ratio. As it can be understood, a significantly stiffer loading frame compared to the tested specimen is required for consistently imposing the target deformation on the tested specimen. These two challenges exist in the current study. The applied strokes are coupled, and the hydraulics are connected to the same loading frame, whose stiffness is not high enough to be considered as rigid. These conditions result in an inaccurate deformation application to the specimen and make the implementation of an error compensation architecture necessary for performing the hybrid simulation. The error sources are described in the following in addition to the employed error compensation technique.

6.3.1 Error Sources

Various sources of error impact the accuracy of the deformation control. The first and most important is the stiffness of the reaction frame. From the experimental investigation, it was proven that significant elastic deformations are developed in the loading frame. Characteristic for applying an axial deformation of 0.8 mm to the specimen, the required stroke elongation of the jack was 7 mm (Figure 6-12). The difference is absorbed by the deformation in the loading frame and by the slackness at the pin connections. This relatively low stiffness results in significant inconsistencies regarding the frame response.

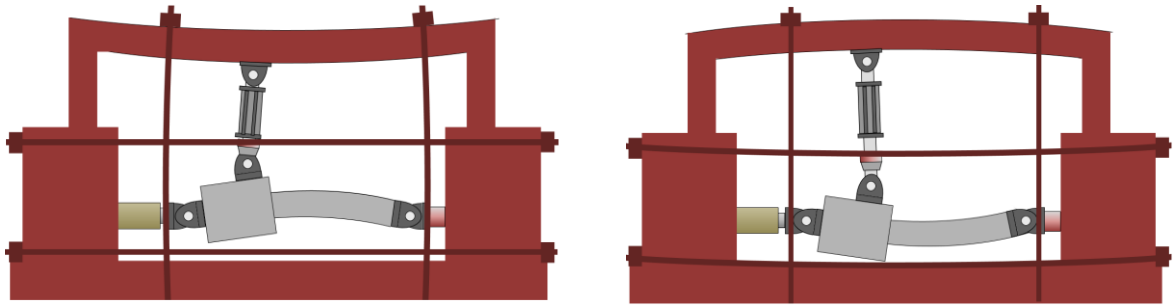


Figure 6-8: Loading frame reaction for positive (left) and negative (right) applied lateral deformation.

These inconsistencies, however, are difficult to be quantitatively assessed and are described only in qualitative terms. In Figure 6-8 the response of the loading frame is illustrated when the applied deformation is positive (left) and negative (right). It can be observed that the stress conditions on the loading frame are different in each case and the theoretical reaction locations are displaced. For example, when the applied lateral deformation is positive the horizontal DYWIDAG bars are stressed, while the vertical ones are loose because of the horizontal upper red beam deformation. Similar is the response for the case of negative lateral deformation. In this case, the vertical bars are stressed while the horizontal bars are loose. In both cases, there is stress developed in the designated “loose” DYWIDAG bars, but there is significant fluctuation due to the loading frame deformations. This response results in a partial loss of the applied stroke, which is absorbed by the frame’s deformation and also modifies the geometric characteristics illustrated in Figure 4-22. This variation in the geometric characteristics affects the initial measurements used in the coordinate transformation, and the produced target strokes may slightly vary from the theoretical ones.

An additional error source is the slackness that occurs in the pins during the changes in the loading magnitude and direction. Slackness is the opening and closing of the gaps between the pin axis and the pin holes which may occur in a systematic way but is difficult to be either quantitatively assessed or modeled interactively with the rest of the error sources. The pin slackness is qualitatively presented in Figure 6-9 for the western pin during different loading conditions. The gap is estimated to be close to 1 mm, which can be essential for the axial deformation force development. Finally, the out of plane deformation is considered as an error source, which has been identified in the specimen from the longitudinal rebar strain gauges’ measurement differences during the loading of the specimen. However, these differences may also partially occur from potential eccentric axial loading in the specimen due to construction deficiencies.

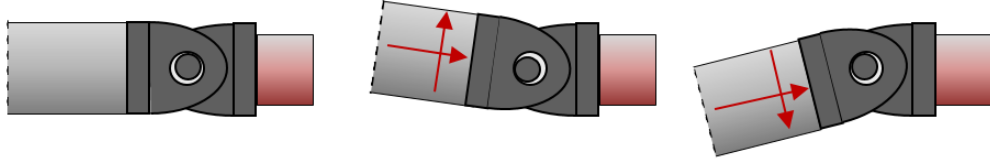


Figure 6-9: Western pins slackness representation for various loading cases.

6.3.2 Error Compensation Scheme

For addressing the deformation control inaccuracies, an error compensation algorithm similar to the one proposed by Chang et al. (Chang et al. 2015) has been implemented. The employed scheme is responsible for restoring the control inconsistencies and is based on the measured actual deformation of the specimen using the external instrumentation described in Section 4.4.3. An iterative technique is employed for applying the proposed error compensation and is summarized within the following equation, which applies both in the axial and lateral deformation.

$$u_{l,k}^{cmd} = u_l^{target} + \sum_{t=0}^t (u_l^{target} - u_t^{msd}) \quad \text{Equation 6-10}$$

where $u_{l,k}^{cmd}$ is the command deformation that is fed into the coordinate transformation and applied on the specimen at the analysis time step l and for the iteration k , u_l^{target} is the target deformation as received from the integration module (i.e. OpenSees) for the analysis time step l , u_t^{msd} is the actual measured deformation at the time before the new iteration. The accumulation of the difference between the target and the current measured deformation is equivalent to the integral control. In this error compensation scheme, more than one iterations may be required for each analysis time step, and the iteration procedure ends when the difference between the target and the measured deformation is below the predefined tolerance δ . The tolerance criterion is described by the following equation.

$$|u_l^{target} - u_t^{msd}| \leq \delta \quad \text{Equation 6-11}$$

The same equation applies for both the axial and the lateral deformations; the tolerance limit was set initially equal to 0.1 mm for the axial deformation and 0.2 mm for the lateral deformation but was later modified to 0.15 mm and 0.3 mm for each case, respectively.

6.3.3 I-modification

In addition to the error compensation scheme, an algorithm to compensate for the displacement slackness error which is referred to as I-modification (Combescure and Pegon 1997) has been implemented in NICON. Within the I-modification scheme, the measured restoring forces are modified by the product of the difference in the measured and the target deformation and the elastic stiffness matrix as shown in the following equation.

$$\bar{\mathbf{R}}_1 = \bar{\mathbf{R}}_{1,\text{msd}} - \mathbf{K}_{\text{elastic}} \cdot (\bar{\mathbf{x}}_1^{\text{msd}} - \bar{\mathbf{x}}_1^{\text{target}}) \quad \text{Equation 6-12}$$

where, $\bar{\mathbf{R}}_1$ is the restoring force vector that is fed back into the integration module, $\bar{\mathbf{R}}_{1,\text{msd}}$ is the restoring force vector after the force transformation, $\mathbf{K}_{\text{elastic}}$ is the stiffness matrix with elastic properties of the DOF that are experimentally controlled, $\bar{\mathbf{x}}_1^{\text{msd}}$ is the measured deformation vector at the current time and $\bar{\mathbf{x}}_1^{\text{target}}$ is the target deformation vector at the current time step.

The I-modification has been proven beneficial for reducing the error propagation related to inaccurate deformation control (Combescure and Pegon 1997) and also has been used effectively in order to overcome experimental limitations, like cases where the available stroke of the hydraulics was less than the required, in which the restoring force inconsistencies were reduced compared to the potential ones when the I-modification scheme would not be used (Murray et al. 2015). However, in the current study, the stiffness component related to the axial response of the specimen is inconsistent, and the I-modification has been proven to induce undesirable force fluctuation. As a result, the I-modification was deactivated during the first test and remained as such for the next tests leading to an improvement in the axial response. In the next section, the axial response of the specimen is extensively discussed.

Overall, the I-modification is not proposed for cases where the stiffness of the specimen is significantly higher than the loading frame stiffness, and the equipment is not as sensitive as required for controlling small deformations, like the axial deformation in columns. In such cases, the effective stiffness of the specimen is lower than the theoretical one, may be inconsistent during the loading conditions (multi-DOF experiments) and results in significant force fluctuations as a result of the second term in Equation 6-12, where the theoretical stiffness is used.

6.4 Investigation on Axial Response

The deformation control of the DOF whose stiffness is significantly more compared to the loading frame's stiffness is one of the most challenging tasks when hybrid simulation is performed. In the current study, this challenge becomes more prevailing due to the additional elastic deformation error sources that were previously discussed. In this section, some results from the first hybrid simulation are presented in order to introduce the axial response inconsistency observed during the experimental study. In addition, a further investigation conducted for understanding the causes of this response is described. The chapter concludes with the findings of this axial response study and some potential solutions.

6.4.1 Axial Force and Deformation Fluctuation

During the hybrid simulation, significant axial force fluctuation was observed. The restoring axial forces and the axial deformation as measured during the hybrid simulation using the first specimen is presented in Figure 6-10.

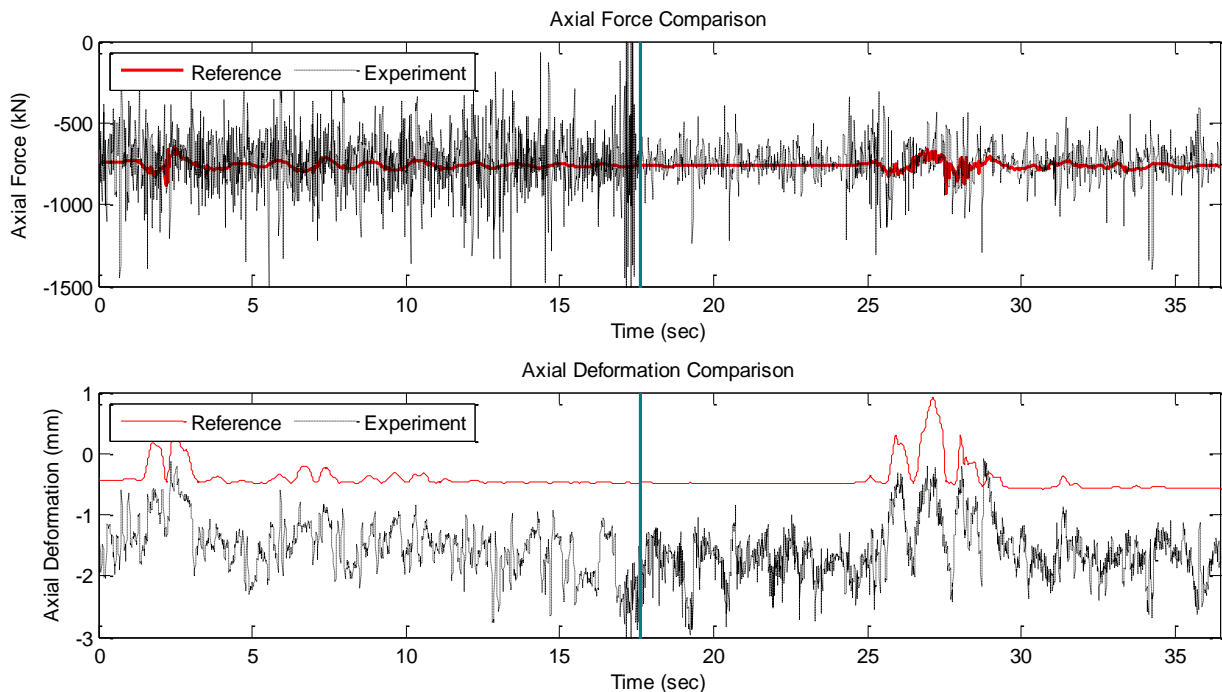


Figure 6-10: Axial force and deformation response during the first hybrid simulation.

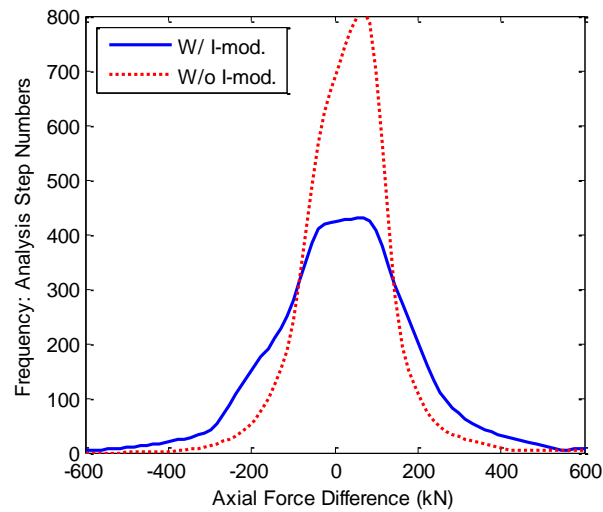


Figure 6-11: Axial force difference histogram (Difference: Preliminary Study - Experiment).

The influence of the I-modification on the axial restoring forces can be identified from the axial force response in Figure 6-10 (upper figure). The I-modification was deactivated at the analysis step corresponding to $t=17.6$. By performing a statistical analysis in the axial force difference between the preliminary investigation and the experimental response before and after the I-modification deactivation, the average difference values are -22.8 kN and -14.8 kN and the standard deviations are 191.9 kN and 106.2 kN for each case, respectively. The axial force difference histogram is presented in Figure 6-11. It should be stated that the number of analysis steps performed with the I-modification was 1,760 while the one performed without the I-modification was 1,902. The response without the I-modification is significantly improved.

Regardless of the improvement achieved after the I-modification deactivation, this measured level of axial force fluctuation is not considered as adequate. Similar to the axial force fluctuation, the axial deformation response is not consistent, and a fluctuating axial deformation was measured with an approximately constant offset equal to 1 mm compared to the axial deformation during the preliminary numerical investigation. Due to these observed inconsistencies, an additional experimental investigation for understanding the axial response was conducted and is described in the following section.

6.4.2 Axial Response Investigation

The additional experimental investigation described in this section was performed using the first specimen after the end of the first seismic event and was conducted to validate that the measured deformation was accurate and to identify the sources that result into the fluctuation observed in the axial response (Figure 6-10). The loading protocol of this study consists of three cycles of axial loading as presented in Figure 6-12. It should be noted that before and after each loading cycle an intermediate step with an axial force equal to 10 kN was used.

For this investigation, a three-dimensional scanner was used which is able to record the relative coordinates of LED targets attached to the specimen. This instrumentation is the most accurate available, but couldn't be utilized for the hybrid simulation because of the fact that the controller of the 3D scanner cannot produce the real time voltage output required for the error compensation scheme. The location of the attached targets (LED1 to LED4) in addition to the deformation measurement spans are illustrated in Figure 6-13. The deformation measurement between LED2 and LED3 is used for measuring the actual column's deformation which is notated as "Def. in H". The deformation measurement from LED1 to LED4 is used for measuring the deformation at the offset axis where the string potentiometers are attached and is notated as "Def. in H+c". The last measured deformation's span includes the western pin and is used for the validation of the string potentiometers measurements and provides an insight regarding the axial response of the system.

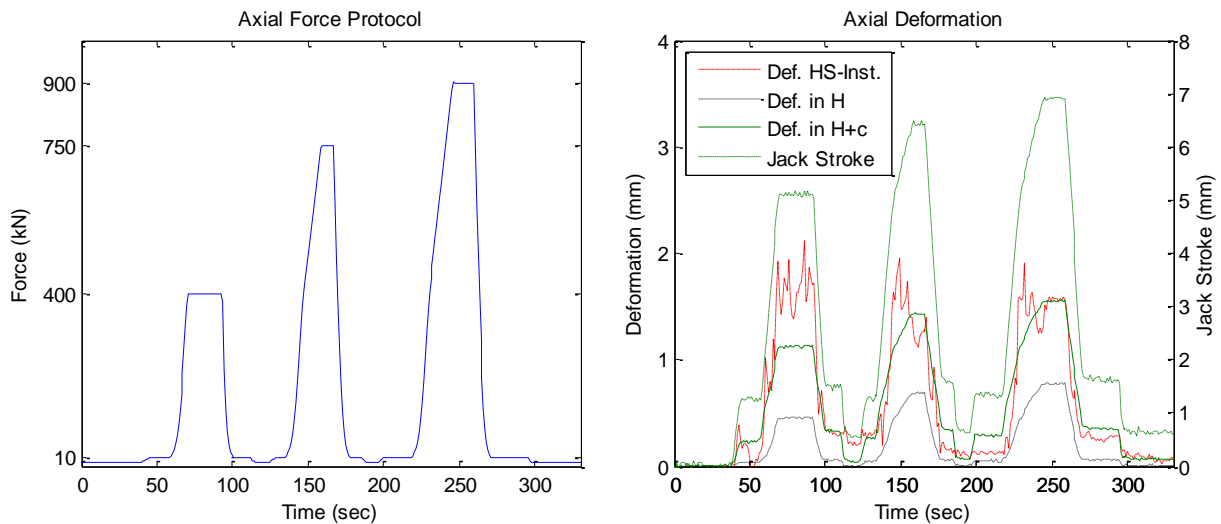


Figure 6-12: Axial response investigation. Left: Loading protocol. Right: Measured deformation.

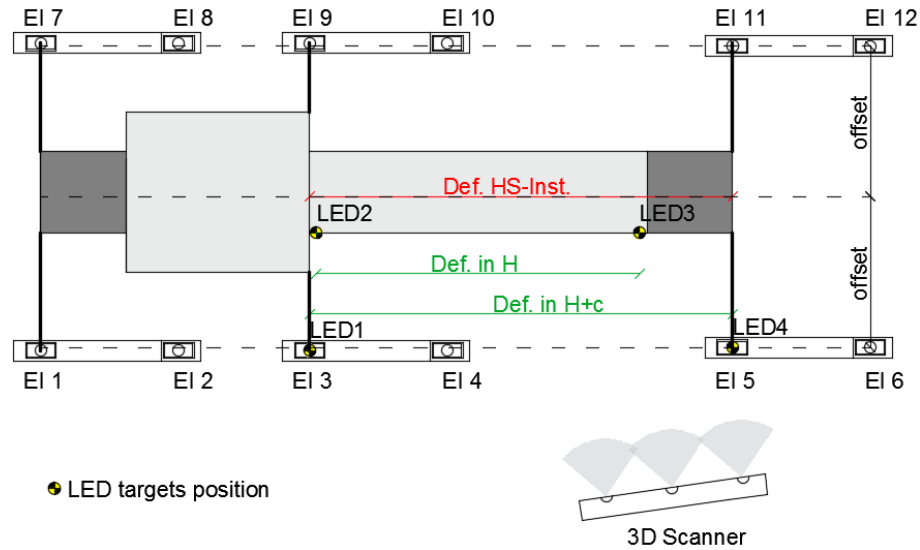


Figure 6-13: Instrumentation employed for the axial response investigation.

The measurement performed by the string potentiometers is notated as “Def. HS-Inst.” and is the averaged measurement between the south and north side. However, the measurements performed using the 3D scanner captured the response only of the specimen’s north face.

The measured deformation by the above described instrumentation sets is presented in Figure 6-12 in addition to the jack’s stroke. First, it can be observed that the deformation measured with the hybrid simulation instrumentation (“Def. HS-Inst.”) during the first loading cycle is different compared to the one measured with the 3D scanner from the targets attached to the same locations (“Def. in H+c”). This difference is eliminated during the second and the third cycles, when a greater axial load is applied and is attributed to the pin’s response, which can be described as a vertical rotation permitted by the pin’s slackness during the first cycle. Additionally, the fact that the instruments are attached on an offset axis deteriorates the effect of the aforementioned rotation for the response recorded from the 3D camera. However, for the hybrid simulation instrumentation, this deterioration is not the case because the averaged measurement from the north and south face is used.

During the second and third loading cycle, the difference between the measurements is reduced because of the higher axial loads that result in the uniform closing of the pin gaps in both the south and north faces of the specimen. The measured deformation from the hybrid simulation instrumentation shows fluctuation during the constant load time intervals. This response occurs due to the physical instruments’ response and partially justifies the deformation fluctuation

recorded in Figure 6-10. The measurement accuracy of the instrumentation during the last two cycles of this axial response investigation can be considered as acceptable for running hybrid simulation given the instruments limitation that exists.

An additional characteristic of the system's axial response can be identified by comparing the two deformation measurements performed with the 3D scanner (Figure 6-12, "Def. in H" & "Def. in H+c"). It can be observed that significant deformation differences were recorded between these two measurement spans, which indicates that the axial response of the specimen is not consistent. More specifically, for the recording between the targets LED1 and LED4, significant deformation, disproportional to the total deformation is developed when 10 kN are applied, which is representative of the slackness embedded into the system. In contrast, when the recording between the targets LED2 and LED3 is studied, it can be observed that the developed deformation is proportional to the applied force. This feature reveals the influence of the pins' slackness in the system, which cannot be reduced.

Finally, the level of the elastic deformations developed in the system can be identified by comparing the measured deformation on the specimen ("Def. in H") to the applied stroke in Figure 6-12. For example, when an axial force equal to 900 kN is applied, the deformation in the specimen is at the level of 0.8 mm, while the required jack stroke is 7 mm. This response, in addition to the aforementioned response characteristics, renders the current control level acceptable for this study but it cannot be described as accurate. For improving the response inconsistencies identified in this section, low slackness pins are required in addition to high-resolution instrumentation, like the high-precision digital displacement encoder used by Whyte and Stojadinovic (2016).

Chapter 7

Seismic Performance of Intact, Repaired and Retrofitted Reinforced Concrete Structure

7 Seismic Performance Assessment

In this chapter, the seismic performance assessment of the structure is evaluated using the developed weakly-coupled hybrid simulation method. In the current study, the structure is tested as intact, repaired and retrofitted using the same seismic scenario.

7.1 Experimental Study Overview

A multiplatform hybrid simulation (i.e. without physical specimen) was conducted in order to predict the damage that the specimen may experience. This multiplatform hybrid simulation was performed using OpenSees, where most of the structure was modeled, and VecTor2, where the critical element was modeled. After the multiplatform simulation, the experimental hybrid simulation was conducted as described below for each specimen.

- The Specimen #1 was first used for the hybrid simulation to evaluate the seismic performance of the intact structure. After the hybrid simulation, the damaged specimen was repaired using the procedure described in Section 4.3.4 and was tested under a quasi-static lateral protocol and constant axial load to understand the hysteretic behavior of a repaired specimen.
- Next, similar to the Specimen #1, the Specimen #2 was initially tested to evaluate the seismic performance of an intact structure. This test was performed for replicating the first test for validation purposes and for developing damage equivalent to the damage on the Specimen #1. Subsequently, the Specimen #2 was repaired, and the hybrid simulation for the repaired structure was carried out. In the hybrid simulation, the numerical model of the repaired columns was developed based on the hysteretic behavior from the quasi-static test of the Specimen #1. Finally, the Specimen #2 was tested under a quasi-static cyclic lateral loading and high constant axial load for capturing its constitutive response.
- The Specimen #3 was upgraded/retrofitted with the method discussed in Section 4.3.4, and it was used for the seismic performance assessment of the retrofitted structure case using a

hybrid simulation. Subsequently, the same hybrid simulation was replicated but with significantly higher axial loads in order to investigate the axial response inconsistency observed during the tests. Finally, after the hybrid simulation, the specimen was tested to failure under quasi static lateral loading and moderate constant axial load for capturing its constitutive response.

- The last constructed specimen was saved for future distributed hybrid simulation and is not presented in the current study.

Following table summarizes specimens and test sequence.

Table 7-1: Test sequence overview.

Specimen	Tests	Objective
#1	Test 1.1: Hybrid simulation of intact specimen – First ground motion with reduced intensity (15% of the actual intensity)	Validation of the testing methodology and the communication protocols
	Test 1.2: Hybrid simulation of intact specimen – First ground motion	Seismic performance assessment of the intact structure and validation of the methodology
	Test 1.3: Axial response investigation (Section 6.4.2)	Investigation of the axial force fluctuation
	Test 1.4: Hybrid simulation of intact specimen – Second ground motion	Seismic performance assessment of the intact structure
	Test 1.5: Quasi-static cyclic test of a repaired specimen. Axial load: 740 kN	Investigation of the repair efficiency and development of the constitutive model for Test 2.2
#2	Test 2.1: Hybrid simulation of intact specimen – Full seismic sequence	Seismic performance assessment of the intact structure and validation of first specimen's results
	Test 2.2: Hybrid simulation of repaired specimen – Full seismic sequence	Seismic performance assessment of the repaired structure
	Test 2.3: Quasi-static cyclic test of a repaired specimen. Axial load: 2430 kN	Investigation of the repair efficiency for higher axial load
#3	Test 3.1: Hybrid simulation of retrofitted specimen – Full seismic sequence	Seismic performance assessment of the retrofitted structure
	Test 3.2: Hybrid simulation of retrofitted specimen for increased weight structure case – Full seismic sequence	Performance assessment of the hybrid simulation framework when higher axial loads are applied
	Test 3.3: Quasi-static cyclic test of a repaired specimen. Axial load: 1173 kN	Investigation of the retrofit efficiency for moderate axial load

For clarity, the notation of the various test cases presented in this chapter is summarized in the following table.

Table 7-2: Various tests notation as presented in Chapter 7.

Test Notation	Study Case	Participating Modules
Reference/ OpenSees	Analytical seismic performance assessment of the structure/element with a standalone model	The full structure/element model is evaluated in OpenSees. This case is the reference for the rest of the tests.
Multiplatform	Analytical seismic performance assessment of the integrated structure without any weak-coupling between the substructures	The critical column is tested in VecTor2, and the rest of the structure is evaluated in OpenSees.
Experiment/ Hybrid Simulation	Experimental seismic performance assessment of the structure by employing the developed WCHS methodology	The critical column is physically tested in addition to the surrogate module developed in OpenSees. The rest of the structure is evaluated in OpenSees.
WCHS: Numerical	Numerical seismic performance assessment of the structure by employing the developed WCHS methodology. This case is required for assessing the methodology approximation.	Both the critical column and the surrogate module are developed in OpenSees. The rest of the structure is evaluated in OpenSees.
VecTor2	Numerical study of the single column's response under quasi-static lateral loading and constant axial load.	Single column model in Vector2.
Quasi-static Test	Experimental study of the single column's response under quasi-static lateral loading and constant axial load.	Column's physical specimen experimentally tested.

7.2 Multiplatform Simulation

Before the experimental investigation, a numerical multiplatform hybrid simulation has been conducted for predicting the damage in the critical element. The integration module is the same as the one presented in Chapter 5, and the substructure module is a column model developed with VecTor2 discussed in Section 3.5.2.2. Because the hybrid simulation is numerically performed in which the boundary conditions can be fully controlled, the weakly coupled hybrid simulation method is not required, and the equilibrium and compatibility at the interface DOFs are fully satisfied. In this section, the multiplatform simulation framework is briefly discussed, and the seismic performance assessment is conducted. Particular care is given to the failure mechanisms developed in the substructure module, which can be used to predict the damage that may develop in the physical substructure during the experimental hybrid simulation.

7.2.1 Multiplatform Simulation Framework

The multiplatform simulation between OpenSees and VecTor2 is performed using the communication architecture described in Section 6.1.1. The special substructure element developed for the OpenSees (Huang and Kwon 2017) is used for the communication between the integration module and the substructure module and is able to directly link OpenSees to VecTor2 by employing the inter-process communication method developed by Sadeghian et al. (2015) and the PARDISO (Schenk and Gartner 2014) C/C++ library. For the coupling of the interface node, the specific elements' configuration presented in Figure 7-1 is required because frame elements were used in OpenSees while membrane elements were used in VecTor2.

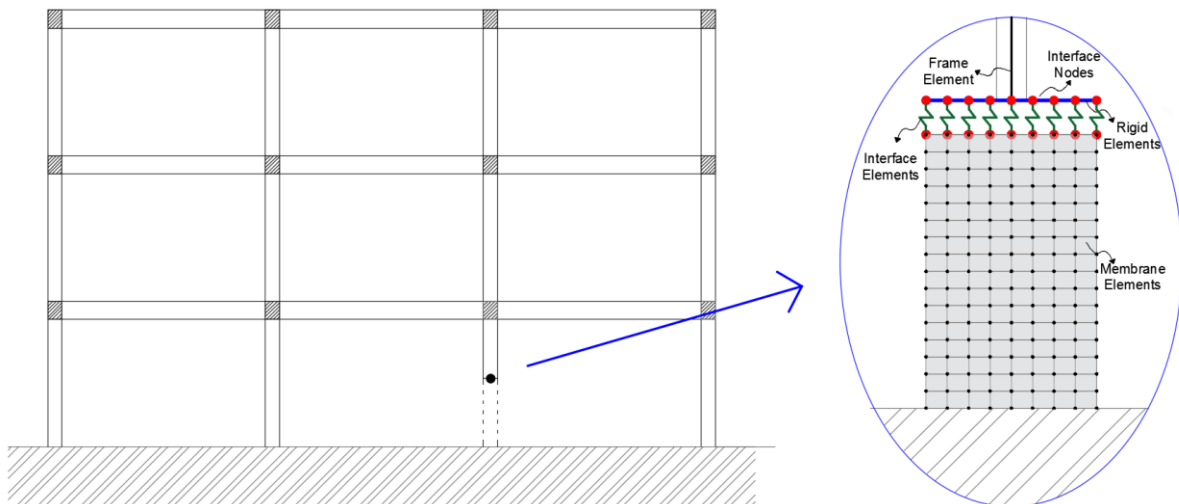


Figure 7-1: Interface node configuration for the frame to membrane elements transition.

With the developed element configuration, the three DOF interface node from OpenSees is able to be properly coupled with the two DOF nodes in VecTor2. Extensive documentation for performing multiplatform simulations equivalent to the one discussed in this section can be found in UT-SIM website (www.ut-sim.ca) and in the UT-SIM manual (Mortazavi et al. 2017).

The previously described numerical model is subjected to the seismic sequence for assessing the structure's performance and identifying the expected damage in the specimen. This investigation can be considered as the most accurate in the current study because 1) no weakly coupling between the integration module and the substructure module is required, resulting in the proper control of the boundary conditions, and 2) VecTor2 is a sophisticated software for concrete elements, which is able to capture their response reasonably accurately. However, this study is also constrained by the approximations and assumptions in the numerical model which may induce bias in the results.

7.2.2 Performance Assessment

The response of the structure from the multiplatform simulation is compared with the one from the preliminary investigation in Section 3.4. The structural performance is evaluated both at the global and local levels by reviewing the displacement histories at each storey and the response of the critical element.

7.2.2.1 Global Response of the Structure

The displacement response history at each floor is presented in Figure 7-2. Overall, it can be observed that the results of the preliminary study (noted as reference) where only frame elements were used in OpenSees and the results from the multiplatform simulation are very similar. The modeling approach in the preliminary study underestimates the capacity of the critical specimen resulting in higher displacement demands. The interstorey drift is presented in Figure 7-3 for the case of the multiplatform simulation. It can be observed that the structure exceeds the Life Safety Performance Level as defined in FEMA-356 (FEMA 356 2000).

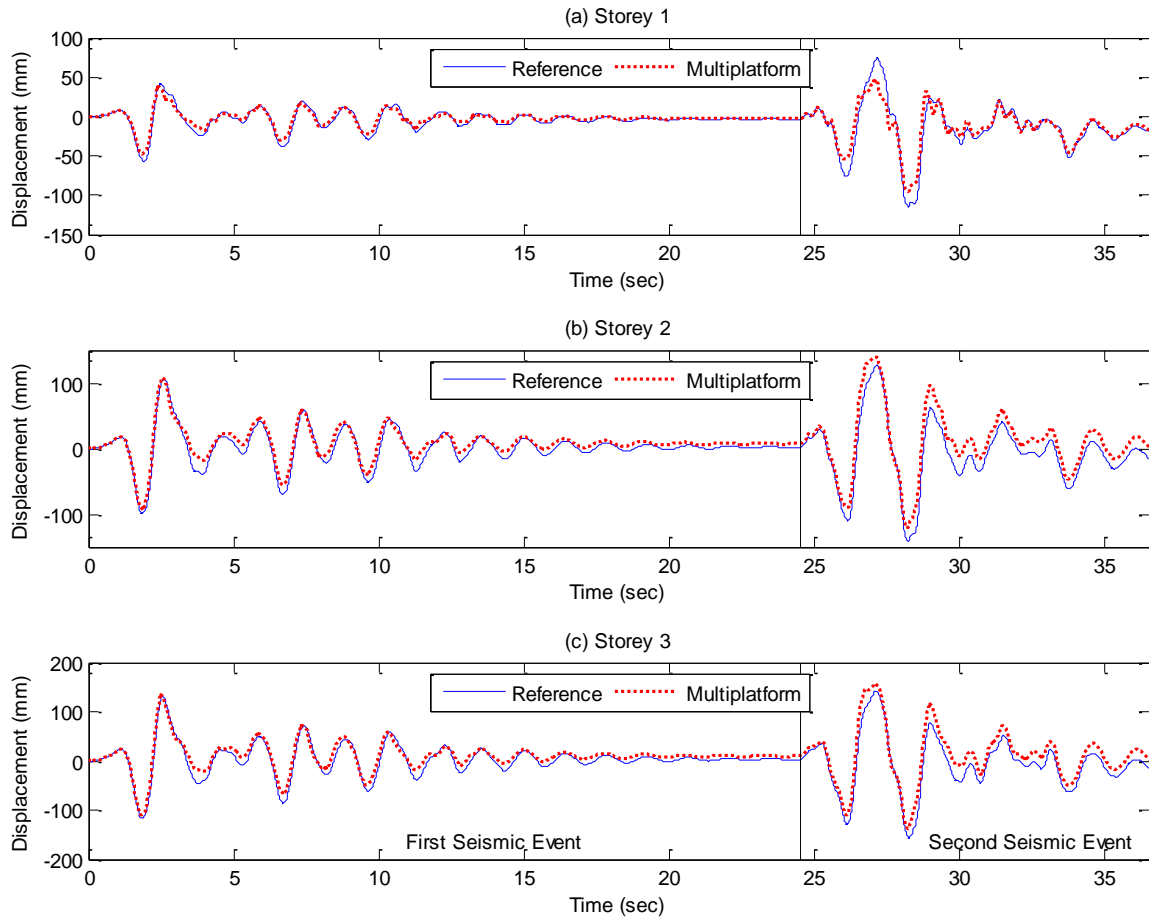


Figure 7-2: Storeys' displacement response history. Multiplatform simulation for intact structure case.

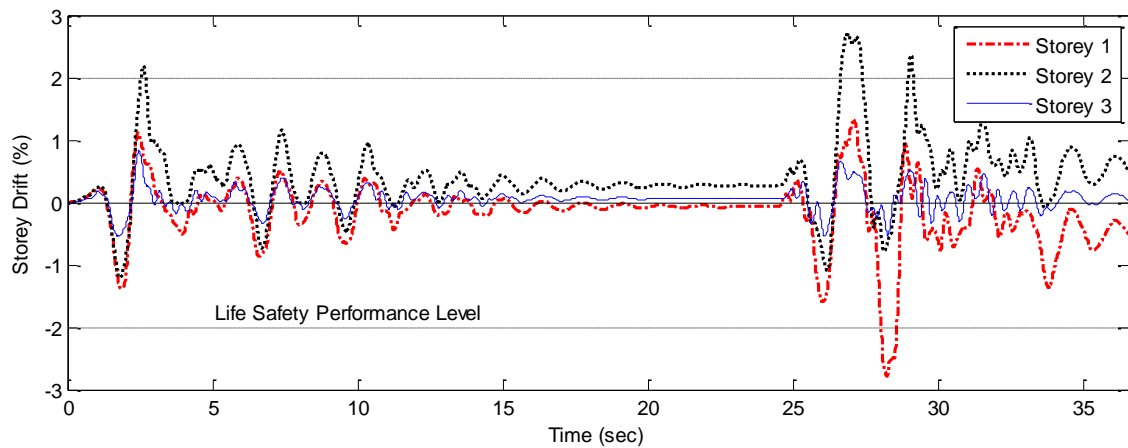


Figure 7-3: Interstorey drifts' response history. Multiplatform simulation for intact structure case.

7.2.2.2 Local Response of the Critical Element

The lateral deformation and shear force histories of the critical element are presented in Figure 7-4. Similar to the global response, the lateral deformation of the critical element from the multiplatform simulation is lower than the reference case. As for the shear response, it can be observed that the shear force from the multiplatform simulation is fluctuating as a result of the disturbed stress zone, where the frame element is transformed in order to be able to connect with the membrane elements. This inconsistency can be identified in Figure 7-5 from the cracks developed into the interface area (column's upper end). The upper set of membrane elements is subjected to inconsistent boundary conditions because of the rigid element used in OpenSees and develop non-realistic stress conditions which result in the force fluctuation introduced above. However, when the displacement is large (i.e. between 2~5 sec and 26~29 sec), it can be observed that the fluctuation is negligible and the shear force matches well with the multiplatform and the reference cases. During the multiplatform simulation the displacement demand observed into the critical specimen was less compared to the preliminary study with OpenSees. This difference is a result of the element modeling technique in OpenSees, which underestimates the stiffness of the specimen as long as it captures only the element's flexural resistance mechanism but not the shear resistance mechanism. On the other side, VecTor2 is developed based on the Modified Compression Field Theory (MCFT) (Vecchio and Collins 1986) and has been proven efficient for capturing the shear response of reinforced concrete elements.

In Figure 7-5 the damage developed in the critical element is presented as it occurred during the multiplatform simulation. The damage is presented at 1) the absolute maximum deformation during the first seismic event, and at 2) the maximum and 3) the minimum deformation during the second seismic event. The results are presented in terms of (a) deformed shape, (b) rebar stresses developed in the cracks and (c) principal compressive stresses in the concrete.

It can be observed that significant flexural cracks, which are accompanied with minor shear cracks, are developed on both sides of the column close to the fixation point, while concrete spalling occurs in the compressive zone during the second seismic event ($t=28.22$ sec). All the rebars yielded in the critical area, and the concrete crushing reached below the depth of the longitudinal reinforcement. Finally, the cracks observed in the top of the element are not realistic and are a result of the disturbed zone that was previously introduced.

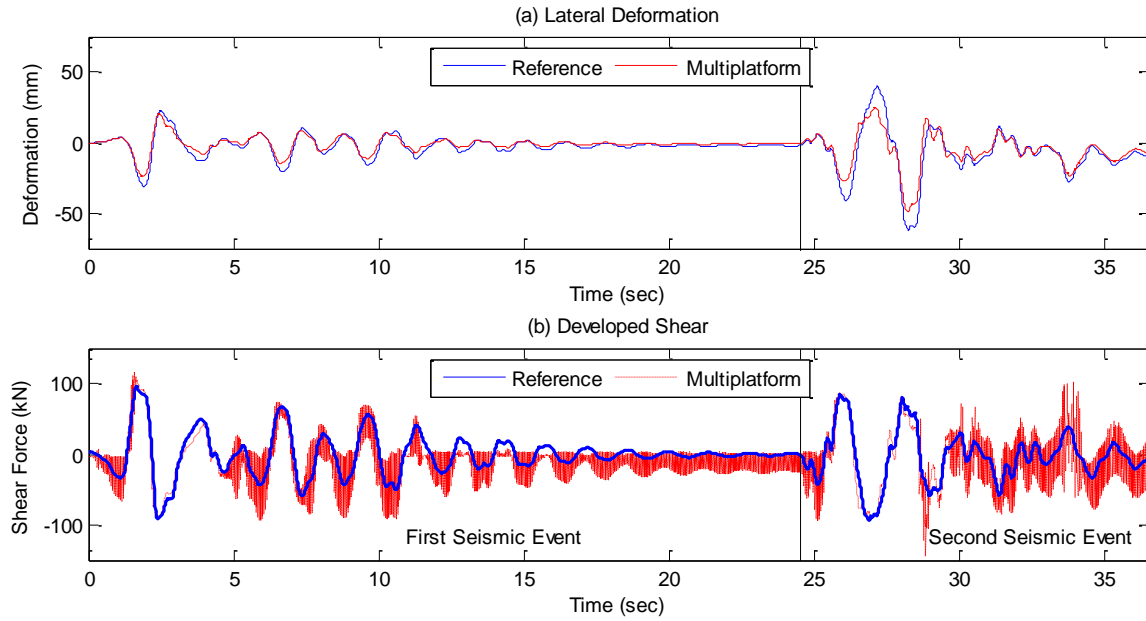


Figure 7-4: Critical element's lateral response. Multiplatform simulation for intact structure case.

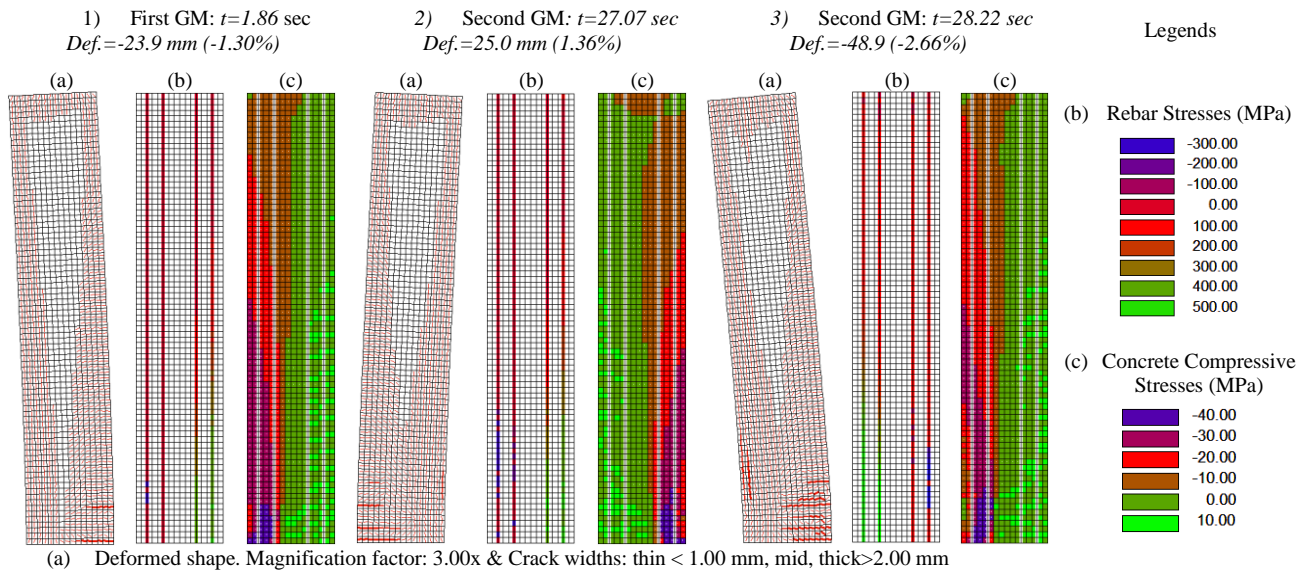


Figure 7-5: Damage developed in the critical column. Multiplatform simulation for intact structure case.

7.3 Intact Structure

The first study case is the intact structure (Table 7-1: Tests 1.2, 1.4 & 2.1). In this case, the numerical model developed in Chapter 3 is used in addition to the intact specimens to perform hybrid simulation. This hybrid simulation was performed twice using the Specimen #1 and #2 to confirm repeatability of the tests and to develop damage in the Specimen #2 equivalent to the one developed in the Specimen #1. The damaged and repaired Specimen #2 is going to be tested later as part of the repaired structure case. The results for the intact structure hybrid simulation case are presented for each specimen separately. Finally, for each case, the hybrid simulation performance is discussed in terms of efficiency related to error compensation steps and slackness tolerance.

7.3.1 Hybrid Simulation using the First Specimen

The Specimen #1 was used for multiple purposes during this study. Initially, a low-intensity hybrid simulation was performed using the first seismic event scaled by a factor of 0.15 for verifying the communication protocols, the transformation schemes and the stability of the hybrid simulation (Table 7-1: Test 1.1). After verifying the testing procedure, the first hybrid simulation was conducted, where the full intensity first seismic event was applied without the free vibration analysis (Table 7-1: Test 1.2). Subsequently, the results of the first test were post-processed in order to evaluate the response of the specimen and the consistency of the hybrid simulation. Finally, before performing the remaining hybrid simulation (free vibration analysis and second seismic event, Table 7-1: Test 1.4), the investigation on the axial displacement control was conducted (Table 7-1: Test 1.3). The two tests were performed on different days by developing the required feature in NICON for restoring a previous hybrid simulation at the last performed analysis step. The hybrid simulation with the Specimen #1 was conducted with some inconsistency related to the measured material properties. This inconsistency is discussed in the next section.

7.3.1.1 Material and Simulation Inconsistencies

The material properties were measured one day before all hybrid simulations using concrete cylinders in order to update the numerical models with the most up-to-date material properties accounting for the concrete curing. However, before the first hybrid simulation, simple compressive strength tests were conducted instead of the full stress-strain tests that were performed for the rest of the hybrid simulations. The compressive strength tests were performed with a lower accuracy testing setup and resulted in slight overestimation of the concrete compressive strength. The concrete properties used for the first hybrid simulation are presented in Table 7-3. This inconsistency led to the development of a numerical model with slightly different properties than the physical specimen's ones. This difference induced an additional error in the numerical model and the hybrid simulation with the Specimen #1, which is not considered as reliable as the one with the Specimen #2. Additionally, the fact that the first hybrid simulation was performed on two different days with the axial response investigation in between, challenges the reliability of the first hybrid simulation because relaxation and creep may have developed in the specimen. However, these inconsistencies do not apply for the Specimen #2 because the material properties were properly defined in the numerical model and the hybrid simulation was performed once for the full seismic study sequence.

Table 7-3: Mechanical properties of concrete materials used for the hybrid simulations with Specimen #1.

Material Type	Compressive Strength f'_c (MPa)	Concrete Peak Strain ϵ_{co} (mm/mm)	Elasticity Modulus E (MPa)	Concrete Ultimate Strain ϵ_{cu} (mm/mm)
Correct Properties	39	0.0024	29,557	0.02 [†]
1 st Hybrid Simulation Properties	41.2	0.0019	30,365	

[†] The concrete ultimate strain was set equal to 0.02 in OpenSees to avoid numerical instabilities

Table 7-4: Hybrid simulation performance for the intact structure case using the Specimen #1 (Tests 1.2 & 1.4).

	Analysis Steps	Error Compensation Steps	Test duration	Axial Slackness Tolerance (mm)	Lateral Slackness Tolerance (mm)
First Part (Test 1.2)	1,452	3,115	5 hrs 46 min	0.1 [†]	0.2 [†]
Second Part (Test 1.4)	2,200	1,830	4 hrs 7 min	0.15 [†]	0.3 [†]

[†] The tolerance were modified when required for reducing the error compensations steps requirements.

7.3.1.2 Hybrid Simulation Performance

As already discussed, the first hybrid simulation was performed in two parts: the first and the second seismic events (Table 7-1: Tests 1.2 and 1.4). During the first section of the test (Test 1.2) the error compensation steps required were 2.14 per analysis step, while the lapsed time for performing 1,452 analysis steps was 5 hours and 46 minutes as presented in Table 7-4. The axial and lateral slackness tolerances were set equal to 0.1 and 0.2 mm, respectively, resulting in a significant number of error compensation steps. However, this level of accuracy was proven unrealistic given the resolution of the available instrumentation. Thus, in the second test (Test 1.4) the tolerances were increased to 0.15 and 0.3 mm for the axial and lateral deformation, respectively. This modification resulted in a significantly lower error compensation step requirement, i.e. on average 0.83 error compensation steps per analysis time step were required, and the test duration was reduced to 4 hours and 7 minutes for 2,200 analysis steps. Given this response, in addition to the results of the hybrid simulation, it can be understood that the second section of the test is more robust than the first. Finally, it should be recalled that the I-modification was deactivated during the second part of the test as discussed in Section 6.4.

7.3.1.3 Global Response of the Structure

The global response during the hybrid simulation is presented in Figure 7-6 and Figure 7-7 in terms of the displacement and interstorey drift histories. Beyond the preliminary reference study and the experimental response, the numerical WCHS is presented. In this way, the difference induced by the approximation of the methodology can be identified by comparing the reference with the WCHS numerical case, while the difference induced by the experimental response can be identified by comparing the experiment case with the WCHS numerical case. From the experimental response, it can be observed that the structure exceeds the Life Safety Performance Level as predicted from the preliminary investigation. The response is compared quantitatively to the remaining cases in Section 7.7.

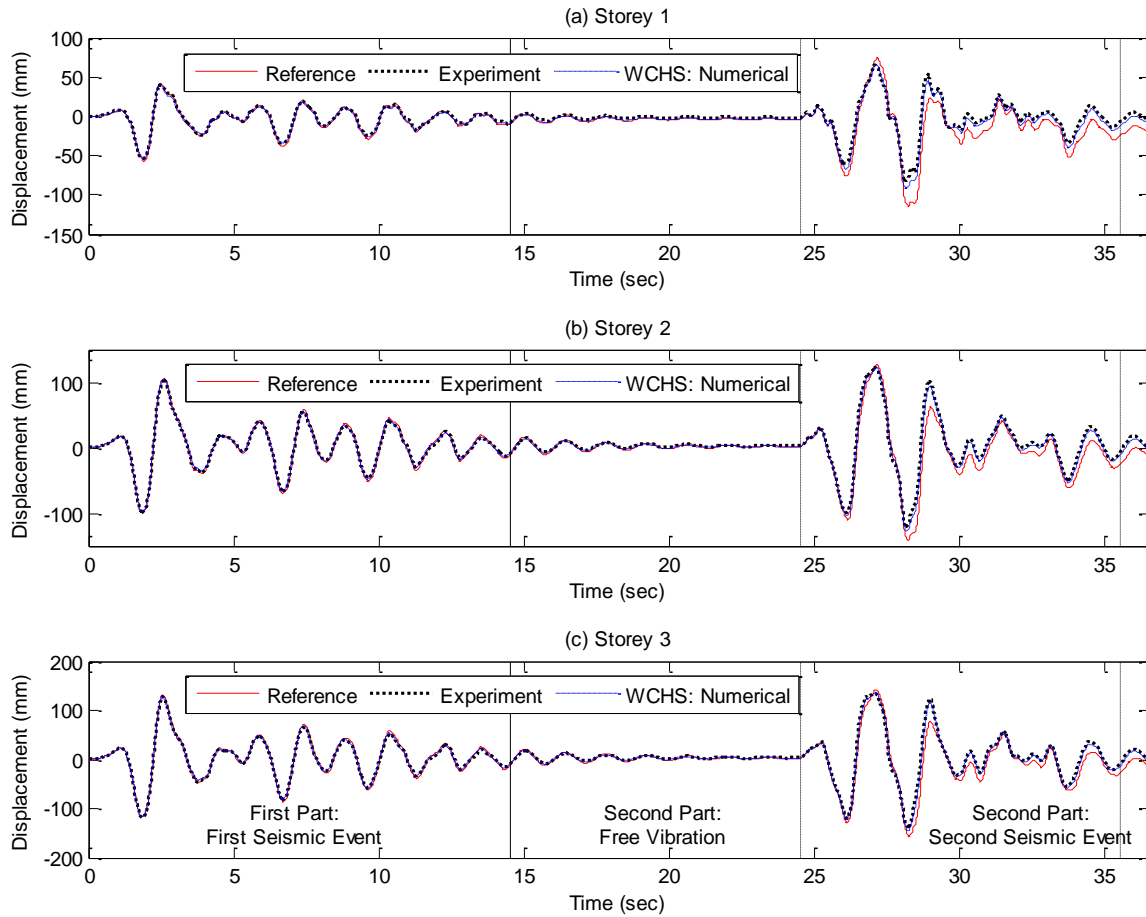


Figure 7-6: Storeys' displacement response history. Hybrid simulation for the intact structure case using the first specimen (Tests 1.2 & 1.4).

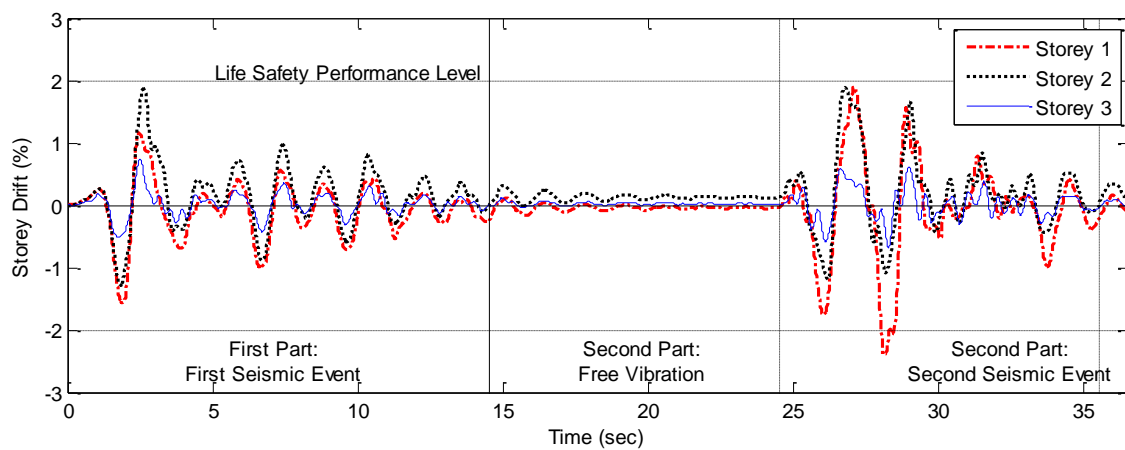


Figure 7-7: Interstorey drifts' response history. Hybrid simulation for the intact structure case using the first specimen (Tests 1.2 & 1.4).

7.3.1.4 Local Response of the Critical Element

Similar to the global response, the local responses from the reference, the experiment, and the WCHS: Numerical cases are presented in this section. The axial and lateral deformation response history is presented in Figure 7-8, while the corresponding restoring forces are shown in Figure 7-9. The axial response inconsistency observed in the local response figures has been extensively discussed in Section 6.4. The lateral response matches well with the reference and the WCHS: Numerical case. The observed difference is primarily induced by the approximate nature of the proposed methodology and mainly occurs during the second seismic event. For the maximum lateral deformation ($t=28.22$ sec) a significant difference is noted between the experimental and the WCHS numerical case which is due to the inconsistencies in the material properties discussed in Section 7.3.1.1. Additionally, due to the material properties' inconsistencies, it can be observed that higher shear forces were developed in the physically tested specimen despite the fact that the lateral deformation during the experimental study is lower compared to the other two cases. The same response can be identified from the hysteresis curve of the critical specimen in Figure 7-10.

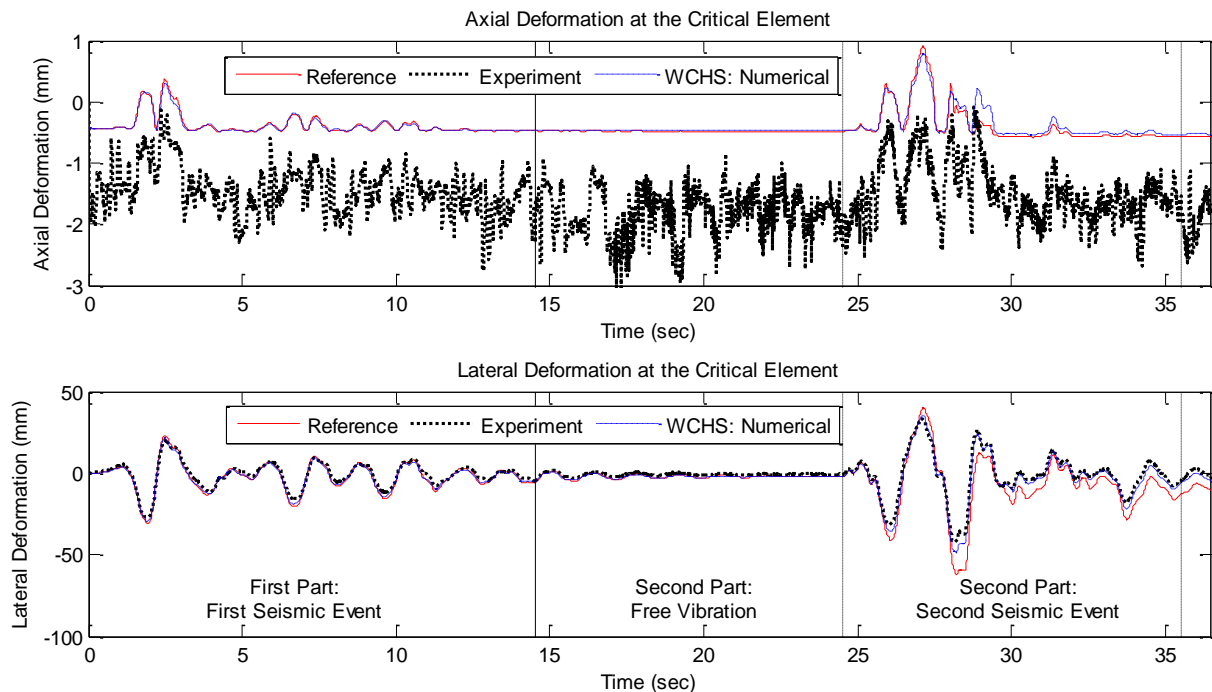


Figure 7-8: Critical element's deformation response history. Hybrid simulation for the intact structure case using the Specimen #1 (Tests 1.2 & 1.4).

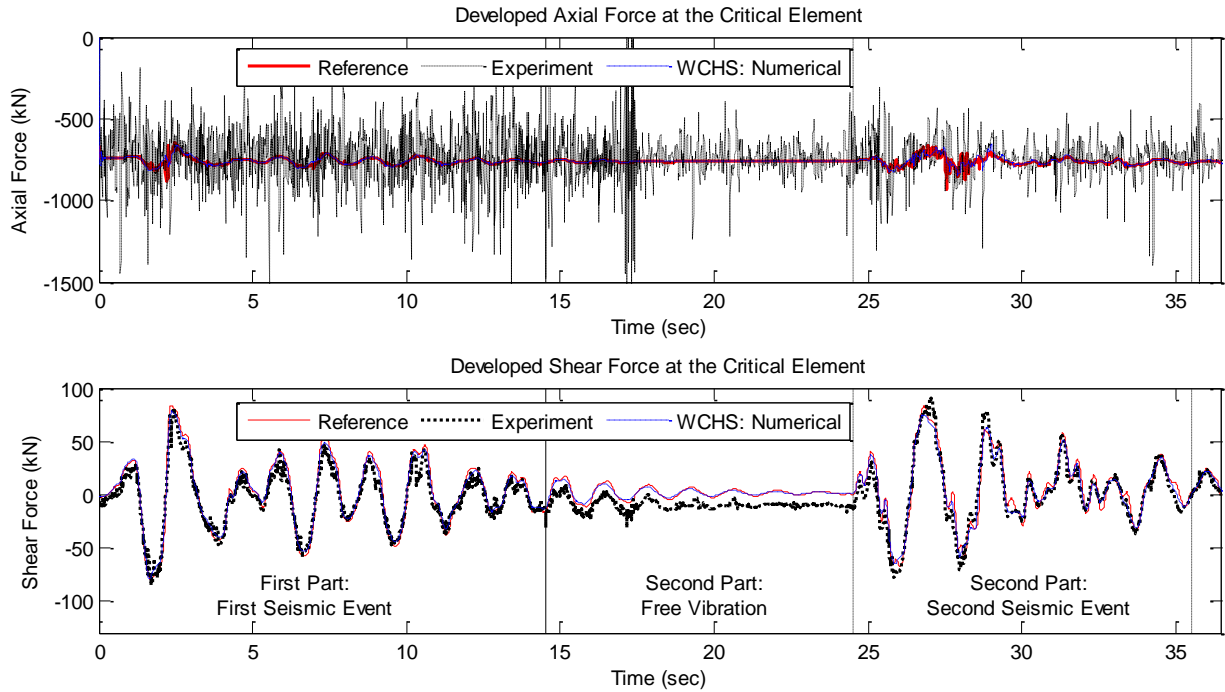


Figure 7-9: Critical element's developed forces response history. Hybrid simulation for the intact structure case using the Specimen #1 (Tests 1.2 & 1.4).

The hysteretic response of the critical element is presented in Figure 7-10, first for the full test and subsequently divided into four equal time intervals for clarity. It can be observed that during the first three time intervals, the matching among the three cases is satisfying both in terms of lateral deformation and shear force development, while during the last time interval, the lateral deformation and the shear forces inconsistencies are developed. This response was improved for the Specimen #2, where a more realistic numerical model was employed. However, this response demonstrates the effect that the modeling of the critical element's response affects the performance assessment of the structure. Finally, the energy dissipation as calculated from the hysteresis loops is presented in Figure 7-11. It can be observed that the energy dissipation during the experiment is almost identical to the reference case. However, as it will be shown in the next experimental cases, the energy dissipation in the critical element during the experimental investigation is higher than that for the numerical cases because complex damage mechanisms, such as the shear response or the bond degradation, are captured during the experimental investigation. As a result, the energy dissipation cannot be used as an index for comparing the weakly-coupling methodology performance between the numerical and experimental investigation.

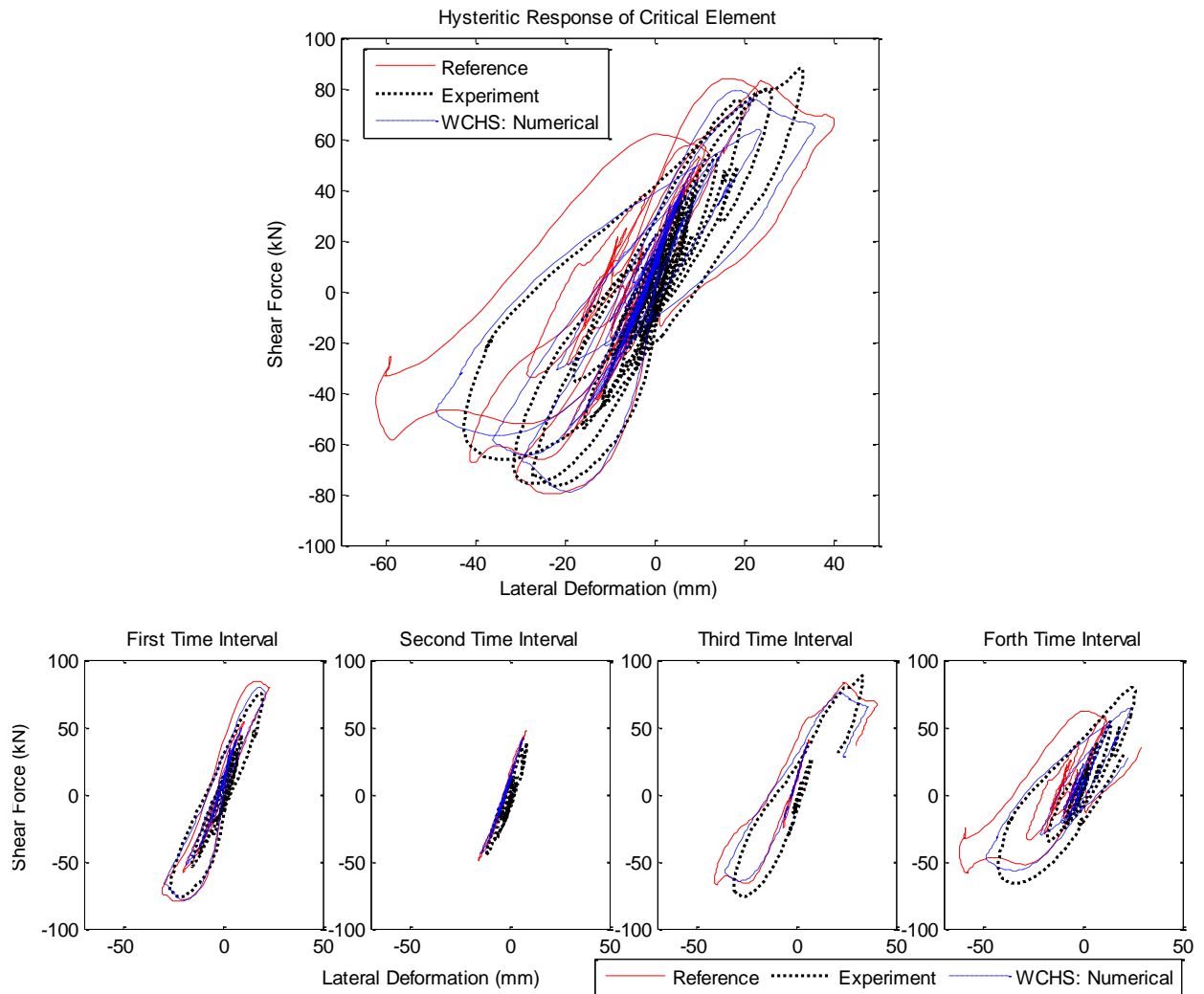


Figure 7-10: Critical element's hysteretic response presented for the full test (upper figure) and separated to four equal time intervals for clarity (lower figures).

Hybrid simulation for the intact structure case using the Specimen #1 (Tests 1.2 & 1.4).

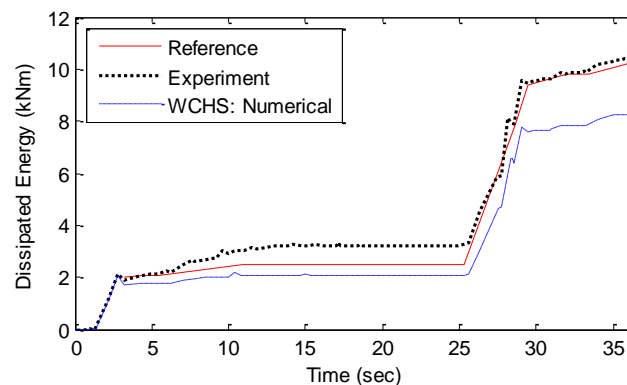


Figure 7-11: Dissipated energy in the critical element using the shear force – lateral deformation hysteretic response. Hybrid simulation for the intact structure case using the Specimen #1(Tests 1.2&1.4).

In Figure 7-12 the moment-curvature relationship of the experimentally tested specimen as measured in three locations from the LVDTs is presented. It can be observed that the stub influences the column's response and offsets the damage in the second spiral hoop (222 mm), which is the location of the greatest curvature development. The damage in the specimen after the end of the second hybrid simulation part (second seismic event) is presented in Figure 7-13. It can be seen that the developed damage is in good agreement with the prediction during the multiplatform simulation. It should be stated that the crack widths illustrated in Figure 7-13 are after the end of the hybrid simulation. Finally, all the longitudinal bars had yielded while the spirals were in the elastic range.

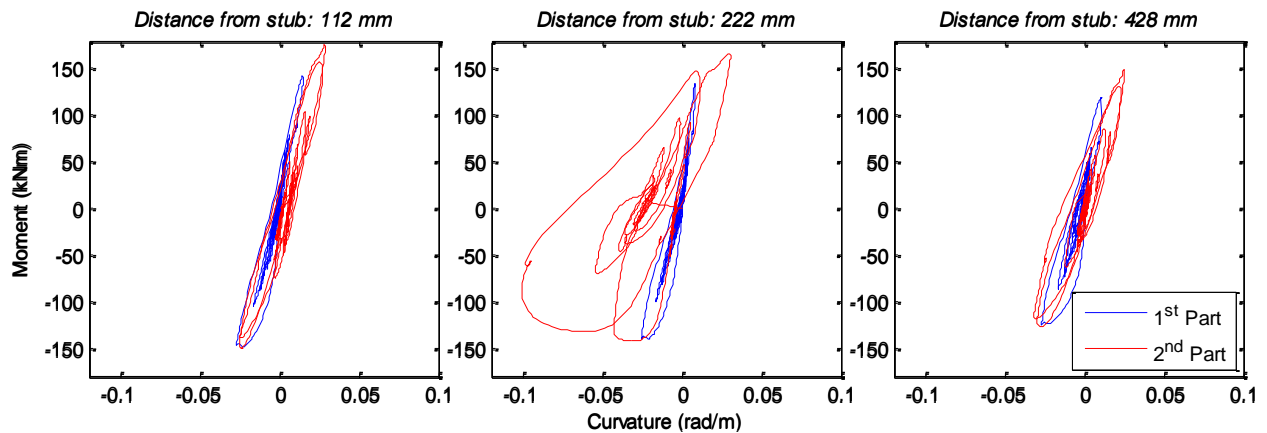


Figure 7-12: Moment-curvature relationship at the critical region. Hybrid simulation for the intact structure case using the Specimen #1 (Tests 1.2 & 1.4).

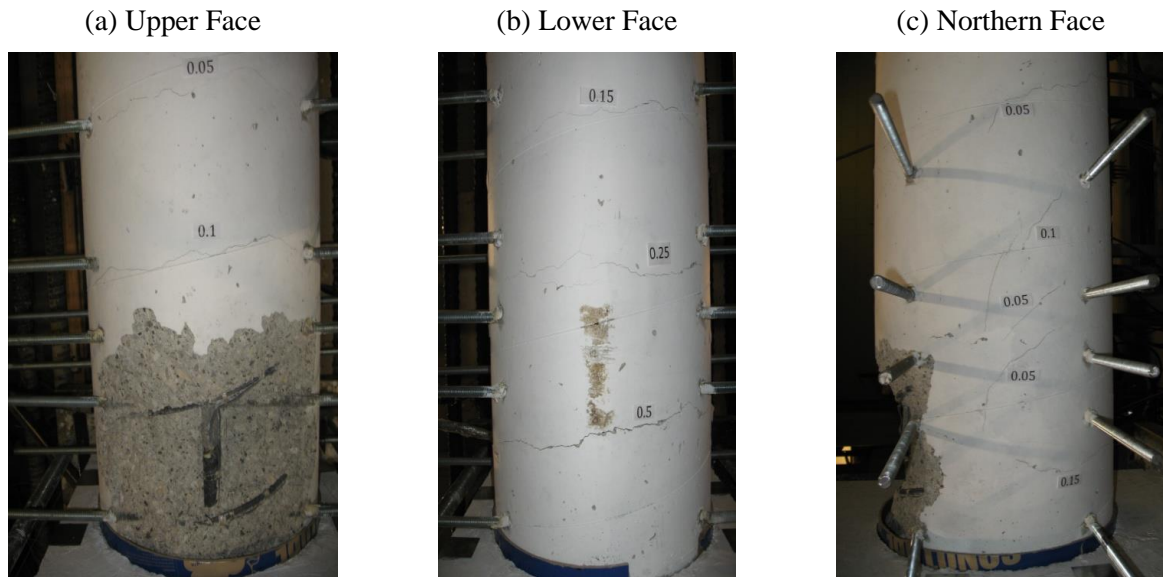


Figure 7-13: Damage developed on the specimen after the second earthquake event (cracks' widths in mm). Hybrid simulation for the intact structure case using the Specimen #1 (Tests 1.2 & 1.4).

7.3.2 Hybrid Simulation using the Second Specimen

The hybrid simulation for the intact case structure was replicated using the Specimen #2 (Test 2.1). For this case, the material properties of the numerical model were redefined to be consistent with the material properties of the specimen, and the hybrid simulation was performed once for the full study seismic sequence. The results in this section are presented in the same sequence as for the previous test.

7.3.2.1 Hybrid Simulation Performance

For the second hybrid simulation, an additional feature was developed in NICON which allowed for the tuning of the error compensation scheme during the test. This resulted in a requirement of one error compensation step per analysis step and required 7 hours and 26 minutes to perform 3,652 analysis steps as shown in Table 7-5. Additionally, for this test, the axial and lateral slackness tolerances were set to 0.15 and 0.3 mm, respectively and remained as such for the rest of the tests. This response constitutes a significant improvement compared to the first test.

7.3.2.2 Global Response of the Structure

The global response during the second hybrid simulation (Test 2.1) is presented in Figure 7-14 and Figure 7-15 in terms of the displacements and interstorey drift histories of each storey. The results of the reference numerical study performed in OpenSees standalone and the numerical weakly-coupled investigation are also included in the figures in order to understand the difference developed due to the methodology's approximation and due to the experimental response. Similar to the previous cases, the structure exceeds the Life Safety Performance Level, and the higher drift requirement is observed in the first storey.

Table 7-5: Hybrid simulation performance for the intact structure case using the Specimen #2 (Test 2.1).

	Analysis Steps	Error Compensation Steps	Time	Axial Slackness Tolerance (mm)	Lateral Slackness Tolerance (mm)
Intact Structure					
2 nd Specimen (Test 2.1)	3,652	3,632	7 hrs 26 min	0.15 [†]	0.3 [†]

[†] The tolerance were modified when required for reducing the error compensations steps requirements.

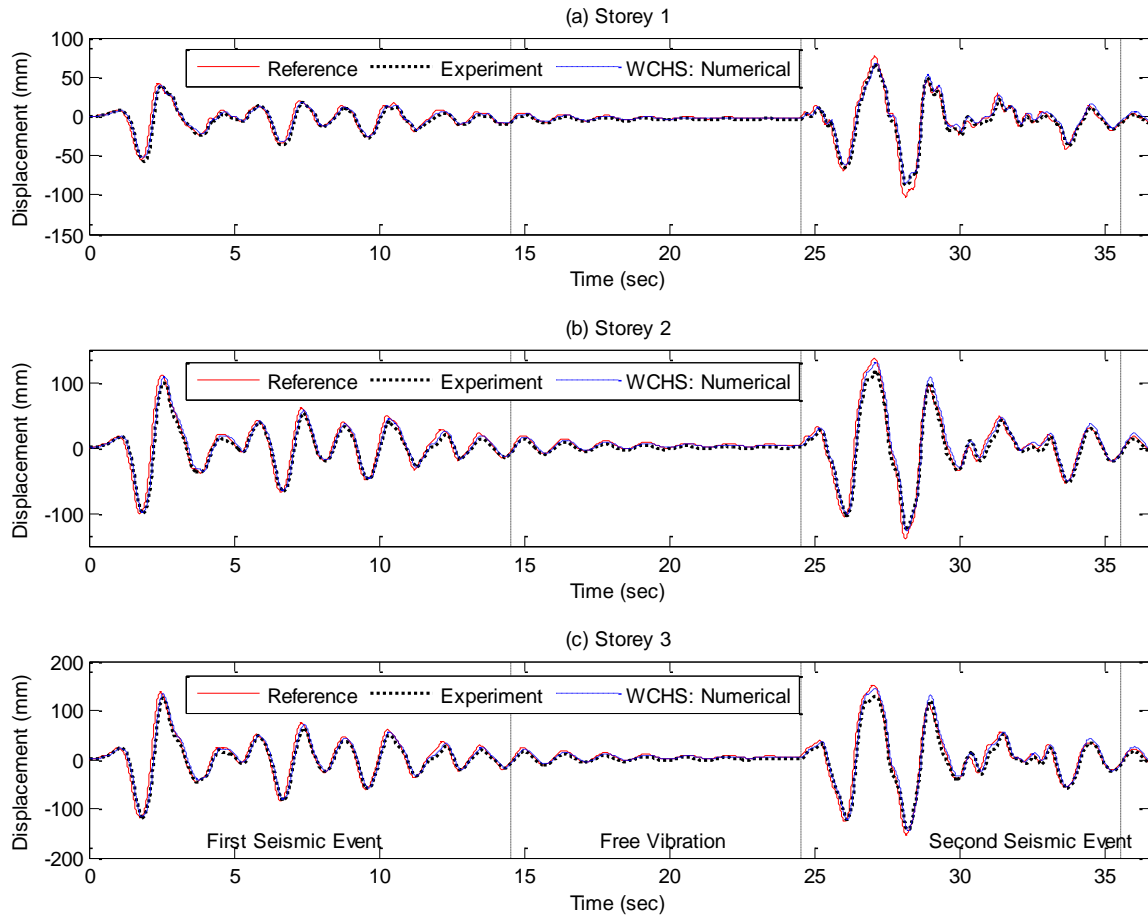


Figure 7-14: Storeys' displacement response history. Hybrid simulation for the intact structure case using the Specimen #2 (Test 2.1).

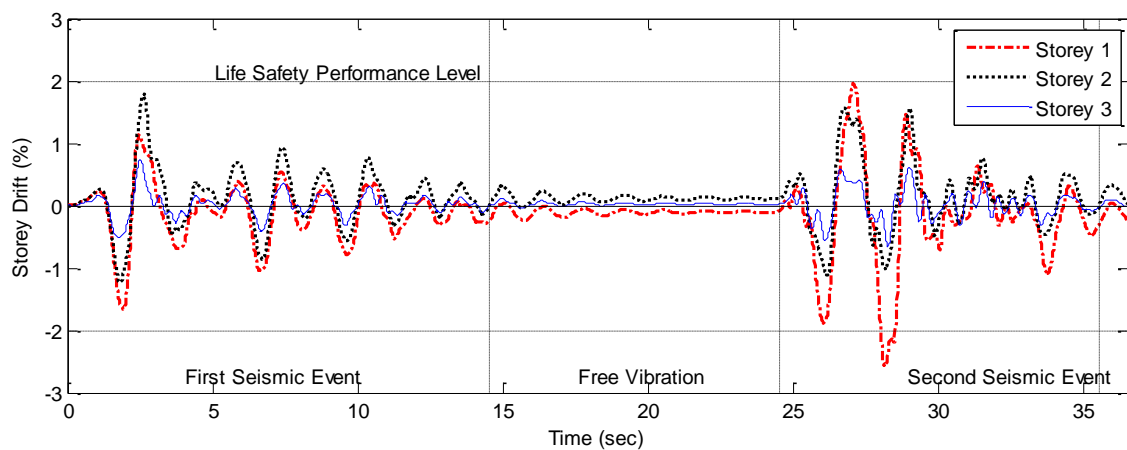


Figure 7-15: Interstorey drifts' response history. Hybrid simulation for the intact structure case using the Specimen #2 (Test 2.1).

7.3.2.3 Local Response of the Critical Element

The axial and lateral deformation response histories are presented in Figure 7-16 and the restoring forces are presented in Figure 7-17. The overall response is similar to the previous case. The axial response experiences similar inconsistencies as the previous case and no further improvement could be achieved for this study. However, the fact that the I-modification was deactivated resulted in less fluctuation in the axial direction compared to the first part of the hybrid simulation conducted with the Specimen #1. The lateral response is improved compared to the first test as a result of the properly defined material properties in the numerical model. This improvement can be better identified from the hysteretic response of the experimentally tested specimen which is presented in Figure 7-18. It can be observed that compared to the experimental values, slightly smaller shear forces are developed in the weakly-coupled cases as a result of the methodology's approximation.

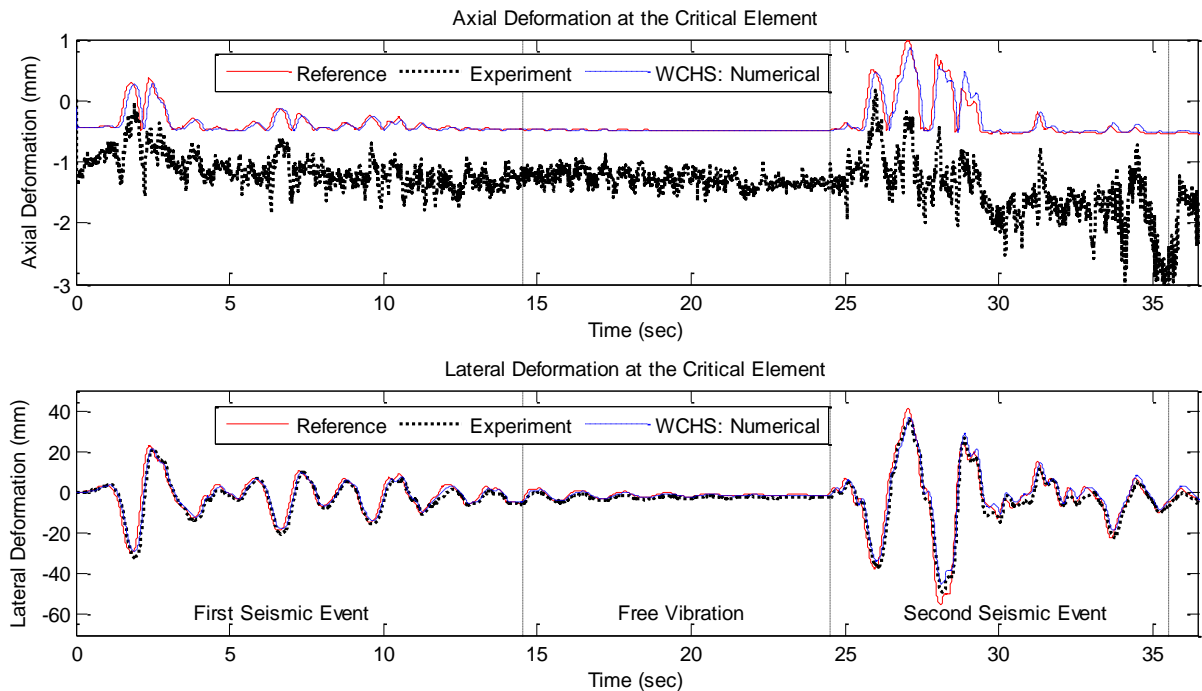


Figure 7-16: Critical element's deformation response history. Hybrid simulation for the intact structure case using the Specimen #2 (Test 2.1).

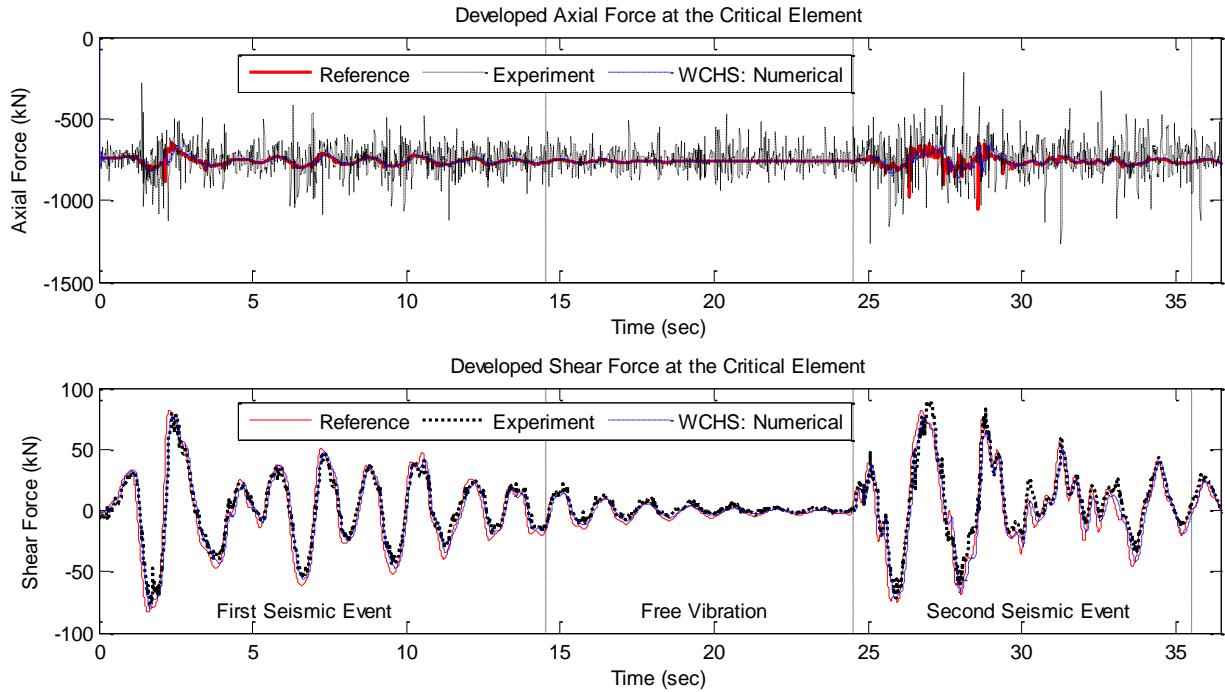


Figure 7-17: Critical element's developed forces response history. Hybrid simulation for the intact structure case using the Specimen #2 (Test 2.1).

The most significant difference is the energy dissipation that occurs during the experimental investigation which can be observed from the hysteretic response figure and is presented in Figure 7-19. The physical specimen develops damage mechanisms that are not able to be captured in the numerical model, and there is significant plastic deformation developed in the critical area of the specimen, mainly during the second seismic event. This response can be identified from the moment-curvature and shear force-shear strain responses presented in Figure 7-20 and Figure 7-21 respectively. The moment-curvature response is measured in three locations of the critical area, and it can be observed that the damage is offset from the column stub interface similar to the first hybrid simulation, as a result of the influence of the stub stiffness to the column. From the shear response, it can be observed that most of the shear deformation occurs at the peak lateral deformation and is developed with an equivalent shear-yielding mechanism. However, this stage is not considered close to a shear failure ($\tau_{yield}=0.014 \text{ mm/mm}$).

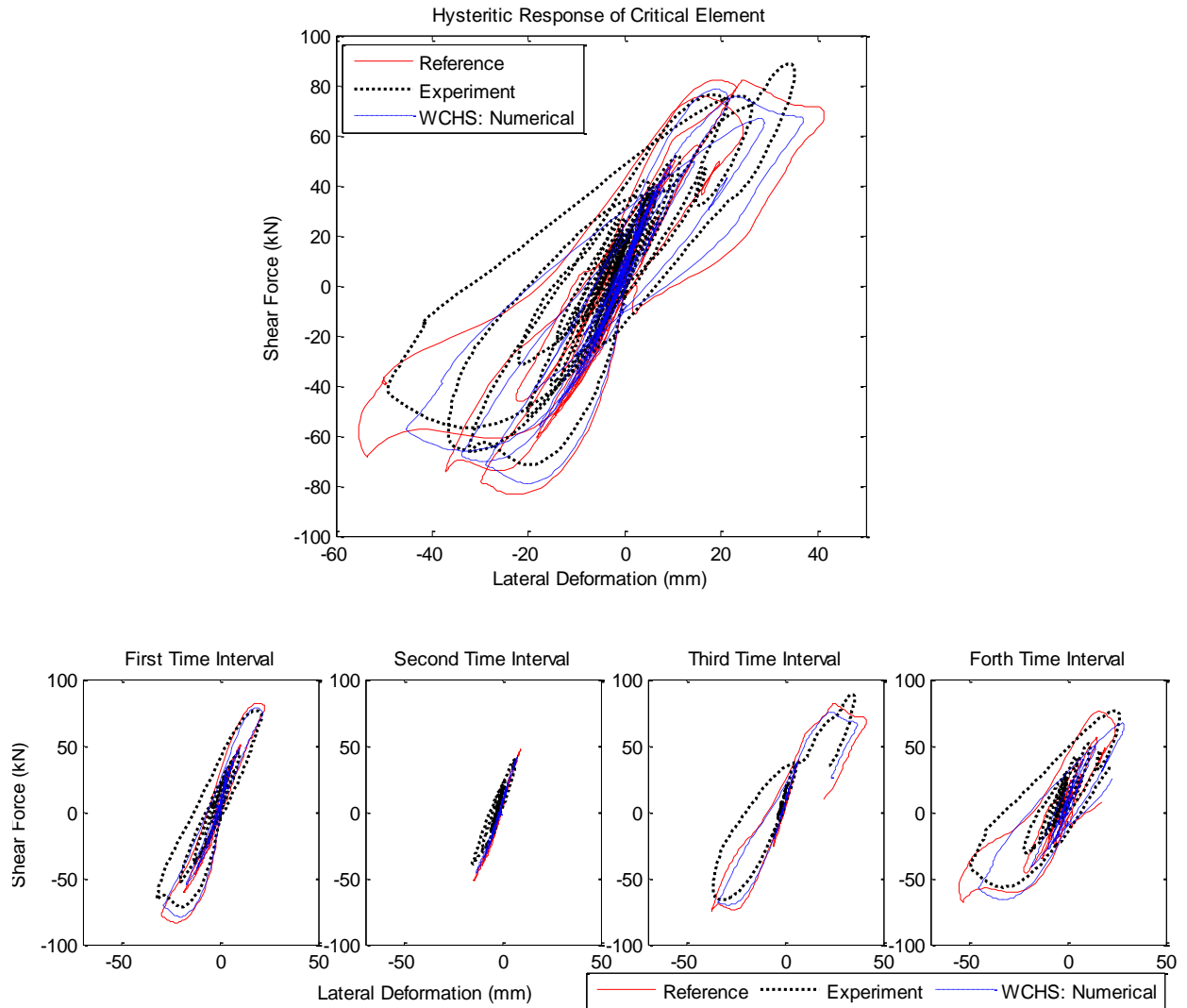


Figure 7-18: Critical element's hysteretic response presented for the full test (upper figure) and separated to four equal time intervals for clarity (lower figures).

Hybrid simulation for the intact structure case using the Specimen #2 (Test 2.1).

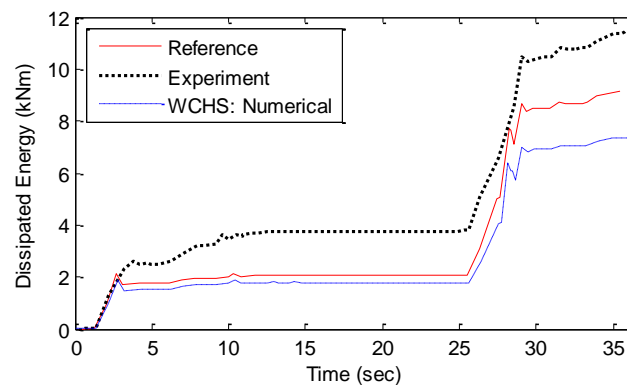


Figure 7-19: Dissipated energy in the critical element using the shear force – lateral deformation hysteretic response. Hybrid simulation for the intact structure case using the Specimen #2 (Test 2.1).

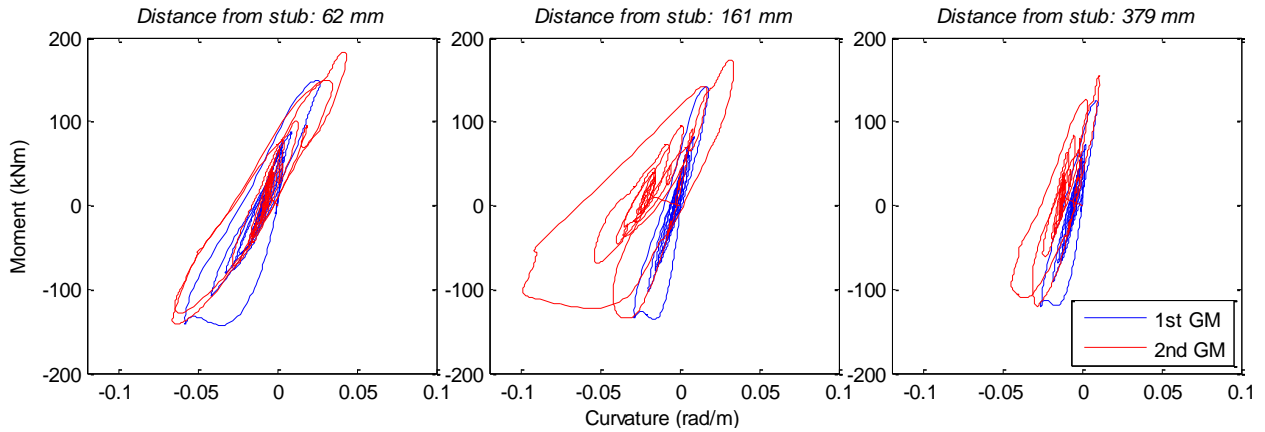


Figure 7-20: Moment-curvature relationship at the critical region. Hybrid simulation for the intact structure case using the Specimen #2 (Test 2.1).

Finally, the damage developed on the specimen as measured at the end of the hybrid simulation is presented in Figure 7-22. The developed damage is consistent with the multiplatform simulation and the first hybrid simulation (Tests 1.2 & 1.4) but can be described as more extensive compared to the one developed in the Specimen #1. More specifically, concrete crushing up to a depth below the longitudinal reinforcing occurred in the upper face at the maximum lateral deformation. The residual flexural cracks were up to 0.65 mm wide, while some minor residual shear cracks were observed on the side surfaces (0.15 mm). All the longitudinal bars and to the spiral were yielded. It should be recalled that for the Specimen #1, no yielding occurred in the spiral, suggesting that the damage developed in the Specimen #2 was greater than the one of the Specimen #1.

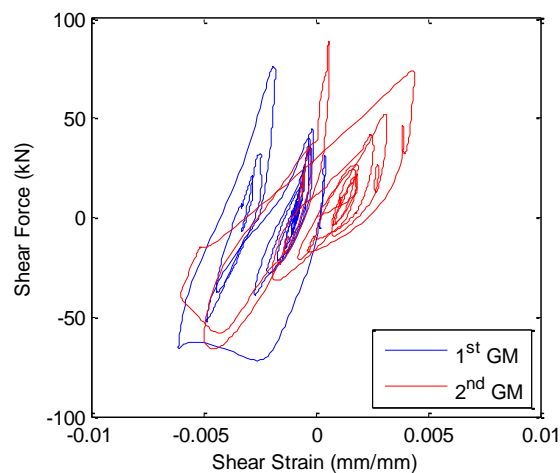


Figure 7-21: Shear force – shear strain relationship at the critical region. Hybrid simulation for the intact structure case using the Specimen #2 (Test 2.1).

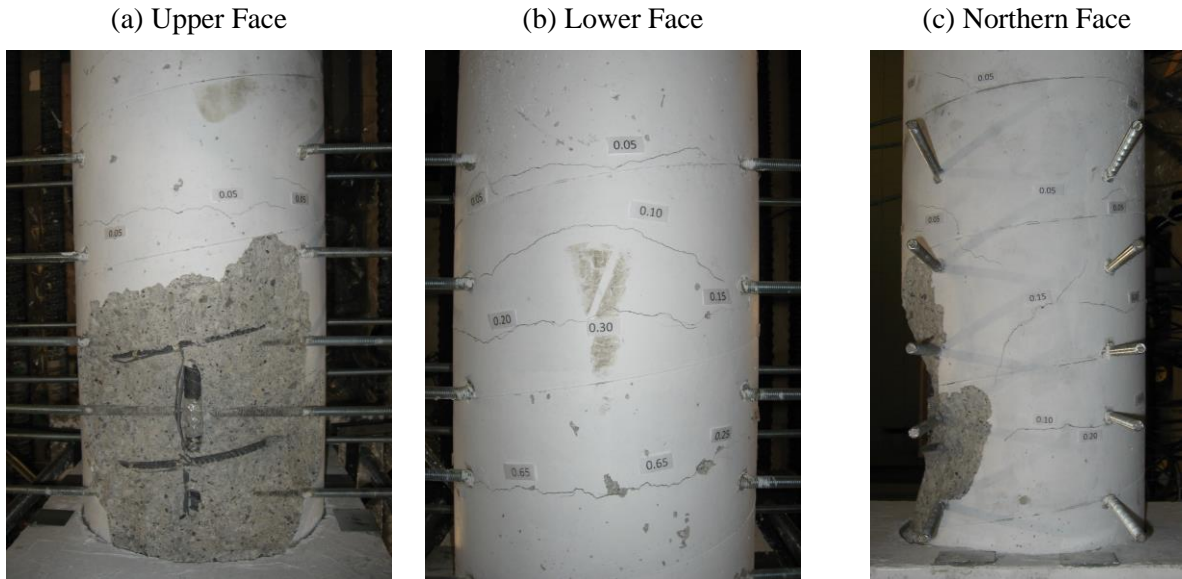


Figure 7-22: Damage developed on the specimen after the second earthquake event (cracks' widths in mm). Hybrid simulation for the intact structure case using the Specimen #2 (Test 2.1).

7.4 Repaired Structure

In this section, the response of the repaired structure during the seismic study sequence is investigated using the proposed WCHS approach. For the seismic performance assessment of a repaired structure using hybrid simulation (Test 2.2), the development of the model for the numerically assessed part of the structure is of significant uncertainty. A repaired element develops various mechanisms that contribute to its response, with the most important ones being the bond development between the healthy concrete and the repair mortar as well as the confinement effect of the applied FRP, which is significantly influenced by the level of the damage prior to the repair. Due to these uncertainties, the calibration of the numerical model with experimental results may be considered necessary for cases where repaired elements are numerically modeled.

In the current study, the developed numerical model for the repaired structure is calibrated using the experimental response of the first repaired specimen as recorded during the quasi-static cyclic test (Section 7.8.1, Table 7-1: Test 1.4). All the columns of the structure are assumed to have been repaired using the procedure discussed in Chapter 4 and the constitutive model mentioned above was employed for all of them. The physical specimen employed for the hybrid simulation of a repaired structure was the Specimen #2 after its hybrid simulation as part of an intact structure (Test 2.1) and its repair with the same technique employed for the Specimen #1. No specific care was taken for the beams, and the same constitutive model as with the intact structure case was employed. The calibrated numerical model for the repaired columns is presented in the next section. However, the use of the same calibrated numerical model for all the columns of the repaired structure is not considered realistic due to the fact that response of different repaired columns is related to the level of their damage during the first seismic sequence excitation and their axial load during the applied excitation.

7.4.1 Numerical Model Calibration

The constitutive law employed in OpenSees for the numerical model of the columns for the repaired case structure is presented in Figure 7-23 in addition to the experimental response during the quasi-static cyclic test (Test 1.4) of the repaired Specimen #1 that was used for the model's calibration. First of all, it can be observed that the response during the quasi-static cyclic test is not symmetric. This asymmetric response is a result of the different damage levels developed at the upper and lower column surfaces prior to the repair because of the different lateral deformation levels, and the difference in the repair mortar strength compared to the concrete's strength.

The calibrated model was defined in order to match the response in the repaired face (with more severe damage) of the specimen as presented in Figure 7-23. This calibration was proven unrealistic as the numerical model overestimates the capacity of the repaired physical specimen and, as a result, significant inconsistencies were developed during the hybrid simulation for the repaired structure case (Test 2.2). This inconsistency was intensified because of the fact that the Specimen #2 developed greater damage than the Specimen #1 during the hybrid simulation of the intact structure case. This inconsistency demonstrates the challenges related to the numerical modeling of elements whose response is of considerable uncertainty and the efficiency of hybrid simulation for capturing the critical element's response realistically.

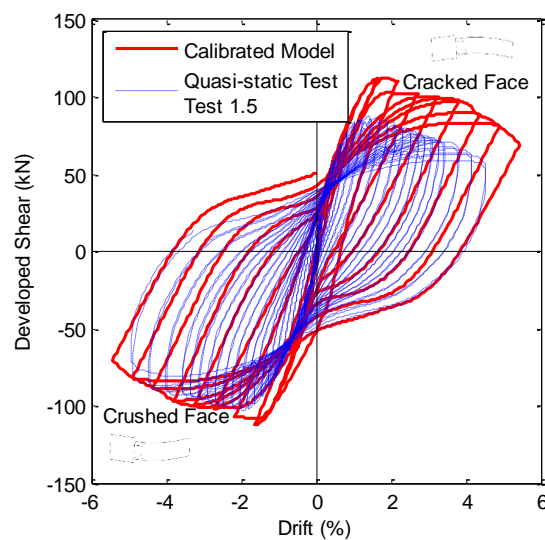


Figure 7-23: Calibrated numerical model for the columns of the repaired case structure.

7.4.2 Hybrid Simulation Performance

During the hybrid simulation performed for the repaired case structure (Test 2.2), nearly 1.4 error compensation steps were required per analysis step, while the required time for performing 3,652 analysis steps was 7 hours and 20 minutes as presented in Table 7-6. Similar to the previous test, the axial and lateral slackness tolerances were set at 0.15 and 0.3 mm. This response is slightly inferior compared to the response during the second hybrid simulation (Test 2.1) for the intact case structure, where one error compensation step was required per analysis step. This difference is attributed to the error compensation convergence tuning performed by the user during the hybrid simulation and to the damaged and repaired state of the specimen.

7.4.3 Global Response of the Structure

The global response during the hybrid simulation of the repaired structure is presented in Figure 7-24 and in Figure 7-25 in terms of storeys' displacements and interstorey drifts, in addition to the results of the reference and the WCHS numerical case. The overall structure's responses match well between the experimental and numerical tests, but higher deformation demands are observed during the experimental investigation, the observation that is contradictory to the WCHS numerical case. This response reveals the already introduced inconsistency related to the numerical model calibration, and it can be claimed that the numerical model overestimated the capacity of the repaired columns. From the interstorey drifts presented in Figure 7-25 it can be observed that the response of the structure is slightly below the Life Safety Performance Level. However, given the overestimation of the first storey column's capacity and the local response of the critical element, the performance level can be considered to exceed the Life Safety limit (Table 7-9). For this case, a distributed hybrid simulation, where all the first-floor columns would be experimentally modeled, could result in a more realistic assessment of the structure's seismic performance.

Table 7-6: Hybrid simulation performance for the repaired structure case using the repaired Specimen #2 (Test 2.2).

	Analysis Steps	Error Compensation Steps	Time	Axial Slackness Tolerance (mm)	Lateral Slackness Tolerance (mm)
Repaired Structure					
2 nd Specimen (Test 2.2)	3,652	5,220	7 hrs & 20 min	0.15 [†]	0.3 [†]

[†] The tolerance were modified when required for reducing the error compensations steps requirements.

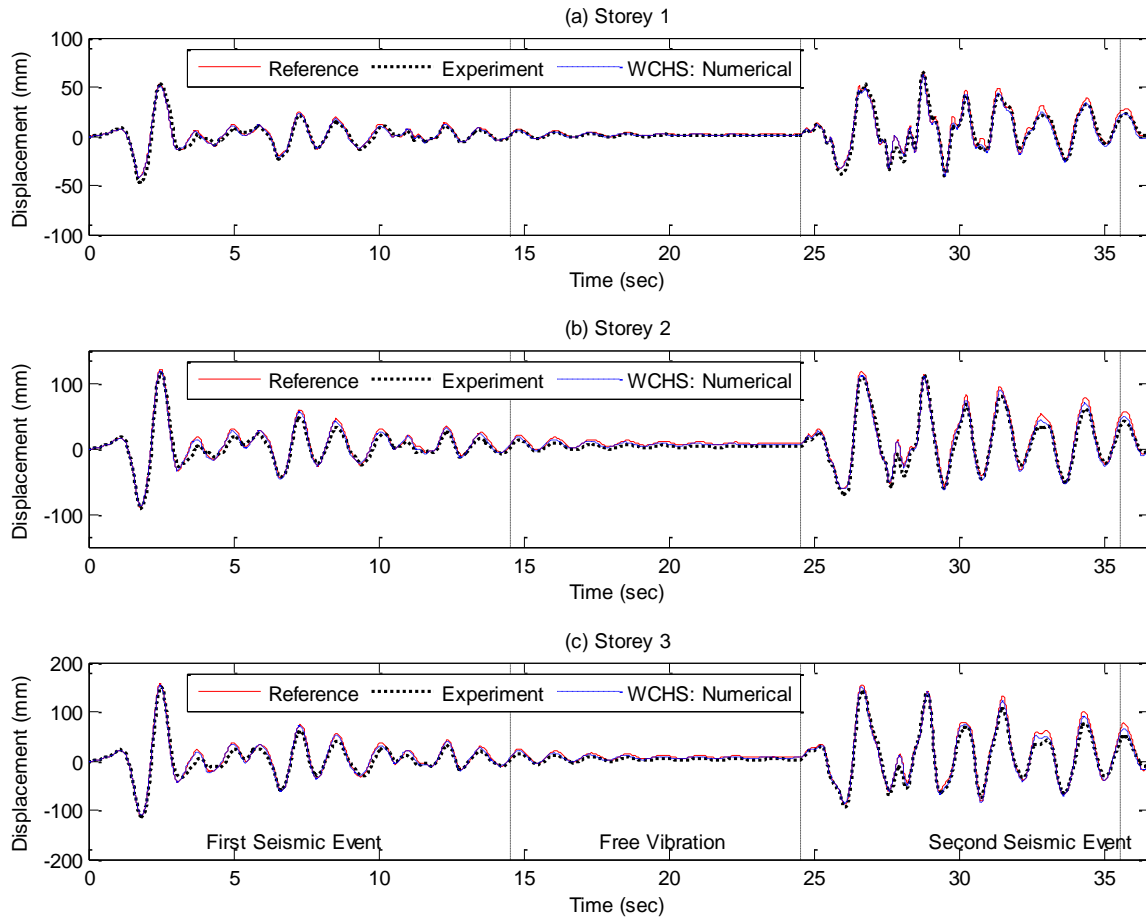


Figure 7-24: Storeys' displacement response history. Hybrid simulation for the repaired structure case using the repaired Specimen #2 (Test 2.2).

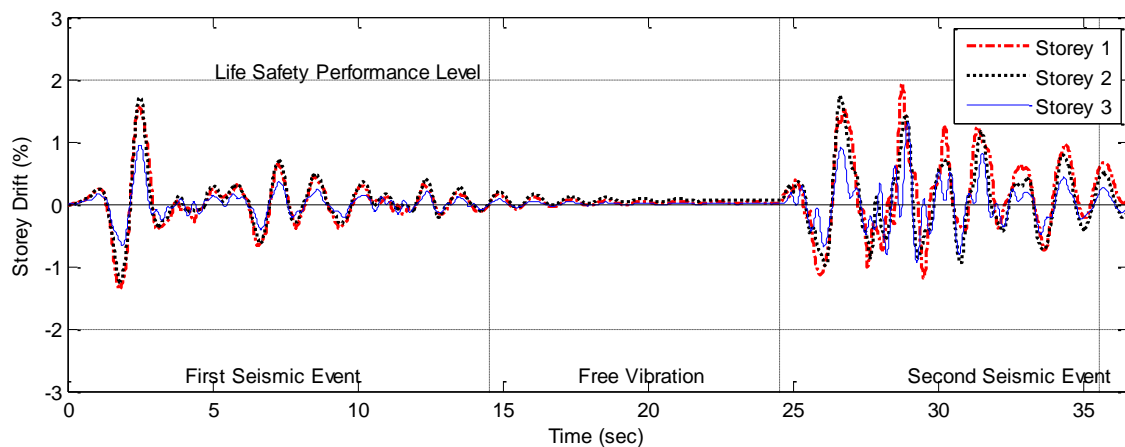


Figure 7-25: Interstorey drifts' response history. Hybrid simulation for the repaired structure case using the repaired Specimen #2 (Test 2.2).

7.4.4 Local Response of the Critical Element

The axial and lateral deformation response histories are presented in Figure 7-26 while the corresponding restoring forces are presented in Figure 7-27. Overall, the response is consistent with the various cases, but it can be observed that some differences are developed in the lateral response during the experimental study. The lateral deformation of the physical specimen is greater than the one predicted from the purely numerical studies, while the developed lateral forces are lower, revealing a softer response of the critical element compared to that from the constitutive model that was employed. This response can also be identified from the critical element's hysteretic response presented in Figure 7-28, while the specimen experiences significantly greater energy dissipation during the experimental study compared to the numerical studies as presented in Figure 7-29. Finally, the axial response experiences similar inconsistencies as the previous hybrid simulations.

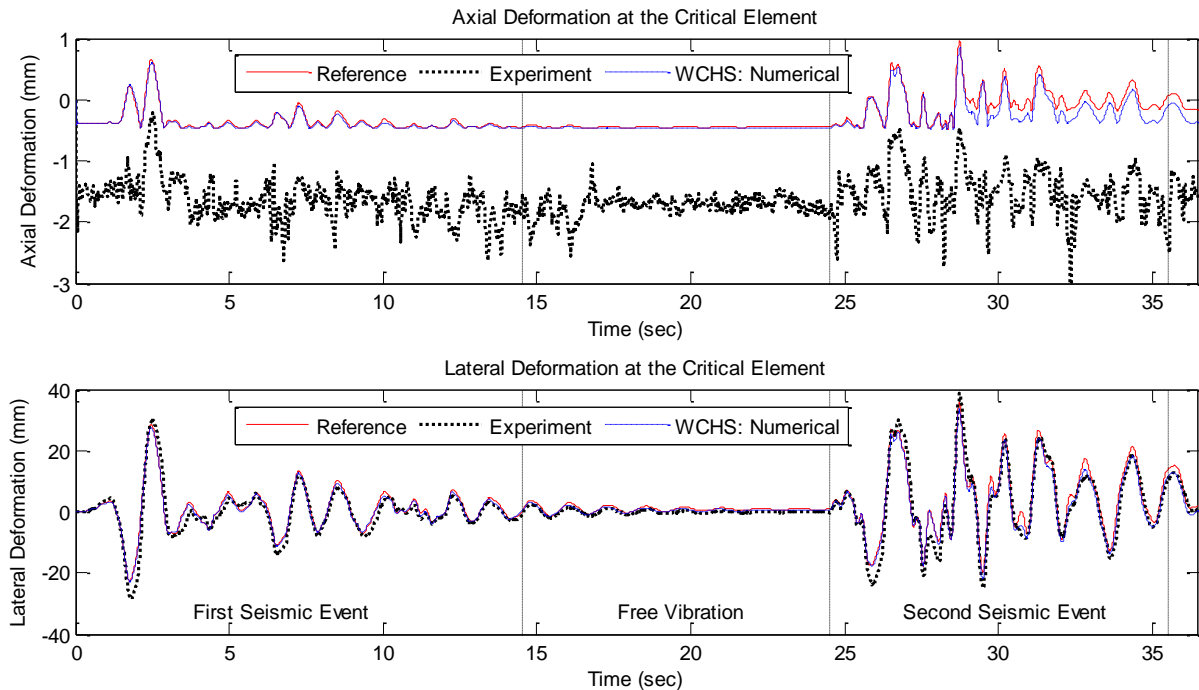


Figure 7-26: Critical element's deformation response history. Hybrid simulation for the repaired structure case using the repaired Specimen #2 (Test 2.2).

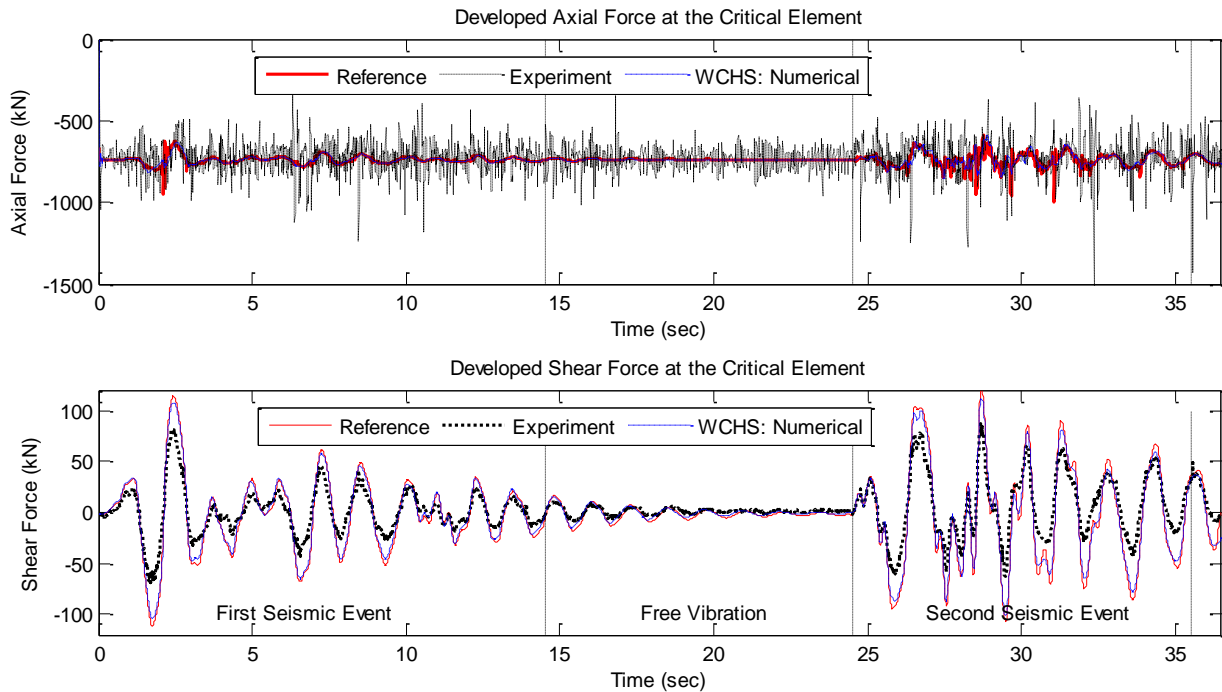


Figure 7-27: Critical element's developed forces response history. Hybrid simulation for the repaired structure case using the repaired Specimen #2 (Test 2.2).

From the moment-curvature relationship presented in Figure 7-30, the following observations can be made: the instrumentation is not working as robustly as it was in the undamaged/intact specimen; due to the damaged condition of the specimen, plastic deformations occurred for the entire duration of the test and not only during the peak deformations as happened with the intact structure case. Additionally, the maximum curvature is at the same magnitude as for the intact structure cases, while the damage is developed in the same area as for the intact case. This response demonstrates that the initially damaged area remains the weak area even after the repair of the specimen. Similar is the shear response recorded in the critical area, which is presented in Figure 7-31. The level of the developed shear deformation is comparable to that in the intact structure. However, residual shear deformations are significantly larger during this test as a result of the pre-existing damaged condition. Since the rebars of this second specimen yielded during the hybrid simulation as part of an intact structure, most of the strain gauges had damaged and no reliable records could be obtained from these gauges during the hybrid simulation of the repaired structure. Finally, after the end of the hybrid simulation, there was no visible damage to the specimen (Figure 7-32), and the specimen was tested again under quasi-static cyclic lateral loading as discussed in Section 7.8.

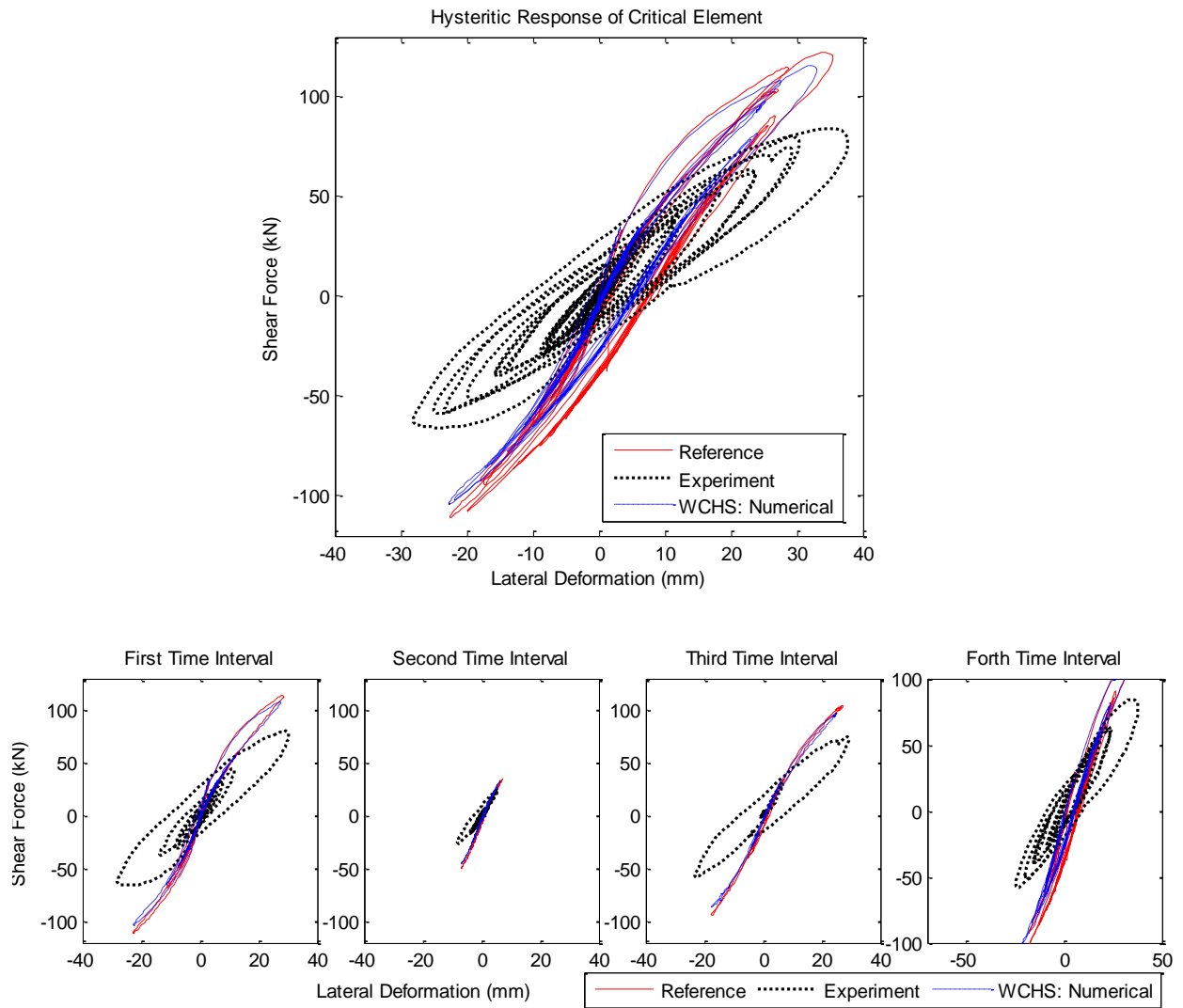


Figure 7-28: Critical element's hysteretic response presented for the full test (upper figure) and separated in four equal time intervals for clarity (lower figures).

Hybrid simulation for the repaired structure case using the repaired Specimen #2 (Test 2.2).

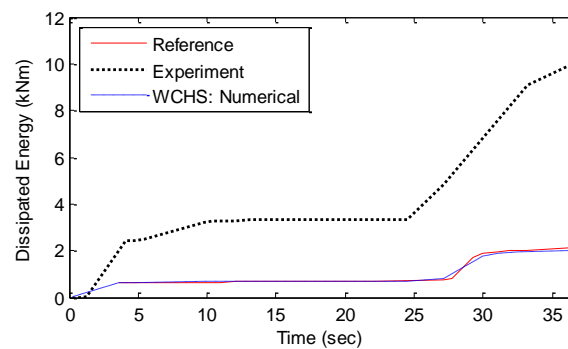


Figure 7-29: Dissipated energy in the critical element using the shear force – lateral deformation hysteretic response. Hybrid simulation for the repaired structure case using the repaired Specimen #2 (Test 2.2).

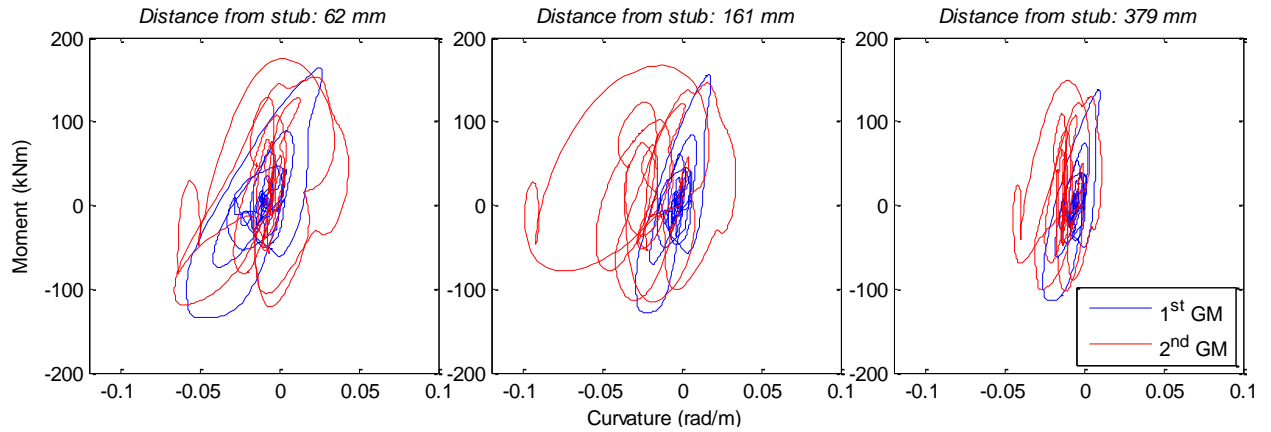


Figure 7-30: Moment-curvature relationship at the critical region from the hybrid simulation for the repaired structure case using the repaired Specimen #2 (Test 2.2).

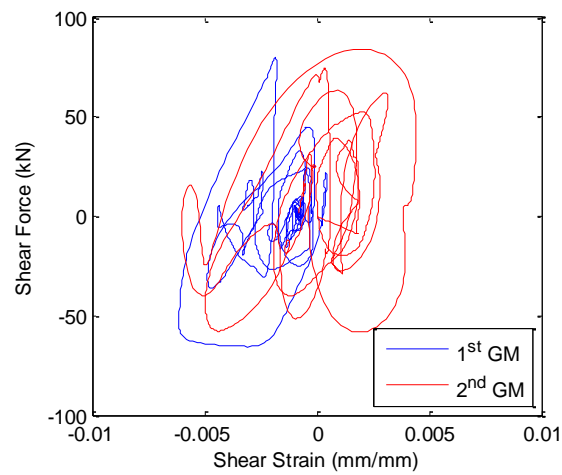


Figure 7-31: Shear force – shear strain relationship at the critical region from the hybrid simulation for the repaired structure case using the repaired Specimen #2 (Test 2.2).

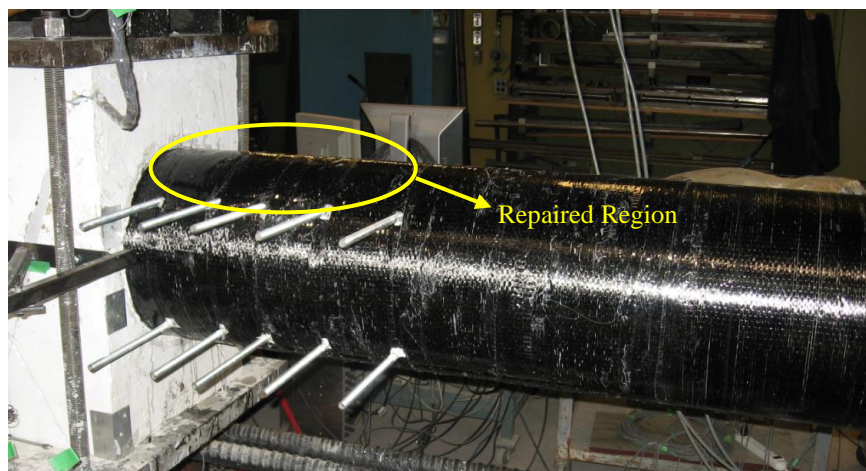


Figure 7-32: Repaired Specimen #2 (Test 2.2) condition after the repaired case structure hybrid simulation.

7.4.5 Numerical Study of the Response of a Non-repaired Damaged Structure

For understanding the efficiency of the repair, the case where a damaged unrepaired structure subjected to the same seismic sequence is numerically investigated. More specifically, the numerical model of the intact structure with the correct material properties is employed and is excited twice by the study seismic sequence. In this way, the response of the structure during the second excitation is equivalent to a damaged structure's response and can be used for identifying the efficiency of the repair of the structure as measured during the hybrid simulation.

The global response of the numerical model of the structure excited twice by the study seismic sequence is presented in Figure 7-33 in terms of interstorey drifts. It can be observed that when the damaged structure is excited by the same seismic sequence a significant soft storey mechanism is developed in the first storey and the structure fails to satisfy the Collapse Prevention Performance Level. Given the response of the damaged structure and the response of the repaired structure during the hybrid simulation, it can be stated that the repair performed on the structure was able to restore the structure response to a level equivalent to the intact structure case and was able to prevent the potential collapse observed in the non-repaired structure's response.

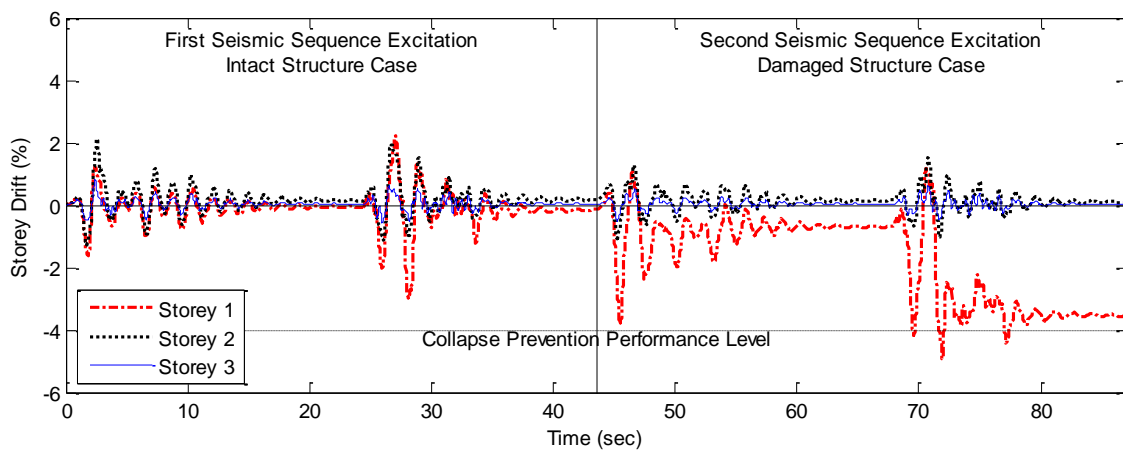


Figure 7-33: Interstorey drifts for the numerical study an intact structure excited twice by the study seismic sequence.

7.5 Retrofitted Structure

In this section, the experimental seismic performance assessment of the reference structure upgraded according to the retrofitting technique discussed in Chapter 4 is performed using the proposed WCHS methodology (Test 3.1). For the development of the numerical model of the retrofitted part of the structure that is to be numerically evaluated, a similar technique to the one employed for the repaired structure was used and is discussed in the next section. The results for this case are presented consistent with the previous chapters' results sequence.

7.5.1 Numerical Model Calibration

In VecTor2 (Wong et al. 2012), the externally applied FRP fabric is modeled similarly to lateral spiral reinforcement as smeared reinforcement in the transverse direction. In this way, the response of a retrofitted element can be predicted from VecTor2 and used for the calibration of the numerical model in OpenSees for the hybrid simulation of the retrofitted structure in the absence of the experimental results. The numerical model employed in VecTor2 is the column's model discussed in Section 3.5, with an equivalent additional smeared reinforcement in the lateral direction accounting for the retrofitting of the specimen. This numerical investigation was performed under a constant axial load of 740 kN, which is the gravity load in the study specimen, and quasi-static lateral deformation up to the failure of the specimen. The numerical response of the specimen as recorded in VecTor2 in addition to the calibrated model in OpenSees is presented in Figure 7-34.

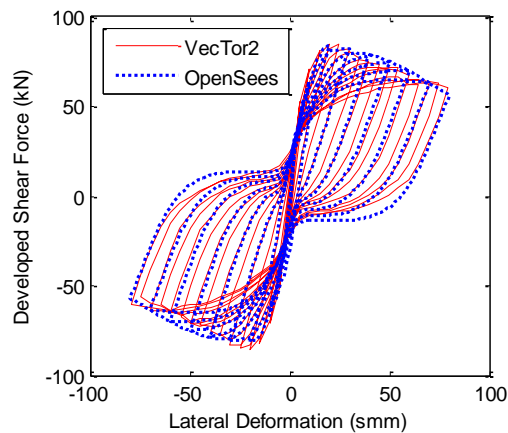


Figure 7-34: Calibrated response for the numerical model development of the retrofitted case structure.

7.5.2 Hybrid Simulation Performance

During the hybrid simulation performed for the retrofitted case structure (Table 7-1: Test 3.1), 0.95 error compensation steps were required per analysis step, while the lapsed time for performing 3,652 analysis steps was 5 hours and 41 minutes as summarized in Table 7-7. Similar to the previous cases, the axial and lateral slackness tolerances were set to 0.15 and 0.3 mm. The performance of this hybrid simulation is the most efficient among all the previous tests. The improvement can be attributed to the lower deformation demands of this test compared to the previous ones in addition to the error compensation convergence tuning performed during the hybrid simulation.

7.5.3 Global Response of the Structure

The global response of the retrofitted structure during the hybrid simulation is presented in Figure 7-35 and in Figure 7-36 in terms of the storeys' displacements and interstorey drifts, in addition to the results of the reference and the numerical weakly-coupled investigation. For this case, the experimental response in the lateral direction matches extremely well with the numerical study since there are no significant nonlinearities developed in the critical element and as a result, the coupling between the experimental controlled and the free DOF was not modified during the experimental study. The retrofitting technique does not significantly improve the structure's response as shown in Figures 7-35 and 7-36 since its effects become obvious beyond the Life Safety Performance Level. However, the maximum drift development was offset in time, and no residual deformation is observed at the end of the study.

Table 7-7: Hybrid simulation performance for the retrofitted structure case using the Specimen #3.

	Analysis Steps	Error Compensation Steps	Time	Axial Slackness Tolerance (mm)	Lateral Slackness Tolerance (mm)
Retrofitted Structure					
3 rd Specimen (Test 3.1)	3,652	3,475	5 hrs 41 min	0.15 [†]	0.3 [†]

[†] The tolerance were modified when required for reducing the error compensations steps requirements.

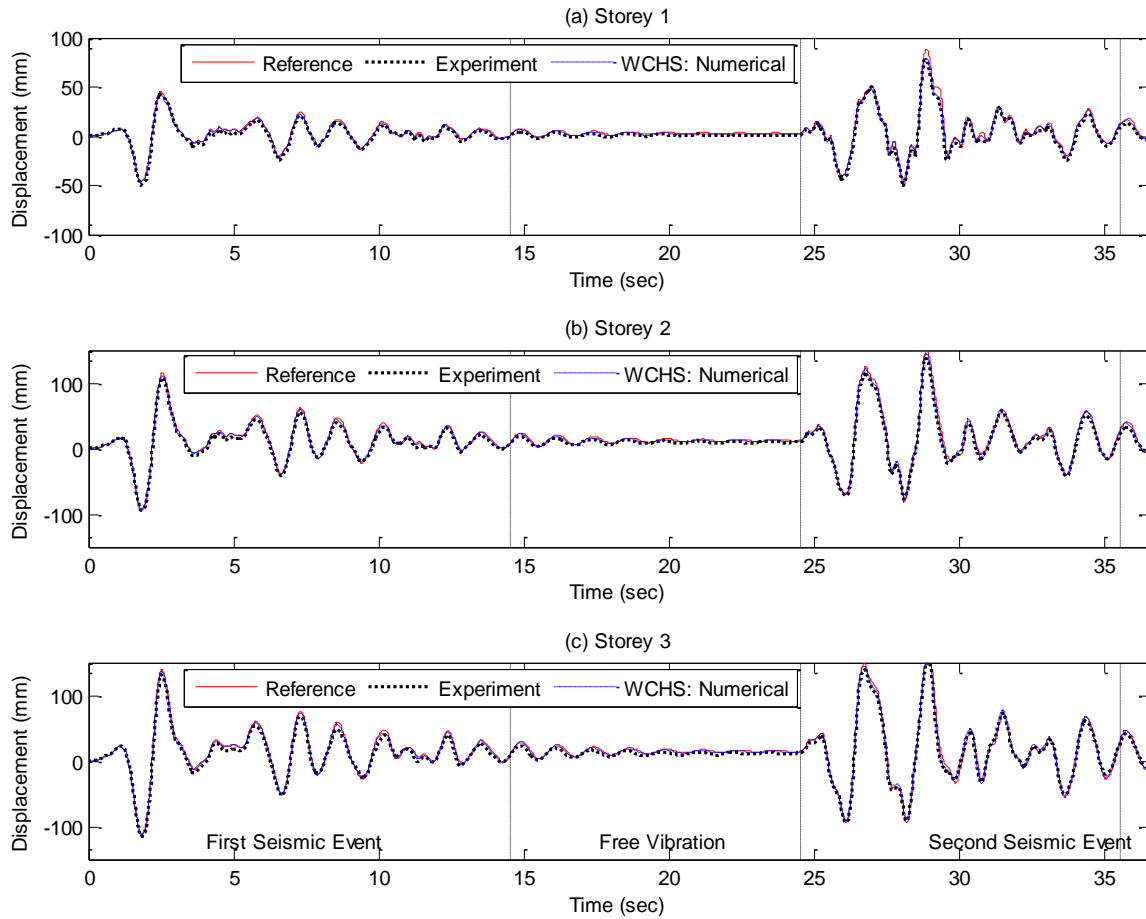


Figure 7-35: Storeys' displacement response history. Hybrid simulation for the retrofitted structure case using the retrofitted Specimen #3.

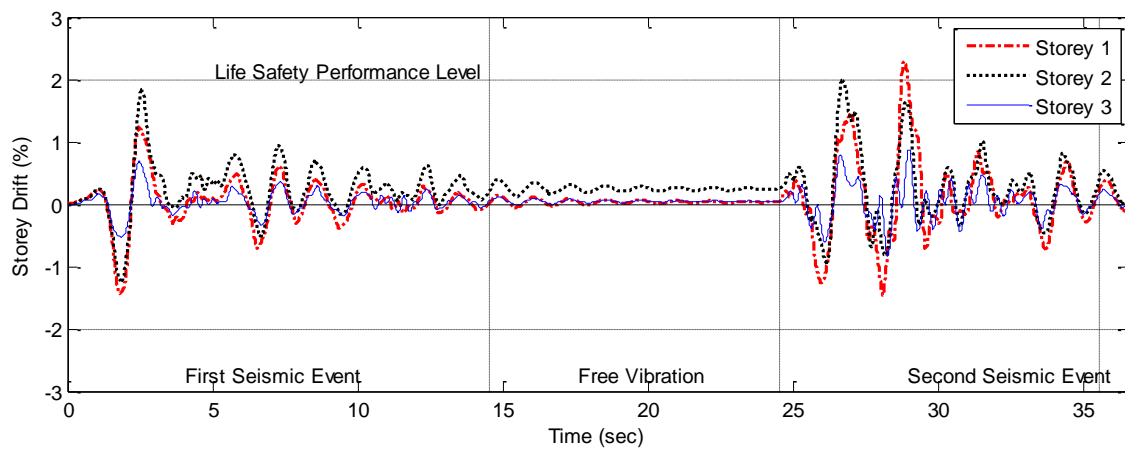


Figure 7-36: Interstorey drifts' response history. Hybrid simulation for the retrofitted structure case using the retrofitted Specimen #3.

7.5.4 Local Response of the Critical Element

The axial and lateral deformation response histories of the critical element are presented in Figure 7-37 while the corresponding developed restoring forces are presented in Figure 7-38. The experimental response is in good agreement with the numerical predictions in the lateral direction, a fact that can also be verified from the critical element's hysteretic response presented in Figure 7-39. The dissipated energy presented in Figure 7-40 in the experimentally tested specimen is greater than the dissipated energy in the equivalent element recorded during the purely numerical studies as a result of the damage mechanism captured during the experimental. Finally, the axial response experiences inconsistencies similar to those in the previous hybrid simulations. These axial restoring force inconsistencies are presented comparatively for all the hybrid simulations in the last section of this chapter.

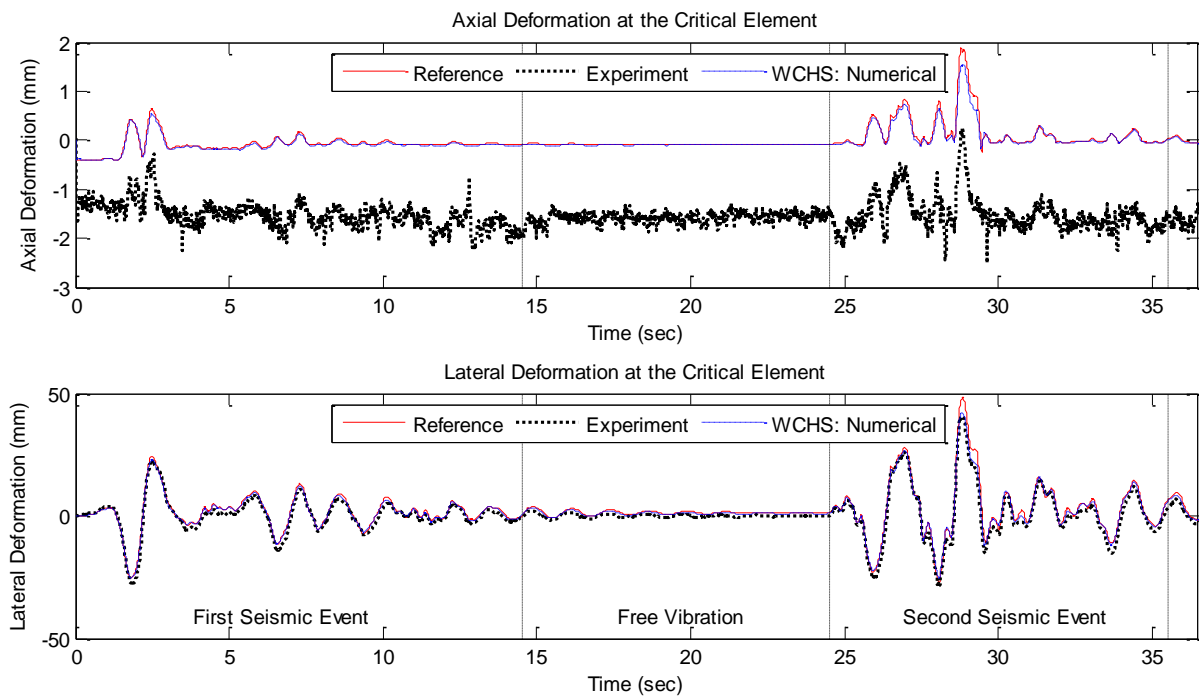


Figure 7-37: Critical element's deformation response history. Hybrid simulation for the retrofitted structure case using the retrofitted Specimen #3.

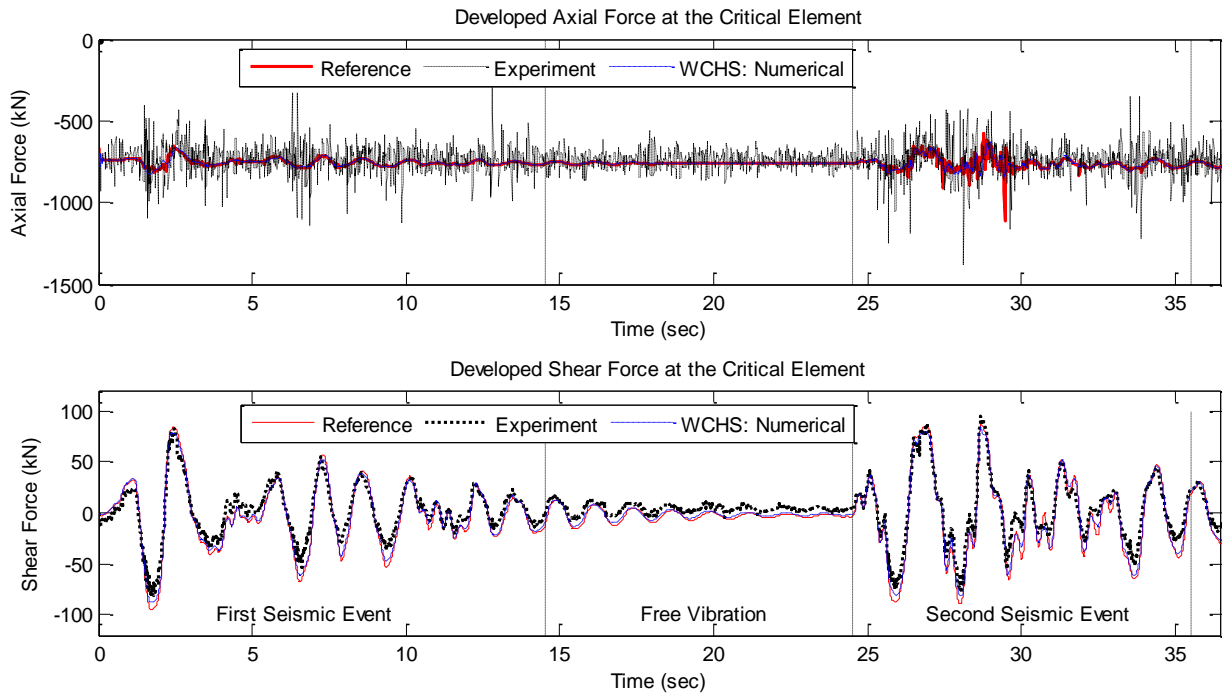


Figure 7-38: Critical element's developed forces response history. Hybrid simulation for the retrofitted structure case using the retrofitted Specimen #3.

From the moment-curvature relationship presented in Figure 7-41 it can be observed that the retrofitting of the column resulted in the offset of the damage development region from the second hoop, which was the critical area for all the previous cases, to the stub column interface, while the rest of the column remained almost within the linear range. The linear response of the element can be identified for the shear response presented in Figure 7-42, which was measured near the second hoop of the column and was captured from the diagonal LVDTs as presented in Figure 4-20. During the hybrid simulation, all the longitudinal bars yielded, but the spiral remained within the linear range throughout the critical region. Finally, no visible damage was identified, and the specimen was used again for the hybrid study discussed in the next section.

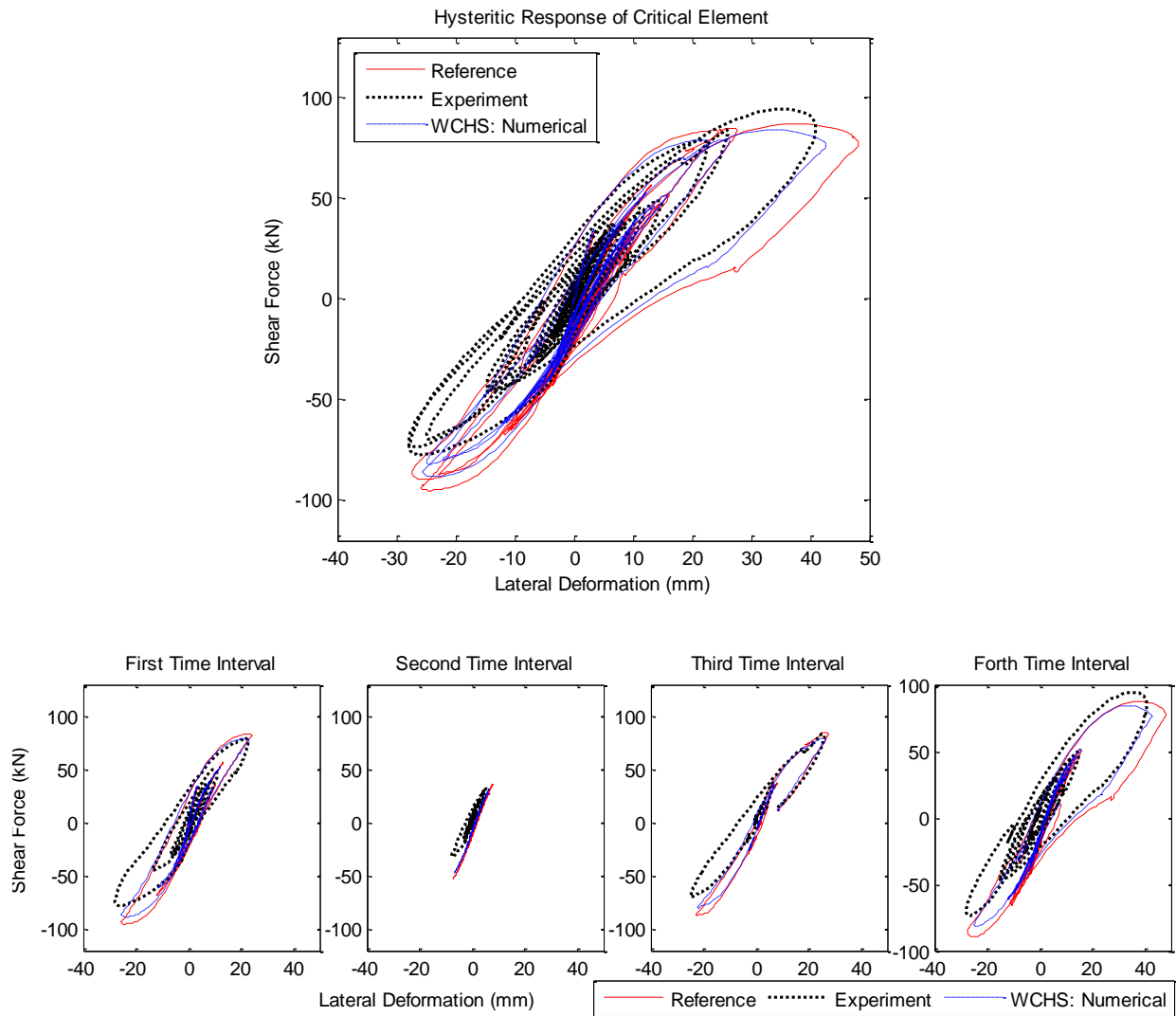


Figure 7-39: Critical element's hysteretic response presented for the full test (upper figure) and separated to four equal time intervals for clarity (lower figures).

Hybrid simulation for the retrofitted structure case using the retrofitted Specimen #3.

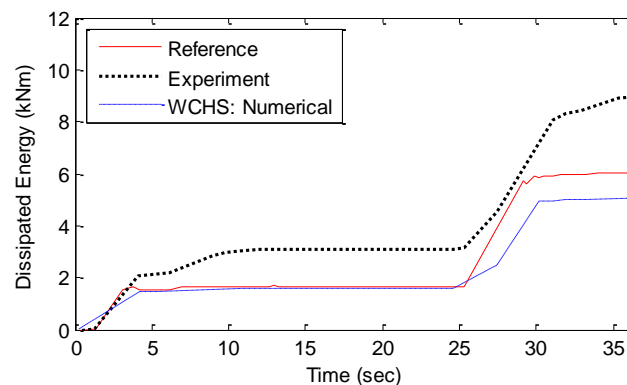


Figure 7-40: Dissipated energy in the critical element using the shear force – lateral deformation hysteretic response. Hybrid simulation for the retrofitted structure case using the retrofitted Specimen #3.

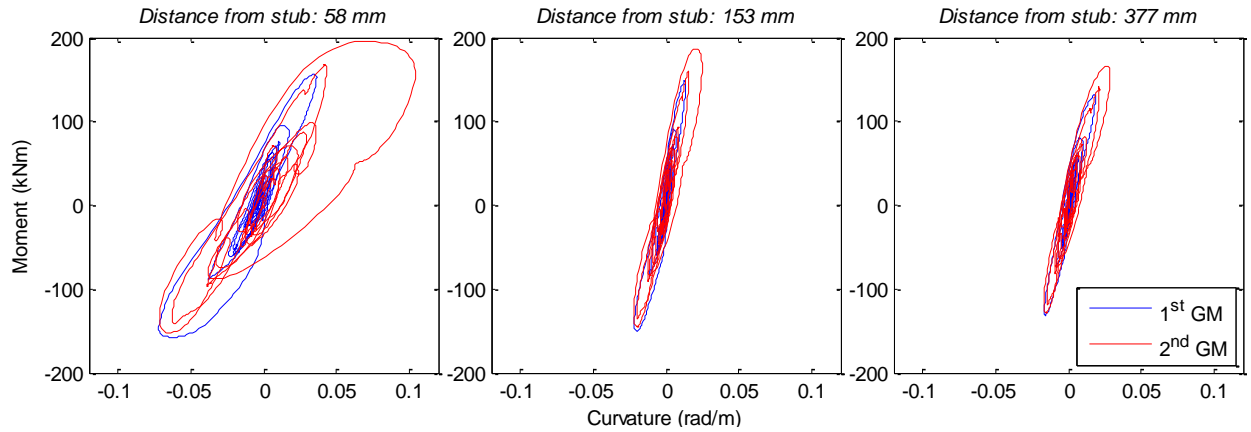


Figure 7-41: Moment-curvature relationship at the critical region. Hybrid simulation for the retrofitted structure case using the retrofitted Specimen #3.

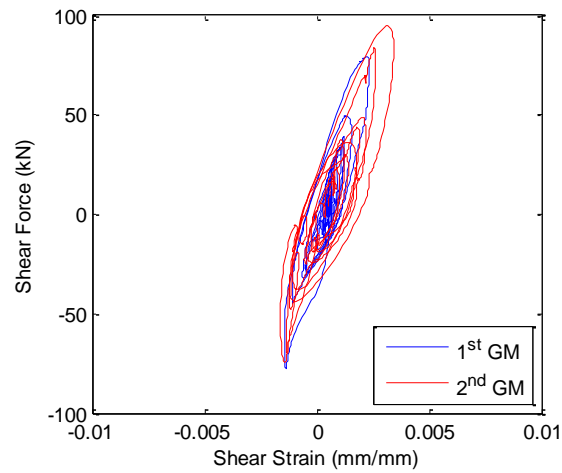


Figure 7-42: Shear force – shear strain relationship at the critical region. Hybrid simulation for the retrofitted structure case using the retrofitted Specimen #3.

7.6 Retrofitted Structure under Increased Gravity Loads

In order to have an in-depth understanding of the actual response inconsistency observed during the previous hybrid simulations and to evaluate the response of the column under higher excitation, an additional hybrid simulation was performed, in which significantly higher gravity loads were applied to the specimen. Since Specimen #3 was already retrofitted for the hybrid simulation of the upgraded structure case (Test 3.1), the numerical model employed for the hybrid simulation in this section is a retrofitted structure as well. The differences between the developed numerical model and the employed calibration technique are discussed in the next section. After developing the numerical model for the structure with increased weight, the numerical studies and the hybrid simulation were performed as described in the previous cases.

7.6.1 Numerical Model Modification

The structure for this increased axial load hybrid simulation is the retrofitted structure of the previous section but with modified gravity loads applied on the first storey. The increase in the axial loads for this study may be unrealistic, but the study was performed as such in order to reach an extreme loading case with respect to the column's axial capacity. This difference renders the re-calibration of the structure's constitutive models necessary because for the previous case the calibration has been performed using an axial load equal to 740 kN. In the next sections, the gravity loads distribution, the numerical model re-calibration and the modification of the study seismic sequence are summarized.

7.6.1.1 Gravity Loads Distribution

The modified load and mass distribution of the increased gravity loads are presented in Figure 7-43. The increase in the gravity loads was performed in a section of the first storey only, in order to maintain the structure's response mechanism. The axial loads developed during the gravity load stage in the first storey were 390 kN, 1,542 kN, 2,045 kN and 1,192 kN for the first, second, third and fourth columns, which are respectively equal to 8.8%, 34.9%, 46.3% and 27% of each column's capacity.

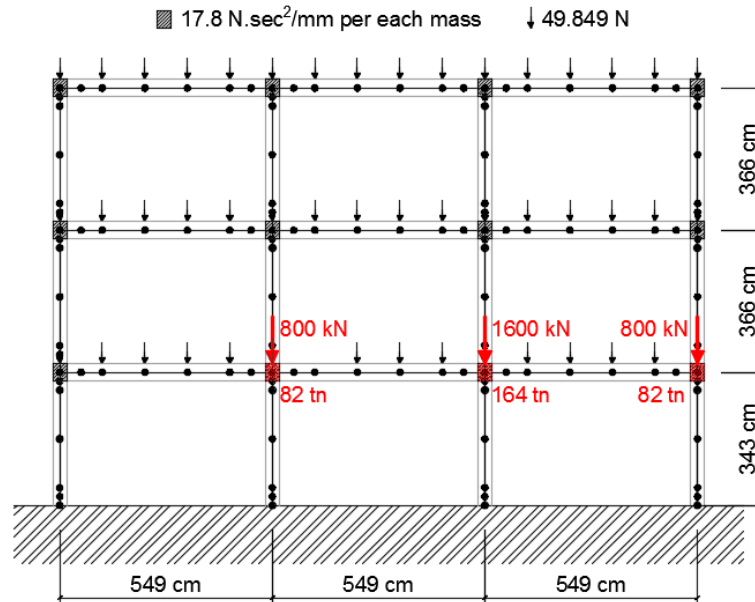


Figure 7-43: Modified load and mass distribution for the increased gravity load case retrofitted structure.

7.6.1.2 Numerical Model Calibration

The modified axial loads in the first storey columns resulted in the need for their constitutive models recalibration. The numerical model for each section of the structure as divided in Figure 7-44 was calibrated using VecTor2, which from the hybrid simulation performed in Section 7.5 (Test 3.1) was shown to capture the retrofitted specimen's response adequately. This constitutive model discretization has been carried out in order to account for the different axial load magnitudes developed in each specimen.

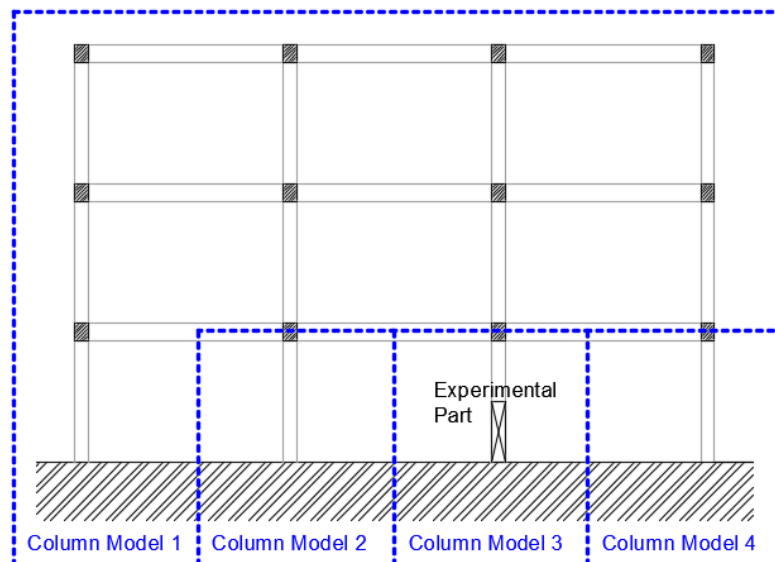


Figure 7-44: Constitutive models' notation used for the increased gravity load structure.

The calibrated numerical models developed as input in OpenSees for the increased gravity load case structure are presented in Figure 7-45. The development of the calibrated models was performed using the concrete material available in OpenSees named as “Concrete01 Material With Stuff In The Cracks”. From the developed numerical models it can be observed that the lateral response of the column is significantly affected by the axial load level and a less ductile response is observed when higher axial loads are applied. It should be noted that the constitutive model used for the first column of the first storey and the upper stories of the structure (“Column Model 1”) was the one employed for the hybrid study of the retrofitted structure in Section 7.5 (Test 3.1).

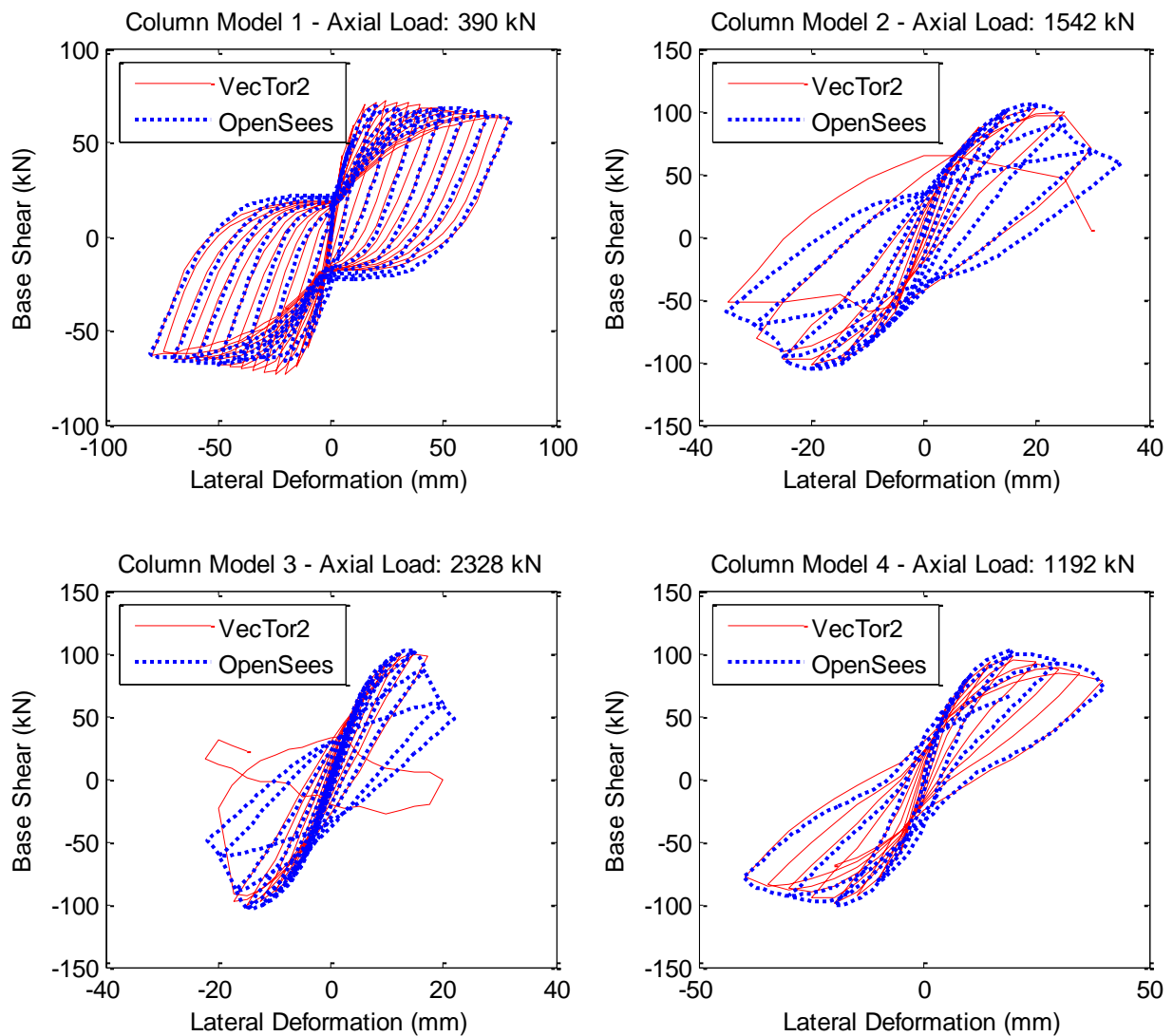


Figure 7-45: Constitutive models' notation used for the increased gravity load structure.

7.6.1.3 Seismic Sequence

For the seismic performance assessment with the increased gravity loads structure (Test 3.2), the seismic sequence was scaled to 40% of the intensity used for the previous hybrid simulation cases due to the fact that the increased weight of the structure resulted in a non-ductile failure mechanism at the first storey for a higher excitation intensity. Because of the unrealistic high gravity load, the structure's performance assessment is improbable. This hybrid simulation is primarily performed to assess the axial response inconsistencies and the axial response of the specimen standalone.

7.6.2 Hybrid Simulation Performance

During the hybrid simulation performed for the increased weight retrofitted structure case (Test 3.2), 0.42 error compensation steps were required per analysis step, while the lapsed time for performing 3,652 analysis steps was 5 hours and 9 minutes as presented in Table 7-8. The error compensation scheme for this hybrid simulation is twice as efficient as the once observed in the previous tests as a result of the significant reduction in the deformation demand for this structure's hybrid simulation.

7.6.3 Global Response of the Structure

The global response during the hybrid simulation of the increased weight retrofitted structure is presented in Figure 7-46 and in Figure 7-47 in terms of the storeys' displacements and interstorey drifts, in addition to the results of the reference and the weakly-coupled investigation. For this case, the lateral deformation observed during the experimental application of the WCHS was of some inconsistency compared to the numerical study performed with OpenSees only for predicting the response. This deference is attributed to the experimental response of the critical element and results into a more realistic assessment compared to the purely numerical study. For this case the interstorey drifts remain below the Immediate Occupancy Performance Level.

Table 7-8: Hybrid simulation performance for the increased weight retrofitted structure (Test 3.2).

	Analysis Steps	Error Compensation Steps	Time	Axial Slackness Tolerance (mm)	Lateral Slackness Tolerance (mm)
Retrofitted Structure					
3 rd Specimen (Test 3.2)	3,652	1,525	5 hrs 9 min	0.15 [†]	0.3 [†]

[†] The tolerance were modified when required for reducing the error compensations steps requirements.

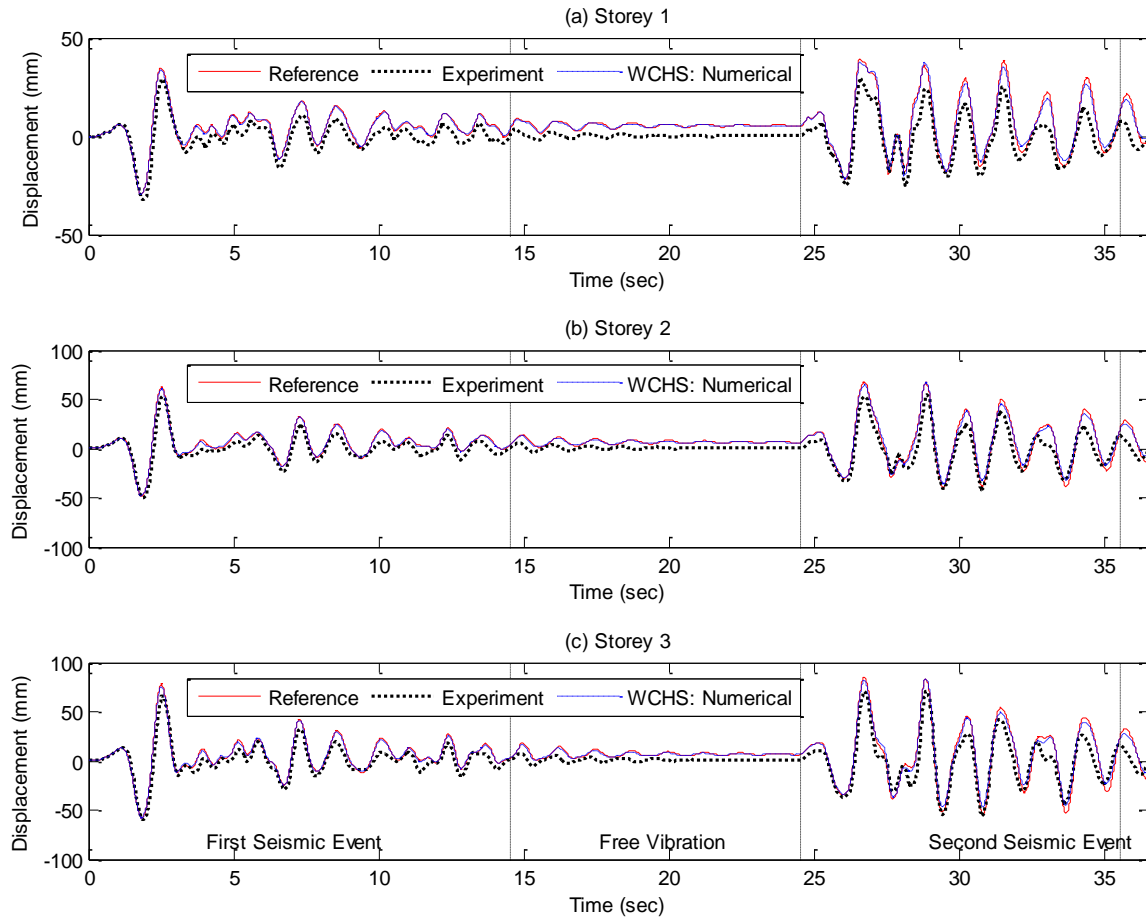


Figure 7-46: Storeys' displacement response history. Hybrid simulation for the increased weight retrofitted structure case performed with Specimen #3 (Test 3.2).

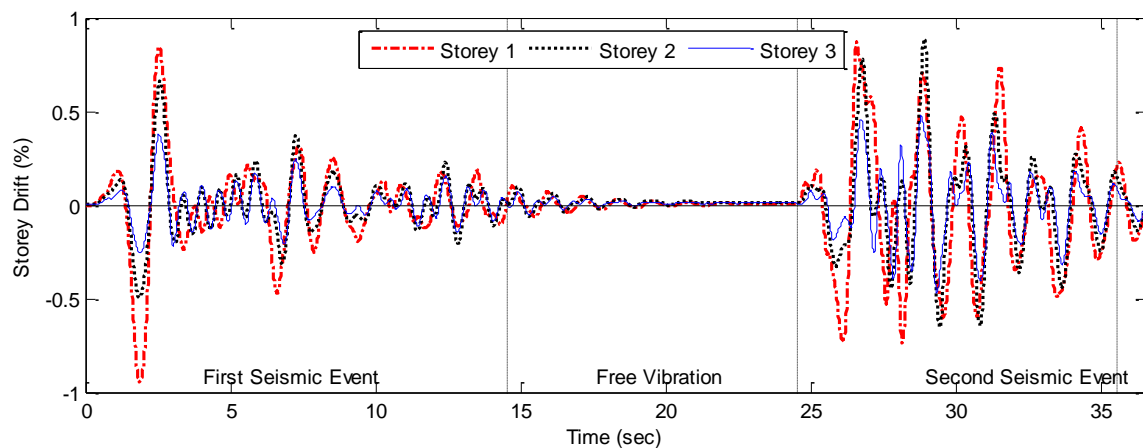


Figure 7-47: Interstorey drifts' response history. Hybrid simulation for the increased weight retrofitted structure case performed with Specimen #3 (Test 3.2).

7.6.4 Local Response of the Critical Element

The axial and lateral deformation response histories of the critical element are presented in Figure 7-48 while the corresponding restoring forces developed are presented in Figure 7-49. Both the lateral deformation response and the shear force response start deviating after the first significant lateral deformation demand ($t=1.81 \text{ sec}$). There are residual inconsistencies which can easily be identified during the time interval of the free vibration after the first ground motion. These differences can also be observed from the hysteretic response of the critical element presented in Figure 7-50, where an offset in the lateral response is developed. Similar to the previous tests, the dissipated energy presented in Figure 7-51 in the experimentally tested specimen is greater than the dissipated energy in the equivalent element during the numerical studies, while the axial response experiences similar deformation and developed force inconsistencies. The critical element's deformation exceeded the Immediate Occupancy Level.

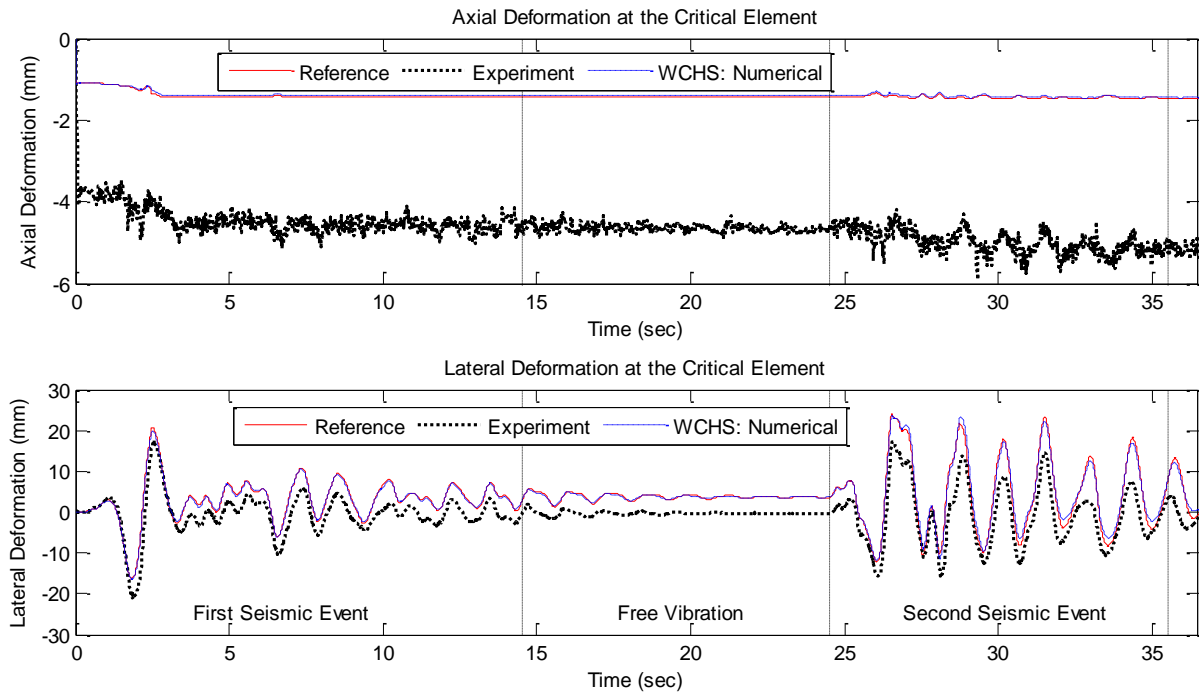


Figure 7-48: Critical element's deformation response history. Hybrid simulation for the increased weight retrofitted structure case performed with Specimen #3 (Test 3.2).

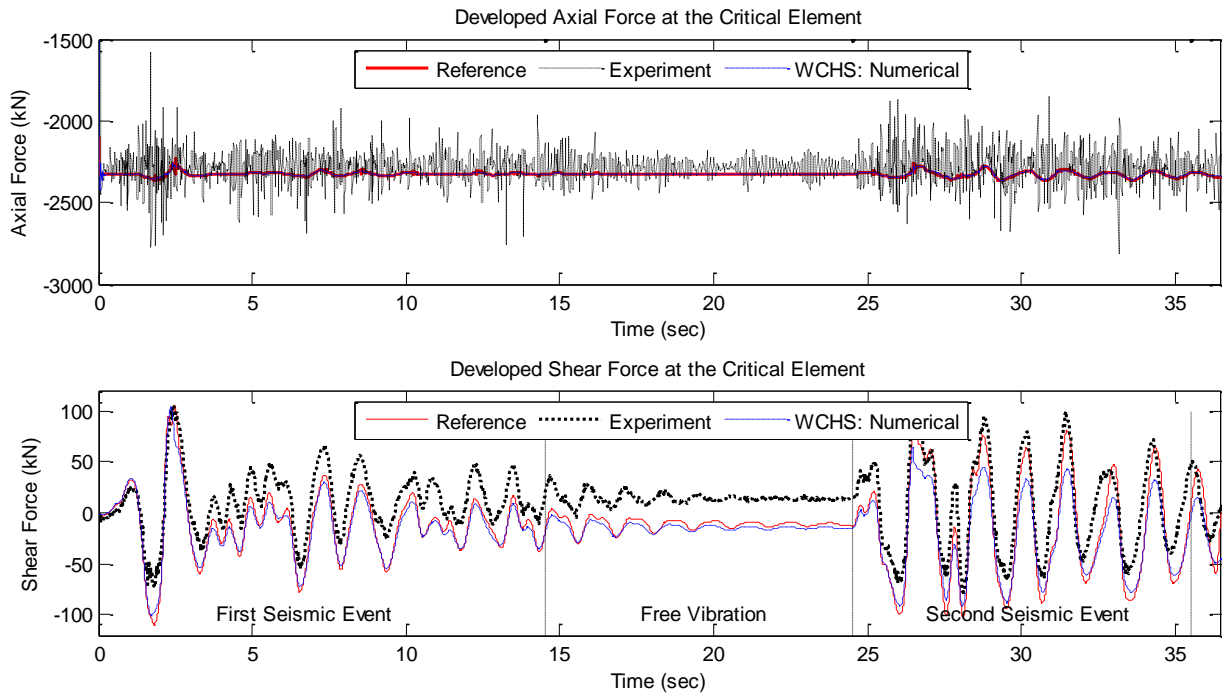


Figure 7-49: Critical element's developed forces response history. Hybrid simulation for the increased weight retrofitted structure case performed with Specimen #3 (Test 3.2).

As for the previous test carried out for the retrofitted structure, from the moment-curvature relationship presented in Figure 7-52 it can be observed that the greater curvature demand is developed in the stub-column interface, which because of the retrofit performed in the critical region of the column becomes the weakest location. However, the response both in the stub-column interface and in the critical region near the second spiral remains in the linear range. No visible damage was identified on the Specimen #3 after the end of the hybrid simulation. For this case, the strains recorded from the strain gauges attached to the longitudinal bars and on the spiral are below the yield limit, which is realistic considering the high axial load applied on the specimen. However, most of the longitudinal rebars yielded during the first hybrid simulation performed with the third specimen, while some of the strain gauges could have been damaged questioning the strain recordings of Test 3.2. During the hybrid simulation discussed in this section, the shear strain was not properly recorded and is not presented.

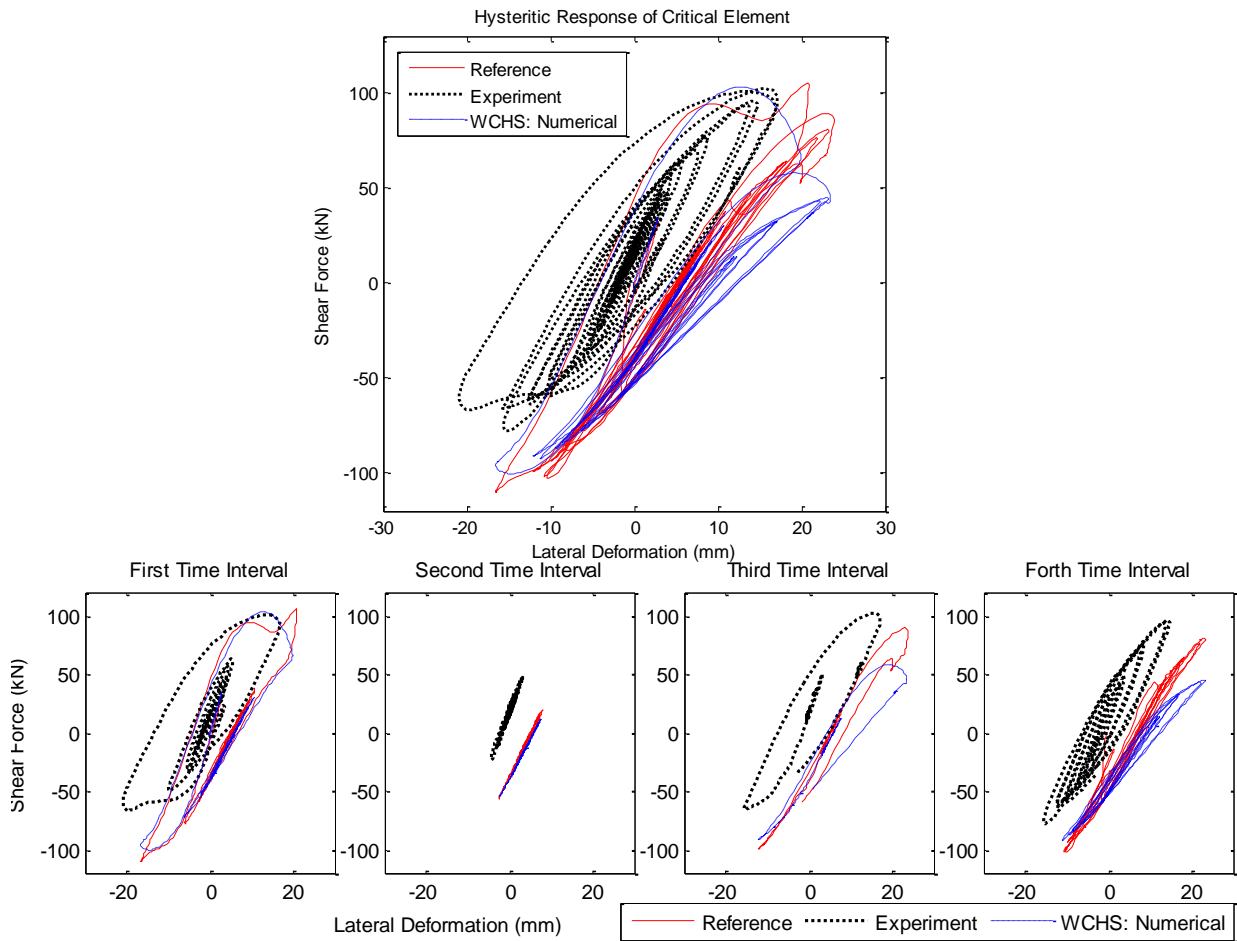


Figure 7-50: Critical element's hysteretic response presented for the full test (upper figure) and separated in four equal time intervals for clarity (lower figures). Hybrid simulation for the increased weight retrofitted structure case performed with Specimen #3 (Test 3.2).

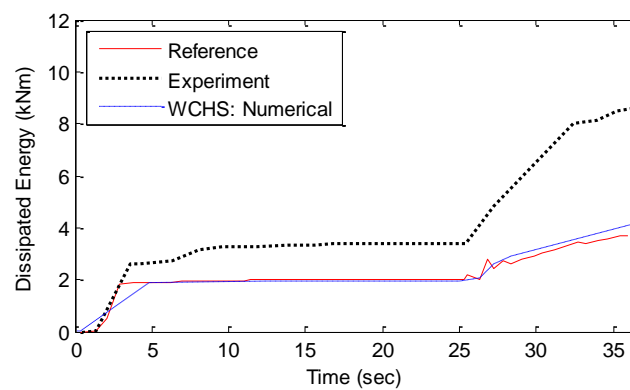


Figure 7-51: Dissipated energy in the critical element using the shear force – lateral deformation hysteretic response. Hybrid simulation for the increased weight retrofitted structure case performed with Specimen #3 (Test 3.2).

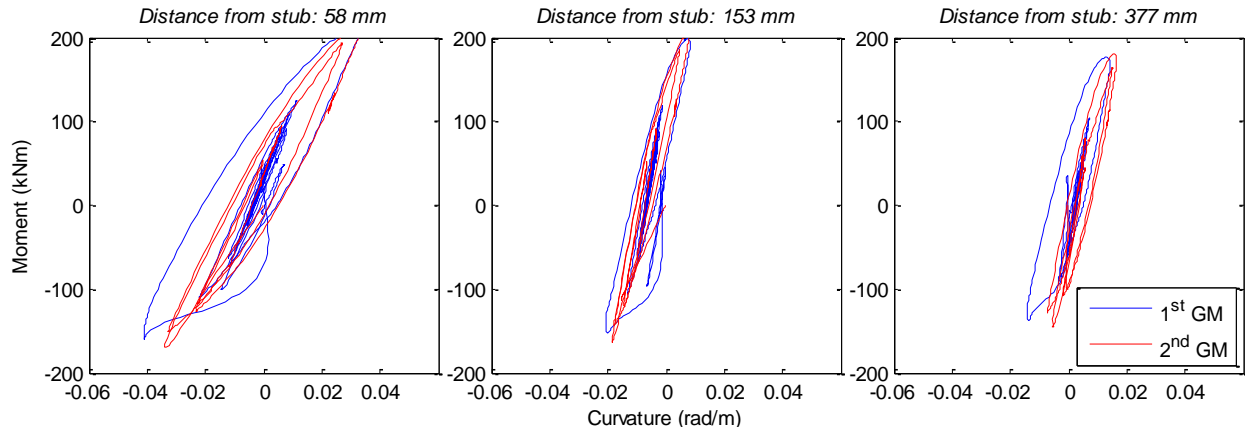


Figure 7-52: Moment-curvature relationship at the critical region. Hybrid simulation for the increased weight retrofitted structure case performed with Specimen #3 (Test 3.2).

7.7 Performance Comparison

The experimental seismic performance assessment of different structure cases as conducted in this study is presented comparatively in Table 7-9 in terms of hybrid simulation efficiency, global and the local response, and the performance level.

Table 7-9: Hybrid simulation performance assessment for the various structure cases.

Experimental Hybrid Simulation (WCHS)	Error Compensation Steps per Analysis Steps	Global Response – Max/Min Interstorey Drifts (%)			Local Response – Max/Min Drifts and Developed Shear into the Critical Element		Seismic Performance Assessment
		1 st Storey	2 nd Storey	3 rd Storey	Lateral Drift (%)	Developed Shear (kN)	
Intact Structure Specimen #1 (Tests 1.2 & 1.4)	2.14* & 0.83 [†]	1.90	1.90	0.75	1.81	90.36	Complies with the Collapse Prevention Level but exceed the Life Safety Level
		-2.41	-1.3	-0.68	-2.32	-84.75	
Intact Structure Specimen #2 (Test 2.1)	1	1.95	1.79	0.75	1.93	89.13	
		-2.56	-1.25	-0.66	-2.66	-77.25	
Repaired Structure Specimen #2 (Test 2.2)	1.4 [±]	1.93	1.75	1.32	2.11	87.74	
		-1.37	-1.25	-0.94	-1.54	-68.53	
Retrofitted Structure Specimen #3 (Test 3.1)	0.95	2.28	1.99	0.89	2.21	95.45	
		-1.48	-1.25	-0.85	-1.55	-80.41	
Retrofitted Structure with Increased Gravity Loads Specimen #3 (Test 3.2)	0.42 [□]	0.87	0.88	0.47	0.95	108.70	Complies with the Life Safety Level but exceeds the Immediate Occupancy Level
		-0.94	-0.65	-0.47	-1.15	-77.77	

* First hybrid simulation where I-modification was activated, and tolerance limits were 0.1 and 0.2 mm for the axial and lateral deformation

[†] First hybrid simulation where I-modification was deactivated, and tolerance limits were 0.15 and 0.3 mm for the axial and lateral deformation.

[±] Increased error compensation demand due to inefficient tuning during the hybrid simulation

[□] Significantly reduced error compensation requirement because of lower displacement demand in the critical element

From the hybrid simulation efficiency comparison performed using the error compensation steps requirement, it can be stated that for the typical cases when the test was conducted without any technical difficulty, one error compensation step is required on average for each analysis step. This response is considered adequate enough given the coupling between the controlled DOF and the slackness of the system. Values like the one reported for Test 1.4 (error compensation per step = 0.83) or for the Test 3.2 (error compensation per step = 0.42) are lower because of the reduced deformation demand. On the other hand, the increased error compensation step requirement during the Test 1.2 occurred because of the unrealistically low tolerance limits used. These tolerance limits are not feasible using the employed string potentiometer instrumentation.

As for the seismic performance assessment of the structure, the response during each test, except for the increased gravity loads structure case, complied with the Collapse Prevention but not with the Life Safety Limits as defined by FEMA-356 (FEMA 356 2000). For the last hybrid simulation conducted for the increased gravity loads, the performance exceeded the Immediate Occupancy Level but not the Life Safety Level. The structure's performance was assessed either by the global response of the structure or by the response of the critical element. Finally, it can be claimed that the repair performed on the damaged specimen and the structure was efficient and ensured the structure's response below the Collapse Prevention Limit, which was exceeded when the damaged, unrepaired structure was numerically assessed in Section 7.4.5. On the other hand, the retrofitting employed on the structure was not of similar efficiency because the structure's response remained at the same performance level as prior to the retrofit regardless of the fact that the maximum developed drift was slightly reduced.

Finally, for understanding the axial force's inconsistency during the test, the force fluctuation histograms for each hybrid simulation are presented in Figure 7-53. In these histograms, the ideal curve is a normal distribution with reduced width and significant peak at the zero fluctuation. Quantitatively, a desirable response is expressed with low standard deviation values. Such a response suggests that most of the analysis steps were performed with minor force fluctuations and the overall magnitude of the fluctuations was low. It can be stated that the hybrid simulations for the cases of the intact structure of the second specimen (Test 2.1), the repaired structure (Test 2.2) and the retrofitted structure (Test 3.1) had an acceptable response, while the test with the Specimen #1 (Test 1.2) and the test under the high gravity loads (Test 3.2) were slightly less accurate.

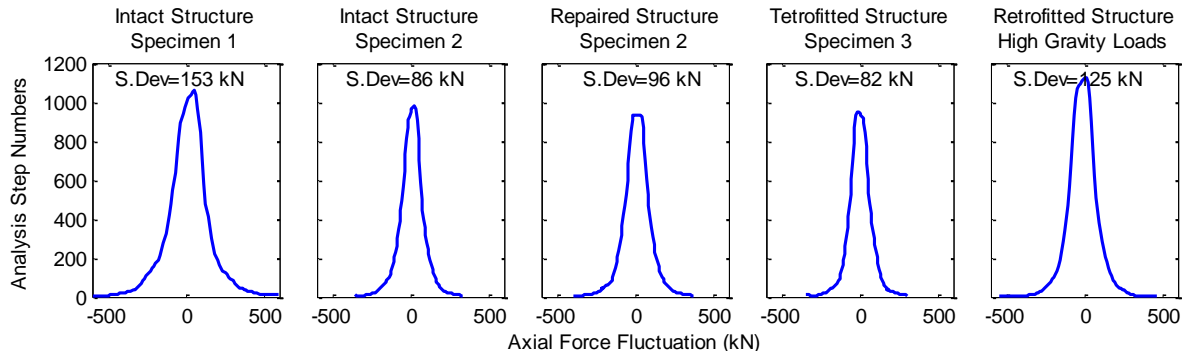


Figure 7-53: Axial force fluctuation histograms for the various hybrid simulations performed.

However, the level of that difference is not significant and is believed that these axial force inconsistencies occur from the string potentiometers' resolutions, which result in the inaccurate measurement of the axial deformation. Because of the large stiffness in the axial direction, a minor inconsistency in the axial deformation may induce a significant force fluctuation. Finally, the response during the first hybrid simulation (Test 1.2) is of lower accuracy because of the unrealistic slackness tolerance limits, which due to the instruments' resolutions were not able to be achieved. The increased error compensation step requirements when unrealistically low slackness limits are used, and the resultant accumulated inaccuracies occurred due to the instrumentation repeatability errors resulted in the increased force fluctuation in the axial direction.

7.8 Repaired Specimens' Constitutive Response

For understanding the efficiency of the repair and retrofit of the specimens, each specimen after the hybrid simulation was tested under quasi-static lateral loading and constant axial load. Three different axial load levels were employed, while the conditions between the repaired and the retrofitted specimens are considered equivalent in terms of damage. For each case, a numerical study of an intact RC column is performed using VecTor2 under the same axial load to demonstrate the improvement induced by the repair or the retrofit.

7.8.1 Quasi-Static Test under Low Constant Axial Load

Initially, the quasi-static cyclic test was performed under the constant axial load of 740 kN, which is equal to the gravity load applied on the critical element of the structure (Test 1.5). This test was carried out on Specimen #1 after its testing as an intact and a repaired structure. The measured response is presented in Figure 7-54 in addition to the envelope of the intact RC column studied in VecTor2, and the response during the hybrid simulation of the Specimen #1 (Tests 1.2 & 1.4). It can be observed that the repair did not increase the capacity of the column beyond that predicted by VecTor2 prediction but it was able to restore the damaged specimen's response. The difference observed in the peak shear for negative drifts was a result of the high strength mortar used for the repair of the column. The repaired specimen developed a slightly more ductile response compared to the intact specimen studied in VecTor2.

The difference observed between the hybrid simulation of the intact specimen (Test 1.2 & 1.4), and the quasi-static test of the repaired specimen (Test 1.5) demonstrates a minor increase in the physical specimen's capacity, but it should be noted that during the hybrid simulation multiple cycles were imposed on the intact specimen before the maximum deformation was applied, resulting in the damage of the specimen and a moderate material loss, which did not happen in the repaired specimen before the FRP rupture.

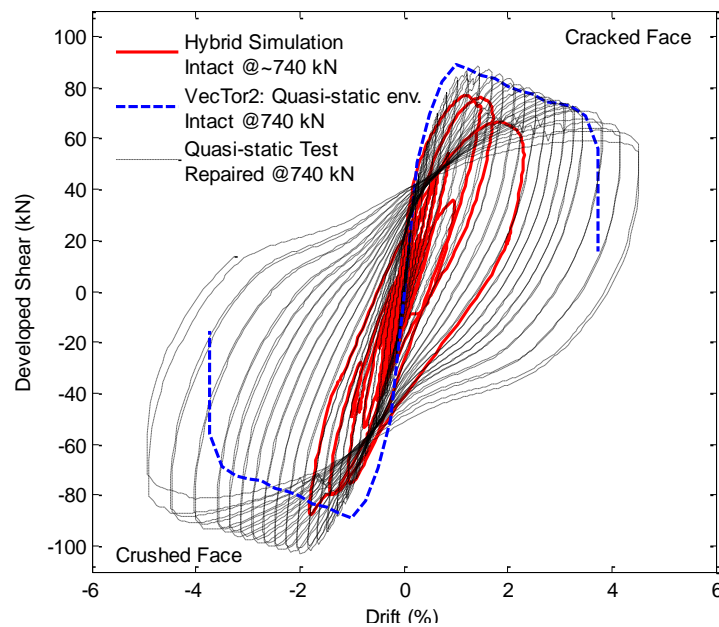


Figure 7-54: Repaired Specimen's #1 response under quasi-static cyclic lateral loading and low constant axial load.

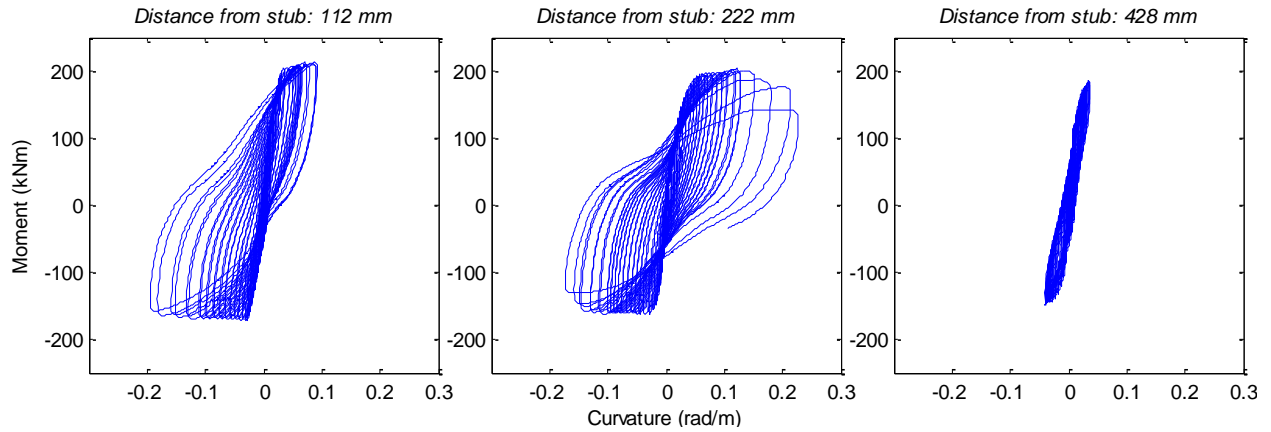


Figure 7-55: Moment-curvature relationship of the repaired Specimen #1 tested under quasi-static cyclic lateral loading and low constant axial load.

From the moment-curvature relationship presented in Figure 7-55 it can be noted that the major damage developed in the specimen is offset from the column-stub interface as recorded for most of the hybrid simulations (Figure 7-55: middle). However, for this case, there is significant energy dissipation in the region close to the stub-column interface (Figure 7-55: left) which demonstrates that equivalent damage development occurred in this area and was accompanied by cracking at the stub-column interface. The response out of the critical region is almost linear. The damaged state of the specimen after the end of the test is presented in Figure 7-56. The failure of the specimen was initiated by the rupture of the FRP, followed by significant material loss and to the buckling of the longitudinal rebars. A shear slip can be identified in Figure 7-56, which resulted in significant strength degradation. The shear response for this test was not properly measured with the employed instrumentation for this test.

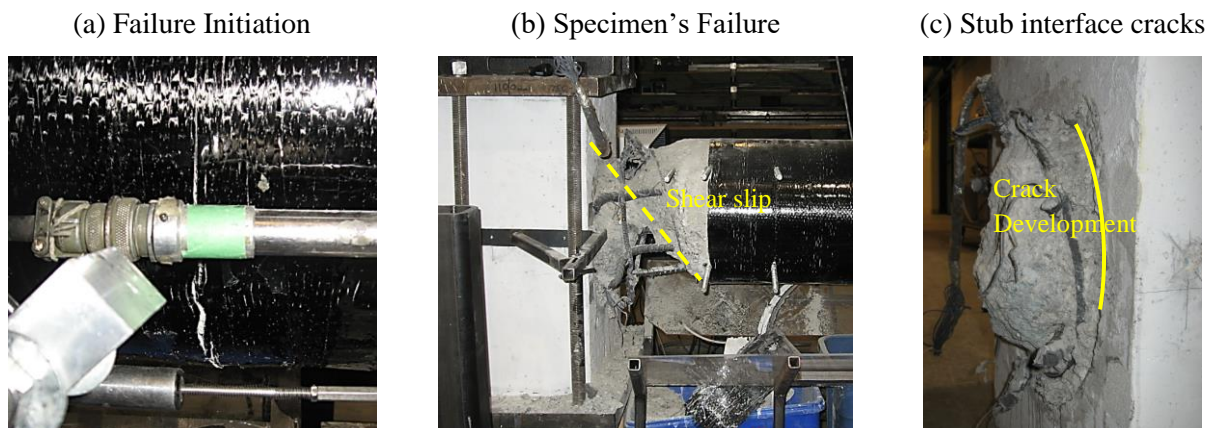


Figure 7-56: Damage in the repaired Specimen #1 at the end of the quasi-static testing under low constant axial load (Test 1.5).

7.8.2 Quasi-static Test under Moderate Constant Axial Load

Next, the Specimen #3 was tested under quasi-static lateral loading protocol (Test 3.3) and moderate constant axial load equal to 1,173 kN (26.6% of the column's axial load capacity). The measured response during the quasi-static test is presented in Figure 7-57, in addition to the envelope of the intact RC specimen's response under the quasi-static investigation performed numerically in VecTor2. Additionally, the response of the Specimen #3 during the hybrid simulation as a part of a retrofitted structure is included in Figure 7-57 for comparison purposes.

It can be noted that the retrofit significantly increased the strength and deformation capacity of the Specimen #3 when compared to the intact RC column studied in VecTor2. This enhancement occurred due to the higher axial load compared to the previous case, which activates the lateral confinement of the FRP wrap efficiently. Additionally, for this section, the experimental response of the Specimen #3 during the quasi-static test is well centered indicating proper alignment. Finally, the differences observed between the hybrid simulation and the quasi-static cyclic response of the retrofitted specimen indicates that the effect axial load is not appropriately considered in the simulation.

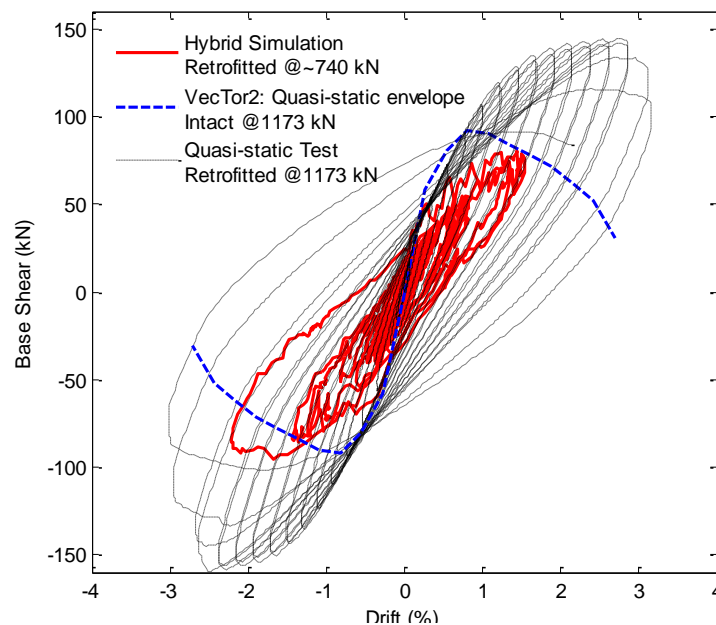


Figure 7-57: Retrofitted Specimen's #3 response under quasi-static cyclic lateral loading and moderate constant axial load.

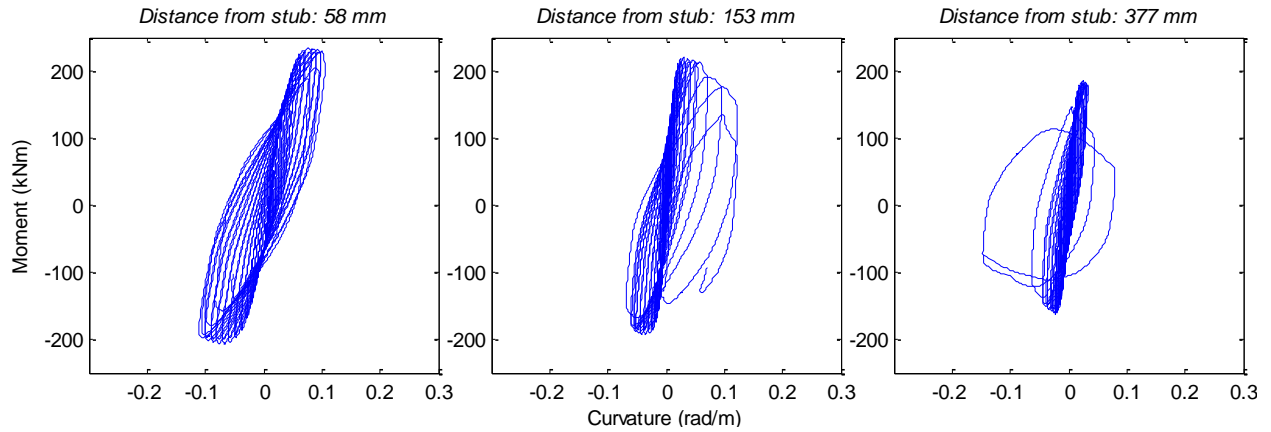


Figure 7-58: Moment-curvature relationship of the retrofitted Specimen #3 tested under quasi-static lateral loading and moderate constant axial load.

From the moment-curvature relationship presented in Figure 7-58, the damage development at the third hoop area, which is significantly offset for the stub column interface, can be identified (Figure 7-58: right). However, there is considerable energy dissipation along the critical area (Figure 7-58: left), but the failure was initiated by the FRP rupture at a distance approximately equal to 377 mm from the stub. The FRP rupture is accompanied by significant material loss and a shear slip, which can be observed in the shear response curve presented in Figure 7-59. Additionally, the longitudinal bars buckled, resulting in a significant strength degradation in the specimen. Finally, the damaged state of the Specimen #3 at the end of Test 3.3 is presented in Figure 7-60.

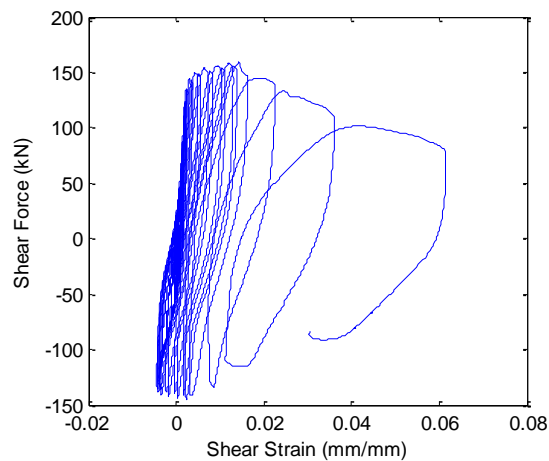


Figure 7-59: Shear strain response of the retrofitted Specimen #3 tested under quasi-static lateral loading and moderate constant axial load.

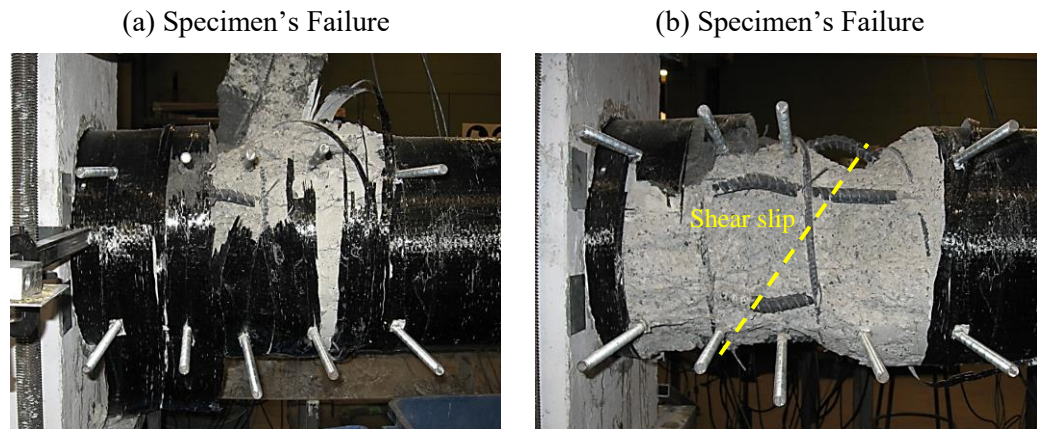


Figure 7-60: Damage developed on the retrofitted Specimen #3 after the quasi-static lateral testing under moderate constant axial load (Test 3.3).

7.8.3 Quasi-static Test under High Constant Axial Load

Finally, a quasi-static investigation was performed under high constant axial load equal to 2,430 kN, which is 55% of the column's axial load capacity (Test 2.3). The Specimen #2 was used for this test after its hybrid simulation as part of the intact and repaired structure cases (Tests 2.1 & 2.2). The measured response is presented in Figure 7-61 in addition to the envelope of an RC column analyzed under quasi-static lateral loading protocol in VecTor2, and to the response of the Specimen #2 during the hybrid simulation as part of a repaired case structure (Test 2.2). Similar to the moderate axial load case, the repair increased the strength and deformation capacity of this specimen significantly compared to the RC column's response studied with VecTor2, but the failure occurs with a brittle, non-ductile mechanism for both cases because of the high axial load.

From the moment-curvature relationship presented in Figure 7-62, it can be noted that the damage is developed at the third hoop region, similar to the moderate axial load case (Figure 7-62: right). However, for this case, the energy dissipation in the area closer to the stub-column interface is minor (Figure 7-58: left & middle) and the response there can be described as linear. The damage mechanism of the specimen is similar to the one of the previous cases. The failure is initiated by the FRP rupture, accompanied by significant material loss and a shear slip, which can be observed in the shear response in Figure 7-63. Subsequently, the buckling of the longitudinal bars occurred resulting in significant strength degradation of the specimen. The damaged state of the specimen at the end of the quasi-static test (Test 2.3) is presented in Figure 7-64.

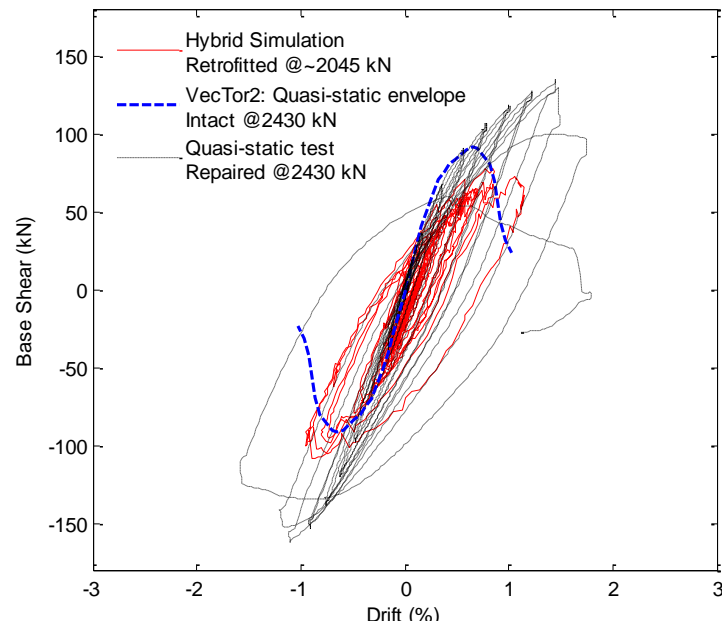


Figure 7-61: Repaired Specimen's #2 response under quasi-static lateral loading and high constant axial load.

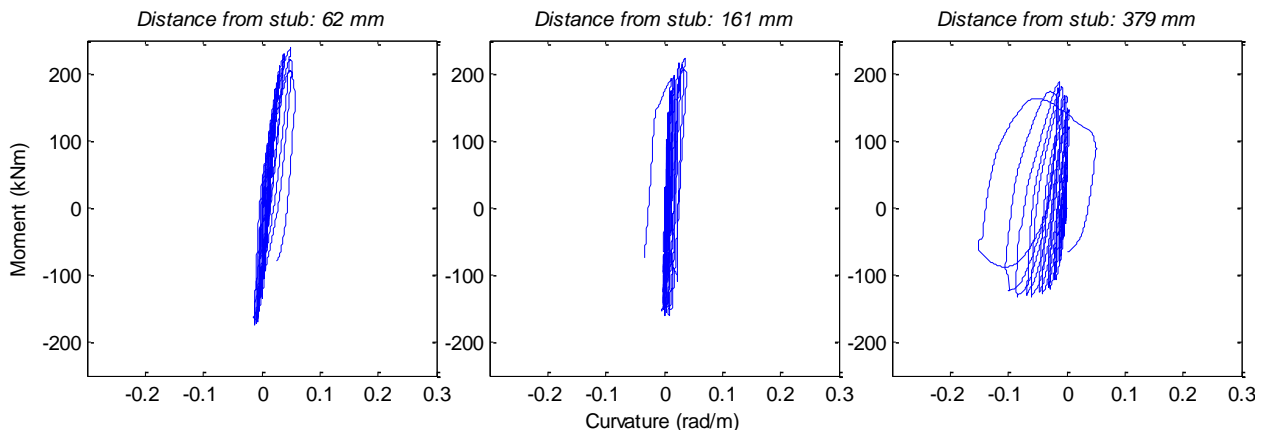


Figure 7-62: Moment-curvature relationship of the repaired Specimen #2 tested under quasi-static lateral loading and high constant axial load.

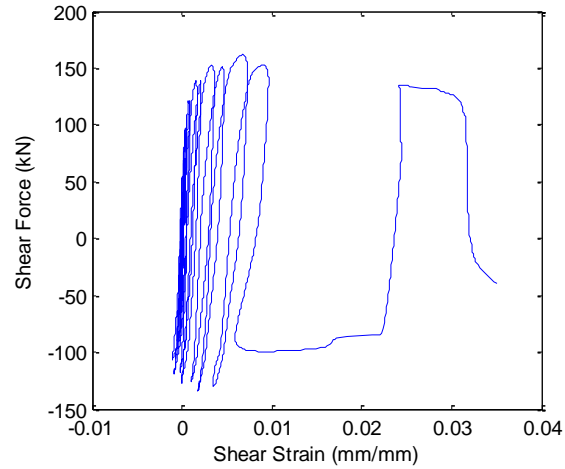


Figure 7-63: Shear strain response of the repaired Specimen #2 tested under quasi-static lateral loading and high constant axial load.

(a) Specimen's Failure



(b) Specimen's Failure

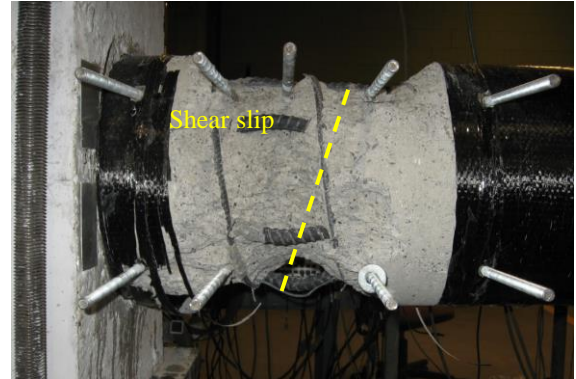


Figure 7-64: Damage of the repaired Specimen #2 after the quasi-static testing under high constant axial load (Test 2.3).

Chapter 8 Conclusions

8 Conclusions

8.1 Summary

In this study, a novel methodology is proposed and applied for conducting hybrid simulations when experimental limitations exist in the testing equipment and are related to the control of the boundary conditions at the transitional, interface nodes connecting the numerical and the experimental substructures. This methodology, namely the weakly-coupled hybrid simulation, is analytically discussed and is numerically and experimentally applied for the seismic performance assessment of an RC structure excited by a seismic sequence of two ground motions. The structure's performance assessment is conducted for three cases, in which the structure is considered as intact, repaired and retrofitted.

The critical component of the structure's response is a first storey internal column with the substructure that is experimentally evaluated. The available experimental facility is developed to test the column portion below the contraflexure point which means that only half of the column is physically represented. Three specimens were employed for this study and tested as intact, repaired and retrofitted, for structural evaluation. The repair and retrofit technique employed consisted of initially repairing the damaged concrete followed by its wrapping with unidirectional CFRP.

Numerical models were developed based on widely accepted constitutive models for the case of the intact structure, while calibrated models were implemented for the cases of the repaired and the retrofitted structures. The calibration performed for the repaired structure is based on the experimentally measured response of a repaired specimen during a quasi-static lateral testing under constant axial load, while for the retrofitted case, the calibration against numerical responses obtained from VecTor2 was performed. The conclusions of the current study are summarized in the next section.

8.2 Conclusions

The major findings of the current study are summarized below for the proposed weakly-coupled hybrid simulation method and the success of the developed methodologies to address some of the most commonly observed experimental difficulties during hybrid simulation. In addition, the performance assessment of different structures and the efficiency of the retrofit and repair techniques are summarized as follows.

- The weakly-coupled hybrid simulation is a promising method for performing hybrid simulations when the testing equipment has a limited number of actuators. The proposed methodology constitutes an approximate solution, whose applicability should be numerically investigated before the physical hybrid simulations are performed. However, the results from the WCHS will always be of equal or lower accuracy compared to the hybrid simulation in which all DOF can be experimentally controlled with actuators.
- While the proposed WCHS method constitutes an approximation, it was demonstrated that a realistic assessment of the seismic performance of the reference structure can be achieved by the developed architecture. During the WCHS experimental implementation, the damage and energy dissipation mechanisms were physically captured, resulting in a greater energy dissipation within the critical element. The developed damage was found to be equivalent to the one predicted by the multiplatform hybrid simulation using VecTor2, a sophisticated concrete modeling software.
- The I-modification correction scheme was shown to induce undesirable errors in the axial restoring forces. This occurs because the stiffness of the specimen is higher than the stiffness of the testing frame and because the axial deformation control is subjected to the accuracy of the employed instrumentation. As a result, the use of the I-modification correction scheme is considered as inappropriate in such cases.
- The hybrid simulation of a stiff specimen requires an accurate control of the specimens' deformation due to the elastic deformation of the loading frame. This can be achieved by measuring the deformation directly from the physical specimen and including error compensation algorithms in the hybrid simulation controller.

- The performance of the deformation control is governed by the performance of the instrumentation. The instrumentation resolution should be high enough for capturing the specimen's deformation at a level that the developed force fluctuation is within acceptable limits. The slackness tolerance limits in the test equipment should be defined consistent with the employed instrumentation's measurement errors. Otherwise, additional irregularities may develop during the hybrid simulation. To account for that, if unrealistic low tolerance limits are set the error compensation procedure becomes time-consuming without demonstrating significant improvement in the deformation control and the restoring force's development.
- When multi-DOF hybrid simulations are performed, a coordinate transformation scheme is required for the proper simultaneous control of more than one actuator. While some generic hybrid simulation platforms are available, there are case-specific applications where a dedicated coordinate transformation scheme is required to be developed. However, this development is possible for any experimental setup through nonlinear transformation schemes by employing the setup's geometric characteristics, given the conditions that the directions of all the installed actuators do not merge at the same location and equivalent rigid blocks like the stub of this study are used for the deformation application.
- The implementation of experimentally or numerically calibrated numerical models can be utilized efficiently for capturing a structure's response when conventional constitutive models are not adequate. However, special care is required for identifying the target experimental response used for the calibrated numerical models, and the calibrated models should be developed under similar loading conditions (e.g. a similar level of axial load).
- The efficiency of the externally applied FRP in terms of improving the response of repaired or retrofitted columns is related to the level of the axial load applied. For low axial load levels, the ductility of the specimen is improved due to the fact that no material loss occurs up to the FRP rupture, but there is no significant improvement in the column's capacity. For moderate axial load levels, both the capacity and the ductility of the specimen are significantly improved, while for high axial load levels, an enhanced capacity is observed, but failure occurs in a brittle manner initiated by the FRP rupture.

- By employing hybrid simulation, inconsistencies related to the numerical model can be identified and a more realistic performance assessment of the structure is achieved. It was proven that the critical element's response can modify the structure's response significantly, and for the case of the repaired structure, where an inaccurately calibrated numerical model has been employed, it was the physically tested specimen's response which demonstrated that the actual performance level of the structure exceeds the Life Safety Performance Level limits.
- FRP-repaired column was able to restore the structures performance to the pre-damage response when excited by the same seismic sequence scenario. The structure's performance was not significantly improved with the use of the retrofitted column because the demand on the column did not use its upgraded performance. Additionally, the retrofitting resulted in the translation of the critical location area to the stub-column interface.

8.3 Recommendations

The following recommendations are provided for future research as a further expansion of the current study:

- A reproduction of the previous experiments with higher accuracy instruments is of significant interest as a way to validate and eliminate the force fluctuation observed in the axial direction. In this way, the error compensation scheme can be optimized and a more efficient hybrid simulation framework can be developed.
- Application of the weakly-coupled simulation can be combined with hybrid simulation with a model updating techniques architecture (Kwon & Kammula, 2013) to enhance the experimental performance assessment of elements with less fluctuating contraflexure point locations. This can reduce the WCHS approximation error.
- Additionally, the application of the WCHS to cases different than the column's hybrid testing simulation should be performed to evaluate its applicability spectrum and expand the hybrid simulation testing application range.

- A possible implementation of the developed testing architecture could be used as part of a distributed hybrid simulation, where different critical elements for the structure's response would be either experimentally tested or numerically evaluated using sophisticated modeling software.

References

- ASTM. 2014. ASTM A370: Standard Test Methods and Definitions for Mechanical Testing of Steel Products. *In* ASTM International. doi:10.1520/A0370-14.2.
- ASTM-C39. 2012. Standard Test Method for Compressive Strength of Cylindrical Concrete Specimens. : 1–7. ASTM International. doi:10.1520/C0039.
- ASTM D3039/3039M. 2006. Standard Test Method for Tensile Properties of Polymer Matrix Composite Materials. ASTM International.
- Azizinamini, A., Brungardt, P., Hatfield, E., and Kuska, S.S.B. 1994. Seismic behavior of square high-strength concrete columns. *ACI Structural Journal*, **91**(3). doi:10.14359/4362.
- BASF: The Chemical Company. 2007. EMACO® S88 CI. Shakopee, MN, USA.
- Bayrak, O., and Sheikh, S.A. 1997. High-strength concrete columns under simulated earthquake loading. *ACI Structural Journal*, **94**(6): 708–722.
- Bentz, E.C. 2000. Sectional analysis of reinforced concrete members. University of Toronto.
- Bousias, S. 2014. Seismic Hybrid Simulation of Stiff Structures: Overview and Current Advances. *Journal of Structures*, **2014**: 1–8. Hindawi Publishing Corporation. doi:10.1155/2014/825692.
- Bracci, J.M., Reinhorn, A.M., and Mander, J.B. 1992. Seismic Resistance of Reinforced Concrete Frame Structures Designed Only for Gravity Loads - Part I: Design and Properties of a 1/3 Scale Model Structure. National Center for Earthquake Engineering Research (NCEER).
- Carrion, J.E., and Spencer, B.F. 2007. Model-based Strategies for Real-time Hybrid Testing. Urbana-Champaign, Illinois.
- Chang, C.-M., Frankie, T.M., Spencer Jr., B.F., and Kuchma, D.A. 2015. Multiple Degrees of Freedom Positioning Correction for Hybrid Simulation. *Journal of Earthquake Engineering*, **19**(2): 277–296. doi:10.1080/13632469.2014.962670.
- Chopra, A.K. 2007. Dynamics of structures : theory and applications to earthquake engineering. Pearson/Prentice Hall.
- Collins, M.P. 1978. Reinforced Concrete in Combined Shear and Flexure. *In* Mark W. Huggins Symposium.
- Combescure, D., and Pegon, P. 1997. α -Operator splitting time integration technique for pseudodynamic testing error propagation analysis. *Soil Dynamics and Earthquake Engineering*, **16**(7): 427–443. Elsevier. doi:10.1016/S0267-7261(97)00017-1.
- CSA-S448.1-10. 2015. Repair of reinforced concrete in buildings and parking structures. Canadian Standards Association, Rexdale, Ontario, Canada.

- Dermitzakis, S.N., and Mahin, S.A. 1985. Development of Substructuring Techniques for On-Line Computer Controlled Seismic Performance Testing. Earthquake Engineering Research Center, Berkeley, California.
- FEMA 356. 2000. Prestandard and Commentary for the Seismic Rehabilitation of Buildings. Federal Emergency Management Agency.
- FEMA 445. 2006. Next-Generation Performance-Based Seismic Design Guidelines Program Plan for New and Existing Buildings. Federal Emergency Management Agency.
- FEMA P-58-1. 2012. Seismic Performance Assessment of Buildings - Methodology. Federal Emergency Management Agency.
- Ghosh, K.K., and Sheikh, S.A. 2008. Seismic Upgrade with Carbon Fiber-Reinforced Polymer of Columns Containing Lap-Spliced Reinforcing Bars. *ACI Structural Journal*, **104**(104): 227–236.
- Hakuno, M., Shidawara, M., and Hara, T. 1969. Dynamic destructive test of a cantilever beam, controlled by an analog-computer. *Proceedings of the Japan Society of Civil Engineers*, **1969**(171): 1–9. doi:10.2208/jscej1969.1969.171_1.
- Hashemi, M.J., and Mosqueda, G. 2014. Innovative substructuring technique for hybrid simulation of multistory buildings through collapse. *Earthquake Engineering & Structural Dynamics*, **43**(14): 2059–2074. doi:10.1002/eqe.2427.
- Heintz, J.A., Hamburger, R.O., and Mahoney, M. 2014. Development of performance-based seismic design criteria. *In* NCEE 2014 - 10th U.S. National Conference on Earthquake Engineering: Frontiers of Earthquake Engineering. Anchorage, Alaska.
- Hosseini, A., Khaloo, A.R., and Fadaee, S. 2005. Seismic performance of high-strength concrete square columns confined with carbon fiber reinforced polymers (CFRPs). doi:10.1139/105-006.
- Huang, X., and Kwon, O. 2015. Numerical models of RC elements and their impacts on seismic performance assessment. *Earthquake Engineering & Structural Dynamics*, **44**(2): 283–298. doi:10.1002/eqe.2471.
- Huang, X., and Kwon, O. 2017. A Generalized Numerical/Experimental Distributed Simulation Framework. *Journal of Earthquake Engineering*, (in review).
- Huang, X., Sadeghian, V., Rong, F., Kwon, O., and Vecchio, F. 2017. An integrated simulation method for performance-based assessment of a structure. *In* 6th International Conference Engineering Mechanics and Materials.
- Hughes, T.J.R., Pister, K.S., and Taylor, R.L. 1979. Implicit-explicit finite elements in nonlinear transient analysis. *Computer Methods in Applied Mechanics and Engineering*, **17–18**(PART 1): 159–182. doi:10.1016/0045-7825(79)90086-0.
- Iacobucci, R.D., Sheikh, S.A., and Bayrak, O. 2003. Retrofit of Square Concrete Columns with

- Carbon Fiber-Reinforced Polymer for Seismic Resistance. *ACI Structural Journal*, **100**(6): 785–794. doi:10.14359/12845.
- Ibarra, L.F., Medina, R.A., and Krawinkler, H. 2005. Hysteretic models that incorporate strength and stiffness deterioration. *Earthquake Engineering & Structural Dynamics*, **34**(12): 1489–1511. John Wiley & Sons, Ltd. doi:10.1002/eqe.495.
- Jiang, J., and Usmani, A. 2013. Modeling of steel frame structures in fire using OpenSees. *Computers and Structures*, **118**: 90–99. doi:10.1016/j.compstruc.2012.07.013.
- Kam, W.Y., and Jury, R. 2015. Performance-based Seismic Assessment : Myths and Fallacies. *In* 2015 New Zealand Society for Earthquake Engineering (NZSEE). Rotorua, New Zealand.
- Kammula, V., Erochko, J., Kwon, O., and Christopoulos, C. 2014. Application of hybrid-simulation to fragility assessment of the telescoping self-centering energy dissipative bracing system. *Earthquake Engineering & Structural Dynamics*, **43**(6): 811–830. doi:10.1002/eqe.2374.
- Karsan, I.D., and Jirsa, J.O. 1969. Behavior of Concrete Under Compressive Loading. *Journal of the Structural Division*, ASCE,.
- Kazantzi, A.K., and Vamvatsikos, D. 2012. A study on the correlation between dissipated hysteretic energy and seismic performance. *In* 15 World Conference on Earthquake Engineering (WCEE). Lisboa, Portugal.
- Kharal, Z., and Sheikh, S.A. 2014. Tension Stiffening and Cracking Behaviour of GFRP Reinforced Concrete. University of Toronto.
- Kwon, O., and Elnashai, A. 2006. The effect of material and ground motion uncertainty on the seismic vulnerability curves of RC structure. *Engineering Structures*, **28**(2): 289–303. doi:10.1016/j.engstruct.2005.07.010.
- Kwon, O., Elnashai, A.S., and Spencer, B.F. 2008. A framework for distributed analytical and hybrid simulations. *Structural Engineering and Mechanics*, **30**(3): 331–350. doi:10.12989/sem.2008.30.3.331.
- Kwon, O., and Kammula, V. 2013. Model updating method for substructure pseudo-dynamic hybrid simulation. *Earthquake Engineering & Structural Dynamics*, **42**(13): 1971–1984. doi:10.1002/eqe.2307.
- Kwon, O., Kanata, N., Elnashai, A., and Spencer, B. 2005. A framework for multi-site distributed simulation and application to complex structural systems. *Journal of Earthquake Engineering*, **9**(5): 741–753. Imperial College Press.
- Légeron, F., and Paultre, P. 2000. Behavior of high-strength concrete columns under cyclic flexure and constant axial load. *ACI Structural Journal*, **97**(4): 591–601. doi:10.14359/7425.
- Liu, J. 2013. Seismic Behaviour of Reinforced Concrete Columns. University of Toronto.
- Magonette, G. 2001. Development and application of large-scale continuous pseudo-dynamic

- testing techniques. *Philosophical Transactions of the Royal Society A: Mathematical, Physical and Engineering Sciences*, **359**(1786): 1771–1799. doi:10.1098/rsta.2001.0873.
- Mander, J.B., Priestley, M.J.N., and R.Park. 1988. Theoretical Stress Strain Model for Confined Concrete. doi:10.1061/(ASCE)0733-9445(1988)114:8(1804).
- Mazzoni, S., McKenna, F., Scott, M.H., and Fenves, G.L. 2007. OpenSees command language manual. Pacific Earthquake Engineering Research (PEER) Center,: 451.
- McCrum, D.P., and Broderick, B.M. 2013. Evaluation of a substructured soft-real time hybrid test for performing seismic analysis of complex structural systems. *Computers & Structures*, **129**: 111–119. doi:10.1016/j.compstruc.2013.02.009.
- McCrum, D.P., and Williams, M.S. 2016. An overview of seismic hybrid testing of engineering structures. *Engineering Structures*, **118**: 240–261. doi:10.1016/j.engstruct.2016.03.039.
- Memon, M.S., and Sheikh, S.A. 2005. Seismic resistance of square concrete columns retrofitted with glass fiber-reinforced polymer. *ACI Structural Journal*, **102**(5): 774–783. doi:10.14359/14673.
- Moehle, J.P., Ghannoum, W.M., and Bozorgnia, Y. 2006. Collapse of Lightly Confined Reinforced Concrete Frames During Earthquakes. *Advances in Earthquake Engineering for Urban Risk Reduction*, **66**: 317–332. doi:10.1007/1-4020-4571-9_21.
- Molina Ruiz, F.J., Pegon, P., Peroni, M., and Viaccoz, V. 2016. Mixed variable control for enhanced testing quality. Formulation of the model. *In* JRC Scientific and Technical Reports, JRC105052. Publications Office of the European Union.
- Mortazavi, P., Huang, X., Kwon, O., and Christopoulos, C. 2017. Example manual for University of Toronto Simulation (UT-SIM) Framework. An open-source framework for integrated multi-platform simulations for structural resilience (Second edition). *In* International Workshop on Hybrid Simulation. Toronto, Canada. Available from http://www.ut-sim.ca/uploads/7/3/8/6/73867701/ut-sim_manual.pdf.
- Mosqueda, G., and Stojadinović, B. 2008. Hybrid seismic response simulation on a geographically distributed bridge model. *Journal of Structural Engineering, ASCE*, **134**(4): 535–543. doi:10.1061/(ASCE)0733-9445(2008)134:4(535).
- Murray, J.A., and Sasani, M. 2016. Near-collapse response of existing RC building under severe pulse-type ground motion using hybrid simulation. *Earthquake Engineering & Structural Dynamics*, **45**(7): 1109–1127. doi:10.1002/eqe.2698.
- Murray, J.A., Sasani, M., and Shao, X. 2015. Hybrid simulation for system-level structural response. *Engineering Structures*, **103**: 228–238. Elsevier Ltd. doi:10.1016/j.engstruct.2015.09.018.
- Nakashima, M. 2008. Roles of Large Structural Testing for the Advancement of Earthquake Engineering. *In* 14 th World Conference on Earthquake Engineering World Conference on Earthquake Engineering. Beijing, China. pp. 1–10.

- Nakashima, M., Kaminosono, T., Ishida, M., and Ando, K. 1990. Integration techniques for substructure pseudo dynamic test. *In* 4th U.S. National Conference on Earthquake Engineering. pp. 515–524.
- Nakashima, M., and Kato, H. 1987. Experimental error growth behavior and error growth control in on-line computer test control method. *In* BRI-Report No.123.
- Nakashima, M., Kato, H., and Takaoka, E. 1992. Development of real-time pseudo dynamic testing. *Earthquake Engineering & Structural Dynamics*, **21**(1): 79–92. John Wiley & Sons, Ltd. doi:10.1002/eqe.4290210106.
- Nakashima, M., and Masaoka, N. 1999. Real-time on-line test for MDOF systems. *Earthquake Engineering & Structural Dynamics*, **28**(4): 393–420. John Wiley & Sons, Ltd. doi:10.1002/(SICI)1096-9845(199904)28:4<393::AID-EQE823>3.0.CO;2-C.
- National Instruments. 2009. NI USB-621x User Manual. Program, **54A**(April): 2008–2008. Available from <https://www.ni.com/pdf/manuals/371931f.pdf> [accessed 17 May 2017].
- National Instruments. 2016. LabVIEW System Design Software. Available from <http://www.ni.com/labview/>.
- NEHRP Consultants Joint Venture. 2012. Soil-Structure Interaction for Building Structures. *In* NIST GCR. doi:12-917-21.
- Pan, P., Nakashima, M., and Tomofuji, H. 2005. Online test using displacement-force mixed control. *Earthquake Engineering and Structural Dynamics*, **34**(8): 869–888. John Wiley & Sons, Ltd. doi:10.1002/eqe.457.
- Pan, P., Tomofuji, H., Wang, T., Nakashima, M., Ohsaki, M., and Mosalam, K.M. 2006. Development of peer to peer (P2P) internet online hybrid test system. *Earthquake Engineering and Structural Dynamics*, **35**(7): 867–890. John Wiley & Sons, Ltd. doi:10.1002/eqe.561.
- Park, R., and Paulay, T. 1975. Reinforced Concrete Structures. J. Wiley & Sons. doi:10.1002/9780470172322.ch3.
- Paultre, P., Eid, R., Robles, H.I., and Bouaanani, N. 2009. Seismic Performance of Circular High-Strength Concrete Columns. *ACI Structural Journal*, **106**(4): 395–404. doi:10.14359/56605.
- Pegon, P., and Pinto, A. V. 2000. Pseudo-dynamic testing with substructuring at the ELSA laboratory. *Earthquake Engineering and Structural Dynamics*, **29**(7): 905–925. doi:10.1002/1096-9845(200007)29:7<905::AID-EQE941>3.0.CO;2-P.
- Popovics, S. 1973. A numerical approach to the complete stress-strain curve of concrete. *Cement and Concrete Research*, **3**(5): 583–599. doi:10.1016/0008-8846(73)90096-3.
- Priestley, M.J.N. 2000. Performance based seismic design. 12th WCEE, **1**(1): 1–22. doi:10.1016/j.engstruct.2003.08.003.

- Priestley, M.J.N., Seible, F., and Calvi, G.M. 1996. *Seismic Design and Retrofit of Bridges*. John Wiley & Sons, Inc.
- Sadeghian, V., Kwon, O.-S., and Vecchio, F.J. (n.d.). Small-scale multi-axial hybrid simulation of a shear-critical RC frame. *Earthquake Engineering and Engineering Vibration*, (in review).
- Sadeghian, V., Kwon, O., and Vecchio, F. 2015. An integrated framework for the analysis of mixed-type reinforced concrete structures. *In* COMPDYN 2015 - 5th ECCOMAS Thematic Conference on Computational Methods in Structural Dynamics and Earthquake Engineering. pp. 25–27.
- Sadeghian, V., and Vecchio, F. 2015. A graphical user interface for stand-alone and mixed-type modelling of reinforced concrete structures. *Computers and Concrete*, **16**(2): 287–309. doi:10.12989/cac.2015.16.2.287.
- Sadjadi, R., Kianoush, M.R., and Talebi, S. 2007. Seismic performance of reinforced concrete moment resisting frames. *Engineering Structures*, **29**(9): 2365–2380. doi:10.1016/j.engstruct.2006.11.029.
- Sawada, T., Hirao, K., Yamamoto, H., and Tsujihara, O. 1992. Relation between maximum amplitude ratio and spectral parameters of earthquake ground motion. *In* 10th World Conference on Earthquake Engineering. Balkema, Rotterdam, Netherlands.
- Schellenberg, A., Mahin, S. a., and Fenves, G.L. 2007. A Software Framework for Hybrid Simulation of Large Structural Systems. *Structural Engineering Research Frontiers*,: 1–16. doi:10.1061/40944(249)3.
- Schellenberg, A.H., Mahin, S.A., and Fenves, G.L. 2009. Advanced implementation of hybrid simulation. *In* Pacific Earthquake Engineering Research (PEER) Center. Available from <http://nisee.berkeley.edu/elibrary/Text/200912145>.
- Schenk, O., and Gartner, K. 2014. Parallel Sparse Direct Solver PARDISO — User Guide. PARDISO Project, **8097**(203): 0–65. Springer.
- SEAOC Vision2000. 1995. Performance based seismic engineering of buildings. *In* Structural Engineers Association of California. Sacramento, California.
- Sextos, A.G., Bousias, S., Taskari, O., Evangeliou, N., Kwon, O., Elnashai, A., DiSarno, L., and Palios, X. 2014. An intercontinental hybrid simulation experiment for the purpose of seismic assessment of a three-span R/C bridge. *In* NCEE 2014 - 10th U.S. National Conference on Earthquake Engineering: Frontiers of Earthquake Engineering. Anchorage, Alaska. doi:10.4231/D3JD4PQ1X.
- Sheikh, S.A., and Khoury, S.S. 1993. Confined Concrete Columns with Stubs. *ACI Structural Journal*, **90**(4): 414–431. doi:10.14359/3960.
- Sheikh, S.A., Shah, D. V., and Khoury, S.S. 1994. Confinement of high-strength concrete columns. *ACI Structural Journal*, **91**(1): 100–111.

- Sheikh, S.A., and Yau, G. 2002. Seismic behavior of concrete columns confined with steel and fiber-reinforced polymers. *ACI Structural Journal*, **99**(1): 72–80.
- Spencer, B., Finholt, T., Foster, I., Kesselman, C., Beldica, C., Futrelle, J., Gullapalli, S., Hubbard, P., Liming, L., Marcusiu, D., Pearlman, L., Severance, C., and Yang, G. 2004. Neesgrid: A Distributed Collaboratory for Advanced Earthquake Engineering Experimentation and Simulation. 13th World Conference on Earthquake Engineering, 15. Vancouver, Canada.
- Taucer, F.F., and Spacone, E. 1991. A Fiber Beam-Column Element for Seismic Response Analysis of Reinforced Concrete Structures. *In Earthquake Engineering Research Center*. Berkeley, California.
- Tavassoli, A. 2013. Behaviour of GFRP-Reinforced Concrete Columns Under Combined Axial Load and Flexure. University of Toronto. Available from <http://hdl.handle.net/1807/42951>.
- Tavassoli, A. 2015. Behaviour of Circular Concrete Columns Internally Reinforced with Steel and GFRP under Combined Axial Load and Bending. University of Toronto.
- Tavassoli, A., and Sheikh, S.A. 2017. Seismic Resistance of Circular Columns Reinforced with Steel and GFRP. *Journal of Composites for Construction*,. doi:10.1061/(ASCE)CC.1943-5614.0000774.
- Vecchio, F.J. 2000. Disturbed stress field model for reinforced concrete: formulation. *Journal of Structural Engineering*, **126**(9): 1070–1077. doi:10.1061/(ASCE)0733-9445(2000)126:9(1070).
- Vecchio, F.J., and Collins, M.P. 1986. The Modified Compression-Field Theory for Reinforced Concrete Elements Subjected to Shear. *ACI Journal Proceedings*, **83**(2): 925–933. doi:10.14359/10416.
- Vecchio, F.J., and Collins, M.P. 1988. Predicting the Response of Reinforced Concrete Beams Subjected to Shear using the Modified Compression Field Theory. *ACI Structural Journal*, **85**(3): 258–268.
- Wang, K.J., Tsai, K.C., Wang, S.J., Cheng, W.C., and Yang, Y. Sen. 2007. ISEE: Internet-based simulation for earthquake engineering- Part II: The application protocol approach. *Earthquake Engineering and Structural Dynamics*, **36**(15): 2307–2323. John Wiley & Sons, Ltd. doi:10.1002/eqe.729.
- Wang, T., McCormick, J., Yoshitake, N., Pan, P., Murata, Y., and Nakashiman, M. 2008. Collapse simulation of a four-story steel moment frame by a distributed online hybrid test. *Earthquake Engineering and Structural Dynamics*, **37**(6): 955–974. John Wiley & Sons, Ltd. doi:10.1002/eqe.798.
- Watanabe, E., Kitada, T., Kunitomo, S., and Nagata, K. 2001. Parallel pseudodynamic seismic loading test on elevated bridge system through the Internet. *In EASEC-8: The Eighth East Asia-Pacific Conference on Structural Engineering and Construction*. Singapore.

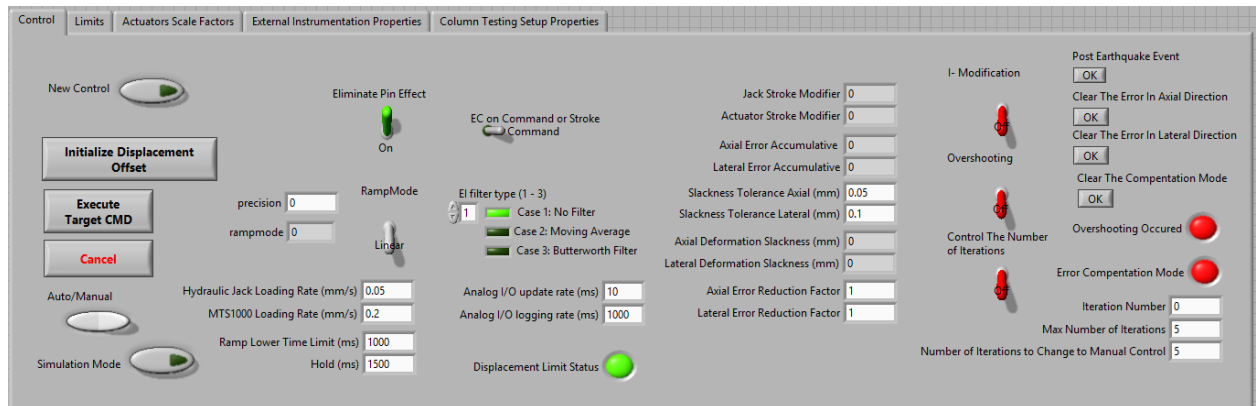
- Whyte, C., and Stojadinovic, B. 2016. Use of a High-Precision Digital Displacement Encoder for Hybrid Simulation of Seismic Response of Stiff Specimens. *Experimental Techniques*, **40**(2): 677–688. Wiley Subscription Services, Inc. doi:10.1007/s40799-016-0069-x.
- Wong, P.S., Vecchio, F.J., and Trommels, H. 2012. *Vector2 & Formworks User's Manual*. University of Toronto.
- Yang, T.Y., Tung, D.P., Li, Y., Lin, J.Y., Li, K., and Guo, W. 2017. Theory and implementation of switch-based hybrid simulation technology for earthquake engineering applications. *Earthquake Engineering & Structural Dynamics*,. doi:10.1002/eqe.2920.
- Yang, Y. Sen, Hsieh, S.H., Tsai, K.C., Wang, S.J., Wang, K.J., Cheng, W.C., and Hsu, C.W. 2007. ISEE: Internet-based simulation for earthquake engineering - Part I: Database approach. *Earthquake Engineering and Structural Dynamics*, **36**(15): 2291–2306. John Wiley & Sons, Ltd. doi:10.1002/eqe.730.
- Zhan, H. 2014. Development of a Generic Controller Interface Program NICON for Multi-Degrees of Freedom PSD Hybrid Simulation Development of a Generic Controller Interface Program NICON for Multi-Degrees of Freedom PSD Hybrid Simulation. University of Toronto.
- Zhan, H., and Kwon, O. 2015. Actuator controller interface program for pseudo-dynamic hybrid simulation. *In Advances in Structural Engineering and Mechanics (ASEM15)*. Incheon, Korea.

Appendix A

The current Appendix is divided in two parts. The first part includes the description of the front panel (user interface) of NICON as developed for the column tester facility in University of Toronto, while the second part is a step-by-step guideline for running hybrid simulation. The discussed NICON version is a modification of the generic version developed by Zhan (Zhan 2014) and more information about the development can be found in his thesis available in University of Toronto T-Space online library.

Front Panel Description – NICON version Dedicated to Column Testing Frame (CTF)

1) *Control Panel:* The control panel is one of the most important tabs in NICON. The control of the test is performed through this tab. The buttons of the Control Panel are described as follows.



- **New Control:** This button is responsible for zeroing all the readings/developing all the offsets after the alignment of the specimen. By hitting this button the actual test of the specimen can be start either by network commands or by manual user input.
- **Initialize Displacement Offset:** This button is required for clear any deformation offset in the specimen at the start of the test. These deformation could be a result of construction deficiencies.
- **Execute Target CMD:** This button is responsible for executing the target command displacement and the target deformation at the specimen is applied.
- **Cancel:** This button stops the command execution and saves the current measured deformation as previous target deformation. In this way the next ramp during the next command starts for the current deformation one without developing any sudden change in the strokes.

- **Auto/Manual:** This switch turn the auto function on and the execution button is automatically activated at each new deformation command. It is proposed the first couple step to be executed in the manual mode of identifying potential inconsistencies.
- **Simulation Mode:** This switch allows for the numerical hybrid simulation using the NICON which is required for verifying all the communication protocols etc. By enabling this switch, the experimental part is skipped, the target command deformation is returned as measured and the restoring forces are calculated using the stiffness matrix defined in the corresponding location. When the error compensation is activated, artificial slackness induced in the returned deformation measurement.
- **Precision:** This value is related to the network communication and correct value is automatically used. Currently, double precision is used for the data communication.
- **Rampmode:** This field is an indicator for the ramp mode employed. The value of 0 is representative for linear mode, while the value of 1 is representative of sine wave mode.
- **Hydraulic Jack/MTS1000 Loading Rate:** These values define the allowable velocity for the jack and the actuator stroke change during the ramp stage.
- **Ramp Lower Time Limit:** This value is the minimum time for the ramp development. During the hybrid simulation the ramp time varies with respect to the stroke change demand and the hydraulics velocity, but it is never lower than the time defined in this field.
- **Hold:** This field is dedicated to the hold time (sec) which is the time interval that no modification occurs after the ramp stage. This stage is required to be defined with respect to the value of the moving average filter employed for the instrumentation.
- **Eliminate Pin Effect:** This switch is responsible for eliminating the pin effect as discussed in Section 6.2.3. The default value is ON, which is the case that the pin effect elimination feature is activated.
- **Ramp Mode:** This switch modifies the ramp mode developed for the stroke change from linear to sine wave. For the case of linear, the stroke is changed linearly with time, while of the sine case, a sine wave is employed for avoiding the sudden change of the hydraulics' strokes.
- **EC on Command or Stroke Command:** This switch allows for the error compensation to occur in the displacement command (default option) or to the stroke command directly. For the first case the updated displacement command (command+slackness) is transformed to actuator strokes, while with the second case only the slackness is transformed to actuator strokes modifying the ones developed from the deformation command transformation. The first case is proposed to be used as it was proven more efficient.

- **EI filter type (1-3):** This switch is responsible for selecting the filter that will be used for the external instrumentation voltage measurements filtering. Case 1 is when no filter is used; Case 2 is when a moving average is employed (proposed filter); and Case 3 is when a Butterworth filter is employed.
- **Analog I/O update/logging rate:** The values of this fields define the update rate (how fast the measurements are performed) and the logging rate (how fast the measurements are saved for post process).
- **Displacement Limit Status:** This indicator is employed for identifying when a displacement limit is tripped. Absolute displacement and displacement increment limits are employed.
- **Jack/Actuator Stroke Modifier:** These fields indicate the integral term of the stroke modification during the error compensation procedure.
- **Axial/Lateral Error Accumulative:** These fields indicate the integral term of the deformation slackness (offset) that is added to each new command for avoiding the relaxation of the specimen.
- **Slackness Tolerance: Axial/Lateral:** In these fields the slackness tolerance is defined for the axial and lateral deformation by the used.
- **Axial/Lateral Deformation Slackness:** These fields indicated the slackness measured at each iteration of the error compensation scheme.
- **Axial/Lateral Error Reduction Factor:** These field were developed for the tuning of the error compensation convergence. The value of the slackness considered at the new iteration of the EC scheme is multiplied by these factors for the axial and lateral direction respectively. For values below 1, under-relaxation occurs, while for values above 1, over-relaxation occurs.
- **I-Modification:** This switch is responsible for activating the I-Modification scheme. When the I-Modification is employed the stiffness matrix definition is required.
- **Overshooting:** This switch is employed for the termination of the error compensation scheme when overshooting occurs. It is a widely employed technique that when the developed deformation is greater than the target one the error compensation stops and the analysis proceeds to the next step.
- **Control The Number of Iterations:** This switch is activated when a specific number of error compensation iterations is allowed. When the iteration number reaches the “Max. Number of Iterations” the error compensation is terminated and the analysis processes to the next time step.

- **Post-Earthquake Event:** This button allows for the continuing of a prematurely terminated test by updating the Communication log file in the NICON folder.
- **Clear the Error in Axial/Lateral Direction:** With these buttons the accumulated error for the axial/lateral direction is cleared. These buttons can be useful for clearing the accumulated slackness error for cases when the error compensation scheme diverges.
- **Clear the Compensation Mode:** This button is used to terminate the error compensation scheme and proceed to the next analysis step.
- **Overshooting Occurred:** This Boolean is an indicator for the cases that overshooting as described previously occurs.
- **Error Compensation Mode:** This Boolean is an indicator for identifying if the procedure is at a new analysis step or iterations within the error compensation scheme occurs.
- **Iteration Number:** This field consist a counter for the iterations number during the error compensation procedure at each analysis step and is reinitialized to zero at each new analysis step.
- **Max. Number of Iterations:** This field is employed for setting the maximum allowable number of iterations when the “Control The Number of Iterations” switch is used.
- **Number of Iterations to Change to Manual Control:** This field is used for changing from auto to manual control when a number of iteration greater that the one set in this field occurs. This is an important tool because it can prevent undesirable stress conditions when the user is not monitoring properly the procedure.

2) *Limit Panel:* The limits panel includes predefined by the user limits for ensuring the safety during the test. The employed limits are described below.

The screenshot shows the 'Limits' panel with the following settings:

Parameter	Value
Displacement Limit 1 - LimitDispMin 1	-40000
Displacement Limit 1 - LimitDispMax 1	40000
Displacement Limit 2 - LimitDispMin 2	-40000
Displacement Limit 2 - LimitDispMax 2	40000
Force Limit 1 - LimitForcMin 1	-1.6E+9
Force Limit 1 - LimitForcMax 1	1.6E+9
Force Limit 2 - LimitForcMin 2	-1.6E+9
Force Limit 2 - LimitForcMax 2	1.6E+9
Displacement Increment Limit 1	0.1
Displacement Increment Limit 2	2
Force Increment Limit 1	1E+7
Force Increment Limit 2	1E+7

- **Displacement Limit:** These limits are defined with respect to the absolute available actuators stroke, in order to ensure that the target stroke can be applied by the equipment.
- **Displacement Increment Limit:** These limits are defined in order to avoid a sudden change in the hydraulics' strokes. When these limits are exceeded the control is turned to manual and the modification of the limits is required for continuing the test.
- **Force Limit:** These limits are defined in accordance with the equipment force limits to ensure the safety of the hydraulics.
- **Force Increment Limit:** Similar to the displacement increment limits, these limits are used to identify a sudden force development and turn the test from auto to manual command.

3) *Actuators Scale Factors Panel*: In this panel the calibration values for the actuators strokes and the load cell readings are defined.

The screenshot shows the 'Actuators Scale Factors' panel with the following data:

Command Output (V) = a+CMD Disp*b			Measured Disp = c+Voltage 1*d			Measured Force = e+Voltage 2*f		
a 1	0	% Dev1/ao0	c 1	0	% Dev1/ai0	e 1	0	% Dev1/ai1
a 2	0	% Dev1/ao1	c 2	0	% Dev1/ai2	e 2	0	% Dev1/ai3
b 1	-0.5		d 1	-15.3994		f 1	-450000	
b 2	-0.05		d 2	-20		f 2	-200000	

- **ai/bi**: These values are employed for the transformation of the displacement command to command voltage output by employing the equation illustrated in the “Actuators Scale Factors” panel.
- **ci/di**: These values are employed for the transformation of the voltage measured at the transducers installed on the hydraulics to measured strokes by employing the equation illustrated in the “Actuators Scale Factors” panel.
- **ei/fi**: These values are employed for the transformation of the measured voltage from the load cells to measured forces by employing the equation illustrated in the “Actuators Scale Factors” panel.

4) *External Instrumentation Properties Panel*: In this panel the calibration values and the geometric characteristics of the external instrumentation are described.

The screenshot shows the 'External Instrumentation Properties' panel. It includes the following data:

External Instrumentation Measured Displacement = g-voltage * h			
g 1	0.46575	h 1	-10.3475
g 2	0.43627	h 2	-10.3878
g 3	-0.080302	h 3	-25.6219
g 4	0.12815	h 4	-10.3182
g 5	-0.69281	h 5	-10.3303
g 6	-0.02504	h 6	-10.3466
g 7	0.40084	h 7	-10.3484
g 8	0.14349	h 8	-10.4341
g 9	-0.38508	h 9	-26.1678
g 10	-0.080302	h 10	-25.6219
g 11	0.88853	h 11	-10.3772
g 12	0.18748	h 12	-10.3873

External Instrumentation Coordinates			
Ei x 1	-1404.63	Ei y 1	-229.032
Ei x 2	-824.161	Ei y 2	-189.404
Ei x 3	-231.415	Ei y 3	-235.172
Ei x 4	331.645	Ei y 4	-201.757
Ei x 5	1610.23	Ei y 5	-238.696
Ei x 6	2188.09	Ei y 6	-197.667
Ei x 7	-1400.66	Ei y 7	-222.004
Ei x 8	-821.619	Ei y 8	-188.518
Ei x 9	-228.963	Ei y 9	-235.171
Ei x 10	331.092	Ei y 10	-202.015
Ei x 11	1614.82	Ei y 11	-236.18
Ei x 12	2192.22	Ei y 12	-191.637

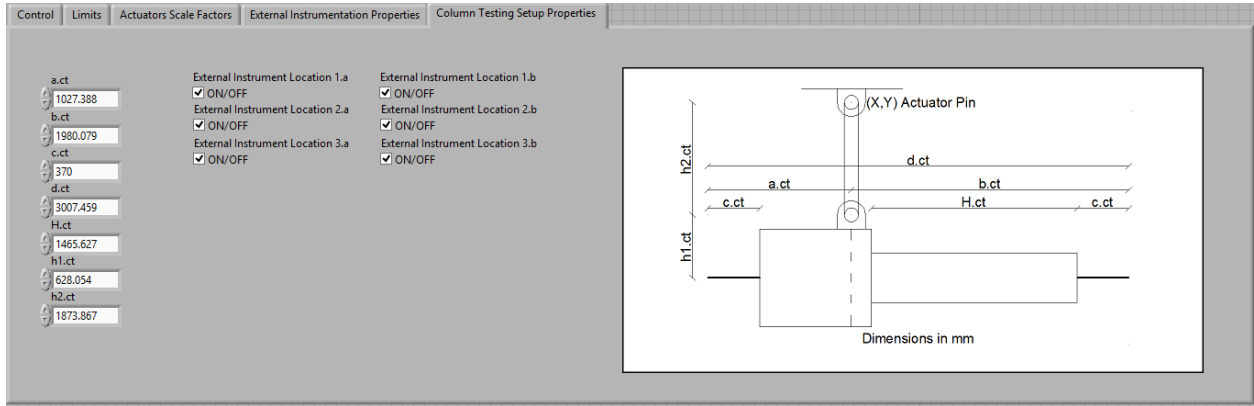
External Instrumentation String Length (mm)	
Ei L 1	988.595
Ei L 2	1107.54
Ei L 3	987.696
Ei L 4	1105.31
Ei L 5	983.597
Ei L 6	1105.29
Ei L 7	978
Ei L 8	1107.2
Ei L 9	982.003
Ei L 10	1099.75
Ei L 11	981.937
Ei L 12	1103.8

The diagram on the right shows a 2D coordinate system with three reference points (1, 2, 3) and their corresponding external instrumentation points (EI 1 through EI 12). It also shows the string lengths (EI L 1 through EI L 12) connecting the reference points to the instrumentation points.

At the bottom, there are three buttons: 'Initialize EI Measurements', 'Error Compensation', and 'Averaging'.

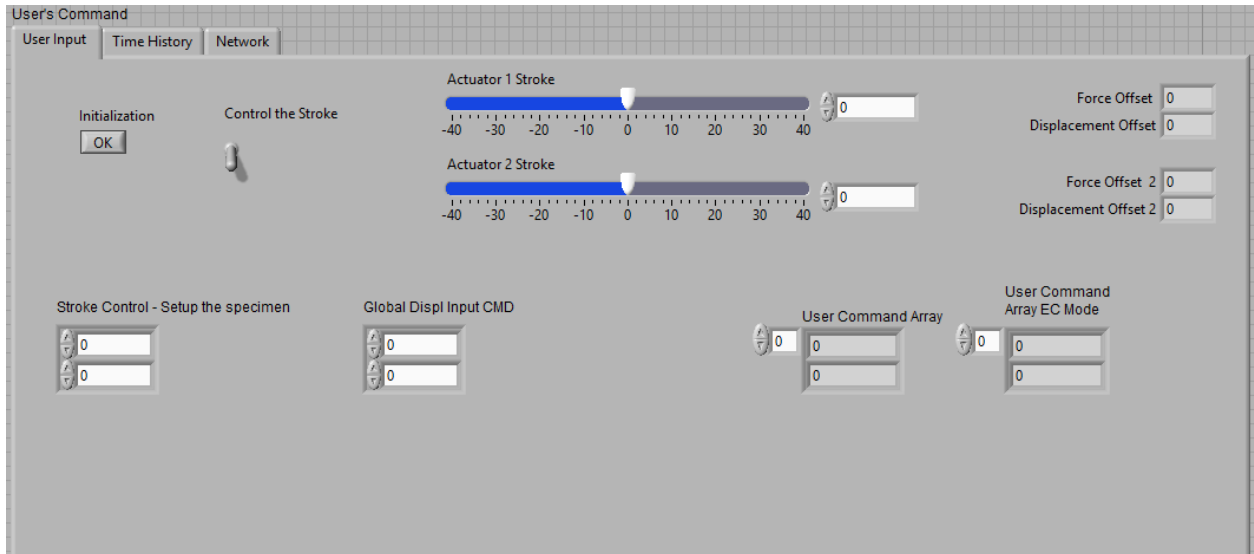
- **g_i/h_i:** These values are employed for the transformation of the measured voltage from the string potentiometers to measured strokes by employing the equation illustrated in the “External Instrumentation Properties” panel. These measurements are used for the specimen’s deformation measurement.
- **Ei x_i/Ei y_i:** These values correspond to the relative coordinates of the external instrumentation as measured with the 3D scanner.
- **Ei L_i:** These values represent the initial length between the instrument position and the strings anchoring position at the start of the test.
- **Initialize EI Measurements:** This button is of significant importance and is used to clear the measurement of the external instruments at the start of the test creating tarred measurements.
- **Error Compensation:** This button is responsible for activation the error compensation scheme.
- **Averaging:** This Boolean is an indicator that the average between the northern and southern measurements is used.

5) *Column Testing Frame Properties Panel:* In this panel geometric properties of the column testing frame and the specimen are presented in addition with the developed feature to turning on/off an instrument at the start or during the test.



- **a/b/c/d/H/h1/h2.ct:** Are the geometric properties as illustrated in the figure included in the “Column Testing Setup Properties” panel.
- **External Instrumentation Location i.a/b (ON/OFF):** These switches are employed for the activation/deactivation of the instruments.

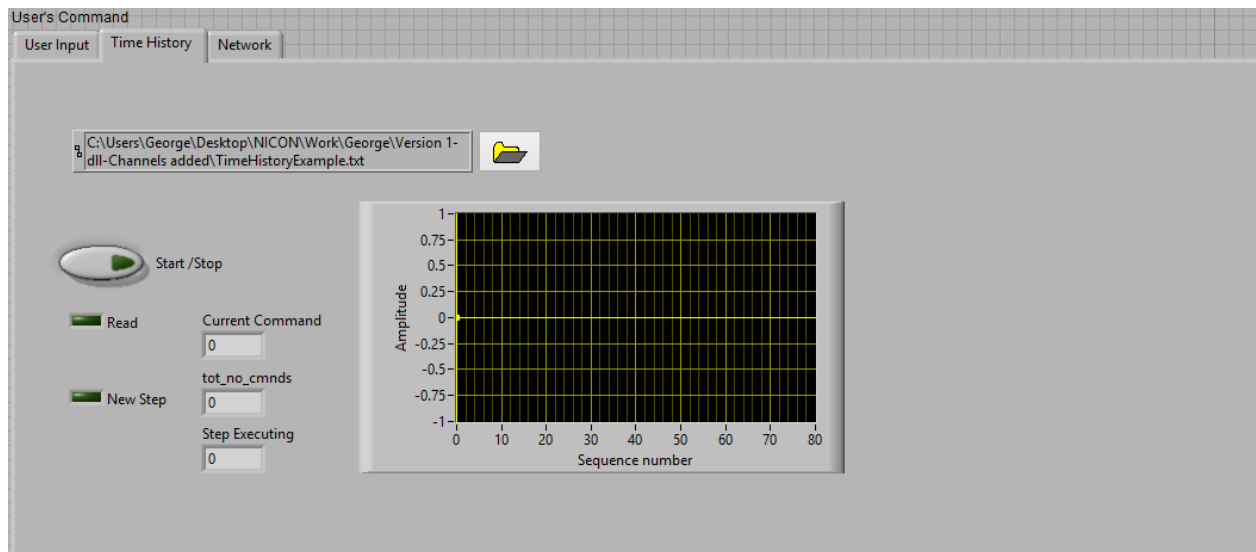
6) *User's Command/User's Input Panel:* This panel includes the features required for the stroke and deformation control. The values can be changed manually from the user when manual control is performed or are updated automatically during hybrid simulation.



- **Initialization:** This button is used for the initialization of the actuators strokes' commands at the current measurements before the start of the experiment in order to avoid a sudden change of their strokes.
- **Control the stroke:** This switch is employed for modifying the manual control of the specimen from direct stroke commands, that can be used for the specimen's alignment, to deformation commands that can be used for the manual testing of the specimen.
- **Actuator 1/2 Stroke:** These sliding bars can be used for manually changing the stroke commands and can be also employed for indicators for the current strokes.
- **Stroke Control – Setup the specimen:** These fields are used for the manual input of stroke commands. This feature is enable when the “Control the stroke” switch is turn on.
- **Global Displ Input CMD:** These fields are employed when the manual control of the specimen's deformation is employed. The first field is used for the lateral deformation and the second for the axial deformation, and for their activation the “Control the stroke” switch should be turned off.
- **User Command Array:** These indicators are used during the hybrid simulation and include the deformation command without the error compensation commands modification.
- **User Command Array EC Mode:** These indicators are used during the hybrid simulation and include the deformation command with the error compensation commands modification.

- **Force/Displacement Offset:** These indicators display the offset in the measurements developed during the initialization and are the values that should be added to the tared values in order to calculate the actual force and measurement readings.

7) *User's Command/Time History Panel:* This panel is used when a predefined deformation time history is going to be used for the specimen's testing. This tab was not employed during this study and requires some further development for the being functional.



- **Start/Stop:** Consists the button employed for the start and the stop of the time history analysis.
- **Read:** Consists an indicator for demonstrating that NICON successfully read the deformation values.
- **New Step:** Consists an indicator for demonstrating the previous step has been completed and a new analysis step can start.
- **Current Command:** Consists an indicator for the current received command.
- **tot_no_cmnds:** Consists an indicator for the total number of the analysis steps.
- **Set Executing:** Consists a counter for tracking the number of the analysis step that is currently executed.
- **File Path:** Demonstrates the path of the time history commands file.

- **Start Communication:** This button is activated when the integration module has been started for the communication establishment.
- **First Event:** This indicator is employed when a hybrid simulation is restored to a previous terminated on and demonstrate the time steps that the feedback from the previous test is returned to the integration module.
- **NC Status:** This indicator is activated when a new deformation command is successfully received from the integration module.
- **Ready to Read the Values:** This indicator is activated when NICON completed the current step and is ready to read a new deformation command from the integration module.
- **Connected:** This indicator is activated when the communication is successfully established.
- **Reporting:** This indicator is activated when NICON reports back to the integration module the restoring forces and the deformation measurements.
- **Waiting CMD:** This indicator is activated when NICON successfully reported back to the integration module and is waiting for the new deformation command.
- **Completed:** This indicator is activated when the test is completed.
- **CMD recvd:** This field demonstrated the command id received from the integration module. The initialization commands are identified by the number 3, the communication commands are identified by the number 10 and the termination command is identified by the number 99.
- **Total No. of Steps:** This feature was employed for demonstrating the total number of the analysis steps but due to the last developments in the communication protocol is not functional any more.
- **Current Step Number:** This field consists a counter for the current analysis step number.
- **Error Compensation Steps:** This field consists a counter for the total error compensation steps occurred during the hybrid simulation.
- **Global Displ CMD:** This array contains the received deformation commands from the integration module as modified by the pin effect elimination procedure.
- **Global CMD Disp Offset:** This array contains the offset developed by the lock offset function that may occur during the specimen's alignment procedure.
- **Global Disp Final:** This array consist the summation of the Global Displ CMD and Global Displ CMD Offset and are the values that are feed in the coordinate transformation scheme.

- **Actuator 1/2 Target Disp:** These fields contain the target strokes are occurred after the coordinate transformation.
- **Error Compensation Target Displacement:** This array includes the hydraulics' strokes after taking into account the error compensations scheme.
- **Global MSD Disp:** This array contains the measured specimen's deformation at the end of an analysis step execution.
- **Global MSD Displ Offset:** This array contains any potential deformation offset at the start of the test which is deducted from the measured deformation before the feedback communication with the integration module.
- **Global MSD Force:** This array contains the measured forces after the force transformation at the end of an analysis step execution.
- **Global MSD Force Offset:** This array contains any potential force offset at the start of the test which is deducted from the measured forces before the feedback communication with the integration module.
- **Measured Disp in Actuators:** This array contains the stroke measurements of the hydraulics at the end of an analysis step execution.
- **Measured Force in Actuators:** This array contains the load cells' force measurements at the end of an analysis step execution.
- **Output to OpenSees (I-mod):** This array contains the measured deformation and the restoring forces after the I-modification, as fed back to the integration module.

9) *Digital Monitor Panel Tab/Actuator Command/Measurements*: This panel contains the digital measurements and commands values of the hydraulics.

- **Previous Target Disp:** This field contains the previous command target stroke and is updated at the end of a command execution or when the execution is cancelled.
- **Current Target Disp:** This field contains the new target stroke command.
- **Current Command Disp:** This field contains the stroke command as modified during the ramp stage in order to achieve the target stroke command.
- **Current Measured Disp:** This field contains the measured strokes of the hydraulics. These measurements may not be identical with the Current Command Disp or a delay related to the consistency of these fields may be observed.
- **Previous Command Disp, mm:** This field is employed for the stroke increment limit check between each time step.
- **Voltage output to controller (command), V:** This field contains the voltage output value from the DAQ to the controlled.
- **Measured Disp, V:** This field contains the voltage input for the stroke measurements.
- **Measured Displacement, mm:** This field contains the absolute stroke measurements after the transformation from voltage to displacement values.
- **Measured Force, V:** This field contains the voltage input for the force measurements.
- **Measured Force, N:** This field contains the absolute force measurements after the transformation from voltage to displacement values.

10) *Digital Monitor Panel Tab/External Instrumentation Measurements*: This panel contains the measurements performed with the External Instrumentation (String Potentiometers).

Digital Monitor Panel Tab

Actuator Command/Measured External Instrumentation Measurements

EI Meas. - Volt, 1	0	EI Meas. - Volt, 2	0	EI Meas. - Volt, 3	0	EI Meas. - Volt, 4	0	EI Meas. - Volt, 5	0	EI Meas. - Volt, 6	0
EI Meas. - Actual Disp (mm), 1	0.46575	EI Meas. - Actual Disp (mm), 2	0.43627	EI Meas. - Actual Disp (mm), 3	-0.08030	EI Meas. - Actual Disp (mm), 4	0.12815	EI Meas. - Actual Disp (mm), 5	-0.69281	EI Meas. - Actual Disp (mm), 6	-0.02504
EI Meas. - Offset (mm), 1	0	EI Meas. - Offset (mm), 2	0	EI Meas. - Offset (mm), 3	0	EI Meas. - Offset (mm), 4	0	EI Meas. - Offset (mm), 5	0	EI Meas. - Offset (mm), 6	0
EI Meas. - Tared Disp (mm), 1	0.46575	EI Meas. - Tared Disp (mm), 2	0.43627	EI Meas. - Tared Disp (mm), 3	-0.08030	EI Meas. - Tared Disp (mm), 4	0.12815	EI Meas. - Tared Disp (mm), 5	-0.69281	EI Meas. - Tared Disp (mm), 6	-0.02504
EI Meas. - Volt, 7	0	EI Meas. - Volt, 8	0	EI Meas. - Volt, 9	0	EI Meas. - Volt, 10	0	EI Meas. - Volt, 11	0	EI Meas. - Volt, 12	0
EI Meas. - Actual Disp (mm), 7	0.40084	EI Meas. - Actual Disp (mm), 8	0.14349	EI Meas. - Actual Disp (mm), 9	-0.38500	EI Meas. - Actual Disp (mm), 10	-0.08030	EI Meas. - Actual Disp (mm), 11	0.88853	EI Meas. - Actual Disp (mm), 12	0.18748
EI Meas. - Offset (mm), 7	0	EI Meas. - Offset (mm), 8	0	EI Meas. - Offset (mm), 9	0	EI Meas. - Offset (mm), 10	0	EI Meas. - Offset (mm), 11	0	EI Meas. - Offset (mm), 12	0
EI Meas. - Tared Disp (mm), 7	0.40084	EI Meas. - Tared Disp (mm), 8	0.14349	EI Meas. - Tared Disp (mm), 9	-0.38500	EI Meas. - Tared Disp (mm), 10	-0.08030	EI Meas. - Tared Disp (mm), 11	0.88853	EI Meas. - Tared Disp (mm), 12	0.18748

Coordinates of Reference Points

X Reference Point 1.a	-1395.37	X Reference Point 2.a	-226.496	X Reference Point 3.a	1609.73	X Reference Point 4.a	-361.676	X Reference Point 5.a	-355.111	X Reference Point 6.a	-362.922
Y Reference Point 1.a	759.985	Y Reference Point 2.a	752.432	Y Reference Point 3.a	744.208	Y Reference Point 4.a	1383.63	Y Reference Point 5.a	3252.07	Y Reference Point 6.a	756.798
X Reference Point 1.b	-1398.95	X Reference Point 2.b	-225.426	X Reference Point 3.b	1610.47	X Reference Point 4.b	-373.831	X Reference Point 5.b	-355.111	X Reference Point 6.b	-377.021
Y Reference Point 1.b	756.395	Y Reference Point 2.b	746.441	Y Reference Point 3.b	746.636	Y Reference Point 4.b	1372.87	Y Reference Point 5.b	3252.07	Y Reference Point 6.b	743.602

Averaged Coordinates and Specimen Deformation

X Reference Point 1	-1397.1	X Reference Point 2	-225.961	X Reference Point 3	1610.1	X Reference Point 4	-367.751	X Reference Point 5	-355.111	X Reference Point 6	-369.971
Y Reference Point 1	758.19	Y Reference Point 2	749.436	Y Reference Point 3	745.422	Y Reference Point 4	1378.25	Y Reference Point 5	3252.07	Y Reference Point 6	750.2
Angle at Ref. Point 1	-0.0032	Angle at Ref. Point 2	3.1363	Angle at Ref. Point 3	0.00205	Angle of the neutral axis	-0.0042	Axial Deformation	0.416113	Lateral Deformation	-9.70897

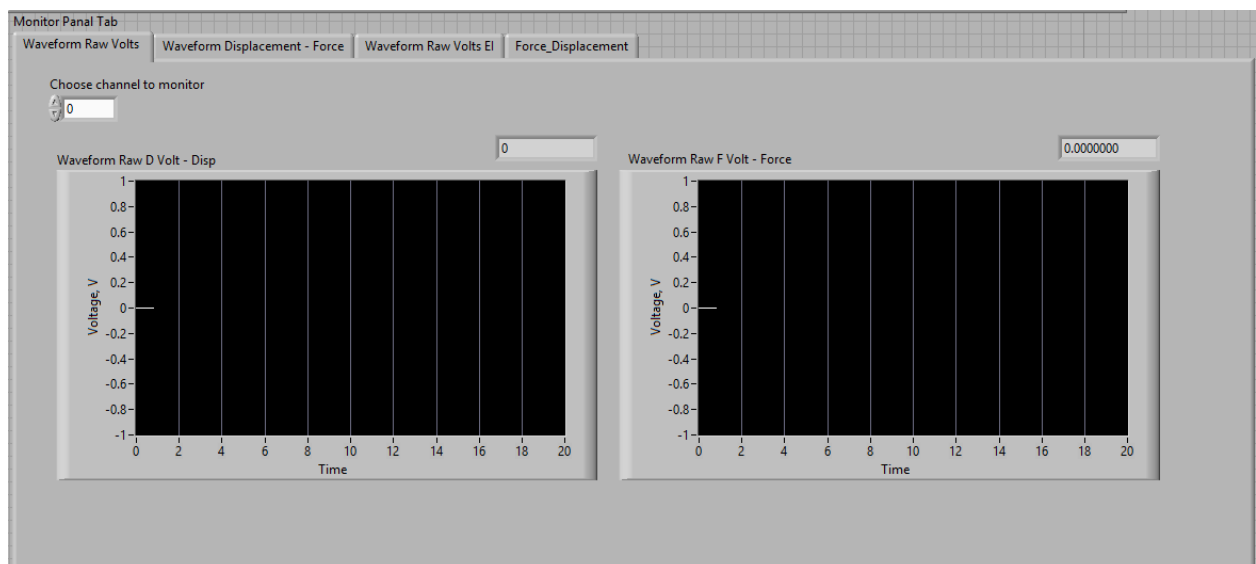
Use of Moving Average into Deformation: Moving Average 100

If this function is used, consider the filtering of the input. The readings may be filtered twice.

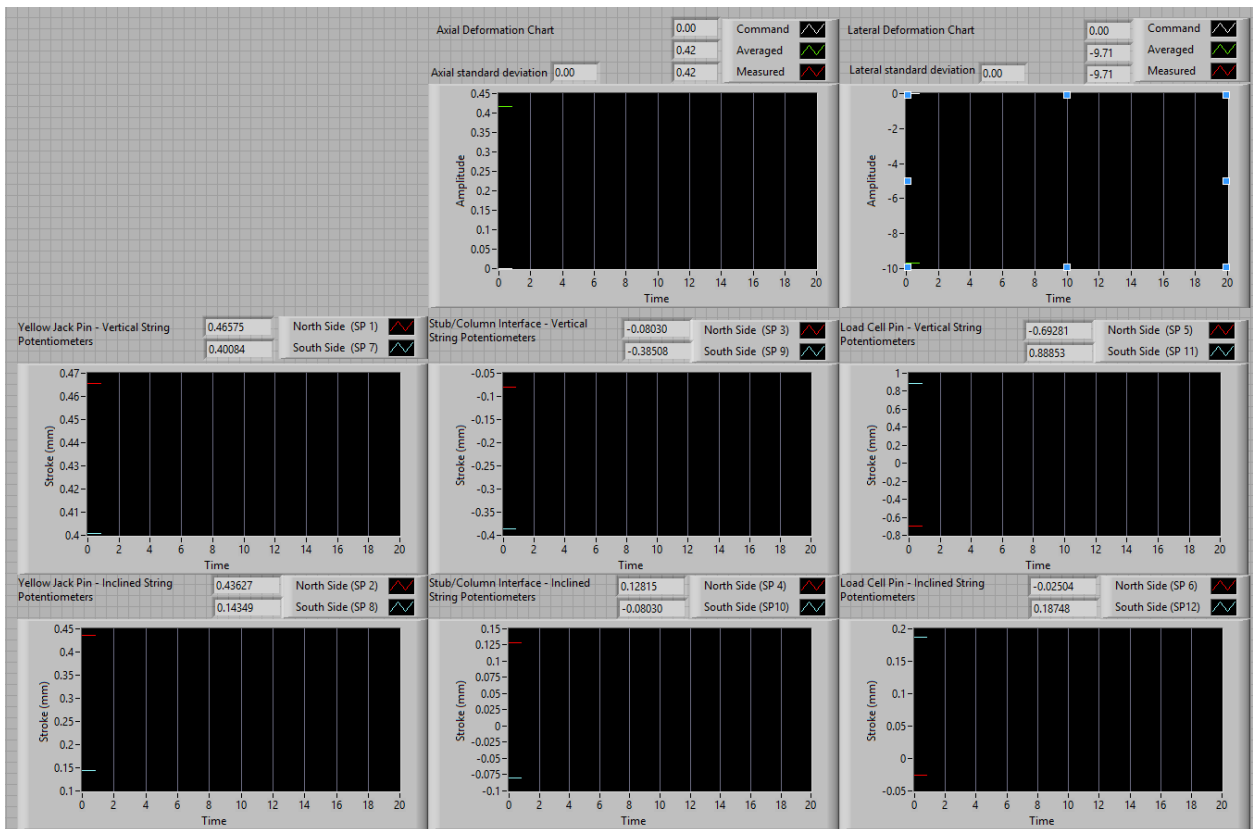
- **EI Meas. - Volt:** This field contains the voltage measurement for the string potentiometers.
- **EI Meas. – Actual Disp (mm):** This field contains the stroke measurements for the string potentiometers.
- **EI Meas. – Offset (mm):** This field contains the offset of the string potentiometer measurement developed at the start of the test.
- **EI Meas. – Tared Disp (mm):** This field contains the string potentiometers' tared measurement (Actual-Offset).
- **X/Y Reference Point i:** This field contains the X and Y relative coordinates of the reference points as measured with the string potentiometer employed instrumentation.
- **Angle at Ref. Point i:** This field contains the angles developed during the lateral deformation at the reference points, which are used for the actual deformation measurement.
- **Angle of the neutral axis:** This field contains horizontal rotation of the specimen due to the pins slackness.
- **Axial/Lateral Deformation:** These field contain the raw (unfiltered) axial and lateral deformation measurements.

- **Moving Average:** This field contains the number of the measurements employed for the moving average filter.
- **Use of Moving Average into Deformation:** This switch allows for the filtering directly at the deformation measurement after the coordinate transformation of the string potentiometers measurements. The filtering directly in the string potentiometers measurements is proposed instead of the filtering employing by this switch.

11) Monitor Panel Tab: This panel allows for the monitoring of the measurement described in the Digital Monitor Panel Tab in waveform representation. This can be achieved by selection the proper tab (Waveform Raw/Voltage Displacement – Force/Waveform Raw Volts EI/Force Displacement) and by selecting a specific channel to monitor.




14) *Monitoring Panels:* These panels were developed for monitoring the axial and lateral deformation and the external instrumentation measurements. For the deformation charts both the command deformations and the averaged (filter) and the measured (raw) deformations are presented. For the instrumentation measurement charts the instruments are grouped with respect to their position (Jack Pin/ Stub-Column Interface/Load Cell Pin) and with respect to their alignment (Inclined/Vertical). Both the measurements of the north and the south face instruments are presented.



Hybrid Simulation Step-by-Step Guideline

In this section the step-by-step procedure for running hybrid simulation using the developed NICON is described. This component is equivalent to the Substructure 1 (NICA1) described in Appendix B, and one of them have to be employed each time. All the aforementioned features can be employed, but in this section the typical experiment case is described. The steps for performing experimental hybrid simulation as summarized as follows.

- 1) Specimen Alignment: The specimen is proposed to be aligned using the MTS Flextest40 terminal for robust accuracy. In such cases the offsets can be clear from the HBM and the implementation on NICON becomes straight forward.
- 2) The NICON is activated by the “Run” button . This should occur after the initialization of the HBM controller.
- 3) Next, the EI filter type in the control tab is selected. The proposed filter is the moving average.
- 4) The external instrument configuration should be activated/deactivated given the testing setup in the Column Testing Frame Properties.
- 5) Next, the external instruments’ measurements are initialized by the “Initialize EI Measurements” button in “External Instrumentation Properties” tab. In the same tab the “Error Compensation” mode should be activated/deactivated given the experiment performed.
- 6) Consequently, the stroke measurements are initialized by the “Initialization” button in “User Input” tab.
- 7) In the “Control” tab the “RampMode” is selected in addition with the desired error compensation properties as described in the previous section. Next the “New Control” button is activated and the platform becomes initialized for the hybrid simulation.
- 8) If a purely numerical representation of the test is performed the button “Simulation Mode” is activated.
- 9) If a continuing analysis is performed the button “Post Earthquake Event” is activated.

- 10) Next, in the “Network” tab, the “Lock Offset” and the “Start Server” buttons are activated. At this stage NICON is ready for the communication with the integration module.
- 11) When the NICON is initialized, the surrogate modules is and the integration module OpenSees scripts are run. If everything is properly set, the indicator “Connected” is turned on.
- 12) When the connection is properly established, the “Start Communication” button can be activated and the test can be started by activating the “Execute Target CMD displacement”.
- 13) After performing some analysis steps manually, the control can be modified to “Auto” and the hybrid simulation will be performed automatically.
- 14) The optimum values for the Axial and Lateral Error Reduction Factors during the experiments performed in this study were 0.7~1.0 given the convergence performance of the deformations during the iterative procedure.
- 15) When the test is over, the “Completed” indicator is the “Network” tab is activated, and the analysis in the integration and the surrogate model substructures are completed. At this stage, NICON can be turned off and all the log files are ready for the post-process.

Appendix B

In the current section, the required files and the developed scripts for running an OpenSees standalone and a multi-platform WCHS analysis are presented. For running WCHS the required files are listed for each substructure separately. The developed scripts are ones employed for the test performed with the first specimen and the intact structure case.

OpenSees Standalone – Reference Case

In order to develop a straightforward and easy to follow .tcl file, multiple scripts are called from the main script named “maingm.tcl”. Initially, the main .tcl file is presented and subsequently the .tcl files called from the main file are presented with the same sequence as called from the main file. The files required for running the OpenSees standalone study are summarized as follows.

- 1) *maingm.tcl*: the main OpenSees file responsible for running the ground motion analysis
- 2) *nodes.tcl*: the file that contains the definition and the coordinates of the structure’s nodes
- 3) *BC.tcl*: the file that contains the boundary conditions of the structure (Fixation, equalDOF)
- 4) *material.tcl*: the file that contains the material properties as described in Chapter 4
- 5) *beamsections.tcl*: the file that contains the definition of the beam sections
- 6) *columnsections.tcl*: the file that contains the definition of the column sections
- 7) *beamelements.tcl*: the file that contains the definition and the connectivity of the beam elements
- 8) *columnelements.tcl*: the file that contains the definition and the connectivity of the column elements
- 9) *masses.tcl*: the file that contains the masses of the structure
- 10) *loads.tcl*: the file that contains the gravity loads applied on the structure
- 11) *AnalysisCommand.tcl*: the file that contains the analysis commands for the dynamic ground motion analysis

The script developed for each of the aforementioned .tcl files is presented as follows.

1) Main Ground Motion Analysis .tcl File: "maingm.tcl"

```
#####
####Frame Building - Georgios Giotis - MASc Thesis####
=====
#units mm, MPa, sec, N
wipe;
file mkdir OutputGM;
model basic -ndm 2 -ndf 3;

set weightfact 1;
set gmfactor 1;

puts "
#####
Georgios Giotis - MASc Thesis
Three Storey - Three Bay RC Building
#####
"

puts "Analysis Units: mm, MPa, N, sec"
#Geometry Definition
puts "
Geometry Definition:
  Create Nodes..."
source nodes.tcl
puts " Create Boundary Conditions..."
source BC.tcl
puts "Done"

#Materials Definition
puts "
Material Definition:"
source materials.tcl
puts "Done"
#Sections Definition
puts "
Beam Sections Definition:"
source beamsections.tcl
puts "Done"
puts "
Column Sections Definition:"
source columnsections.tcl
puts "Done"

#Elements Definition
puts "
Create Elements:"
geomTransf Linear 1;
geomTransf PDelta 2;
geomTransf Corotational 3;set np 9;
set columntransf 2;
set beamtransf 2;
source columnelements.tcl
source beamelements.tcl
puts "Done"
```

```

#Assign Masses
puts "
Assign Masses:"
set mass 17.8; #tn or N sec2 / mm
source masses.tcl
puts "Done"

#Create Recorders
recorder Node -file [format "OutputGM/NodesDisp.out"] -time -nodes 1 2 3 4 11 12 13 14 21 22 23 24 31 32 33
34 41 42 43 44 51 52 53 54 101 102 103 104 111 112 113 114 121 122 123 124 131 132 133 134 141 142 143
144 151 152 153 154 201 202 203 204 211 212 213 214 221 222 223 224 231 232 233 234 241 242 243 244 251
252 253 254 301 302 303 304 1101 1102 1103 1104 1105 1106 1111 1112 1113 1114 1115 1116 1121 1122
1123 1124 1125 1126 1201 1202 1203 1204 1205 1206 1211 1212 1213 1214 1215 1216 1221 1222 1223 1224
1225 1226 1301 1302 1303 1304 1305 1306 1311 1312 1313 1314 1315 1316 1321 1322 1323 1324 1325 1326
-dof 1 2 3 disp;
recorder Node -file [format "OutputGM/Node1R.out"] -time -node 1 -dof 1 2 3 reaction;
recorder Node -file [format "OutputGM/Node2R.out"] -time -node 2 -dof 1 2 3 reaction;
recorder Node -file [format "OutputGM/Node3R.out"] -time -node 3 -dof 1 2 3 reaction;
recorder Node -file [format "OutputGM/Node4R.out"] -time -node 4 -dof 1 2 3 reaction;

#Recorders for the moment curvature relationship
#1st column
recorder Element -ele 01 -file [format "OutputGM/C1S1D.out"] -time section 1 deformations
recorder Element -ele 01 -file [format "OutputGM/C1S1F.out"] -time section 1 force
#2nd column
recorder Element -ele 11 -file [format "OutputGM/C2S1D.out"] -time section 1 deformations
recorder Element -ele 11 -file [format "OutputGM/C2S1F.out"] -time section 1 force
#3rd column
recorder Element -ele 21 -file [format "OutputGM/C3S1D.out"] -time section 1 deformations
recorder Element -ele 21 -file [format "OutputGM/C3S1F.out"] -time section 1 force
#4th column
recorder Element -ele 31 -file [format "OutputGM/C4S1D.out"] -time section 1 deformations
recorder Element -ele 31 -file [format "OutputGM/C4S1F.out"] -time section 1 force

recorder Element -ele 23 -file [format "OutputGM/InterfaceLocalForces.out"] -time localForce
recorder Element -ele 23 -file [format "OutputGM/InterfaceSection9forces.out"] -time section 1 force
recorder Element -ele 23 -file [format "OutputGM/InterfaceSection9deformations.out"] -time section 1
deformation
recorder Element -ele 23 -file [format "OutputGM/InterfaceLocalFiber1.out"] -time section 1 fiber -177.8 0
stressStrain
recorder Element -ele 23 -file [format "OutputGM/InterfaceLocalFiber2.out"] -time section 1 fiber 0 0
stressStrain
recorder Element -ele 23 -file [format "OutputGM/InterfaceLocalFiber3.out"] -time section 1 fiber 177.8 0
stressStrain
recorder Element -ele 23 -file [format "OutputGM/InterfaceLocalFiber4.out"] -time section 1 fiber 0 177.8
stressStrain
recorder Element -ele 23 -file [format "OutputGM/InterfaceLocalFiber5.out"] -time section 1 fiber 0 -177.8
stressStrain
recorder Element -ele 21 26 -file [format "OutputGM/Confpoint.out"] -time localForce

```

```

#Eigenvalue Analysis
puts "
Eigenvalue Analysis:"
set numModes 3;
for { set k 1 } { $k <= $numModes } { incr k } {
    recorder Node -file [format "OutputGM/mode%i.out" $k] -node 1 101 201 301 -dof 1 "eigen $k"
}
set lambda [eigen $numModes];
set omega {}
set f {}
set T {}
set pi 3.141593
foreach lam $lambda {
    lappend omega [expr sqrt($lam)]
    lappend f [expr sqrt($lam)/(2*$pi)]
    lappend T [expr (2*$pi)/sqrt($lam)]
}
puts " The time periods are: $T"
set period "OutputGM/Periods.txt"
set Periods [open $period "w"]
foreach t $T {
    puts $Periods " $t"
};
close $Periods
record
wipeAnalysis;
#Gravity Analysis
puts "Gravity Analysis:"
pattern Plain 1 Linear {
source gravityloads.tcl
};
set Tol 1.0e-6;                                # convergence tolerance for test
set NGSteps 10;                                # number of gravity load steps
constraints Plain;                              # how it handles boundary conditions
numberer RCM;                                  # renumber dof's to minimize band-width
(optimize), if you want to
system BandGeneral ;                           # how to store and solve the system of equations in the analysis
(large model: try UmfPack)
test NormDispIncr $Tol 2000 5;                  # determine if convergence has been achieved at the end
of an iteration step
algorithm ModifiedNewton -initial;
#algorithm NewtonLineSearch 0.8;                # use Newton's solution algorithm: updates
tangent stiffness at every iteration
integrator LoadControl [expr 1.0/$NGSteps];    # determine the next time step for an analysis
analysis Static;                                # define type of analysis static or transient

# run analysis -----
analyze $NGSteps;                               # apply gravity
#Maintain Constant Gravity Load
loadConst -time 0.0
puts "Gravity Analysis Done!"

```

```

# _____ GM ANALYSIS _____ # Start
set GMdirection 1; # ground-motion direction
set GMfile "Bucharest-14.5-cm2s-0.01" ; # ground-motion filenames
set GMfact [expr (1/(100*9.81))]; # ground-motion scaling factor
# set up ground-motion-analysis parameters
set DtAnalysis 0.01; # time-step Dt for lateral analysis
set TmaxAnalysis 43.51; # maximum duration of ground-motion analysis -- should be 50*$sec
# ----- set up analysis parameters
source AnalysisCommand.tcl; # constraintsHandler,DOFnumberer,system-
ofequations,convergenceTest,solutionAlgorithm,integrator
# ----- define & apply damping
# RAYLEIGH damping parameters, Where to put M/K-prop damping, switches
(http://opensees.berkeley.edu/OpenSees/manuals/usermanual/1099.htm)
# D=$alphaM*M + $betaKcurr*Kcurrent + $betaKcomm*KlastCommit + $beatKinit*$Kinitial
set xDamp 0.05; # damping ratio
set MpropSwitch 1.0; ###???
set KcurrSwitch 0.0; ###???
set KcommSwitch 1.0; ###???
set KinitSwitch 0.0; ###???
set nEigenI 1; # mode 1
set nEigenJ 3; # mode 3
set lambdaN [eigen 3]; # eigenvalue analysis for nEigenJ modes
set lambdaI [lindex $lambdaN [expr $nEigenI-1]]; # eigenvalue mode 1
set lambdaJ [lindex $lambdaN [expr $nEigenJ-1]]; # eigenvalue mode 3
set omegaI [expr pow($lambdaI,0.5)];
set omegaJ [expr pow($lambdaJ,0.5)];
set alphaM [expr $MpropSwitch*$xDamp*(2*$omegaI*$omegaJ)/($omegaI+$omegaJ)];

# M-prop. damping; D = alphaM*M
set betaKcurr [expr $KcurrSwitch*2.*$xDamp/($omegaI+$omegaJ)]; # current-K;
+beatKcurr*KCurrent
set betaKcomm [expr $KcommSwitch*2.*$xDamp/($omegaI+$omegaJ)]; # last-committed
K; +betaKcomm*KlastCommitt
set betaKinit [expr $KinitSwitch*2.*$xDamp/($omegaI+$omegaJ)]; # initial-K; +beatKinit*Kini
#set alphaM 1.653190569742563
#set betaKcurr 0
#set betaKinit 8.402979944748105e-05
#set betaKcomm 0

rayleigh $alphaM $betaKcurr $betaKinit $betaKcomm; # RAYLEIGH
damping
puts "GM analyses start"
# ----- perform Dynamic Ground-Motion Analysis
# the following commands are unique to the Uniform Earthquake excitation
set IDloadTag 400; # for uniformSupport excitation
# Uniform EXCITATION: acceleration input
# set inFile $GMDir$GMfile.at2
set outFile $GMfile.txt; # set variable holding new filename (PEER files have .at2/dt2 extension)
# ReadSMDFile $inFile $outFile dt; # call procedure to convert the ground-motion file
set GMfatt [expr $gmfactor*9810*$GMfact]; # data in input file is in g Units --
ACCELERATION TH
set AccelSeries "Series -dt 0.01 -filePath $outFile -factor $GMfatt"; # time series information
pattern UniformExcitation $IDloadTag $GMdirection -accel $AccelSeries ; # create Uniform
excitation

set Nsteps [expr int($TmaxAnalysis/$DtAnalysis)];
set ok [analyze $Nsteps $DtAnalysis]; # actually perform anal

wipe all;

```


3) Boundary Conditions .tcl File: "BC.tcl"

```
#boundary conditions: Fixations & equalDOF
#fixations
#fix-    node-    DOFx- DOFy- DOFz  ;
fix      1 1 1 1 ;
fix      2 1 1 1 ;
fix      3 1 1 1 ;
fix      4 1 1 1 ;
#diaphragm at each storey
#equalDOF-    master node-    slave node-    DOFs  ;
equalDOF      101      102      1;
equalDOF      101      103      1;
equalDOF      101      104      1;

equalDOF      201      202      1;
equalDOF      201      203      1;
equalDOF      201      204      1;

equalDOF      301      302      1;
equalDOF      301      303      1;
equalDOF      301      304      1;
```

4) Material Properties .tcl File: "material.tcl"

```
puts " Create Identifiers..."
set MTag_UnConf 1; #Unconfined Concrete
set MTag_ConfCM 2; #Confined Concrete for the middle part of the columns
set MTag_ConfCE 3; #Confined Concrete for the end part of the columns
set MTag_ConfCB 4; #Confined Concrete for the beams
set MTag_SteelM20 5; #Steel for the longitudinal bars of the columns
set MTag_SteelG60 6; #Steel for the rest

puts " Create Material..."

##Unconfined Concrete
set fpc -41.16; # concrete compressive strength at 28 days (compression is negative)
set epsc0 -0.00192; # concrete strain at maximum strength
set epsU -0.02;#-0.00546; # concrete strain at crushing strength
#set Ec [expr $fpc*(2)/$epsc0];
set Ec [expr 57000.0 * [expr {sqrt($fpc*(-145.0374))} ]/ 145.0374]
uniaxialMaterial Concrete04 $MTag_UnConf $fpc $epsc0 $epsU $Ec
#uniaxialMaterial Concrete04 $MTag_ConfCM $fpc $epsc0 $epsU $Ec
#uniaxialMaterial Concrete04 $MTag_ConfCE $fpc $epsc0 $epsU $Ec
#uniaxialMaterial Concrete04 $MTag_ConfCB $fpc $epsc0 $epsU $Ec

##Confined Concrete Column-Middle
set fpcCM -43.54; # concrete compressive strength at 28 days (compression is negative)
set epsc0CM -0.002495; # concrete strain at maximum strength
set epsUCM -0.02;#-0.01035;#-0.00477; # concrete strain at crushing strength
#set Ec [expr 57000.0 * [expr {sqrt($fpc*(-145.0374))} ]/ 145.0374] ; ## Elasticity modulus is the same
uniaxialMaterial Concrete04 $MTag_ConfCM $fpcCM $epsc0CM $epsUCM $Ec
```

##Confined Concrete Column-End

```

set fpcCE -48.07;      # concrete compressive strength at 28 days (compression is negative)
set epsc0CE -0.003508; # concrete strain at maximum strength
set epsUCE -0.02;#-0.01531;#-0.0054; # concrete strain at crushing strength
#set Ec [expr 57000.0 * [expr {sqrt($fpc*(-145.0374))} ]/ 145.0374] ; ## Elasticity modulus is the same
uniaxialMaterial Concrete04 $MTag_ConfCE $fpcCE $epsc0CE $epsUCE $Ec

```

##Confined Concrete Beam: same for all the confined part of the beams

```

set fpcB -41.42;      # concrete compressive strength at 28 days (compression is negative)
set epsc0B -0.002029; # concrete strain at maximum strength
set epsUB -0.02;#-0.007673; # concrete strain at crushing strength
#set Ec [expr 57000.0 * [expr {sqrt($fpc*(-145.0374))} ]/ 145.0374] ; ## Elasticity modulus is the same
uniaxialMaterial Concrete04 $MTag_ConfCB $fpcB $epsc0B $epsUB $Ec

```

Steel materials

```

set FyM20 400;          # STEEL yield stress
set EsM20 191555;       # modulus of steel
set BsM20 0.005;        # strain-hardening ratio
set FuM20 550;          # Ultimate stress in tension
set EshM20 5000;        # Tangent at initial strain hardening
set eshM20 0.015;       # Strain corresponding to initial strain hardening
set eultM20 0.164;      # Strain at peak stress
#uniaxialMaterial Steel01 $MTag_SteelM20 $FyM20 $EsM20 $BsM20
uniaxialMaterial ReinforcingSteel $MTag_SteelM20 $FyM20 $FuM20 $EsM20 $EshM20 $eshM20 $eultM20

```

Steel materials

```

set FyG60 435;          # STEEL yield stress
set EsG60 196500;       # modulus of steel
set BsG60 0.005;        # strain-hardening ratio
set FuG60 656;          # Ultimate stress in tension
set EshG60 7200;        # Tangent at initial strain hardening
set eshG60 0.0145;      # Strain corresponding to initial strain hardening
set eultG60 0.13;       # Strain at peak stress
#uniaxialMaterial Steel01 $MTag_SteelG60 $FyG60 $EsG60 $BsG60
uniaxialMaterial ReinforcingSteel $MTag_SteelG60 $FyG60 $FuG60 $EsG60 $EshG60 $eshG60 $eultG60

```

5) Beam Sections' Definition .tcl File: "beamsections.tcl"

```

puts " Create Identifiers..."
set STag_BeamA 1;
set STag_BeamB 2;
set STag_BeamC 3;
set STag_BeamD 4;
set STag_BeamE 5;
set STag_BeamF 6;

set A5 200;
set A6 284;
set A3 71;

puts " Create Sections..."
#Section A
set beffA 1047
section fiberSec $STag_BeamA {;# Define the fiber section for the beam
# Define the core patch
    patch quadr $MTag_ConfCB 16 16 -193 79 -193 -79 193 -79 193 79          #Confined Core
    # Define the four cover patches
    patch quadr $MTag_UnConf 2 20 -228.6 114.3 -193 79 193 79 228.6 114.3    #left
    patch quadr $MTag_UnConf 2 20 -193 -79 -228.6 -114.3 228.6 -114.3 193 -79 #right
    patch quadr $MTag_UnConf 20 2 -228.6 114.3 -228.6 -114.3 -193 -79 -193 79 #down
    patch quadr $MTag_UnConf 20 2 193 79 193 -79 228.6 -114.3 228.6 114.3    #up
#Define the flange parts (left & right)
    patch quadr $MTag_UnConf 10 2 76.2 $beffA 76.2 114.3 228.6 114.3 228.6 $beffA
    patch quadr $MTag_UnConf 10 2 76.2 -114.3 76.2 -$beffA 228.6 -$beffA 228.6 -114.3

# Define reinforcement layers
    layer straight $MTag_SteelG60 2 $A6 193 79 193 -79;          # top layer reinforcement
    fiber 193 0 $A5 $MTag_SteelG60
    layer straight $MTag_SteelG60 2 $A6 -193 79 -193 -79;      # bottom layer reinforcement

    layer straight $MTag_SteelG60 6 $A3 101.6 $beffA 101.6 114.3 #lower face of the flange
    layer straight $MTag_SteelG60 6 $A3 101.6 -114.3 101.6 -$beffA
    layer straight $MTag_SteelG60 6 $A3 203.2 $beffA 203.2 114.3 #upper face of the flange
    layer straight $MTag_SteelG60 6 $A3 203.2 -114.3 203.2 -$beffA
};    # end of fibersection definition

#Section B
set beffB 1047
section fiberSec $STag_BeamB {;# Define the fiber section for the beam
# Define the core patch
    patch quadr $MTag_ConfCB 16 16 -193 79 -193 -79 193 -79 193 79          #Confined Core
    # Define the four cover patches
    patch quadr $MTag_UnConf 2 20 -228.6 114.3 -193 79 193 79 228.6 114.3    #left
    patch quadr $MTag_UnConf 2 20 -193 -79 -228.6 -114.3 228.6 -114.3 193 -79 #right
    patch quadr $MTag_UnConf 20 2 -228.6 114.3 -228.6 -114.3 -193 -79 -193 79 #down
    patch quadr $MTag_UnConf 20 2 193 79 193 -79 228.6 -114.3 228.6 114.3    #up
#Define the flange parts (left & right)
    patch quadr $MTag_UnConf 10 2 76.2 $beffB 76.2 114.3 228.6 114.3 228.6 $beffB
    patch quadr $MTag_UnConf 10 2 76.2 -114.3 76.2 -$beffB 228.6 -$beffB 228.6 -114.3

```

```

# Define reinforcement layers
    layer straight $MTag_SteelG60 2 $A6 193 79 193 -79;          # top layer reinforcement
    layer straight $MTag_SteelG60 2 $A6 -193 79 -193 -79;       # bottom layer reinforcement
    layer straight $MTag_SteelG60 2 $A5 -193 26 -193 -26;       # bottom layer reinforcement

    layer straight $MTag_SteelG60 6 $A3 101.6 $beffB 101.6 114.3 #lower face of the flange
    layer straight $MTag_SteelG60 6 $A3 101.6 -114.3 101.6 -$beffB
    layer straight $MTag_SteelG60 3 $A3 203.2 $beffB 203.2 114.3 #upper face of the flange
    layer straight $MTag_SteelG60 3 $A3 203.2 -114.3 203.2 -$beffB
}; # end of fibersection definition

#Section C
set beffC 1047
section fiberSec $STag_BeamC {;# Define the fiber section for the beam
# Define the core patch
    patch quadr $MTag_ConfCB 16 16 -193 79 -193 -79 193 -79 193 79 #Confined Core
# Define the four cover patches
    patch quadr $MTag_UnConf 2 20 -228.6 114.3 -193 79 193 79 228.6 114.3 #left
    patch quadr $MTag_UnConf 2 20 -193 -79 -228.6 -114.3 228.6 -114.3 193 -79 #right
    patch quadr $MTag_UnConf 20 2 -228.6 114.3 -228.6 -114.3 -193 -79 -193 79 #down
    patch quadr $MTag_UnConf 20 2 193 79 193 -79 228.6 -114.3 228.6 114.3 #up
#Define the flange parts (left & right)
    patch quadr $MTag_UnConf 10 2 76.2 $beffC 76.2 114.3 228.6 114.3 228.6 $beffC
    patch quadr $MTag_UnConf 10 2 76.2 -114.3 76.2 -$beffC 228.6 -$beffC 228.6 -114.3

# Define reinforcement layers
    layer straight $MTag_SteelG60 2 $A6 193 79 193 -79;          # top layer reinforcement
    layer straight $MTag_SteelG60 2 $A6 -193 79 -193 -79;       # bottom layer reinforcement
    layer straight $MTag_SteelG60 2 $A5 -193 26 -193 -26;       # bottom layer reinforcement

    layer straight $MTag_SteelG60 6 $A3 101.6 $beffC 101.6 114.3 #lower face of the flange
    layer straight $MTag_SteelG60 6 $A3 101.6 -114.3 101.6 -$beffC
}; # end of fibersection definition

#Section D
set beffD 443
section fiberSec $STag_BeamD {;# Define the fiber section for the beam
# Define the core patch
    patch quadr $MTag_ConfCB 16 16 -193 79 -193 -79 193 -79 193 79 #Confined Core
# Define the four cover patches
    patch quadr $MTag_UnConf 2 20 -228.6 114.3 -193 79 193 79 228.6 114.3 #left
    patch quadr $MTag_UnConf 2 20 -193 -79 -228.6 -114.3 228.6 -114.3 193 -79 #right
    patch quadr $MTag_UnConf 20 2 -228.6 114.3 -228.6 -114.3 -193 -79 -193 79 #down
    patch quadr $MTag_UnConf 20 2 193 79 193 -79 228.6 -114.3 228.6 114.3 #up
#Define the flange parts (left & right)
    patch quadr $MTag_UnConf 10 2 76.2 $beffD 76.2 114.3 228.6 114.3 228.6 $beffD
    patch quadr $MTag_UnConf 10 2 76.2 -114.3 76.2 -$beffD 228.6 -$beffD 228.6 -114.3

# Define reinforcement layers
    layer straight $MTag_SteelG60 2 $A6 193 79 193 -79;          # top layer reinforcement
    fiber 193 0 $A5 $MTag_SteelG60
    layer straight $MTag_SteelG60 2 $A6 -193 79 -193 -79;       # bottom layer reinforcement

    layer straight $MTag_SteelG60 2 $A3 101.6 $beffD 101.6 114.3 #lower face of the flange
    layer straight $MTag_SteelG60 2 $A3 101.6 -114.3 101.6 -$beffD
    layer straight $MTag_SteelG60 2 $A3 203.2 $beffD 203.2 114.3 #upper face of the flange
    layer straight $MTag_SteelG60 2 $A3 203.2 -114.3 203.2 -$beffD
}; # end of fibersection definition

```

```

#Section E
set beffE 882
section fiberSec $STag_BeamE {; # Define the fiber section for the beam
# Define the core patch
    patch quadr $MTag_ConfCB 16 16 -193 79 -193 -79 193 -79 193 79          #Confined Core
    # Define the four cover patches
    patch quadr $MTag_UnConf 2 20 -228.6 114.3 -193 79 193 79 228.6 114.3    #left
    patch quadr $MTag_UnConf 2 20 -193 -79 -228.6 -114.3 228.6 -114.3 193 -79 #right
    patch quadr $MTag_UnConf 20 2 -228.6 114.3 -228.6 -114.3 -193 -79 -193 79 #down
    patch quadr $MTag_UnConf 20 2 193 79 193 -79 228.6 -114.3 228.6 114.3    #up
#Define the flange parts (left & right)
    patch quadr $MTag_UnConf 10 2 76.2 $beffE 76.2 114.3 228.6 114.3 228.6 $beffE
    patch quadr $MTag_UnConf 10 2 76.2 -114.3 76.2 -$beffE 228.6 -$beffE 228.6 -114.3

# Define reinforcement layers
    layer straight $MTag_SteelG60 2 $A6 193 79 193 -79;          # top layer reinforcement
    layer straight $MTag_SteelG60 2 $A6 -193 79 -193 -79;       # bottom layer reinforcement
    layer straight $MTag_SteelG60 2 $A5 -193 26 -193 -26;       # bottom layer reinforcement

    layer straight $MTag_SteelG60 5 $A3 101.6 $beffE 101.6 114.3    #lower face of the flange
    layer straight $MTag_SteelG60 5 $A3 101.6 -114.3 101.6 -$beffE
    layer straight $MTag_SteelG60 3 $A3 203.2 $beffE 203.2 114.3    #upper face of the flange
    layer straight $MTag_SteelG60 3 $A3 203.2 -114.3 203.2 -$beffE
}; # end of fibersection definition

#Section F
set beffF 882
section fiberSec $STag_BeamF {; # Define the fiber section for the beam
# Define the core patch
    patch quadr $MTag_ConfCB 16 16 -193 79 -193 -79 193 -79 193 79          #Confined Core
    # Define the four cover patches
    patch quadr $MTag_UnConf 2 20 -228.6 114.3 -193 79 193 79 228.6 114.3    #left
    patch quadr $MTag_UnConf 2 20 -193 -79 -228.6 -114.3 228.6 -114.3 193 -79 #right
    patch quadr $MTag_UnConf 20 2 -228.6 114.3 -228.6 -114.3 -193 -79 -193 79 #down
    patch quadr $MTag_UnConf 20 2 193 79 193 -79 228.6 -114.3 228.6 114.3    #up
#Define the flange parts (left & right)
    patch quadr $MTag_UnConf 10 2 76.2 $beffF 76.2 114.3 228.6 114.3 228.6 $beffF
    patch quadr $MTag_UnConf 10 2 76.2 -114.3 76.2 -$beffF 228.6 -$beffF 228.6 -114.3

# Define reinforcement layers
    layer straight $MTag_SteelG60 2 $A6 193 79 193 -79;          # top layer reinforcement
    layer straight $MTag_SteelG60 2 $A6 -193 79 -193 -79;       # bottom layer reinforcement
    layer straight $MTag_SteelG60 2 $A5 -193 26 -193 -26;       # bottom layer reinforcement

    layer straight $MTag_SteelG60 5 $A3 101.6 $beffF 101.6 114.3    #lower face of the flange
    layer straight $MTag_SteelG60 5 $A3 101.6 -114.3 101.6 -$beffE
}; # end of fibersection definition

```

6) Column Sections' Definition .tcl File: "columnsections.tcl"

```
puts " Create Identifiers..."
set STag_Col_M 7;
set STag_Col_E 8;

set A20 300;

puts " Create Sections..."

# Interior Column Section
section fiberSec $STag_Col_M {
    # Define the core patch
    patch circ $MTag_ConfCM 10 8 0 0 0 133.5 0 360

    # Define the cover patches
    patch circ $MTag_UnConf 10 2 0 0 133.5 177.8 0 360

    # define reinforcing layers
    layer circ $MTag_SteelM20 6 $A20 0 0 133.5
};

# End Column Section
section fiberSec $STag_Col_E {
    # Define the core patch
    patch circ $MTag_ConfCE 10 8 0 0 0 133.5 0 360

    # Define the cover patches
    patch circ $MTag_UnConf 10 2 0 0 133.5 177.8 0 360

    # define reinforcing layers
    layer circ $MTag_SteelM20 6 $A20 0 0 133.5
};
```

7) Beam Elements' Definition .tcl File: "beamelements.tcl"

```
puts " Create Beam Elements..."
element dispBeamColumn 1101 101 1101 $np $STag_BeamA $beamtransf;
element dispBeamColumn 1102 1101 1102 $np $STag_BeamA $beamtransf;
element dispBeamColumn 1103 1102 1103 $np $STag_BeamB $beamtransf;
element dispBeamColumn 1104 1103 1104 $np $STag_BeamC $beamtransf;
element dispBeamColumn 1105 1104 1105 $np $STag_BeamB $beamtransf;
element dispBeamColumn 1106 1105 1106 $np $STag_BeamD $beamtransf;
element dispBeamColumn 1107 1106 102 $np $STag_BeamD $beamtransf;

element dispBeamColumn 1108 102 1111 $np $STag_BeamD $beamtransf;
element dispBeamColumn 1109 1111 1112 $np $STag_BeamD $beamtransf;
element dispBeamColumn 1110 1112 1113 $np $STag_BeamE $beamtransf;
element dispBeamColumn 1111 1113 1114 $np $STag_BeamF $beamtransf;
element dispBeamColumn 1112 1114 1115 $np $STag_BeamE $beamtransf;
element dispBeamColumn 1113 1115 1116 $np $STag_BeamD $beamtransf;
element dispBeamColumn 1114 1116 103 $np $STag_BeamD $beamtransf;

element dispBeamColumn 1115 103 1121 $np $STag_BeamD $beamtransf;
element dispBeamColumn 1116 1121 1122 $np $STag_BeamD $beamtransf;
element dispBeamColumn 1117 1122 1123 $np $STag_BeamB $beamtransf;
element dispBeamColumn 1118 1123 1124 $np $STag_BeamC $beamtransf;
element dispBeamColumn 1119 1124 1125 $np $STag_BeamB $beamtransf;
element dispBeamColumn 1120 1125 1126 $np $STag_BeamA $beamtransf;
element dispBeamColumn 1121 1126 104 $np $STag_BeamA $beamtransf;

element dispBeamColumn 1201 201 1201 $np $STag_BeamA $beamtransf;
element dispBeamColumn 1202 1201 1202 $np $STag_BeamA $beamtransf;
element dispBeamColumn 1203 1202 1203 $np $STag_BeamB $beamtransf;
element dispBeamColumn 1204 1203 1204 $np $STag_BeamC $beamtransf;
element dispBeamColumn 1205 1204 1205 $np $STag_BeamB $beamtransf;
element dispBeamColumn 1206 1205 1206 $np $STag_BeamD $beamtransf;
element dispBeamColumn 1207 1206 202 $np $STag_BeamD $beamtransf;

element dispBeamColumn 1208 202 1211 $np $STag_BeamD $beamtransf;
element dispBeamColumn 1209 1211 1212 $np $STag_BeamD $beamtransf;
element dispBeamColumn 1210 1212 1213 $np $STag_BeamE $beamtransf;
element dispBeamColumn 1211 1213 1214 $np $STag_BeamF $beamtransf;
element dispBeamColumn 1212 1214 1215 $np $STag_BeamE $beamtransf;
element dispBeamColumn 1213 1215 1216 $np $STag_BeamD $beamtransf;
element dispBeamColumn 1214 1216 203 $np $STag_BeamD $beamtransf;

element dispBeamColumn 1215 203 1221 $np $STag_BeamD $beamtransf;
element dispBeamColumn 1216 1221 1222 $np $STag_BeamD $beamtransf;
element dispBeamColumn 1217 1222 1223 $np $STag_BeamB $beamtransf;
element dispBeamColumn 1218 1223 1224 $np $STag_BeamC $beamtransf;
element dispBeamColumn 1219 1224 1225 $np $STag_BeamB $beamtransf;
element dispBeamColumn 1220 1225 1226 $np $STag_BeamA $beamtransf;
element dispBeamColumn 1221 1226 204 $np $STag_BeamA $beamtransf;
```

```

element dispBeamColumn 1301 301 1301 $np $STag_BeamA $beamtransf;
element dispBeamColumn 1302 1301 1302 $np $STag_BeamA $beamtransf;
element dispBeamColumn 1303 1302 1303 $np $STag_BeamB $beamtransf;
element dispBeamColumn 1304 1303 1304 $np $STag_BeamC $beamtransf;
element dispBeamColumn 1305 1304 1305 $np $STag_BeamB $beamtransf;
element dispBeamColumn 1306 1305 1306 $np $STag_BeamD $beamtransf;
element dispBeamColumn 1307 1306 302 $np $STag_BeamD $beamtransf;

element dispBeamColumn 1308 302 1311 $np $STag_BeamD $beamtransf;
element dispBeamColumn 1309 1311 1312 $np $STag_BeamD $beamtransf;
element dispBeamColumn 1310 1312 1313 $np $STag_BeamE $beamtransf;
element dispBeamColumn 1311 1313 1314 $np $STag_BeamF $beamtransf;
element dispBeamColumn 1312 1314 1315 $np $STag_BeamE $beamtransf;
element dispBeamColumn 1313 1315 1316 $np $STag_BeamD $beamtransf;
element dispBeamColumn 1314 1316 303 $np $STag_BeamD $beamtransf;

element dispBeamColumn 1315 303 1321 $np $STag_BeamD $beamtransf;
element dispBeamColumn 1316 1321 1322 $np $STag_BeamD $beamtransf;
element dispBeamColumn 1317 1322 1323 $np $STag_BeamB $beamtransf;
element dispBeamColumn 1318 1323 1324 $np $STag_BeamC $beamtransf;
element dispBeamColumn 1319 1324 1325 $np $STag_BeamB $beamtransf;
element dispBeamColumn 1320 1325 1326 $np $STag_BeamA $beamtransf;
element dispBeamColumn 1321 1326 304 $np $STag_BeamA $beamtransf;

```

8) Column Elements' Definition .tcl File: "columnelements.tcl"

```

puts " Create Column Elements..."
element dispBeamColumn 01 1 11 $np $STag_Col_E $columntransf;
element dispBeamColumn 02 11 21 $np $STag_Col_E $columntransf;
element dispBeamColumn 03 21 31 $np $STag_Col_M $columntransf;
element dispBeamColumn 04 31 41 $np $STag_Col_M $columntransf;
element dispBeamColumn 05 41 51 $np $STag_Col_E $columntransf;
element dispBeamColumn 06 51 101 $np $STag_Col_E $columntransf;

element dispBeamColumn 11 02 12 $np $STag_Col_E $columntransf;
element dispBeamColumn 12 12 22 $np $STag_Col_E $columntransf;
element dispBeamColumn 13 22 32 $np $STag_Col_M $columntransf;
element dispBeamColumn 14 32 42 $np $STag_Col_M $columntransf;
element dispBeamColumn 15 42 52 $np $STag_Col_E $columntransf;
element dispBeamColumn 16 52 102 $np $STag_Col_E $columntransf;

element dispBeamColumn 21 03 13 $np $STag_Col_E $columntransf;
element dispBeamColumn 22 13 23 $np $STag_Col_E $columntransf;
element dispBeamColumn 23 23 33 $np $STag_Col_M $columntransf;
element dispBeamColumn 24 33 43 $np $STag_Col_M $columntransf;
element dispBeamColumn 25 43 53 $np $STag_Col_E $columntransf;
element dispBeamColumn 26 53 103 $np $STag_Col_E $columntransf;

```



```

element dispBeamColumn 31 04 14 $np $STag_Col_E $columntransf;
element dispBeamColumn 32 14 24 $np $STag_Col_E $columntransf;
element dispBeamColumn 33 24 34 $np $STag_Col_M $columntransf;
element dispBeamColumn 34 34 44 $np $STag_Col_M $columntransf;
element dispBeamColumn 35 44 54 $np $STag_Col_E $columntransf;
element dispBeamColumn 36 54 104 $np $STag_Col_E $columntransf;

element dispBeamColumn 101 101 111 $np $STag_Col_E $columntransf;
element dispBeamColumn 102 111 121 $np $STag_Col_E $columntransf;
element dispBeamColumn 103 121 131 $np $STag_Col_M $columntransf;
element dispBeamColumn 104 131 141 $np $STag_Col_M $columntransf;
element dispBeamColumn 105 141 151 $np $STag_Col_E $columntransf;
element dispBeamColumn 106 151 201 $np $STag_Col_E $columntransf;

element dispBeamColumn 111 102 112 $np $STag_Col_E $columntransf;
element dispBeamColumn 112 112 122 $np $STag_Col_E $columntransf;
element dispBeamColumn 113 122 132 $np $STag_Col_M $columntransf;
element dispBeamColumn 114 132 142 $np $STag_Col_M $columntransf;
element dispBeamColumn 115 142 152 $np $STag_Col_E $columntransf;
element dispBeamColumn 116 152 202 $np $STag_Col_E $columntransf;

element dispBeamColumn 121 103 113 $np $STag_Col_E $columntransf;
element dispBeamColumn 122 113 123 $np $STag_Col_E $columntransf;
element dispBeamColumn 123 123 133 $np $STag_Col_M $columntransf;
element dispBeamColumn 124 133 143 $np $STag_Col_M $columntransf;
element dispBeamColumn 125 143 153 $np $STag_Col_E $columntransf;
element dispBeamColumn 126 153 203 $np $STag_Col_E $columntransf;

element dispBeamColumn 131 104 114 $np $STag_Col_E $columntransf;
element dispBeamColumn 132 114 124 $np $STag_Col_E $columntransf;
element dispBeamColumn 133 124 134 $np $STag_Col_M $columntransf;
element dispBeamColumn 134 134 144 $np $STag_Col_M $columntransf;
element dispBeamColumn 135 144 154 $np $STag_Col_E $columntransf;
element dispBeamColumn 136 154 204 $np $STag_Col_E $columntransf;

element dispBeamColumn 201 201 211 $np $STag_Col_E $columntransf;
element dispBeamColumn 202 211 221 $np $STag_Col_E $columntransf;
element dispBeamColumn 203 221 231 $np $STag_Col_M $columntransf;
element dispBeamColumn 204 231 241 $np $STag_Col_M $columntransf;
element dispBeamColumn 205 241 251 $np $STag_Col_E $columntransf;
element dispBeamColumn 206 251 301 $np $STag_Col_E $columntransf;

element dispBeamColumn 211 202 212 $np $STag_Col_E $columntransf;
element dispBeamColumn 212 212 222 $np $STag_Col_E $columntransf;
element dispBeamColumn 213 222 232 $np $STag_Col_M $columntransf;
element dispBeamColumn 214 232 242 $np $STag_Col_M $columntransf;
element dispBeamColumn 215 242 252 $np $STag_Col_E $columntransf;
element dispBeamColumn 216 252 302 $np $STag_Col_E $columntransf;

element dispBeamColumn 221 203 213 $np $STag_Col_E $columntransf;
element dispBeamColumn 222 213 223 $np $STag_Col_E $columntransf;
element dispBeamColumn 223 223 233 $np $STag_Col_M $columntransf;
element dispBeamColumn 224 233 243 $np $STag_Col_M $columntransf;
element dispBeamColumn 225 243 253 $np $STag_Col_E $columntransf;
element dispBeamColumn 226 253 303 $np $STag_Col_E $columntransf;

```

```

element dispBeamColumn 231 204 214 $np $STag_Col_E $columntransf;
element dispBeamColumn 232 214 224 $np $STag_Col_E $columntransf;
element dispBeamColumn 233 224 234 $np $STag_Col_M $columntransf;
element dispBeamColumn 234 234 244 $np $STag_Col_M $columntransf;
element dispBeamColumn 235 244 254 $np $STag_Col_E $columntransf;
element dispBeamColumn 236 254 304 $np $STag_Col_E $columntransf;

```

9) Masses Definition .tcl File: "masses.tcl"

```

puts " Assign Masses at Joints..."
puts " Mass at each joint: $mass tn"
    mass 101 $mass $mass 0.0;
    mass 102 $mass $mass 0.0;
    mass 103 $mass $mass 0.0;
    mass 104 $mass $mass 0.0;
    mass 201 $mass $mass 0.0;
    mass 202 $mass $mass 0.0;
    mass 203 $mass $mass 0.0;
    mass 204 $mass $mass 0.0;
    mass 301 $mass $mass 0.0;
    mass 302 $mass $mass 0.0;
    mass 303 $mass $mass 0.0;
    mass 304 $mass $mass 0.0;

```

10) Gravity Definition .tcl File: "loads.tcl"

```

puts " Gravity loads applied..."
load 101      0 [expr $weightfact*-46849] 0
load 102      0 [expr $weightfact*-46849] 0
load 103      0 [expr $weightfact*-46849] 0
load 104      0 [expr $weightfact*-46849]0
load 1102     0 [expr $weightfact*-46849]0
load 1103     0 [expr $weightfact*-46849]0
load 1104     0 [expr $weightfact*-46849]0
load 1105     0 [expr $weightfact*-46849]0
load 1112     0 [expr $weightfact*-46849]0
load 1113     0 [expr $weightfact*-46849]0
load 1114     0 [expr $weightfact*-46849]0
load 1115     0 [expr $weightfact*-46849]0
load 1122     0 [expr $weightfact*-46849]0
load 1123     0 [expr $weightfact*-46849]0
load 1124     0 [expr $weightfact*-46849]0
load 1125     0 [expr $weightfact*-46849]0

```

```

load 201      0      [expr $weightfact*-46849] 0
load 202      0      [expr $weightfact*-46849] 0
load 203      0      [expr $weightfact*-46849] 0
load 204      0      [expr $weightfact*-46849]0
load 1202     0      [expr $weightfact*-46849]0
load 1203     0      [expr $weightfact*-46849]0
load 1204     0      [expr $weightfact*-46849]0
load 1205     0      [expr $weightfact*-46849]0
load 1212     0      [expr $weightfact*-46849]0
load 1213     0      [expr $weightfact*-46849]0
load 1214     0      [expr $weightfact*-46849]0
load 1215     0      [expr $weightfact*-46849]0
load 1222     0      [expr $weightfact*-46849]0
load 1223     0      [expr $weightfact*-46849]0
load 1224     0      [expr $weightfact*-46849]0
load 1225     0      [expr $weightfact*-46849]0

load 301      0      [expr $weightfact*-46849] 0
load 302      0      [expr $weightfact*-46849] 0
load 303      0      [expr $weightfact*-46849] 0
load 304      0      [expr $weightfact*-46849]0
load 1302     0      [expr $weightfact*-46849]0
load 1303     0      [expr $weightfact*-46849]0
load 1304     0      [expr $weightfact*-46849]0
load 1305     0      [expr $weightfact*-46849]0
load 1312     0      [expr $weightfact*-46849]0
load 1313     0      [expr $weightfact*-46849]0
load 1314     0      [expr $weightfact*-46849]0
load 1315     0      [expr $weightfact*-46849]0
load 1322     0      [expr $weightfact*-46849]0
load 1323     0      [expr $weightfact*-46849]0
load 1324     0      [expr $weightfact*-46849]0
load 1325     0      [expr $weightfact*-46849]0

```

11) Ground Motion Analysis Command .tcl File: "AnalysisCommand.tcl"

```

variable constraintsTypeDynamic Plain;
constraints $constraintsTypeDynamic ;
variable numbererTypeDynamic RCM
numberer $numbererTypeDynamic
system $systemTypeDynamic
variable TolDynamic 1.e-8;          # Convergence Test: tolerance
variable maxNumIterDynamic 10;      # Convergence Test: maximum number of iterations that will be
performed before "failure to converge" is returned
variable printFlagDynamic 0;        # Convergence Test: flag used to print information on convergence
(optional)      # 1: print information on each step;
variable testTypeDynamic EnergyIncr; # Convergence-test type
test $testTypeDynamic $TolDynamic $maxNumIterDynamic $printFlagDynamic;
variable algorithmTypeDynamic Linear;
algorithm $algorithmTypeDynamic -initial;
integrator AlphaOS 1.0;
variable analysisTypeDynamic Transient
analysis $analysisTypeDynamic

```

Multi-Platform Simulation

For the numerical WCHS the file requirements can be separated in three groups: the numerically assessed structure component-integration module (“OS” Folder), the equivalent to the physical specimen experimental substructure (“NICA1” Folder) and the surrogate numerical component (“NICA2” Folder). The required files for each folder are presented and when necessary the developed script is attached.

Integration Module: Numerically Assessed Structure – “OS” Folder

The .tcl set employed for that standalone analysis is also required for the integration module due to the fact that most of the structure is numerically modelled in the integration module substructure. As a result the file requirements numbering continues from the Standalone section. In other words, the following files are additional to the OpenSees standalone case.

- 12) *dataexchange.dll*: a dynamic library file required for the communication between the various substructures developed by Huang (Huang and Kwon 2017)
- 13) *substructure.dll*: a dynamic library file required for the OpenSees software function as integration module between the various substructures developed by Huang (Huang and Kwon 2017)
- 14) *Structfile1.txt*: the configuration file that connects the integration module with the Substructure 1 (NICA1)
- 15) *Structfile2.txt*: the configuration file that connects the integration module with the Substructure 2 (NICA2)
- 16) *Kinit.txt*: the .txt file that contains the condensed stiffness matrix of the experimentally tested substructure.

The modifications performed within the 1 to 11 .tcl files when required for facilitating the multi-platform simulation in addition to the content of the aforementioned .txt files are presented as follows.

1) Main Ground Motion Analysis .tcl File: “maingm.tcl”

```

...
source columnelements.tcl
source beamelements.tcl
puts "Done"

#Integration Module
#####Pin Connected Column1 8090
element SubStructure 1000 -file Structfile1.txt -Kinit Kinit.txt
#####Overlapping Part Column2 9000
element SubStructure 2000 -file Structfile2.txt -Kinit Kinit.txt
puts "Integration Part OK!"

#Assign Masses
puts "
Assign Masses:"
set mass 17.8; #tn or N sec2 / mm
source masses.tcl
puts "Done"
recorder Node -file [format "OutputGM/NodesDisp2.out"] -time -nodes 1 101 201 301 -dof 1 2 3 disp;

#Gravity Analysis
puts "Gravity Analysis:"
pattern Plain 1 Linear {
source gravityloads.tcl
...

```

2) Nodes Location .tcl File: "nodes.tcl"

```

...
node 2 5486 0 ;
node 4 16458 0 ;
node 11 0 229 ;
node 12 5486 229 ;
node 14 16458 229 ;
node 21 0 458 ;
node 22 5486 458 ;
node 24 16458 458 ;
...

```

3) Boundary Conditions .tcl File: "BC.tcl"

```

...
#fix- node- DOFx- DOFy- DOFz ;
fix 2 1 1 1 ;
fix 4 1 1 1 ;
#diaphragm at each storey
...

```

8) Column Elements' Definition .tcl File: "columnelements.tcl"

```

...
element dispBeamColumn 14 32 42 $np $STag_Col_M $columntransf;
element dispBeamColumn 15 42 52 $np $STag_Col_E $columntransf;
element dispBeamColumn 16 52 102 $np $STag_Col_E $columntransf;

element dispBeamColumn 24 33 43 $np $STag_Col_M $columntransf;
element dispBeamColumn 25 43 53 $np $STag_Col_E $columntransf;
element dispBeamColumn 26 53 103 $np $STag_Col_E $columntransf;
...

```

14) Substructure 1 Configuration File: “Substructure1.txt”

```

#Configuration file for substructures
# Port number
Port = 8090
# Remote server address
IP = 127.0.0.1
# Connected node tag
NumNode = 1
33
# Substructure type (1-opensees (default), 2-zeusNL, 3-Abaqus, 4-VecTor)
SubType = 1
# Number of DOFs of each node
NumDOFs = 2
CommLog = 2

```

Only two DOF are coupled for replicating the experimental setup response

15) Substructure 2 Configuration File: “Substructure2.txt”

```

#Configuration file for substructures
# Port number
Port = 9000
# Remote server address
IP = 127.0.0.1
# Connected node tag
NumNode = 1
33
# Substructure type (1-opensees (default), 2-zeusNL, 3-Abaqus, 4-VecTor)
SubType = 1
# Number of DOFs of each node
NumDOFs = 3
CommLog = 2

```

All the DOF are coupled between the integration and the surrogate substructure modules

16) Condensed Stiffness Matrix at the Interface Location: “Kinit.txt”

51303.11055	0.00000	47070603.92837
0.00000	1800827.68850	0.00000
47070603.92837	0.00000	57583038805.70280

The stiffness matrix is multiplied by 1.3 for improved hybrid simulation stability

Substructure 1: Equivalent to the physical specimen numerical model – “NICA1” Folder

In this section the file requirements for the numerical substructure equivalent to the experimental component are presented. When the experimental hybrid simulation is performed the NICON is employed for capturing the columns response instead of the numerical substructure described in this section. These files must be included on a separate folder (NICA1), are required for the first substructure and are summarized as follows. It should be recalled that for this numerical substructure only the two translational DOF are coupled.

- 4) *material.tcl*: the file that contains the material properties as described in Chapter 4
- 5) *beamsections.tcl*: the file that contains the definition of the beam sections
- 6) *columnsections.tcl*: the file that contains the definition of the column sections
- 12) *dataexchange.dll*: a dynamic library file required for the communication between the various substructures developed by Huang (Huang and Kwon 2017)
- 17) *column1.tcl*: the .tcl file employed for the column’s model development
- 18) *msvcp110d.dll/msvrc11d.dll*: .dll files required for the multi-platform simulation
- 19) *NICA.exe*: the Network Interface for Console Applications required for the multi-platform simulation
- 20) *NICA.cfg*: the configuration file for the NICA in Substructure 1

The files numbered up to 16 are the ones described in the previous sections. The files employed for NICA only are presented as follows.

17) Column’s Model Employed for the Substructure 1: “column1.tcl”

```

#units mm, MPa, sec, N
wipe;                                #
file mkdir Output;                  #
model basic -ndm 2 -ndf 3;
#Geometry Definition
puts "
Geometry Definition:
  Create Nodes..."
node    3      10972    0      ;
node   13      10972   229    ;
node   23      10972   458    ;
node   33      10972  1835    ;
puts " Create Boundary Conditions..."
fix 3 1 1 1;
puts "Done"
#Materials Definition
puts "
Material Definition:"
source materials.tcl
puts "Done"

#Sections Definition
puts "
Beam Sections Definition:"
source beamsections.tcl
puts "Done"

puts "
Column Sections Definition:"
source columnsections.tcl
puts "Done"

#Elements Definition
puts "
Create Elements:"

geomTransf Linear 1;
geomTransf PDelta 2;
geomTransf Corotational 3;

set np 9;

set columntransf 2;
set beamtransf 2;
element dispBeamColumn 21 03 13 $np $STag_Col_E $columntransf;
element dispBeamColumn 22 13 23 $np $STag_Col_E $columntransf;
element dispBeamColumn 23 23 33 $np $STag_Col_M $columntransf;
puts "Done"

recorder Node -file [format "Output/NodesDisp.out"] -time -nodes 3 13 23 33 -dof 1 2 3 disp;

```

20) NICA Configuration File for the Substructure 1: "NICA.cfg"

The configuration file is self-explanatory. The most significant feature is the EFF_DOF, where the coupling between the translational DOF only can be observed.

```
#=====
# Configuration parameters for NICA
# SDOF cantilever model with gravity load
#
# Unit: mm, N, sec
#
# Generated by Oh-Sung Kwon, Ph.D.
# Univ. of Toronto
# Last updated on Nov. 1, 2010
#=====

# Connection port to NICA
Port = 8090

# Application: 1 for Zeus-NL, 2 for OpenSees, 3 for Abaqus, 4 for Vector,
#             and 9 for generic console-in console-out application. Vector has
#             not been implemented yet.
MDL_Type = 2

# Control node numbers
# Note: The sequence of nodes should be consistent with Nodes in SimCor.
MDL_Node = [33]

# Model dimension
# Note: This tag is used only for OpenSees and Abaqus. Ignore for other analysis types.
#       In the current version, 2D 3DOF system and 3D 6DOF system are supported.
MDL_Dim = 2

# Effective DOFs in control point.
# Note: 1.The sequence of DOFs should be consistent with sequence of DOFs in UI-SimCor.
#       2.Use one line per each controlled node.
#       2.For 2D 3DOF model, use DOF 1, 2, 6 (not 1, 2, 3) for x, y, rz DOFs.
EFF_DOF =
1 1 0 0 0 0

# Model file name (include extension)
MODEL = column1.tcl
```

In this section the file requirements for the surrogate numerical substructure are presented. This component is activated both for the numerical and the experimental WCHS. These files must all be included in a separate folder (NICA2), are required for the second substructure and are summarized as follows. For this substructure all the DOF are coupled but only the restoring moment is returned into the integration module.

- 7) *material.tcl*: the file that contains the material properties as described in Chapter 4
- 8) *beamsections.tcl*: the file that contains the definition of the beam sections
- 9) *columnsections.tcl*: the file that contains the definition of the column sections
- 13) *dataexchange.dll*: a dynamic library file required for the communication between the various substructures developed by Huang (Huang and Kwon 2017)
- 18) *msvcpl110d.dll/msvrc11d.dll*: .dll files required for the multi-platform simulation
- 21) *column2.tcl*: the .tcl file employed for the column's surrogate model development
- 22) *NICA-WCHS.exe*: the modified Network Interface for Console Applications required for the weakly-coupled multi-platform simulation
- 23) *NICA.cfg*: the configuration file for the NICA in Substructure 2

The files numbered up to 18 are the ones described in the previous sections. The files employed for NICA only are presented as follows.

21) Surrogate Column's Model Employed for the Substructure 2: "column2.tcl"

```

#units mm, MPa, sec, N
wipe; #
file mkdir Output; #
model basic -ndm 2 -ndf 3;
#Geometry Definition
puts "
Geometry Definition:
Create Nodes..."
node 3 10972 0 ;
node 13 10972 229 ;
node 23 10972 458 ;
node 33 10972 1835 ;
puts " Create Boundary Conditions..."
fix 3 1 1 1;
puts "Done"
#Materials Definition
puts "
Material Definition:"
source materials.tcl
puts "Done"

#Sections Definition
puts "
Beam Sections Definition:"
source beamsections.tcl
puts "Done"

puts "
Column Sections Definition:"
source columnsections.tcl
puts "Done"

#Elements Definition
puts "
Create Elements:"

geomTransf Linear 1;
geomTransf PDelta 2;
geomTransf Corotational 3;

set np 9;

set columntransf 2;
set beamtransf 2;
element dispBeamColumn 21 03 13 $np $STag_Col_E $columntransf;
element dispBeamColumn 22 13 23 $np $STag_Col_E $columntransf;
element dispBeamColumn 23 23 33 $np $STag_Col_M $columntransf;
puts "Done"

recorder Node -file [format "Output/NodesDisp.out"] -time -nodes 3 13 23 33 -dof 1 2 3 disp;

```

23) NICA Configuration File for the Substructure 2: “NICA.cfg”

For this case all the three DOF are coupled between the integration module and the surrogate substructure.

```
#=====
# Configuration parameters for NICA
# SDOF cantilever model with gravity load
#
# Unit: mm, N, sec
#
# Generated by Oh-Sung Kwon, Ph.D.
# Univ. of Toronto
# Last updated on Nov. 1, 2010
#=====

# Connection port to NICA
Port = 9000

# Application: 1 for Zeus-NL, 2 for OpenSees, 3 for Abaqus, 4 for Vector,
#             and 9 for generic console-in console-out application. Vector has
#             not been implemented yet.
MDL_Type = 2

# Control node numbers
# Note: The sequence of nodes should be consistent with Nodes in SimCor.
MDL_Node = [33]

# Model dimension
# Note: This tag is used only for OpenSees and Abaqus. Ignore for other analysis types.
#       In the current version, 2D 3DOF system and 3D 6DOF system are supported.
MDL_Dim = 2

# Effective DOFs in control point.
# Note: 1.The sequence of DOFs should be consistent with sequence of DOFs in UI-SimCor.
#       2.Use one line per each controlled node.
#       2.For 2D 3DOF model, use DOF 1, 2, 6 (not 1, 2, 3) for x, y, rz DOFs.
EFF_DOF =
1 1 0 0 1

# Model file name (include extension)
MODEL = column2.tcl
```

More information about running multi-platform and experimental hybrid simulation can be found in University of Toronto Simulation framework (UT-SIM) website <http://www.ut-sim.ca/> (Mortazavi et al. 2017).